

UNCLASSIFIED

AD NUMBER

AD893701

LIMITATION CHANGES

TO:

Approved for public release; distribution is unlimited.

FROM:

Distribution authorized to U.S. Gov't. agencies only; Test and Evaluation; FEB 1972. Other requests shall be referred to Air Force Weapons Laboratory, Kirtland AFB, NM 87117.

AUTHORITY

AFWL ltr, 6 Nov 1973

THIS PAGE IS UNCLASSIFIED

AD 893701

AFWL-TR-71-156

AFWL-TR-71-156

2

# DYNAMIC FRACTURE CRITERIA OF HOMOGENEOUS MATERIALS

L. Seaman  
T. W. Barbee, Jr.  
D. R. Curran  
Stanford Research Institute



AD No. \_\_\_\_\_  
DDC FILE COPY

TECHNICAL REPORT NO. AFWL-TR-71-156

February 1972

**AIR FORCE WEAPONS LABORATORY**  
Air Force Systems Command  
Kirtland Air Force Base  
New Mexico



Distribution limited to US Government agencies only because of test and evaluation (February 1972). Other requests for this document must be referred to AFWL (SRR), Kirtland AFB, NM 87117

**Best  
Available  
Copy**

AIR FORCE WEAPONS LABORATORY  
Air Force Systems Command  
Kirtland Air Force Base  
New Mexico 87117

When US Government drawings, specifications, or other data are used for any purpose other than a definitely related Government procurement operation, the Government thereby incurs no responsibility nor any obligation whatsoever, and the fact that the Government may have formulated, furnished, or in any way supplied the said drawings, specifications, or other data, is not to be regarded by implication or otherwise, as in any manner licensing the holder or any other person or corporation, or conveying any rights or permission to manufacture, use, or sell any patented invention that may in any way be related thereto.

DO NOT RETURN THIS COPY. RETAIN OR DESTROY.

WHITE SECTION <input type="checkbox"/>	
BUFF SECTION <input checked="" type="checkbox"/>	
BY _____	
DISTRIBUTION/AVAILABILITY CODES	
DIST.	AVAIL. and/or SPECIAL
B	



DYNAMIC FRACTURE CRITERIA OF  
HOMOGENEOUS MATERIALS

L. Seaman  
T. W. Barbee, Jr.  
D. R. Curran

Stanford Research Institute

TECHNICAL REPORT NO. AFWL-TR-71-156

Distribution limited to US Government agencies only because of test and evaluation (February 1972). Other requests for this document must be referred to AFWL (SRR), Kirtland AFB, NM 87117

FOREWORD

This report was prepared by the Stanford Research Institute, Menlo Park, California, under Contract F29601-7-0000. The research was performed under Program Element 61102H, Project 5710, Task AA114, and was funded by the Defense Nuclear Agency (DNA).

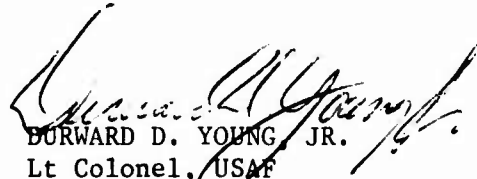
Inclusive dates of research were June 1970 through October 1971. The report was submitted 11 January 1972 by the Air Force Weapons Laboratory Project Officer, Major Charles S. Lee (SRR).

The contractor report number is SRI Project PYU 8678.

This report has been reviewed and is approved.



CHARLES S. LEE  
Major, USAF  
Chief, Radiation Response Branch



EDWARD D. YOUNG, JR.  
Lt Colonel, USAF  
Chief, Radiation Division

## ABSTRACT

(Distribution Limitation Statement B)

A successful computational and experimental procedure has been developed for predicting shock-induced damage in brittle and ductile materials. This procedure results in the determination of two material functions namely, the nucleation rate and the growth rate for microscopic voids, which eventually coalesce to form fracture. These nucleation and growth rate material functions are dependent on stress, temperature, and time. During this project we have measured the stress and time dependence of these functions at room temperature for 1145 Al, OFHC copper, and Armco iron. Additional but less complete data have been obtained for 2024-T81 Al, high purity Al, high purity iron, and Los Alamos Scientific Laboratory (LASL) graphite.

The dependence of the growth rate functions on other material properties has been found in some detail for ductile aluminum and copper and for brittle Armco iron. A comparable understanding of the measured nucleation rate functions has not yet been attained.

In addition to the progress listed above, the following new contributions have been made during the course of the project:

- Development of a computer code, BABS 2, which converts observed crack surface distributions to crack volume distributions, and which shows promise of wide application.
- Development of computer subroutines DFRACT and BFRACT which, together with SRI PUFF, allow the computation of stress waves in materials that undergo ductile fracture by void growth or brittle fracture by crack growth.
- Development of the computer code VOID, which computes void growth and collapse in two space dimensions. Modifications of the code are already in use at Stanford Research Institute in applications ranging from cavitation in liquid propellants

to prediction of impact damage in human heads. This finite element code includes a new method for computing momentum transfer and utilizes a multidimensional stress relaxation model.

- Development of an experimental technique, using a tapered projectile head, for obtaining incipient damage data from a single impact experiment.
- Development of constitutive relations for damaged material.

## CONTENTS

<u>Section</u>		<u>Page</u>
I	INTRODUCTION	1
II	CONCLUSIONS AND RECOMMENDATIONS	4
III	DUCTILE FRACTURE	8
	1. Ductile Fracture Mechanisms	8
	2. Ductile Fracture Model	1
	a. Nature of the Model	1
	b. Nucleation Rate	14
	c. Growth Rate and Growth Threshold	19
	d. Constitutive Relations	22
	3. Experimental Observations	23
	a. 1145 Aluminum	24
	b. High Purity Aluminum	32
	c. 2024-T81 Aluminum	39
	d. OFHC Copper	45
	4. Quantifying the Damage	48
	5. Wave Propagation Calculations and Comparison with Data	55
	a. Nucleation Rate	55
	b. Void Growth	56

CONTENTS (Continued)

<u>Section</u>	<u>Page</u>
c. Constitutive Relations	63
d. Wave Propagation Results	67
6. Simplified Damage Criteria	82
a. Void Growth Criterion	83
b. Void Volume Criterion	89
c. Example of the Use of Simplified Damage Criteria: OFHC Copper	90
7. Summary of Ductile Fracture	96
IV BRITTLE FRACTURE	97
1. Brittle Fracture Model	97
a. Nature of the Model	97
b. Nucleation Rate	99
c. Growth Rate and Growth Threshold	100
d. Constitutive Relations	101
2. Experimental Phase	102
a. Graphite	103
b. Armco Iron	125
c. 99.9 Percent Pure Iron	133
3. Quantifying the Damage	138

## CONTENTS (Concluded)

<u>Section</u>	<u>Page</u>
4. Wave Propagation Calculations and Comparison with Data	144
a. Nucleation Rate	144
b. Crack Growth	144
c. Constitutive Relations	145
d. Wave Propagation Results	146
5. Summary of Brittle Fracture	157
APPENDICES	
I TAPERED FLYER TECHNIQUE	159
II OTHER EXPERIMENTAL TECHNIQUES	163
III DYNAMIC SPHERICAL BUBBLE GROWTH	167
IV STATIC SPHERICAL GROWTH OF VOIDS	180
V TWO-DIMENSIONAL VOID GROWTH CALCULATIONS: VOID	202
VI MATERIAL VISCOSITY DERIVED FROM THE STEADY-STATE SHOCK FRONT	281
VII DUCTILE FRACTURE SUBROUTINE: DFRAC	292
VIII BRITTLE FRACTURE SUBROUTINE: BFRAC	311
IX STATISTICAL ANALYSIS OF CRACKS	331
X STATISTICAL ANALYSIS PROGRAM: BABS 2	352
REFERENCES	365

## ILLUSTRATIONS

<u>Figure</u>	<u>Page</u>
1 Modes of Ductile Fracture	9
2 Damage Observed in 1145 Aluminum for a Constant Shot Geometry (i.e., Time at Stress) for Increasing Impact Velocities (i.e., Stress)	15
3 Distribution of Voids: Shot 849	16
4 Effect of Damage (Voids) on Stress History at Damage Plane of an 8.2 kbar Tension Shot in 1145 Al	17
5 Comparison of Void Distributions with Time at Stress Distribution in 1145 Aluminum	18
6 Void Radius at Constant Void Concentration, Plotted as a Function of Time at Stress	20
7 Micrographs of Damage Achieved in a Single Tapered Flyer Shot on 1145 Al (Shot S4)	28
8 Micrographs of 1145 Aluminum Samples Impacted at 400°C (Shot S34)	29
9 Micrographs of 1145 Aluminum Samples Impacted at Room Temperature and 400°C	31
10 Shock Damage in High Purity Aluminum	35
11 Full Separation in High Purity Aluminum	36
12 Comparison of Fracture Surfaces for 1145 and High Purity Aluminum	37
13 Stereo Pair of the Fracture Surface of High Purity Aluminum	38



ILLUSTRATIONS (Continued)

<u>Figure</u>		<u>Page</u>
14	Nucleation Sites and Structure at Joining of Voids	39
15	Damage in the Form of Ductile Cracks that Follow Stringer Planes as a Function of Impact Velocity (Stress) at Constant Sample Projectile Geometry (Time at Stress) for 2024-T81 Aluminum	42
16	Cracking of Inclusions in 2024-T81 Aluminum	43
17	Damage Observed in Three Tapered Flyer Experiments in OFHC Copper	47
18	Stress Wave Position in an Impact Specimen and the Derived Duration of the Peak Tensile Stress for a Simple Square Wave with an Elastic Precursor	49
19	Photomicrographs Ruled into Zones for Counting of Voids	50
20	Surface Distributions of Voids on the Free Surface Side of the Spall Plane in OFHC Copper: Shot S24	53
21	Volume Distribution of Voids on the Free Surface Side of the Spall Plane in OFHC Copper : Shot S24	54
22	Comparison of Void Size Distributions with a Constant and a Variable Form	62
23	Computed and Observed Damage in 1145 Al: Shot 847	70
24	Computed and Observed Damage in 1145 Al: Shot 873	71
25	Computed and Observed Damage in 1145 Al: Shot 849	72
26	Computed and Observed Damage in 1145 Al: Shot 872	73
27	Computed and Observed Damage in 1145 Al: Shot 939	74
28	Computed and Observed Damage in OFHC Copper: Shot S24	76

## ILLUSTRATIONS (Continued)

<u>Figure</u>		<u>Page</u>
29	Computed and Observed Damage in OFHC Copper: Shot S27	77
30	Comparison of Stress Record from Manganin Gage in PMMA Behind OFHC Copper with Computed Stress: Shot S24	79
31	Comparison of Stress Record from Manganin Gage in PMMA Behind OFHC Copper with Computed Stress: Shot S27	80
32	Damage Distribution Observed in a Tapered Flyer Shot on Armco Iron (Shot S1)	98
33	Cutaway View of Quasi-static Compression Device	106
34	Static Compression and Unloading Curves for LASL Graphite	108
35	Comparison of Static and Dynamic Compression Curves for Several Graphites	112
36	Comparison of Shock Velocity-Particle Velocity Data Generated from Static and Dynamic Experiments on Graphite	113
37	Comparison of Stress-Particle Velocity Data Generated from Static and Dynamic Experiments on Graphite	114
38	Intermediate Damage in LASL Graphite, Shot S36	117
39	Intermediate Damage in LASL Graphite: Radiograph of Sample from Shot S36	118
40	Heavy Damage in LASL Graphite: Radiograph of Sample from Shot S49	118
41	Full Separation of LASL Graphite: Shot S35	119
42	Light Damage in LASL Graphite: Shot S41	120
43	Isodamage Curves for LASL Graphite	122
44	Damage Distribution Observed in a Tapered Flyer Shot on Armco Iron: Shot S1	128
45	Effect of Damage on Stress-Strain Curves of Armco Iron	132
46	Effect of Damage on the Ultimate Tensile Strength and the Yield Strength of Armco Iron	133
47	Threshold Damage in 99.9% Pure Iron	135

ILLUSTRATIONS (Continued)

<u>Figure</u>		<u>Page</u>
48	Intermediate Damage in 99.99% Pure Iron	136
49	Details of Fracture Surface in 99.99% Pure Iron	137
50	Circular Crack Intersecting the Plane of Polish	140
51	Cumulative Crack Surface Concentration for Armco Iron: Shot S25	142
52	Computed Cumulative Crack Volume Concentration for Armco Iron: Shot S25	143
53	Crack Size Distributions in Zones Near the Spall Plane in Armco Iron: Shot 886	149
54	Computed Crack Size Distributions for Armco Iron: Shot 886	150
55	Crack Size Distributions in Zones Near the Spall Plane in Armco Iron: Shot S25	151
56	Computed Crack Size Distributions for Armco Iron: Shot S25	152
57	Comparison of Computed and Experimental Concentrations of Cracks Larger than 40 Microns in Armco Iron: Shot 886	153
58	Comparison of Computed and Experimental Concentrations of Cracks Larger than 40 Microns in Armco Iron: Shot S25	154
59	Comparison of Stress Record from a Manganin Gage with the Computed Stress History of Armco Iron: Shot S25	155
60	Schematic Curve Showing the Time Dependence of the Stress for Threshold Damage	159
61	Time at Stress as a Function of Position in a Sample Impacted with a Tapered Flyer: Shot S1	161
62	Damage Observed in Shot S1, a Tapered Flyer Shot on Armco Iron	162
63	Experimental System for Dynamic Flyer Plate Experiments	164
64	Target Plate Assembly Showing Tapered Specimen (Plug)	166

ILLUSTRATIONS (Continued)

<u>Figure</u>		<u>Page</u>
65	Growth Velocity of a Void as a Function of Void Radius: Comparison of Numerical and Analytical Results for a Tensile Stress of 10 kbar	175
66	Relationship Between Velocity and Void Radius as a Function of Stress Level	177
67	Geometry and Nomenclature for Spherical Void	182
68	Trajectories of the Void Radius, Elastic-Plastic Boundary, and Selected Radii for Tensile Loading where yield = 2 kbar	188
69	Relationship Between Flow Stress and Yield Strength in Tension	189
70	Relation Between Stress and Specific Volume for Porous Material under Tension, where yield = 2 kbar	191
71	Variation of Bulk Modulus with Tensile Load on a Porous Material	192
72	Variation of Elastic Bulk Modulus from MacKenzie's Equation and the Present Results	193
73	Trajectories of the Void Radius, Elastic-Plastic Boundary, and Selected Radii for a Porous Material under Compression, where yield = 2 kbar	194
74	Stress Versus Specific Volume for Porous Materials Undergoing Compression, where yield = 2 kbar	195
75	Variation of Bulk Modulus during Compressive Loading on Materials with Various Porosities, where yield = 2 kbar	196
76	Cell Layout for Axisymmetric Void Problem	205
77	Types of Cells for Stress and Momentum Computations	209
78	Stress and Coordinate Nomenclature for a Cell	210
79	Quadrilateral Element Produced from Two Triangles	214
80	Response of Viscous and Stress Relaxation Models to a Constant Shear Rate for the Case $T = \Delta t$	222

ILLUSTRATIONS (Concluded)

<u>Figure</u>		<u>Page</u>
81	Variations of Axial Stress and Pressure with Time for Computation 5	236
82	Successive Void Surfaces During Calculation 4	237
83	Eccentricity of the Void and of the Loading	238
84	Pressure-Volume Relation from Calculation 4	240
85	Pressure-Volume Relation from Calculation 5	241
86	Pressure-Volume Relation from Calculation 8	242
87	Variation of $\alpha$ from Computations 4 and 5	244
88	Deviator Stress Variations from Calculation 4	245
89	Deviator Stress Variations from Calculation 5	246
90	Deviator Stress Variations from Calculation 8	247
91	Void Growth Velocity as a Function of Pressure from Calculation 4	249
92	Void Growth Velocity as a Function of Pressure from Calculation 5	250
93	Void Growth Velocity as a Function of Pressure from Calculation 8	251
94	Shock Front Thickness as a Function of Stress Level	288
95	Nondimensional Shock Front Thickness as a Function of Stress Level	289
96	Shock Front Profiles at Several Stress Levels	290
97	Circular Crack Intersecting Plane of Polish	332
98	Region of Integration for Computing Elements of the Angle Function, $G_{ir}$	344
99	Test Case: Computed Volume Distributions Compared with True Volume Distributions	348

## TABLES

<u>Table</u>		<u>Page</u>
I	Levels of Dynamic Fracture Analysis Completed for the Materials Studied	5
II	Summary of Dynamic Flyer Plate Experiments in 1145 Aluminum	26
III	Summary of Dynamic Flyer Plate Experiments in 99.999% Pure Aluminum	32
IV	Summary of Dynamic Flyer Plate Experiments in 2024-T81 Aluminum	41
V	Summary of Dynamic Flyer Plate Experiments in OFHC Copper	46
VI	Impact Conditions for Experiments in 1145 Aluminum	69
VII	Ductile Fracture Parameters for 1145 Aluminum and OFHC Copper	69
VIII	Impact Conditions for Experiments in OFHC Copper	75
IX	Mechanical Viscosities of Copper and Aluminum at High Strain Rates	91
X	Predicted Damage Threshold Conditions for OFHC Copper	93
XI	Predicted and Experimentally Observed Damage Threshold Conditions for 3/4 Hard OFHC Copper	95
XII	Measured Wave Velocities and Calculated Elastic Constants for Graphite	110
XIII	Dynamic Fracture Experiments for Graphite	116
XIV	Summary of Dynamic Flyer Impact Experiments for Armco Iron	127

TABLES (Concluded)

<u>Table</u>		<u>Page</u>
XV	Summary of Dynamic Flyer Plate Experiments in 99.99% Pure Iron	134
XVI	Brittle Fracture Parameters	147
XVII	Impact Conditions for Experiments in Armco Iron	147
XVIII	Void Growth Computations	235

## NOMENCLATURE

A	$(p - p_0)/4\eta$ , a viscous growth parameter, 1/sec
B	viscous drag coefficient, dyn-sec/cm <sup>2</sup>
$C_L$	longitudinal wave velocity, cm/sec
$C_s$	shear velocity, cm/sec
D	gross density, gm/cm <sup>3</sup>
E	Young's modulus, dyn/cm <sup>2</sup>
K	bulk modulus, dyn/cm <sup>2</sup>
$K_{IC}$	fracture toughness in the opening mode, dyn/cm <sup>3/2</sup>
N	number of voids or cracks, number/cm <sup>3</sup>
$\dot{N}$	nucleation rate of voids or cracks, number/cm <sup>3</sup> /sec
$N_0$	total number of voids, number/cm <sup>3</sup>
$N_g(R)$	number of voids greater than R, number/cm <sup>3</sup>
$N_i(\sigma, t)$	number of observed voids that intersect a surface, number/cm <sup>2</sup>
$P_{0s}$	pressure in solid at zero time, dyn/cm <sup>2</sup>
$P_s$	pressure in solid material, dyn/cm <sup>2</sup>
R	radius of void, or one-half the length of a crack, cm
$R^*$	critical crack radius, cm
$R_0$	initial void radius, cm



$R_1$	parameter of a void size distribution, cm
$R_2$	void distribution parameter following some growth, cm
$R_{10}$	value of $R_1$ at zero time, cm
$R_{cr}$	upper limit of void radius for which the viscous growth law is valid, cm
$R_n$	parameter in the distribution of nucleated voids, cm
$V$	gross specific volume, $\text{cm}^3/\text{gm}$
$V_c$	growth velocity for cracks, cm/sec
$V_D$	dislocation velocity, cm/sec
$V_n$	nucleated volume of voids per unit volume of material, dimensionless
$V_s$	specific volume of solid material, $\text{cm}^3/\text{gm}$
$V_t$	terminal growth velocity for cracks, cm/sec
$V_v$	volume of voids per unit mass of solid, $\text{cm}^3/\text{gm}$
$V_{vr}$	void volume per unit volume of material, dimensionless
$W$	true crack opening displacement, cm
$Y$	yield strength, $\text{dyn}/\text{cm}^2$
$a_n$	parameter of a void size distribution
$\vec{b}$	dislocation Burger's vector, cm
$c$	one half the length of the crack trace in the plane of polish, cm
$\dot{n}_0$	constant crack or void nucleation rate, number/ $\text{cm}^3/\text{sec}$
$p$	pressure, $\text{dyn}/\text{cm}^2$
$p_0$	threshold pressure, $\text{dyn}/\text{cm}^2$
$p_1$	parameter in the void nucleation function, $\text{dyn}/\text{cm}^2$

$p_a$	average pressure on gross section of porous material, dyn/cm <sup>2</sup>
$p_l$	local pressure, average of three principal stresses, dyn/cm <sup>2</sup>
$p_{n0}$	nucleation threshold pressure, dyn/cm <sup>2</sup>
$r$	radius of circle of intersection of a void with a plane, cm
$t$	time or duration, sec
$t(z)$	duration of peak tensile stress at position $z$ , sec
$v$	volume of a crack, cm <sup>3</sup>
$w$	width of the crack opening in the plane of polish, cm
$x$	position, cm
$x$	distance into the plane of polish, cm
$y$	location coordinate for apparent center of crack, in plane of polish and directed normal to direction of the major stress, cm
$z$	location coordinate for apparent center of crack, in plane of polish and in direction of major stress, cm
$\alpha$	angle between the normal to the trace of the crack on the plane of polish and the $z$ axis
$\alpha_c$	constant relating void volume to relative void area on a plane
$\gamma$	surface energy, erg/cm <sup>2</sup>
$\dot{\gamma}$	plastic shear strain rate, 1/sec
$\gamma_c$	critical apparent surface energy or crack extension force, erg/cm <sup>2</sup>
$e$	strain
$\eta$	material viscosity, poise or dyn-sec/cm <sup>2</sup>
$\theta$	angle of rotation around the $z$ axis
$\mu$	shear modulus, dyn/cm <sup>2</sup>

$\nu$	Poisson's ratio
$\rho$	density, gm/cm <sup>3</sup>
$\rho$	number of cracks per unit volume, number/cm <sup>3</sup>
$\rho_m$	mobile dislocation density, number/cm <sup>2</sup>
$\rho(R)$	concentration of voids at the radius R, number/cm <sup>4</sup>
$\sigma$	stress, dyn/cm <sup>2</sup>
$\sigma'$	deviator stress, dyn/cm <sup>2</sup>
$\sigma_0$	threshold stress for growth
$\sigma_1$	parameter in the nucleation function for cracks, dyn/cm <sup>2</sup>
$\sigma_F$	critical stress for brittle fracture, dyn/cm <sup>2</sup>
$\sigma_{n0}$	threshold stress for nucleation, dyn/cm <sup>2</sup>
$\sigma_y$	stress at yield, dyn/cm <sup>2</sup>
$t$	time, sec
$\psi$	angle between the z axis and the normal to the actual crack surface

## SECTION I

### INTRODUCTION

Dynamic fracture by plane (or nearly plane) stress waves is an important response mode in reentry vehicles exposed to intense bursts of radiation. This response mode is important for reentry vehicle survivability studies and also for Anti-Ballistic Missile (ABM) fratricide studies because it occurs at relatively low fluence. It may also be important in heavy damage studies because it can affect the momentum distribution in the vehicle wall. The present program has been motivated by the reentry vehicle survivability problem; however, the results apply to the other two problems as well. Dynamic fracture caused by stress waves is also important in other applications, such as in fragmentation weapons and lightweight ceramic armor.

The need for understanding dynamic fracture is particularly important for radiation spectra for which laboratory simulation methods are inadequate. With such an understanding, it will be possible to produce a critical damage curve giving the fluence needed to produce fracture as a function of spectrum. Such a capability is important in planning nuclear weapons effects tests and in interpreting and generalizing the test results. An example of the successful application of the present fracture work in interpreting nuclear test results is given in Volume Two of reference 1.

The goal of our work has been to predict in detail the microscopic damage induced in ductile and brittle materials by known shock-loading histories. This goal has to a great extent been reached; the degree to

which successful predictions can now be made is discussed in detail in this report.

Dynamic fracture by stress waves differs from static fracture in that the duration of the stress causing fracture is very short--often a microsecond or less. It has been shown in this program that under such short duration loads the fracture process can be described by the nucleation and growth of voids or cracks, which ultimately coalesce to produce fracture. The approach has been to use plane impacts to determine experimentally the stress-dependent nucleation rates and growth rates for internal damage. These functions govern the development of damage and, hence, of fracture and can be used with arbitrary stress histories (as observed, for example, in the radiation environment) to predict the extent and location of damage.

The nucleation rate and growth rate functions are determined from experiments using known stress histories (from flying plates, for example). The stress history is calculated using a PUFF code with appropriate constitutive relations. Unmodified constitutive relations for the material can be used to calculate the stress history for small amounts of damage. However, for even moderate damage levels the effect of the damage on the stress history is significant, and a modified equation of state is used that treats the material as a porous solid consisting of damaged regions and undamaged regions.

After loading by a known pulse, the specimen is sectioned normal to the damage plane; this shows the intersection of the damage with the plane of the section. In ductile fracture the internal damage appears as spherical voids, and in brittle fracture it appears as plane cracks. An important aspect of the analysis is determination of the volume distribution of damage from such surface observations.

Thus, with this approach, the main components in developing a method for predicting fracture by stress waves are:

- To load dynamically and to recover specimens.
- To achieve experimental control so that the damage can be stopped in different stages of growth.
- To describe quantitatively the size and the spatial distribution of damage in the volume of the material.
- To specify the macroscopic stress and the stress duration at any location in the specimen under conditions of nucleation and growth of damage.

The nucleation rate and growth rate functions can be determined completely by combining the information gained in the steps above. However, theoretical work in the nucleation and growth processes has made it possible to obtain estimates of these functions for materials other than those tested.

During the course of this project we have studied dynamic ductile fracture in aluminum, aluminum alloys, and copper, and dynamic brittle fracture in iron and graphite. In this report we first summarize our conclusions and recommendations in Section II and then describe the main features of our work on ductile fracture (Section III) and on brittle fracture (Section IV). In addition, in a series of ten appendices we describe in detail our experimental techniques (Appendices I and II), our mathematical models related to growth of damage (Appendices III through VI), and the computer codes that were developed for this program (Appendices V and VII through X). These codes calculate void growth in two dimensions, stress wave propagation in partially fractured material, and the statistical transformation of void surface distributions to void volume distributions.

## SECTION II

### CONCLUSIONS AND RECOMMENDATIONS

A successful experimental and computational procedure has been developed for predicting shock-induced damage in brittle and ductile materials. This procedure results in the determination of two material functions, namely, the nucleation rate and the growth rate for microscopic voids and cracks, which eventually coalesce to form fracture. These nucleation and growth rate material functions are dependent on stress, temperature, and time. During this project we have measured the stress and time dependence of these functions at room temperature for 1145 Al, OFHC copper, and Armco iron. Additional but less complete data have been obtained for 2024-T81 Al, high purity Al, high purity iron, and LASL graphite.

Although the nucleation and growth rate functions for damage in brittle and ductile materials are valid material properties, it is desirable to understand their dependence on other microscopic material properties because damage predictions could then be made for other, similar materials. We have been largely successful in gaining such an understanding of the growth rate functions for the ductile and brittle metals studied. A comparable understanding of the measured nucleation rate functions has not yet been attained, although several promising avenues of research are evident.

In Table I we list the materials studied during the course of our dynamic fracture work and the varying levels of analysis completed for each material.

Table I

LEVELS OF DYNAMIC FRACTURE ANALYSIS COMPLETED FOR THE MATERIALS STUDIED

Material	Number of Controlled Impact Experiments	Metallographic Examination	Quantitative Description of Damage	Code Calculations of Stress Histories in Materials with Growing Damage	Determination of Damage Nucleation and Growth Functions N and R	Complete Fracture Model (Understanding of Dependence of Nucleation Rate and Growth Rate on Other Material Properties)
Ductile						
1145 Al	9	●	●	●	●	●
OFHC Cu	8	●	●	●	●	●
2024-T81 Al	4	●	●	●	●	●
99.999% Al	4	●	○	○	○	○
Brittle						
Armco Fe	7	●	●	●	●	●
99.99% Fe	4	●	○	○	○	○
LASL graphite	12	●	○	○	○	○

Legend: ● Task completed.  
 ◐ Task partially completed.  
 ○ Task uncompleted.



In the course of the project, computer codes were written to calculate stress histories in fracturing brittle and ductile materials. In addition, several auxiliary computer codes were developed that show promise of wide application. One of these codes, BABS2, converts observed crack surface distributions to crack volume distributions. Another of these codes, VOID, computes void growth and collapse in two space dimensions. Modifications of this code are already in use at Stanford Research Institute (SRI) in applications ranging from cavitation in liquid propellants to prediction of impact damage in human heads. This code has, of course, direct application to wave propagation in porous materials.

Productive areas of future research include the following:

- Metals:
  - Study the dependence of the damage nucleation rate on other microscopic material properties in ductile and brittle metals.
  - Extend the study to obtain the nucleation and growth rate functions for other metals of interest. (This is currently being done for beryllium under contract to the Air Force Weapons Laboratory.)
  - Correlate results of dynamic and static tests to find the values of the nucleation and growth rate functions over a wide range of loading rates. This is a possible approach to the problem of determining fracture toughnesses ( $K_{Ic}$ ) of ductile materials.
- Composites: Apply the procedure for measuring nucleation and growth rate functions to composite materials such as the new carbon-carbon heat shield materials.
- Graphite: The preliminary work performed at SRI and elsewhere on the dynamic fracture of graphite indicates that the fracturing behavior of this brittle material is strongly dependent on microstructure and porosity. This dependence could be profitably investigated further using the techniques developed in this program.
- Correlation of underground nuclear test data: In reference 1 it was shown that the fracture model developed in this project was able to predict correctly the location and extent of shock damage

in a metal sample exposed to radiation deposition in an underground nuclear test. It would appear fruitful to extend this work to fracture data that have been gathered in past underground nuclear tests. These data need further analysis coordinated with computations made with the fracture model developed on this program to provide a reliable prediction of damage under radiation deposition.

## SECTION III

### DUCTILE FRACTURE

In this section we will discuss the work performed on the metals that exhibited ductile fracture by nucleation and growth of spherical voids under dynamic loading.

We will first present an overview of our approach to the ductile fracture problem and will then describe in detail our experimental observations and our methods of data analysis. This will be followed by a discussion of the stress history calculations and illustrations of the results of these computations. We will next describe simplified damage criteria that can be used to predict approximate levels of damage in shock-loaded samples. Finally, a summary of the results of our ductile fracture work will be given.

#### 1. DUCTILE FRACTURE MECHANISMS

The term "ductile fracture" implies failure or fracture occurring after large plastic deformation. This is not wholly accurate since cleavage or brittle failure can also occur after substantial plastic deformation in some materials. Ductile fracture under quasi-static conditions is commonly characterized by failure described as cup-and-cone, following the formation of a neck in the sample after significant deformation. This classic form of failure (cup-and-cone) results from a complex process arising from the stress distribution experienced in a uniaxial tensile test and the work-hardening characteristics of the material being tested.

Three general modes of ductile fracture are classified by the macroscopic form of the fractured sample, as shown in Fig. 1. The first, the cup-and-cone, is the classic type; it is observed in ductile materials having an average work-hardening and a relatively high inclusion or imperfection content. The second is a double cup-and-cone that is observed in ductile materials with an average work-hardening and a low inclusion

The third, planar, is characteristic of high-strength materials with a high inclusion content and a low work-hardening rate.

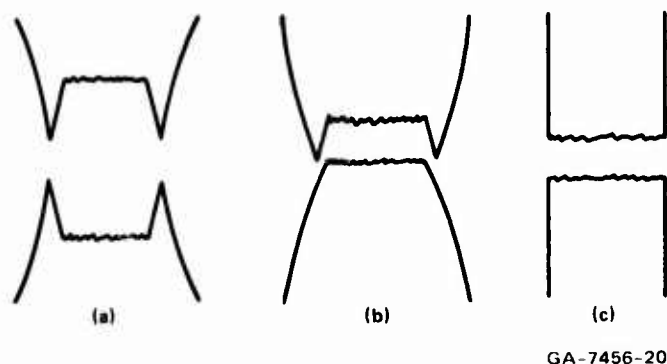


FIGURE 1 MODES OF DUCTILE FRACTURE:

- (a) Double cup-and-cone;
- (b) Cup-and-cone;
- (c) Planar.

The formation of these macroscopic structures is dependent on microscopic fracture mechanisms and the development of the neck. Necking occurs when the increase in tensile stress due to the reduction in cross-sectional area resulting from plastic deformation cannot be supported by the concurrent strain hardening. Once a neck is formed a triaxial stress state occurs in the neck region because of its nonuniformity. This stress state is important in controlling the fracture characteristics.

Metallographic examination of sections of the neck region in deformed metals has shown that in the early stages of necking only slip is occurring.

Upon larger deformation small voids are observed that grow and coalesce into cracks leading to failure. The nucleation and growth of these voids is directly related to the triaxial stress state in the necked region. These pores form at small inclusions or particles of a second phase in the material. This has been substantiated for copper of varying purity, aluminum, iron, and various iron alloys.

Electron micrographs of replicas taken from the fracture surfaces of ductile metals have shown that they are covered with dimples varying in diameter from a few microns to over 100  $\mu$ . These dimples often contain inclusions indicating that voids were nucleated at inclusions. The areas showing this simple structure in Figure 1 are the flat regions. The cone areas result from rapid shear occurring after the central regions have failed.

Of the materials studied here 1145 Al, pure Al, and OFHC copper represent low-strength ductile materials that exhibit failure modes (a) or (b) shown in Figure 1 because they have a high strain-hardening rate and are of commercial purity, containing few microscopically observable inclusions. The 2024-T81 aluminum exhibits failure by mode (c) of Figure 1 because of its high strength, low strain hardening, and high inclusion content.

The observations above on static fracture of ductile materials are pertinent to the understanding dynamic fracture. Under plate impact loading, one-dimensional strain conditions are imposed on the material. In this state large triaxial tensile stresses develop during loading. Then, depending on the mechanisms for nucleation, voids may nucleate and grow upon plate impact induced tensile loading.

Nucleation mechanisms can be separated into two classes, atomic and microscopic. In both cases the mechanisms are directly related to the deviation of a material from a perfect lattice. Further, almost all

mechanisms are based on dislocation motion; those that occur at the lowest stresses are associated with microscopic imperfections including precipitates and inclusions. Subsequent growth of voids after nucleation is necessary for failure to occur. In plate impact dynamic fracture tests, large triaxial tensile stresses of 5 to 20 times the yield strength may occur. These stresses generate very high rates of deformation about the void, especially in low strength materials such as commercially pure aluminum and other ductile metals. The result is that very rapid growth of the voids occurs, and short time durations (0.01 to 1.0  $\mu$ sec) of tensile stress loading are sufficient for development of observable damage. Void growth mechanisms have not been investigated from an atomic or microscopic viewpoint, however. Descriptions based on continuum mechanics concepts and idealized material behavior are available (Ref. 2). These descriptions have been used in the development of models (Refs. 3, 4) for ductile failure by void growth and coalescence under static conditions. Such models predict strains rather larger than those observed experimentally but give the correct dependence of strain to fracture on void concentration in materials studied. The essential result is that at high void densities the material has the lowest ductility (strain to fracture). Therefore, high inclusion or precipitate content will act to reduce the strain to fracture by providing nucleation sites for voids. This generalization is pertinent to the behavior of ductile materials under dynamic conditions since the degree of damage sustained will be a strong function of the number of available nucleation sites.

It has been shown in quasi-static tests (Ref. 5) that the higher the purity of a metal (aluminum), the lower the tendency for void formation, and the more likely fully ductile failure will be observed. Similar work (Ref. 6) has also demonstrated that at very low temperatures voids will form in materials in which void formation is not observed at

room temperature. This indicates that some new nucleation mechanism becomes operative at low temperatures or that the higher stress necessary for low-temperature deformation is sufficient to activate sites not accessible at lower stresses. This is pertinent to the results on pure Al.

The distribution of inclusions is also important since specific regions of high inclusion density can act as crack propagators. Inhomogeneous inclusion distributions are commonly observed in forged, extruded, drawn, and rolled stock, where material flow during forming defines the inclusion distribution. The structures formed are termed stringers and have a marked effect on the fracture characteristics of ductile materials.

## 2. DUCTILE FRACTURE MODEL

### a. Nature of the Model

Observations of fracture damage in several grades of aluminum led us to the formulation of the present theoretical model for ductile fracture. The model provides for the nucleation of voids as a function of tensile stress level, for growth of the voids under tensile loading, and for the relaxation of stress and reduction of strength as a function of the developing damage. The growth and stress relaxation aspects of the model are based on material viscosity, yield strength, bulk modulus, and other material properties. Because of this dependence on standard material properties, we believe that this fracture model will be applicable to fracture in the whole class of ductile materials. This belief has been justified by the results with copper.

The ductile fracture model differs greatly from other fracture models, such as that of Tuler and Butcher (Ref. 7), the tensile impulse model, or the ultimate strength model. The main differences are:

- The amount of damage is computed as a function of time and position in the sample; the simpler models indicate only whether the sample has failed or give the impact conditions causing some arbitrary damage level.
- The equation of state is modified to account for damage; hence, the stress is relaxed from the value it would have in undamaged material. In the simpler models the stress is unaffected by damage.

In addition, because our fracture model can be related to material properties, it is more likely to lead to an understanding of the nature of ductile fracture.

The ductile fracture model was developed primarily from a study of partially fractured samples of 1145 aluminum. Thin target plates of the aluminum were subjected to planar impacts with thinner aluminum flyer



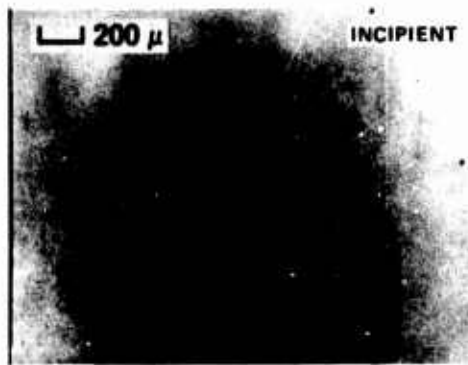
plates. After the impact the target plate was sectioned and mechanically polished (see Figure 2 for a sample), revealing the presence of nearly spherical voids. The voids were counted, noting the number of each size as a function of depth into the target. This count on the surface was then transformed to a volume distribution through a statistical transformation similar to Scheil's method. A series of distributions obtained at six depths in an aluminum target is shown in Figure 3. The ordinate is the cumulative number of voids larger than a given radius. Zone F01 is at the expected spall plane. The size of voids and total number of voids decrease with increasing distance away from the spall plane.

The stress histories computed for points in the aluminum targets near the incipient spall plane indicated, as shown in Figure 4, that a compressive pulse was followed by a tensile pulse. The tensile pulse was initially approximated as a square pulse characterized by a peak stress and a duration of stress. From these data the nucleation rate and growth rate were determined as described in the following sections. These rates were combined with constitutive relations for damaged material to produce the complete model.

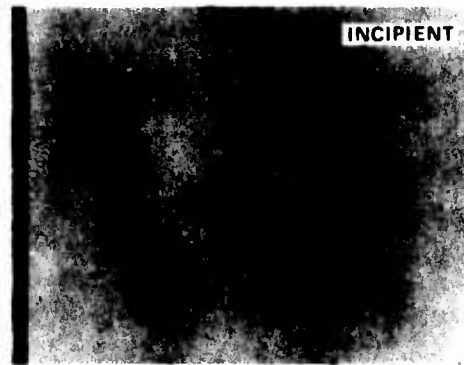
b. Nucleation Rate

Nucleation of voids in the aluminum appeared to occur by the decohesion of aluminum from hard inclusions distributed through the material.

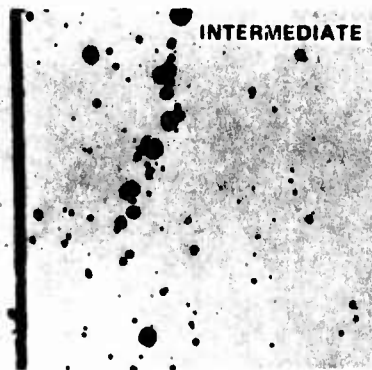
The nucleation rate used in our quantification of the damage and in the wave propagation calculations is actually an "observation" rate, the rate at which voids reach an observable size. The nucleation rate was determined for specimens with low damage by noting the correlation between the number of voids and the duration of stress as shown in Figure 5. A comparison of the curves in Figure 5 for either Shot 847



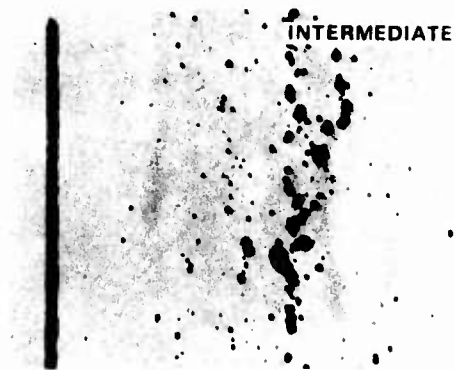
IMPACT VELOCITY - 423 fps



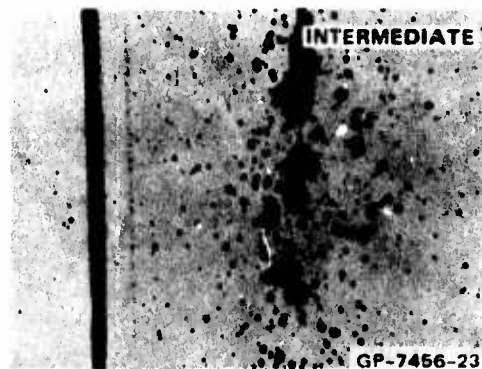
IMPACT VELOCITY - 433 fps



IMPACT VELOCITY - 468 fps



IMPACT VELOCITY - 506 fps



IMPACT VELOCITY - 668 fps

**FIGURE 2** DAMAGE OBSERVED IN 1145 ALUMINUM FOR A CONSTANT SHOT GEOMETRY (i.e., TIME AT STRESS) FOR INCREASING IMPACT VELOCITIES (i.e., STRESS). More voids and larger sizes result from increasing impact velocities. Projectile thickness is 0.093 in., sample thickness is 0.25 in.

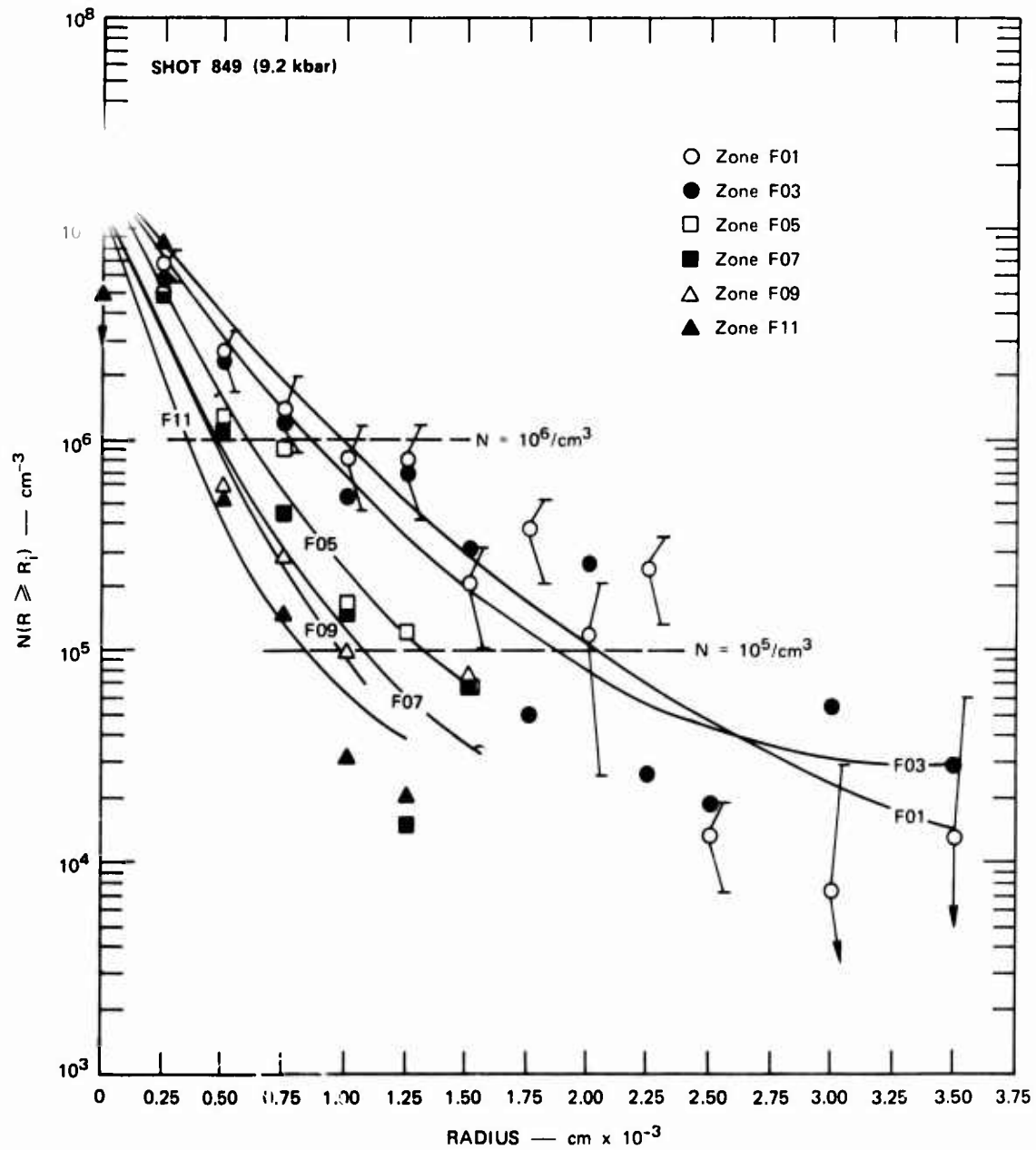


FIGURE 3 DISTRIBUTION OF VOIDS: SHOT 849 (error lines are slanted to avoid overlap)

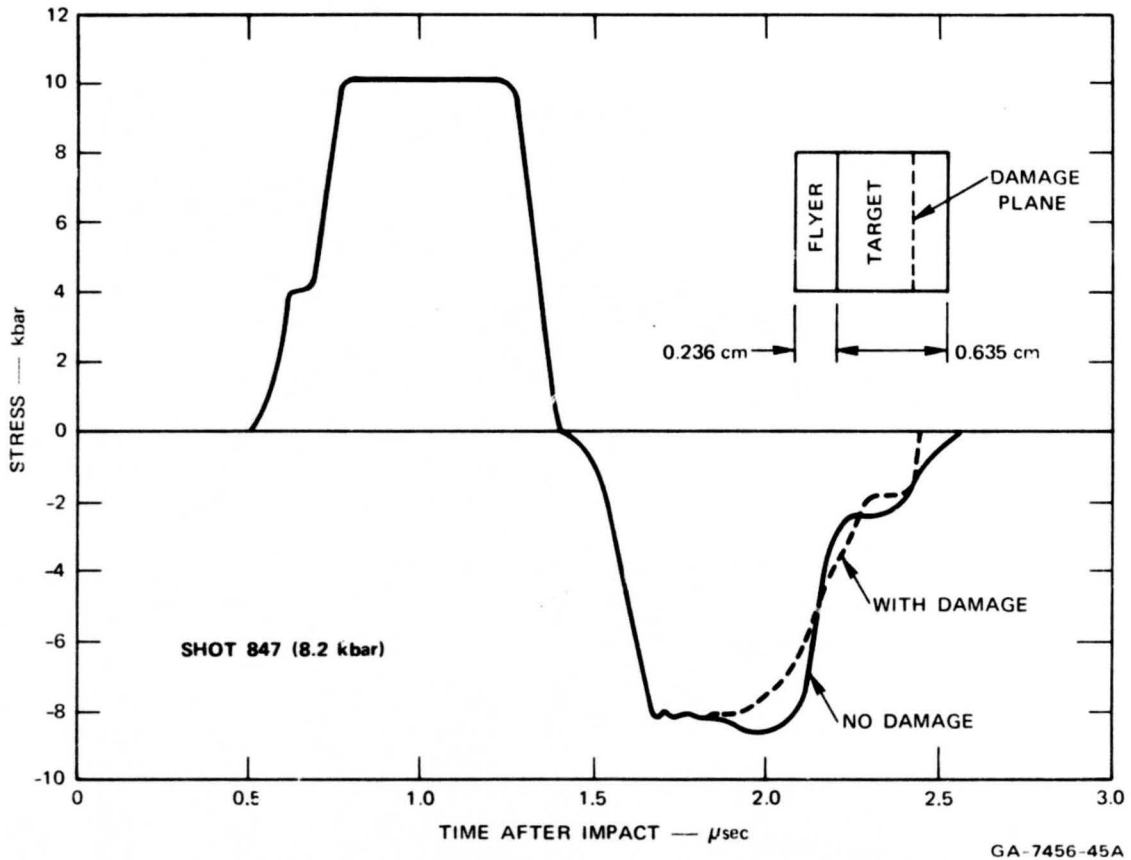


FIGURE 4 EFFECT OF DAMAGE (voids) ON STRESS HISTORY AT DAMAGE PLANE OF AN 8.2 kbar TENSION SHOT IN 1145 ALUMINUM. Calculation was done with 8 kbar threshold rather than with present model.

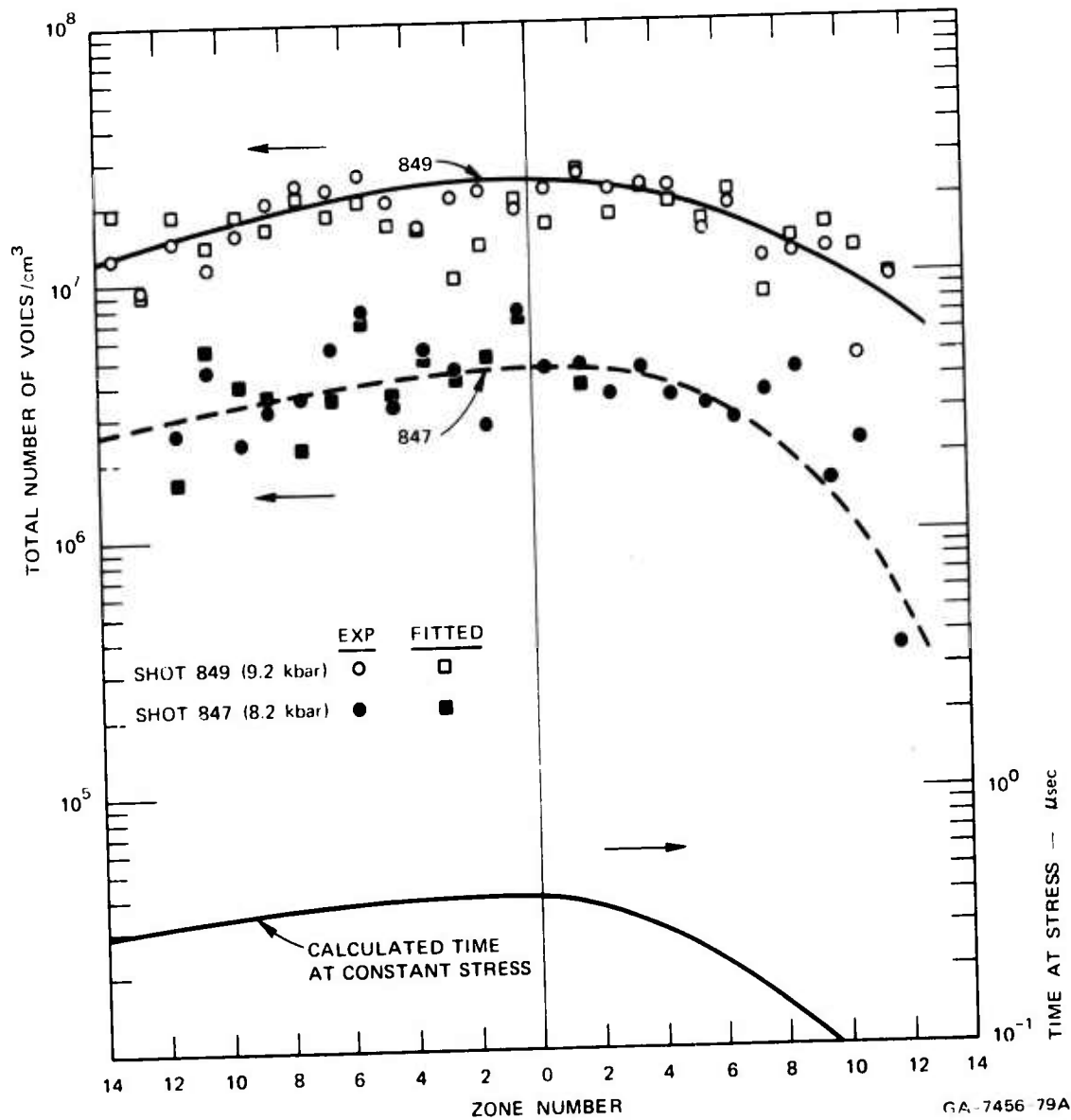


FIGURE 5 COMPARISON OF VOID DISTRIBUTIONS WITH TIME AT STRESS DISTRIBUTION IN 1145 ALUMINUM

or Shot 849 with the bottom curve indicates a linear relation between concentration of voids and duration of the stress. A plot of concentration versus duration gave the nucleation rate for each stress level.

For shots with high damage (high enough that the stress history was seriously altered by the damage), an initial estimate of nucleation rate was made from stress histories computed with no damage permitted. Then wave propagation calculations with damage were made, and the nucleation parameters were varied until a reasonable correlation with the experimental damage was obtained.

c. Growth Rate and Growth Threshold

The voids appeared to increase in size with time at peak stress and to retain their spherical shape. The void distributions in Figure 3 show that the larger voids are associated with the longer durations of peak stress. Because the whole distribution appears to shift as a function of stress duration, the series of distributions can be visualized as a historical sequence at one location. Considered in this way, the curves provide a growth rate when we consider the rate of change of the radius of a particular void. For example, consider the void that is number 1 million when ranked by size, i.e.,  $N = 10^6$ . Under our assumptions, this void will remain number 1 million throughout the loading. A plot of successive radii of this void as a function of time, as shown in Figure 6, yields the growth velocity for the imposed stress level. From these plots the radius was found to have the form

$$R = R_0 \exp (At) \quad (1)$$

or, by differentiating,

$$\dot{R} = AR \quad (2)$$

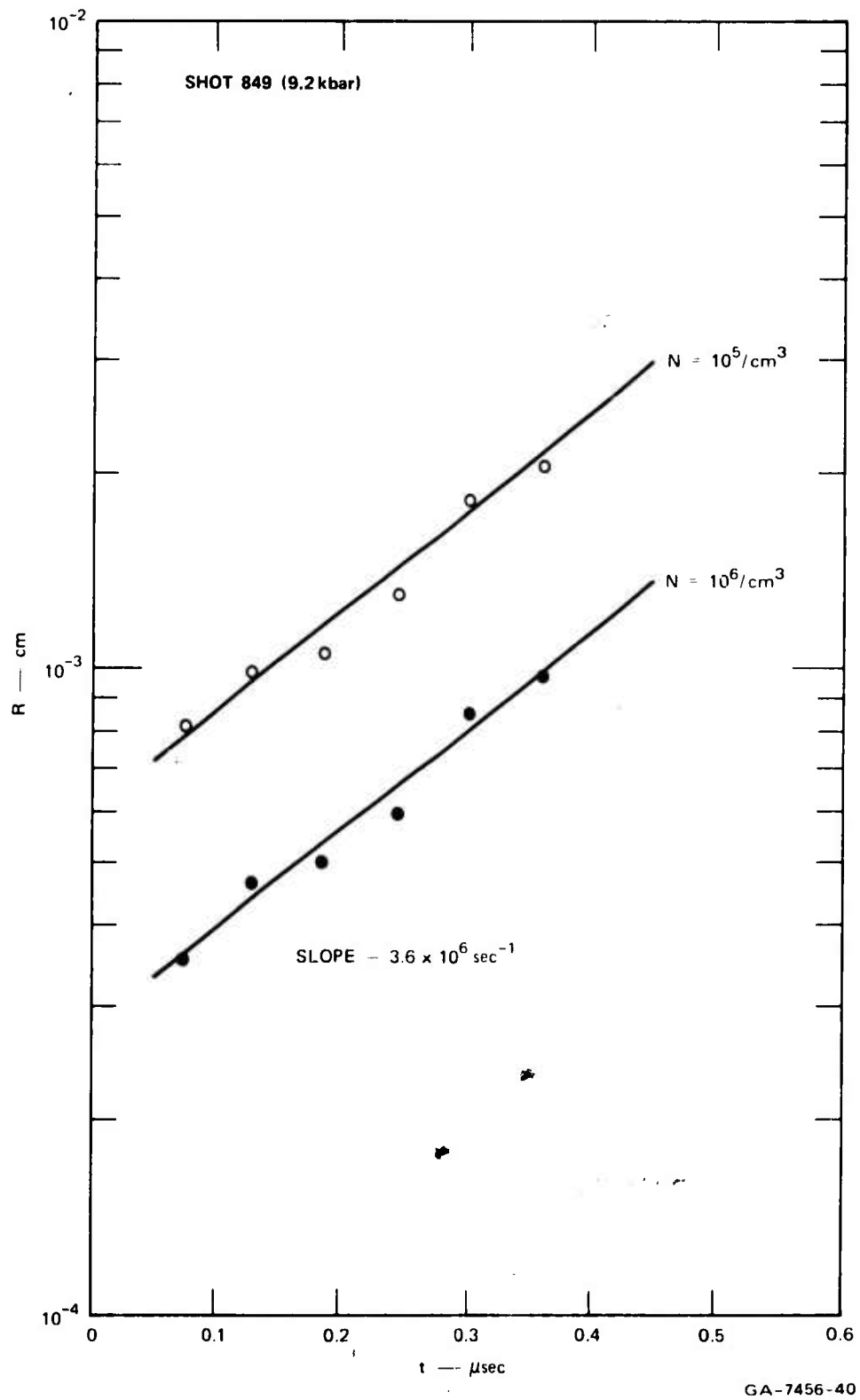


FIGURE 6 VOID RADIUS AT CONSTANT VOID CONCENTRATION, PLOTTED AS A FUNCTION OF TIME AT STRESS

where

- R = the radius
- $R_0$  = the initial void radius
- $\dot{R}$  = the velocity of growth
- A = a growth parameter

This growth law is exactly that expected for a slowly growing void in a substance in which growth is controlled by viscous forces (Refs. 2, 3, 4 and Appendix III). The solutions for viscous void growth show that A should have the form

$$A = \frac{p - p_0}{4\eta} \quad (3)$$

where

- p = the average (tensile) pressure at a large distance from the void
- $p_0$  = a threshold pressure
- $\eta$  = the material shear viscosity

The experimental results in aluminum at low damage indicated that the linear relationship between A and pressure in Eq. (3) is correct. We conclude that, for void growth, two material parameters of interest are the material viscosity and threshold stress.

The threshold pressure is that pressure at which significant flow can occur in the vicinity of the void. Hence the threshold is related to the yield strength. For pressures above the threshold, the flow is limited by viscosity rather than by the material yield strength.



d. Constitutive Relations

The stress-strain relations for a material undergoing damage differ from those for undamaged material. The decreased elastic stiffness of material with voids has been studied by MacKenzie (Ref. 5), by Buch and Goldschmidt (Ref. 6), and by many others. More general equations of state for porous material were developed by Herrmann (Ref. 8) and by Seaman and Linde (Ref. 9).

In the current development the stress was divided into a pressure and a deviator stress, and constitutive relations were derived for each component. Thus the developing void damage alters the bulk modulus, shear modulus, and yield strength. As the stress reduces with increasing damage, recompression waves proceed away from the regions of damage. These recompressions lead to reduced damage in adjacent areas and hence to a marked peak of damage at one point. (In low-damage experiments large areas of nearly uniform damage are found; at high damage, an area of maximum damage, the incipient spall plane, is clearly defined.) The recompression waves lead to a compressive hump, or spall signal, on stress histories, similar to those observed experimentally.

### 3. EXPERIMENTAL OBSERVATIONS

In this section observations of dynamic fracture of 1145 Al, high purity (99.999 percent) Al, 2024-T81 Al, and dead soft OFHC copper will be described. Samples of the same material were impacted at several different velocities in tests using the experimental techniques described in Appendix II. Symmetric shot design was used to ensure as accurate a stress calculation as possible. Shot geometry (i.e., flyer and sample thicknesses) was varied to vary the time at stress, and tapered flyers were used so that wide ranges of the time-at-stress damage threshold plane could be studied in a single experiment (see Appendix I).

Two types of data were obtained from these experiments. First, metallographic observations of the damage were made by sectioning the recovered samples on planes parallel to the direction of shock propagation passing through the center of the sample and by observing the fracture surfaces, using the scanning electron microscope. These observations were used to determine damage thresholds and damage level and to investigate mechanisms for nucleation of damage. Quantitative analyses of the observed damage discussed in a following section, were also made. In this section metallographic results pertinent to nucleation, growth, and coalescence of damage are discussed.

Second, experiments instrumented using manganin piezoresistive gages mounted in polymethylmethacrylate (PMMA) on the back surface of the samples were used to measure the imposed stress history. The techniques used are described in detail in Appendix II. The manganin stress gage records obtained by this technique are indicative of damage formed in the material directly in front of the gage element caused by the modification of the tensile stress history resulting from the incomplete stress release at the sample-PMMA interface.

a. 1145 Aluminum

The aluminum was received as 2-in.-thick plates 24 in. X 24 in. and was tested in the fully annealed, 0-temper state. Metallographic examination of the 1145 Al revealed an elongated grain structure expected for a rolled material. Observations of etched 1145 Al at higher magnifications showed this material to have a structure interpretable as resulting from a recovery rather than a full recrystallization anneal. The effect of this on the fracture behavior is unknown, and the information is given only to characterize the initial state of this material. Typical compositions for these materials are shown below.

<u>Material</u>	<u>1145 Al*</u> <u>(max % wt)</u>
Si	0.55
Fe	
Cu	0.05
Mn	0.05

The impurity levels are consistent with the mechanical properties observed. The solubilities of silicon and iron in aluminum are smaller than the concentrations shown, and formation of Fe-Si inclusions is expected. These will have large effects on the fracture characteristics but are near the limit of optical resolution in size.

Uniaxial tensile tests were made on 1145 aluminum. The 0.2 percent offset yield strength of this material was observed to be 4500 psi, in agreement with handbook values. At the higher strain rates a yield plateau is seen that was reproducible in several tests. This is not expected but may be the result of the apparent incomplete anneal this

---

\* Minimum 99.45 percent aluminum.

material received. Double cup-and-cone fractures were observed with 1145 aluminum as well as a very high reduction in area. The Knoop hardness (15-g load) was 25 for the as-received material.

Nine recovery experiments were performed on 1145 Al. Four of these were tapered flyer experiments (see Appendix I), three were instrumented with a manganin pressure transducer directly behind the target sample, and two were at a temperature of 400°C. The experimental method is described in Appendices I and II, and the experimental details and damage levels observed at 50X on metallographically prepared section are given in Table II. Damage observed in these samples is described in the following. Several of the micrographs are taken from samples impacted under Contract F29601-68-C-0118 for the Air Force Special Weapons Center, titled Dynamic Fracture Criteria of Homogeneous Materials which ran from 8 May 1968 through 15 July 1970.

Damage in the form of individually nucleated spherical voids that grow and coalesce to induce failure, observed in 1145 Al for a single shot geometry (i.e., time at stress), was shown earlier in Figure 2 for increasing impact velocities (i.e., stress). The straight lines observed are fiducial marks used in the quantitative analysis described in a later section. Three characteristics are apparent from these pictures. First, the damage observed has a circular cross section in the plane of view. These cross sections are, in fact, sections through spherical voids. This was proved by sectioning the samples normal to the direction of shock propagation. Circular cross sections were observed in this case also, showing that the voids are spherical. Second, there is a size distribution of voids within regions with the same shock history, which suggests that nucleation occurs throughout the loading time. Third, at higher damage levels it is the interaction of the growing voids that leads to the formation of large defects and finally to fracture.

Table II

## SUMMARY OF DYNAMIC FLYER PLATE EXPERIMENTS IN 1145 ALUMINUM

Shot No.	Impact Velocity (mm/ $\mu$ sec)	Sample (mm)	Projectile (mm)	Comments
S3 <sup>a</sup>	0.118	6.313	1.578 to 3.156	Incipient to intermediate damage
S4 <sup>a</sup>	0.163	3.156	0.789 to 1.578	Incipient to intermediate damage
S9 <sup>a</sup>	0.204	1.578	0.394 to 0.789	Intermediate to heavy damage
S18 <sup>b</sup>	0.213	6.313	2.275	Intermediate damage
S20 <sup>b</sup>	0.278	3.156	1.138	Intermediate damage
S28 <sup>b</sup>	0.234	1.578	0.568	Intermediate damage
S33	0.146	6.313	2.27	Temperature 400°C, intermediate damage
S34 <sup>a</sup>	0.172	6.313	3.156 to 1.578	Temperature 400°C, full separation
S60	0.228	6.313	1.0	Heavy damage to full separation

<sup>a</sup> Tapered flyer shots designed so that the time at stress was varied over a wide range for a constant stress experiment.

<sup>b</sup> Instrumented with a manganin pressure transducer directly behind the sample.

The sphericity of the voids is consistent with a concept that a near hydrostatic tensile stress or pressure characteristic of one-dimensional strain conditions is most important. In uniaxial stress tests the voids are ellipsoids of revolution, because of the triaxial stress distribution resulting from necking. Further, the existence of

a size distribution is generally consistent with a nucleation and growth concept. The coalescence of voids is also consistent with the failure mode in a standard tensile test. We can conclude, therefore, that observations of damage produced in 1145 aluminum under impact conditions are consistent with observations on quasi-static tensile test samples.

In the 1145 Al experiments, damage levels varying from incipient to intermediate were observed in a single tapered flyer experiment (Shot S4) as shown in Figures 7a through 7d. The damage in Figure 7a is the result of a 10.8 kbar tensile stress pulse of approximately 0.34  $\mu$ sec, a fairly high damage. Further, the damage is produced by essentially midplane spall conditions (i.e., the projectile is half the sample thickness). The damage in Figure 7b was generated in 0.29  $\mu$ sec, in Figure 7c in 0.23  $\mu$ sec, and in Figure 7d in 0.17  $\mu$ sec. The variation in the damage level and distribution with time at constant stress is very well demonstrated in this experiment.

These observations complement those given in Figure 2 in that they represent a time-at-stress variation at constant stress rather than a stress level variation for nominally constant time at stress. The comparability of the two sets of observations demonstrates the applicability of tapered flyers.

The results obtained in the impact tests on samples at 400°C were consistent with the observations presented above. Scanning electron microscope studies of full fracture surfaces of Shot S34 were made. These showed that failure occurred by void coalescence and that random nucleation was the mode of void formation. No correlation with inclusion content was possible because of contamination of the fracture surface during recovery. Typical results are shown in Figures 8a and 8b. These figures of the broken surfaces show that void coalescence occurred

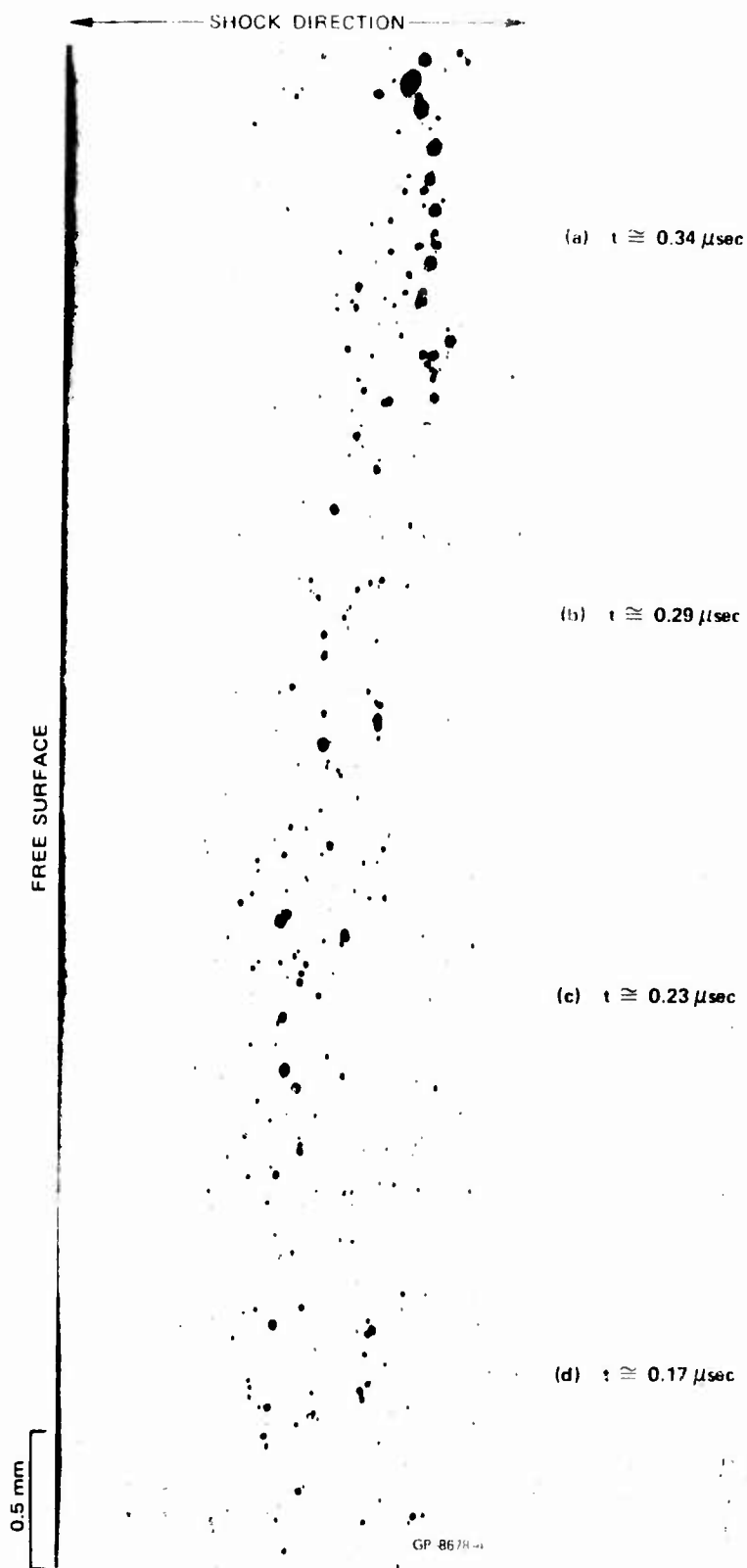


FIGURE 7 MICROGRAPHS OF DAMAGE ACHIEVED IN A SINGLE TAPERED FLYER SHOT ON 1145 ALUMINUM (Shot S4). Demonstrates the dependence of the damage level on the time at constant stress.

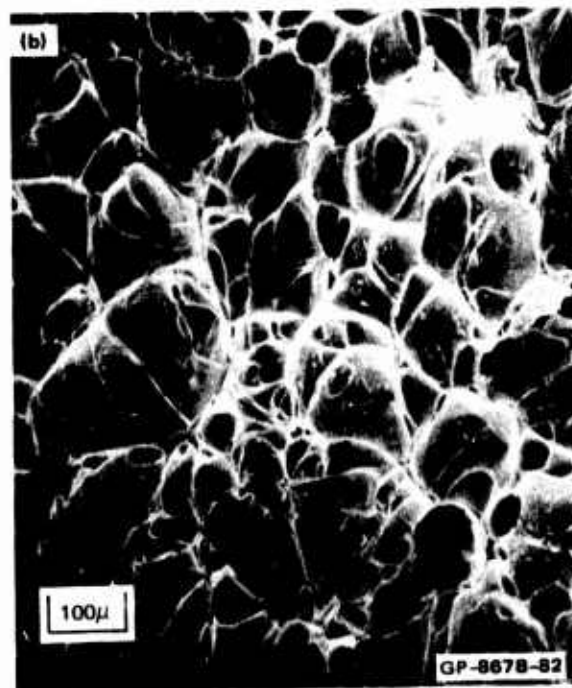
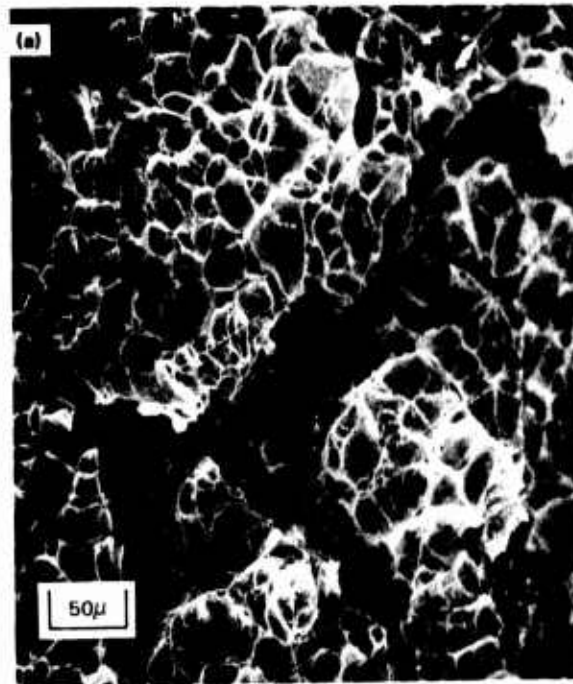


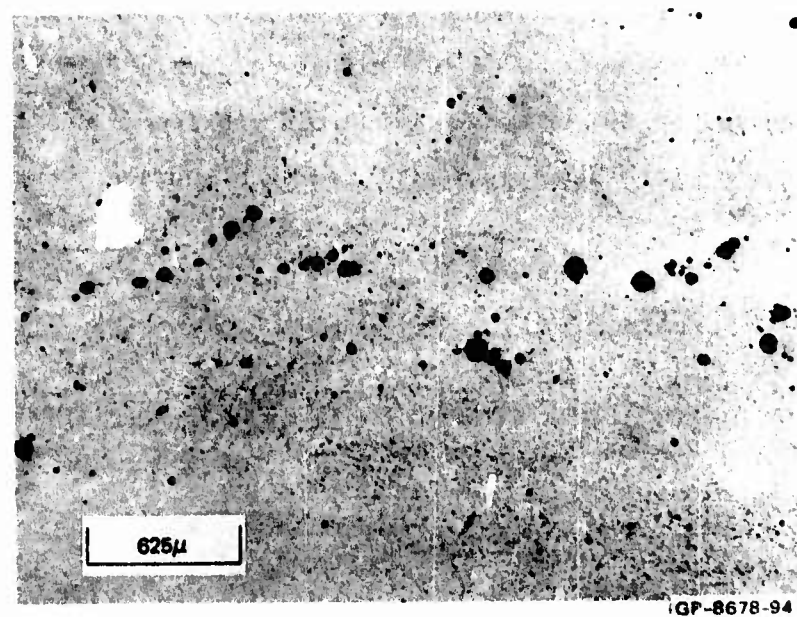
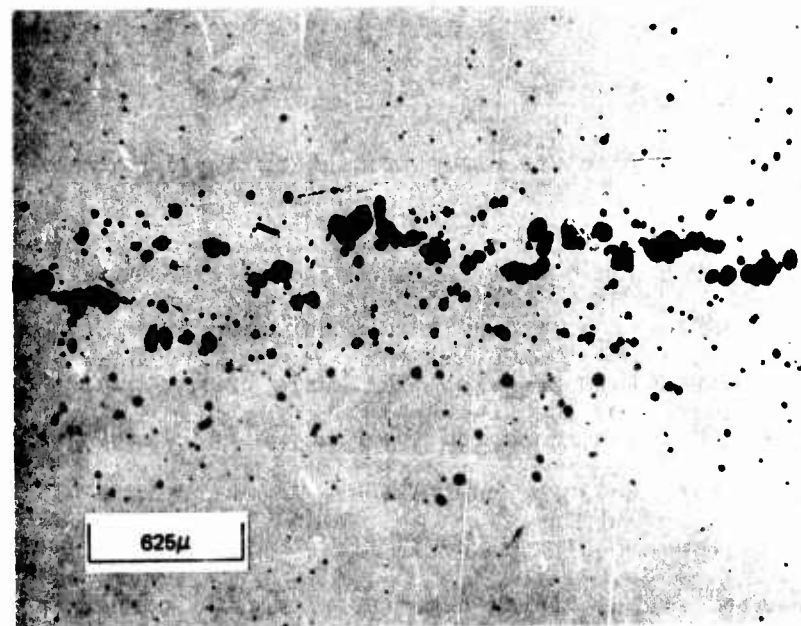
FIGURE 8 MICROGRAPHS OF 1145 ALUMINUM SAMPLES IMPACTED AT 400°C (Shot S34)



over the whole surface to cause failure. The separation was by knife-edge fracture in the material surrounding the voids. The three-dimensional nature of the damage is illustrated in Figure 8b, in which one can see through one void to deeper voids. This suggests that, in the vicinity of the plane of separation, the material is honeycombed with voids. These amply verify the previously described results and show a surface roughness that demonstrates the distribution of voids away from the fracture plane as shown in Figures 7 and 8. Further, there was no correlation of the damage structure with the grain size or with grain boundaries in the material. These results will be contrasted with those for 99.999 percent pure Al later.

Full fracture occurred at 400°C at an impact velocity of 0.171 mm/μsec, whereas at room temperature full fracture was not observed until an impact velocity of approximately 0.244 mm/μsec was achieved. Further, as shown in Figure 9, the damage levels resulting from impacts at velocities of 0.145 mm/μsec at room temperature and 400°C are different, with higher damage occurring at 400°C. These differences indicate in a quantitative manner the effect of temperature on the dynamic fracture threshold of 1145 Al. It is likely that this results from a decrease in the yield strength with temperature, which lowers the threshold stress for void nucleation.

The general result here is that at temperatures about 75 percent of the absolute melting temperature a large decrease in the fracture strength of 1145 Al occurs. Also, the fracture morphology remains the same, indicating that the mechanisms are the same but that physical properties are changing to produce a lower damage threshold.



(b) 1145 ALUMINUM AT ROOM TEMPERATURE; 477 ft/sec = 0.145 mm/ $\mu$ sec

FIGURE 9 MICROGRAPHS OF 1145 ALUMINUM SAMPLES  
IMPACTED AT ROOM TEMPERATURE AND  
400°C. Impact velocity = 0.145 mm/ $\mu$ s:c.

b. High Purity Aluminum

The dynamic fracture study of high purity aluminum (HP Al) was designed to investigate the effects of sample purity on the nucleation of voids and the subsequent failure process. This was intended to ascertain the effects of inclusion content, and possibly of material structure, on the fracture process. The basic premise was that the increased purity would decrease the frequency of nucleation and possibly raise the stress threshold for nucleation. The structure of the material studied was large equiaxial grain size,  $\sim 3$  mm. It was in the dead soft annealed state, having been annealed at a temperature of  $500^{\circ}\text{C}$  for 6 hours in an inert atmosphere.

Four recovery experiments were performed on HP Al. The experimental details are described in Table III along with a description of damage observed at 50X on metallographically prepared sections. Scanning electron microscope studies of fracture surfaces were also carried out.

Table III

SUMMARY OF DYNAMIC FLYER EXPERIMENTS IN 99.999% PURE ALUMINUM

<u>Shot No.</u>	<u>Impact Velocity (mm/<math>\mu</math>sec)</u>	<u>Sample (mm)</u>	<u>Projectile (1145 Al) (mm)</u>	<u>Comments</u>
S30	0.168	6.313	2.35	Intermediate
S31 <sup>a</sup>	0.166	6.313	3.156 to 1.578	Incipient to intermediate
S32	0.184	6.313	2.35	Full separation
S43	0.136	6.313	2.27	No damage

<sup>a</sup> Tapered flyer shots designed so that the time at stress was varied over a wide range for a constant stress experiment.

First, it is necessary to note that the impact velocity at which damage was not observed was 0.136 mm/ $\mu$ sec for the high purity aluminum. In the 1145 Al the damage threshold was observed to be, for experiments of identical geometry, 0.129 mm/ $\mu$ sec. Therefore, a material of higher yield strength exhibited a lower damage threshold stress. The threshold stresses, in these cases, for unbounded void growth are considerably different and can be estimated from the known yield strengths of these materials and the rate dependence of the yield strength.

In the growth equation for voids the threshold stress for void growth is taken to be

$$\sigma_0 = \sigma_y \left( 1 + \ln \frac{2E}{3Y} \right) \quad (4)$$

where

E is the Young's modulus, and Y the yield strength. (See Appendix IV) For 1145 Al, the predicted threshold stress is approximately 3 kbar, whereas for HP Al the threshold stress is 2.0 kbar. Therefore, the stress necessary for void nucleation may be controlling in the development of damage in the HP Al.

Since we observe voids when a size of 1.0  $\mu$  is attained, it is possible that the size attained in the experiments may be smaller than that in 1145 Al since the initial nucleation size is smaller. The major result is that either the growth, the initial size, or the threshold stress for void nucleation is determining the behavior of the HP Al. At present it is not possible to determine which of these is controlling. In all likelihood, a smaller void nucleation size is present in this material and the growth time to observation is longer. It is also likely that nucleation stress may be larger leading to a higher threshold.

Observation on Shot S31 shows that the damage structure differs greatly from that observed in the 1145 Al. This is shown in Figure 10. The voids are very definitely arranged in an ordered manner, indicating an ordered nucleation size distribution. These rows of voids (as planes) are essentially parallel to the plane of first tension. Also, for any given area of the specimen, the spacing of voids appears to be uniform; in Figure 10 this is approximately 40  $\mu$ . Another characteristic is that the voids are not of uniform size for any one group. This shows either that the line of voids is skew to the surface of polish or that they are nucleated at different times and the line of voids is parallel to the polish surface. Whatever the significance of the appearance of the voids on the surface in terms of their size distribution, it is their spatial distribution that is important. This spatial distribution leads to a failure mode that probably occurs in a systematic manner because of the correlations between adjacent voids. This is also seen in the fully fractured sample (Shot S2) and shown in Figure 11. Fracture has obviously occurred by coalescence of the voids in the correlated structure shown in the surface distribution, forming a failure plane. The concentration of voids away from this fracture plane is low, indicating that this ordered nucleation of voids has a large effect on the fracture process.

At low magnifications the fracture surface definitely shows the ordered structure implied from the previous two figures. Figure 12a is an SEM micrograph of the fracture surface of Shot S32. The center of the sample lies at the lower right hand corner of the picture, and the damage structure indicates a rough planar surface. A fracture surface observed on 1145 Al is shown in Figure 12a and shows a much more random void nucleation structure than that seen in Figure 12b for HP Al.



FIGURE 10 SHOCK DAMAGE IN HIGH PURITY ALUMINUM



FIGURE 11 FULL SEPARATION IN HIGH PURITY ALUMINUM

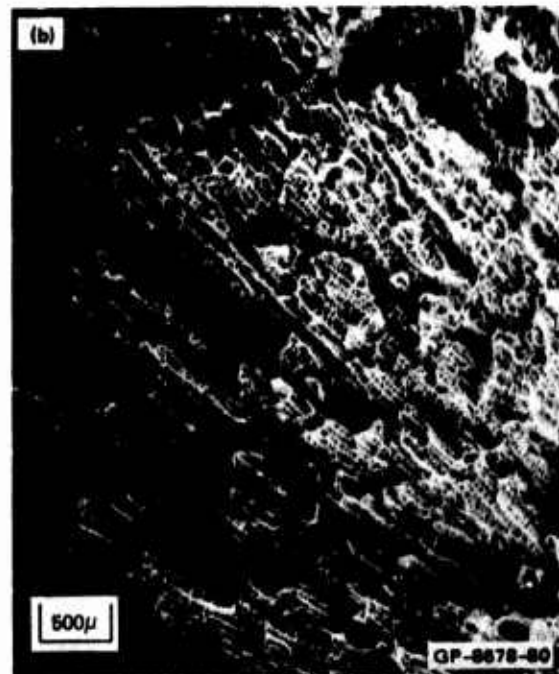
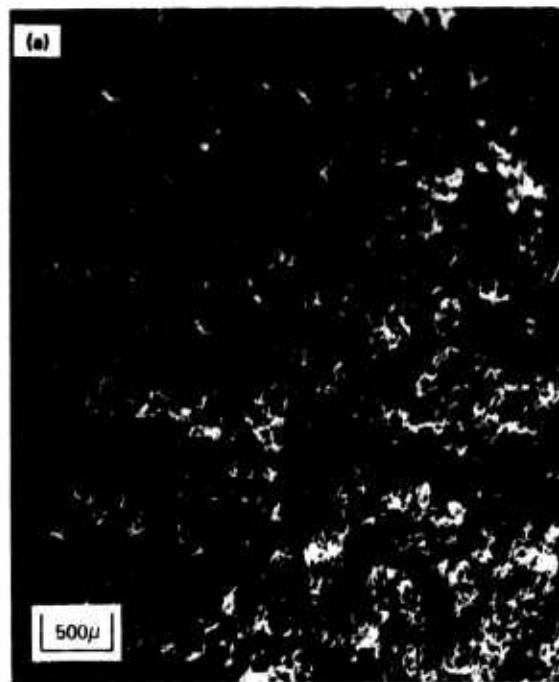


FIGURE 12 COMPARISON OF FRACTURE SURFACES FOR 1145 AND HIGH PURITY ALUMINUM



The degree of surface roughness is seen in Figure 13, which is a stereo pair of the fracture surface on Shot S32 (HP Al). This micrograph also shows the ordered structure of the voids on a given fracture plane. This is better demonstrated in Figure 14, which shows a higher magnification view of the same area. Nucleation at what appears to be an inclusion is also shown in this micrograph (Figure 14). This indicates that even in high purity aluminum heterogeneous nucleation sites are present.

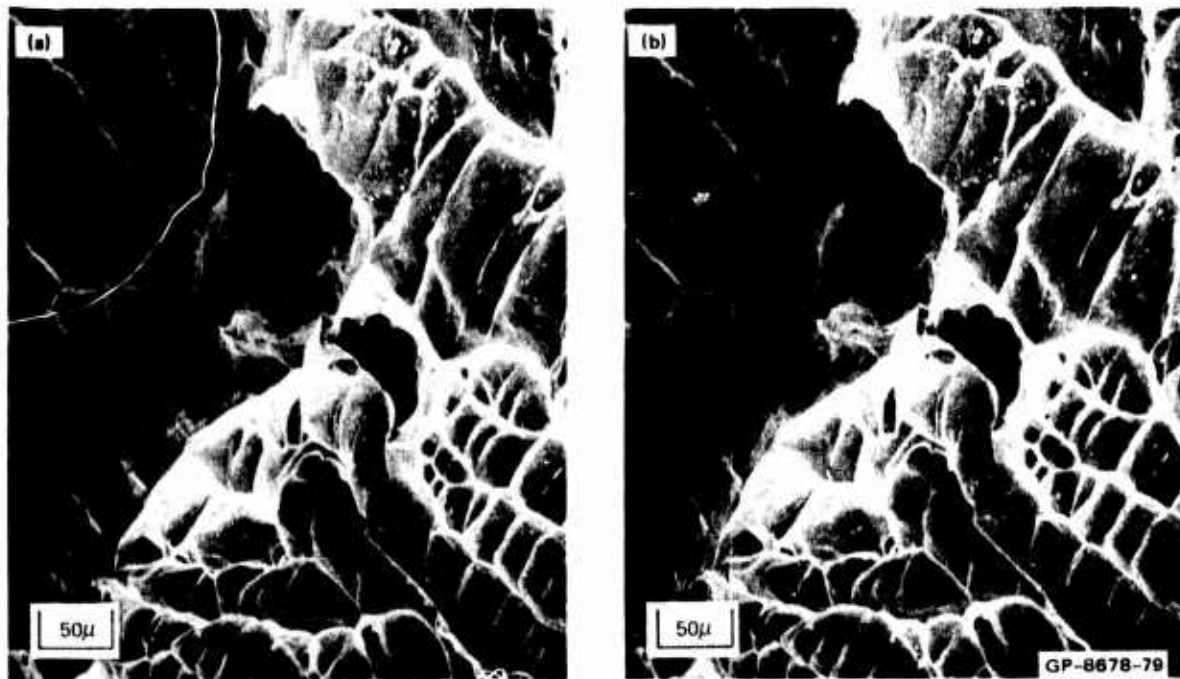


FIGURE 13 STEREO PAIR OF THE FRACTURE SURFACE OF HIGH PURITY ALUMINUM

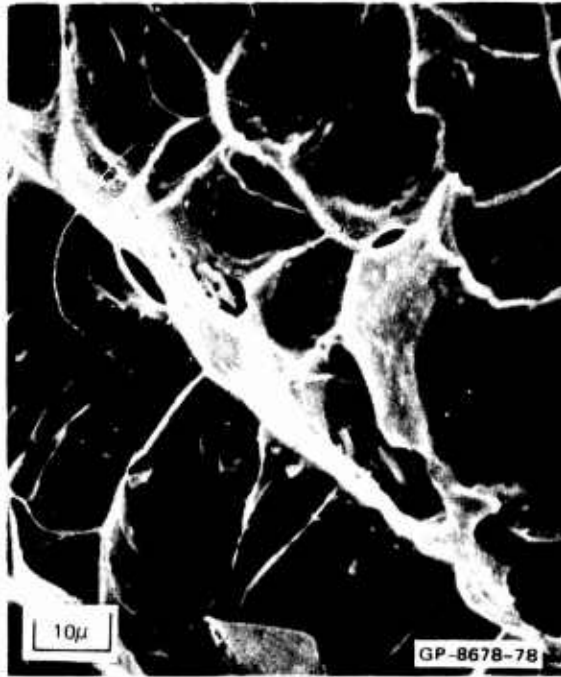


FIGURE 14 NUCLEATION SITES AND STRUCTURE AT JOINING OF VOIDS. Knife-edge failure around voids.

c. 2024-T81 Aluminum

The stock used in this study was received in the form of rolled plates 24 inches X 24 inches X 1.1 inches, and samples were prepared with the expected damage plane parallel to the rolling plane of the plates. The 2024 aluminum is an age-hardening alloy having the typical composition given below.

<u>Material</u>	2024-T81 Aluminum
	<u>(wt %)</u>
	3.8 to 4.9
	0.5
Fe	0.5
Zn	0.25
Mn	0.3 to 0.9
Mg	1.2 to 1.8
Cr	0.10

The Si, Fe, Mn, and Mg form basically insoluble inclusions that act as strengthening agents. These inclusions also form into stringer planes during rolling and, in this form, have a large effect on the fracture characteristics of this material.

The designation, T81, describes the fabrication history of this material, and indicates, according to ASTM standards, that it has been solution heat treated, cold worked, and then artificially aged. High strength and improved corrosion properties are achieved by this thermomechanical sequence.

The as-received 2024 Al showed an elongated grain structure, indicating that the material was heavily rolled before solution treatment and artificial aging. Inclusions are observed that lie parallel to the planes of the grains in the form of stringers. These stringers are regions of weakness in the material and are preferred sites for failure initiation and propagation.

The dynamic fracture of 2024-T81 aluminum was also studied and recovery experiments were carried out. The details of these experiments are presented in Table IV.

Table IV

## SUMMARY OF DYNAMIC FLYER PLATE EXPERIMENTS IN 2024-T81 ALUMINUM

Shot No.	Impact Velocity (mm/ $\mu$ sec)	Sample (mm)	Projectile (mm)	Comments
S6 <sup>a</sup>	0.133	3.156	1.578 to 0.789	Inclusion cracking
S7 <sup>a</sup>	0.161	1.578	0.789 to 0.394	Inclusion cracking
S10 <sup>a</sup>	0.153	3.156	1.578 to 0.789	Inclusion cracking
S29 <sup>b</sup>	0.233	1.578	0.568	Inclusion cracking

<sup>a</sup> Tapered flyer shots designed so that the time at stress was varied over a wide range for a constant stress experiment.

<sup>b</sup> Instrumented with a manganin pressure transducer directly behind the sample.

The damage produced in the 2024-T81 aluminum differs from that found in the 1145 aluminum and the HP aluminum in that it is very localized and in the form of ductile cracks. These damage structures are shown in Figure 15 for three samples, impacted at velocities of 343, 474, and 660 fps. Fractures are nucleated in this material by cracking of the inclusions as shown in Figure 16. This figure also shows that cracks propagate along the stringer planes. This is the damage mechanism observed in similar aluminum alloys tested under quasi-static conditions at room temperature.

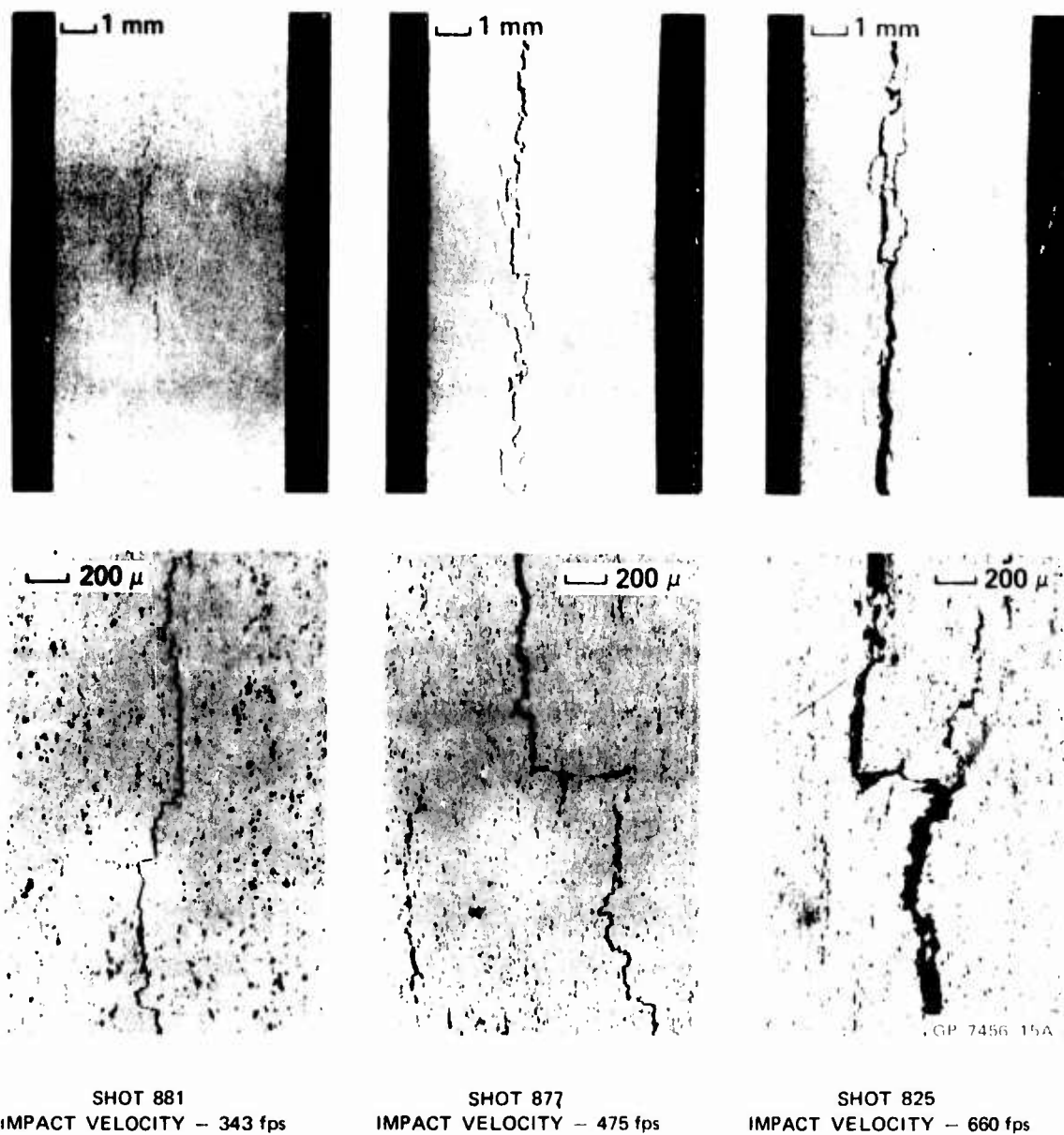


FIGURE 15 DAMAGE IN THE FORM OF DUCTILE CRACKS THAT FOLLOW STRINGER PLANES AS A FUNCTION OF IMPACT VELOCITY (stress) AT CONSTANT SAMPLE PROJECTILE GEOMETRY (time at stress) FOR 2024-T81 ALUMINUM

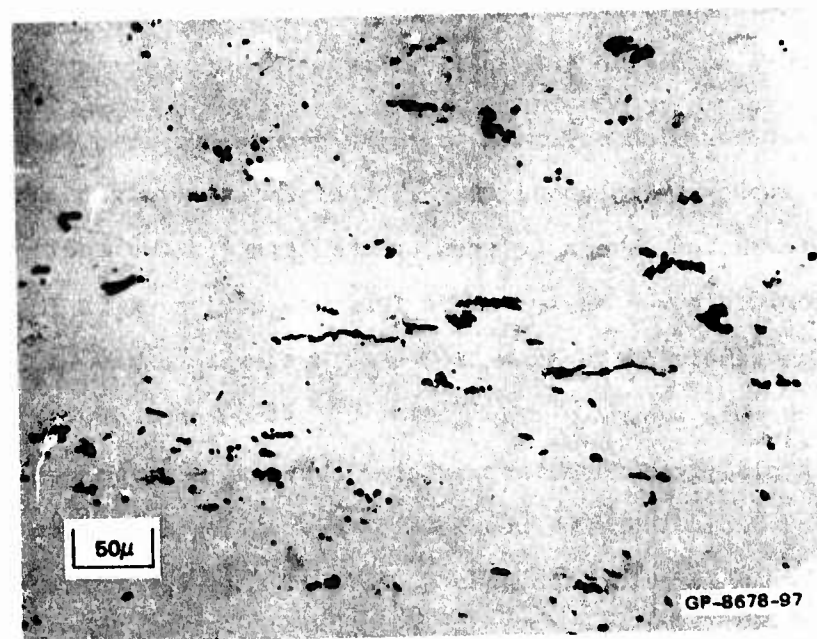


FIGURE 16 CRACKING OF INCLUSION IN 2024-T81 ALUMINUM

These experiments show that failure is a function of the inclusion distribution, as well as of the intrinsic properties of this alloy. This is consistent with the observations of Butcher (Ref. 10), who determined the incipient spall thresholds for 6061-T6 aluminum samples oriented so that the stringer planes were parallel to, at a  $45^\circ$  angle to, and normal to the spall plane. Damage was observed at the same stress level for all sample orientations. The morphology of the fractures was identical to the morphology of the stringers of inclusions (i.e., parallel to the spall plane when the stringers were parallel to the spall plane and normal to the spall plane when the stringers were normal to the spall plane).

Butcher also observed that the damage produced is less connected in samples oriented at  $90^\circ$ . Therefore, a larger amount of plastic deformation (shear between cracks lying on the spall plane) of the material is necessary before fracture can occur in this orientation. The sample oriented at  $90^\circ$  should therefore have a higher full-spall stress than a sample oriented at  $0^\circ$ , since more energy must be expended in plastic deformation. This behavior is in agreement with the observed variation with respect to the rolling direction of  $K_{IC}$ , the plane strain fracture toughness (Ref. 11), in several forged aluminum alloys. The toughness is largest parallel to the rolling direction for sheet or the extrusion direction for extruded shapes. It is lowest normal to the rolling plane of sheet and in the direction of the smallest dimension in extruded stock. These directions correspond to the  $0^\circ$  and  $90^\circ$  orientations of the stringer planes, respectively. This simple correlation indicates that it may be possible to make at

least qualitative conclusions about the spall fracture characteristics of a material from fracture toughness data, particularly for high-strength materials.

One can also describe the fracture characteristics of 2024-T81 aluminum as localized ductile fracture. Voids are nucleated at the large inclusions contained in stringer planes. These interact with other closely spaced inclusions to nucleate new voids. Fracture or damage development is therefore localized because the nuclei are ordered within the material. Thus, despite superficial brittle appearances, the cracks are of a ductile type.

The primary conclusion of this work is that the incipient spall threshold observed for 2024-T81 Al is determined not only by the matrix itself but also by the inclusions. If the inclusions were removed, substantially higher spall stresses would be observed.

d. OFHC Copper

A total of eight symmetric impact experiments were carried out, using the 2-1/2-inch-diameter-barrel light gas gun to investigate the dynamic fracture of ductile OFHC copper. The details of these experiments are given in Table V.

Three tapered flyer experiments were carried out, as indicated in Table V. Damage developed in these experiments as shown in Figure 17.

The damage was very similar to that in aluminum, and the void nucleation and growth behavior is discussed later. A further discussion of the behavior of copper is found in reference 1, where it is shown that the damage levels produced in the tapered flyer shots of Table V were successfully predicted before the experiments by extrapolating the results for aluminum.



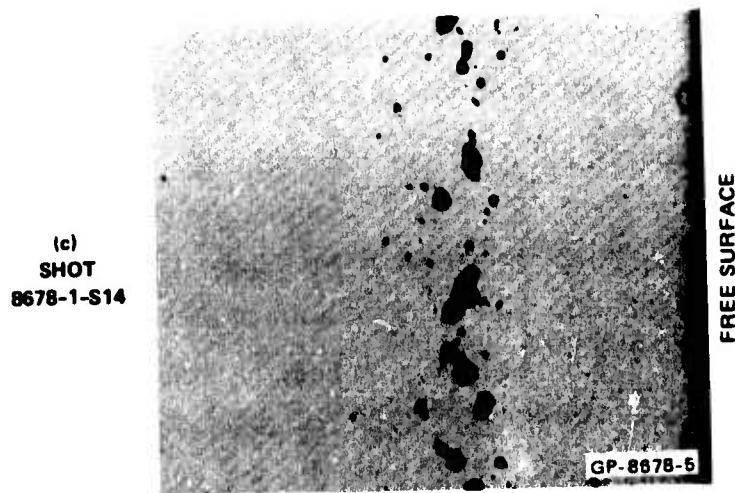
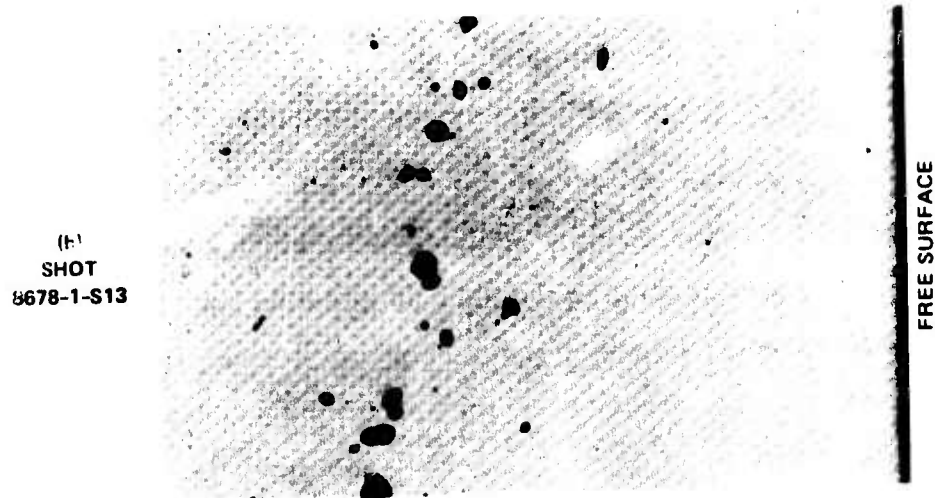
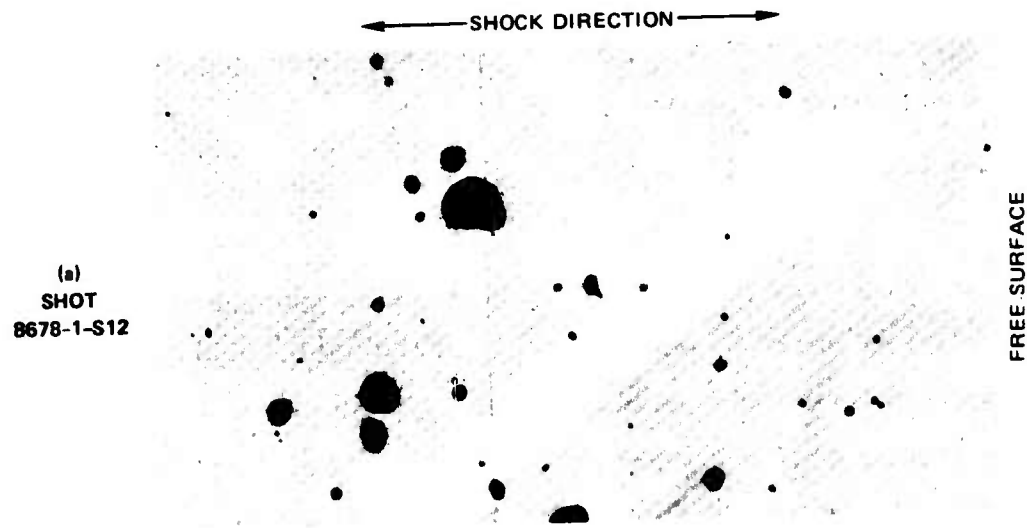
Table V

## SUMMARY OF DYNAMIC FLYER PLATE EXPERIMENTS IN OFHC COPPER

<u>Shot No.</u>	<u>Impact Velocity (mm/<math>\mu</math>sec)</u>	<u>Sample (mm)</u>	<u>Projectile (mm)</u>	<u>Comments</u>
S12 <sup>a</sup>	0.0269	6.313	3.156 to 1.578	Incipient to Intermediate damage
S13 <sup>a</sup>	0.0883	3.156	1.578 to 0.789	Incipient to intermediate
S14 <sup>a</sup>	0.119	1.578	0.789 to 0.394	Incipient to intermediate
S17 <sup>b</sup>	0.0984	6.313	2.275	Intermediate damage
S21 <sup>b</sup>	0.129	3.156	1.138	Intermediate damage
S23 <sup>b</sup>	0.121	6.313	2.275	Intermediate damage
S24 <sup>b</sup>	0.1585	1.587	0.622	Intermediate damage
S27 <sup>b</sup>	0.128	3.175	1.143	Intermediate damage

<sup>a</sup> Tapered flyer shots designed so that the time at stress was varied over a wide range for a constant stress experiment.

<sup>b</sup> Instrumented with a manganin pressure transducer directly behind the sample.



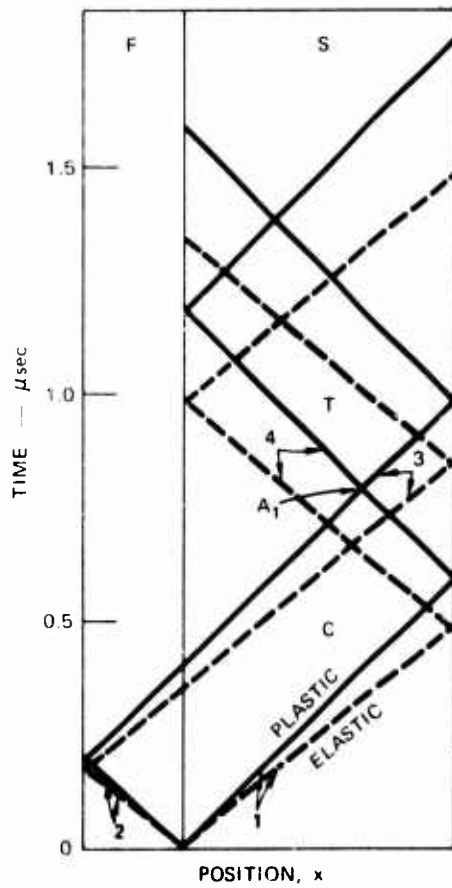
0.5 mm

FIGURE 17 DAMAGE OBSERVED IN THREE TAPERED FLYER EXPERIMENTS ON OFHC COPPER

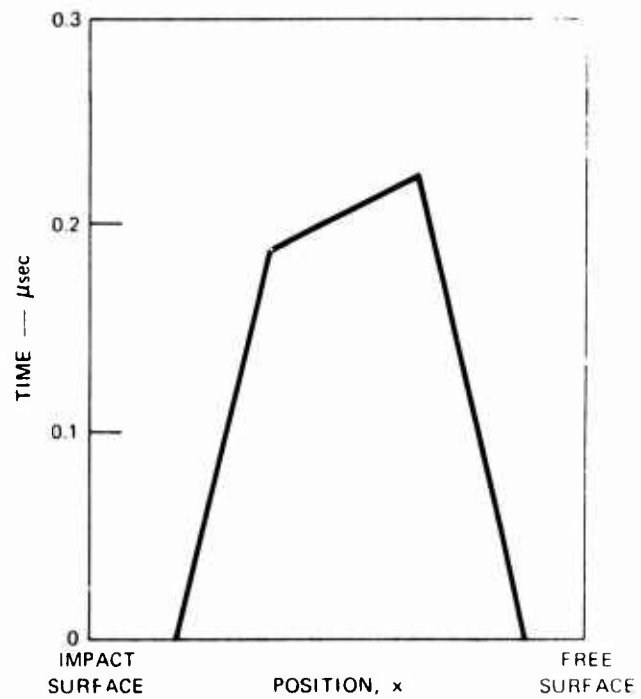
#### 4. QUANTIFYING THE DAMAGE

To predict shock-induced microscopic damage in ductile and brittle materials, we must first define what we mean by damage. Previous investigators have usually been content to describe shock damage qualitatively as "incipient spall," "heavy spall," and the like. However, a more detailed description of damage is needed if we are to build a predictive model that is good for damage levels ranging from the presence of a few voids or microcracks to levels that cause appreciable loss of structural strength. The method that we use is described in a previous report by Barbee et al. (Ref. 12) and reviewed briefly in the following paragraphs.

In our experiments the impact-loaded material samples are discs that, except for a region near the outer rim, have experienced uniaxial strain only. These shocked samples are sectioned parallel to the direction of impact, lapped, and polished. As explained earlier, in a typical impact experiment all elements of the samples have experienced the same peak tensile stress, but the stress duration varies with distance into the sample in the direction of impact, as shown in Figure 18. The plane of polish of a sectioned sample is divided into zones several microns wide and parallel to the free surfaces, as shown in Figure 19. Each zone is assumed to have experienced a different constant stress duration. Photographic enlargements (100X) of the polish plane are made. It usually requires five to ten photographs to cover the entire plane of polish of a sample. The microscopic damage in the ductile metals is in the form of spherical voids that intersect the plane of polish as circular holes. Each photograph is placed on a Telereadex machine, and the locations and apparent diameters of every hole in each zone are recorded on punched cards.



(a) SIMPLE  $x-t$  PLOT OF IMPACT EXPERIMENT



(b) TIME AT STRESS VERSUS POSITION  
DERIVED FROM SIMPLE  $x-t$  PLOT

GA-7456-16B

FIGURE 18 STRESS WAVE POSITION IN AN IMPACT SPECIMEN AND THE DERIVED DURATION OF THE PEAK TENSILE STRESS FOR A SIMPLE SQUARE WAVE WITH AN ELASTIC PRECURSOR

SHOT 873

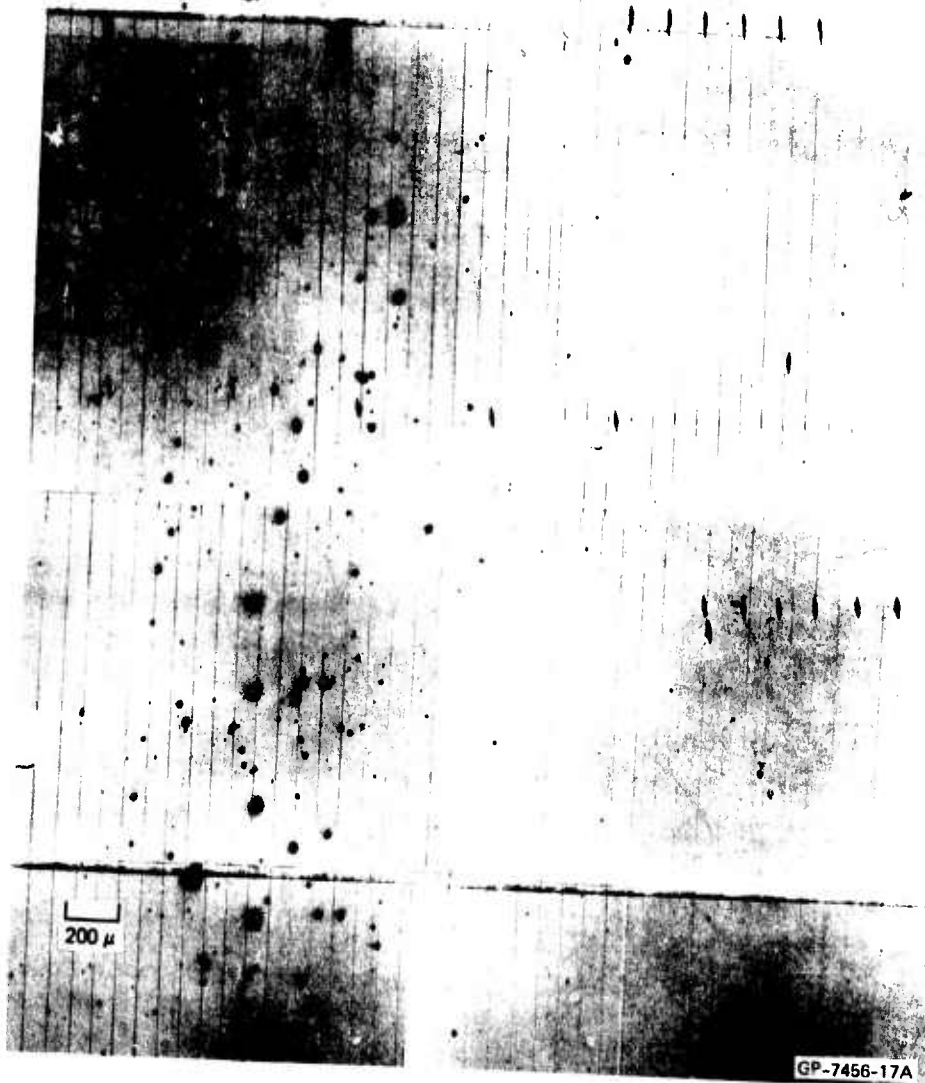


FIGURE 19 PHOTOMICROGRAPHS RULED INTO ZONES FOR COUNTING OF VOIDS

Thus, for each zone (and corresponding stress duration) a distribution is obtained, giving the number density of holes per unit area of surface in the plane of polish as a function of apparent hole diameter. In short, we describe the microscopic damage with statistical distribution functions. This is a fruitful approach because it eliminates the difficult problem of analyzing individual void behavior and provides a link between the discrete microscopic damage and continuum mechanics. The same general approach is used in the kinetic theory of gases, in dislocation dynamics, and in many other fields of study where a large number of interacting objects must be investigated.

Thus, for each zone we obtain a surface size distribution count  $N_i(\sigma, t)$ , where  $N_i(\sigma, t)$  is the number of voids intersecting a unit area of polish plane with hole radii between  $r_i$  and  $r_{i+1}$ , and where  $\sigma$  refers to the peak tensile stress and  $t$  is the stress duration corresponding to the given zone. This surface distribution, however, is not the distribution of interest. We really want to know the size distribution of voids per unit volume in the material, that is, what is the volume distribution of voids that, when the material is intersected by a plane of polish, results in the observed surface distribution? This statistical question has arisen in various other guises over the years, and standard statistical procedures have been developed for mapping such surface distributions into volume distributions. This question is reviewed in the previous report by Barbee et al. (Ref. 12), and a computer program, BABS 1, which was developed by SRI for the Air Force Weapons Laboratory to perform this operation, is described in that report.

An extension and generalization of BABS 1 has been developed to handle the much more difficult case of brittle cracks. It is discussed later in this report and described in detail in Appendices IX and X.

Examples of an observed surface count size distribution and the corresponding computed volume count size distribution are shown in Figures 20 and 21. The bounds in Fig. 21 are probable error limits on given mean values.

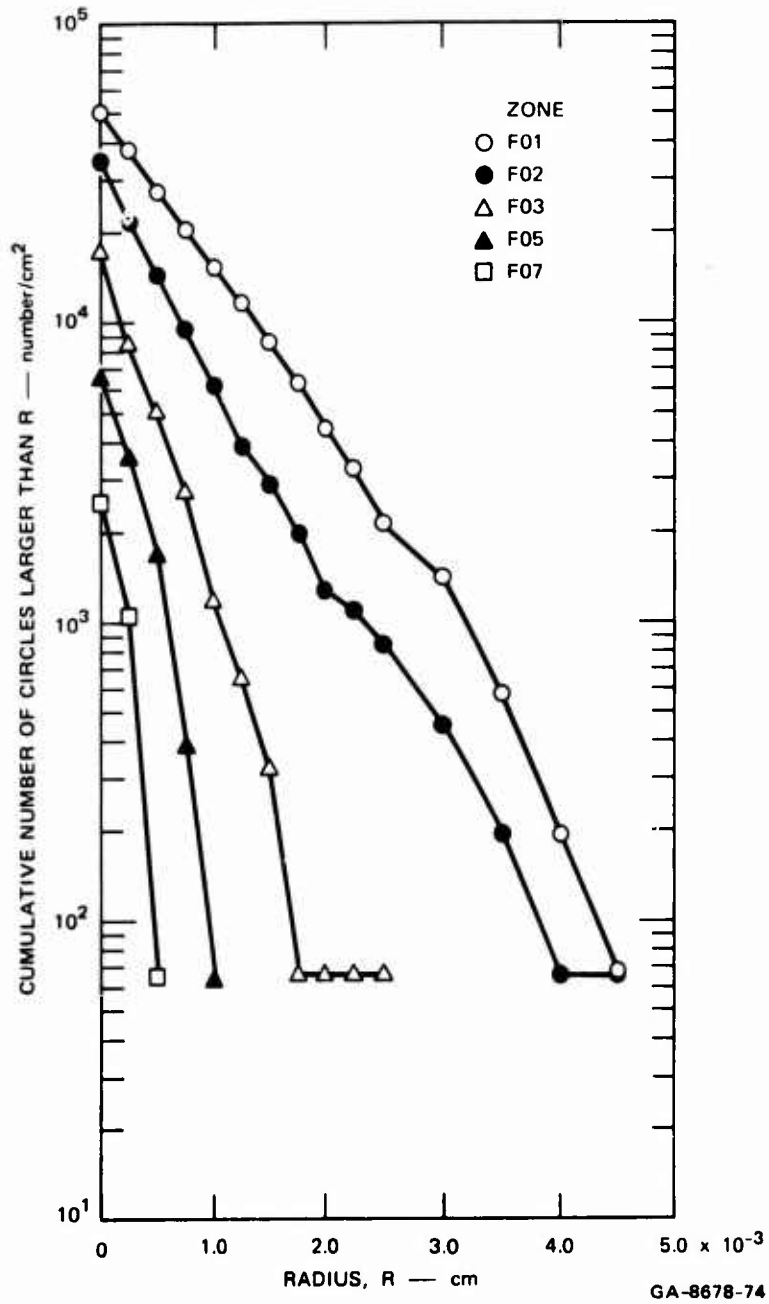


FIGURE 20 SURFACE DISTRIBUTIONS OF VOIDS ON THE FREE SURFACE SIDE OF THE SPALL PLANE IN OFHC COPPER: SHOT S24



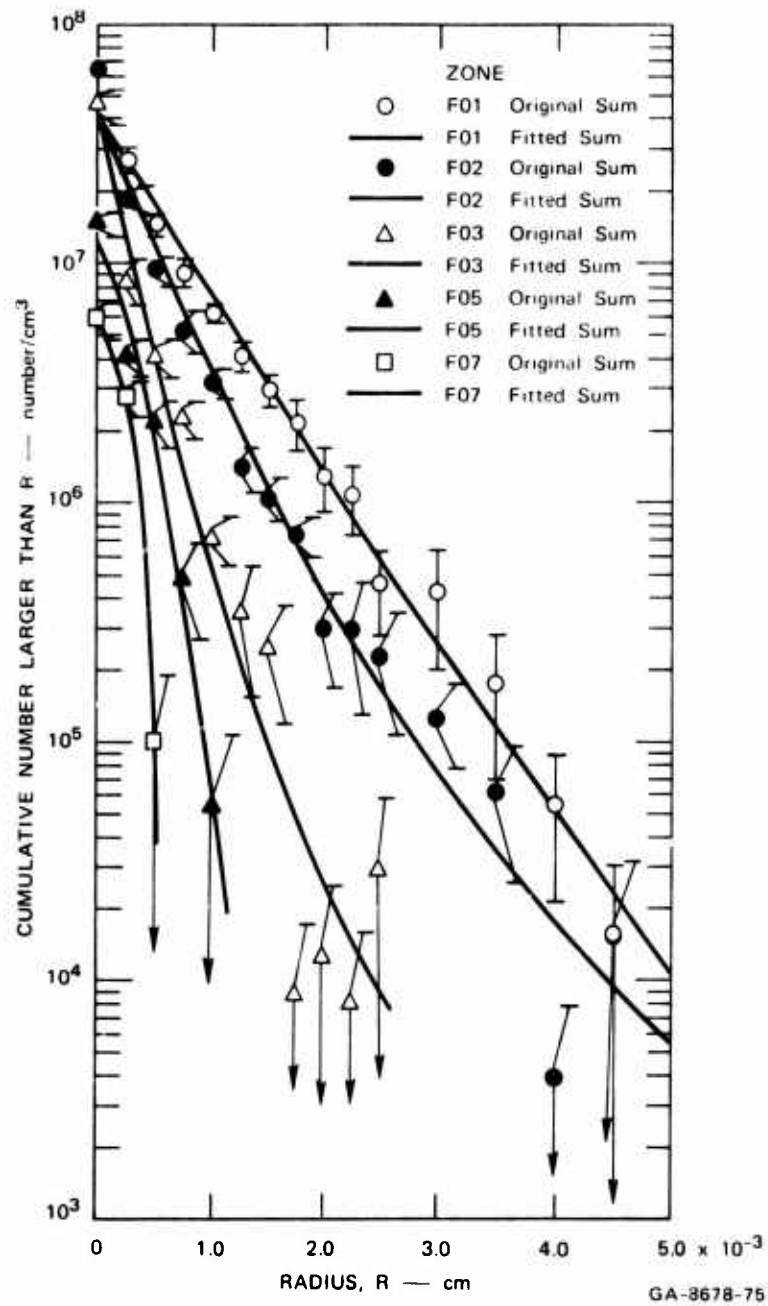


FIGURE 21 VOLUME DISTRIBUTION OF VOIDS ON THE FREE SURFACE SIDE OF THE SPALL PLANE IN OFHC COPPER: SHOT S24

## 5. WAVE PROPAGATION CALCULATIONS AND COMPARISON WITH DATA

The equations used for nucleation and growth of voids and the constitutive relations for damaged material are derived in this section. These equations are then used in wave propagation calculations to compute the damage in impacts of aluminum and copper plates. The correlations of computed and observed damage are shown.

### a. Nucleation Rate

The experimentally obtained nucleation rate of voids appears to have the following form

$$\dot{N} = \dot{n}_0 \exp\left(\frac{p - p_{n0}}{p_1}\right) \quad (5)$$

where

$p_{n0}$  = threshold (tensile) pressure for nucleation

$\dot{n}_0, p_1$  = constants

This form of nucleation function is consistent with static results in which no voids appear for stresses less than the yield or ultimate strength.

The voids are assumed to be nucleated with various initial radii. The assumed distribution is

$$\rho(R) = -\frac{\Delta N}{R_n} \exp(-R/R_n) \quad (6)$$

where

$\rho(R)$  = the concentration of voids at the radius  $R$  (number/cm<sup>3</sup>)

$\Delta N$  = the total number nucleated/cm<sup>3</sup>

$R_n$  = a parameter of the nucleation distribution

The nucleated number,  $\Delta N_g$ , larger than a radius R is

$$\Delta N_g(R) = \int_R^{\infty} \rho(R) dR = \Delta N \exp(-R/R_n) \quad (7)$$

The nucleated volume of voids is found by multiplying the volume of each void by the number of voids having that radius

$$\begin{aligned} \Delta V_n &= \frac{4\pi}{3} \int_0^{\infty} R^3 \rho(R) dR = -\frac{4\pi\Delta N}{R_n} \int_0^{\infty} R^3 \exp(-R/R_n) dR \\ &= 8\pi\Delta NR_n^3 \end{aligned} \quad (8)$$

b. Void Growth

Void growth is assumed to follow the simple viscous law

$$\dot{R} = \frac{(p - p_0)}{4\eta} R \equiv AR \quad (9)$$

where

$p, p_0$  = (tensile) pressure and threshold pressure

$\eta$  = material viscosity

This form for the growth relation was observed in the experimental data for aluminum. According to the dynamic analysis of Appendix III, the viscous law is accurate within 5 percent up to a radius of

$$R_{cr}^2 = \frac{0.32\eta^2}{\rho(p - p_0)} \quad (10)$$

For aluminum in the stress range tested and with  $\eta = 200$  poise, the limiting radius is about 10 microns. For larger radii, inertia effects become important and the growth velocity is less than that given by Eq. (9).

In a planar impact, the stress field is not spherically symmetric as it is in the analysis that led to the viscous growth law, Eq. (9). Our macroscopic stress field more closely resembles a one-dimensional flow. The two-dimensional calculations of Appendix V show that the viscous growth law is also valid for the case of one-dimensional flow.

The threshold pressure for growth is the pressure at which yielding occurs throughout the region near the void. According to the static, axisymmetric calculations of Appendix IV, the threshold stress is four to five times the yield strength. However, in one-dimensional flow without voids, overall yielding occurs at the lower stress of

$$\sigma_y = \left( \frac{1 - \nu}{1 - 2\nu} \right) Y \quad (11)$$

where

$\sigma_y$  = the Hugoniot elastic limit,

$\nu$  = Poisson's ratio,

$Y$  = the yield strength.

For  $\nu = 1/3$ ,  $\sigma_y$  is twice the yield strength. Therefore, the threshold pressure,  $p_0$  equals  $\sigma_y - 2Y/3$  and thus is only slightly larger than the yield strength. The value of  $Y$  used in the estimate of threshold should be increased both for dynamic effects and for the work hardening that may occur during the preceding compressive pulse.

The material viscosity used in the growth equation must pertain to the stress levels, loading rates, and temperatures that occur during the void growth. Since the stress levels and loading rates are similar to those in shock fronts, data on shock front thicknesses may be used to estimate the viscosity. Appendix VI contains an analysis of viscosity-governed shock front thickness to aid in the estimate. It should be noted that the viscosities apparent in the shock front are one or two orders of magnitude less than those obtained by other methods.

In our analysis of growth and nucleation of voids as part of the one-dimensional wave-propagation calculations, it is assumed that the void size distribution law,

$$N_g(R) = N_0 \exp(-R/R_1) \quad (12)$$

holds at all times. This assumption is consistent with the equation for growth or nucleation but not for the combination. To investigate the compatibility of this assumption with the growth law, let  $N_g(R) = N_0 \exp(-R/R_{10})$  at  $t = 0$ . Then, allow some growth to occur at a constant stress. The new radii are obtained by integrating Eq. (9)

$$R'(t) = R e^{At} \quad (13)$$

where

$R'$  = the radius at the current time

$R$  = the radius at  $t = 0$

The new distribution function is determined from Eq. (12) by inserting the new values of radius and solving for  $R_1$  from the condition that  $N'_g(R') = N_g(R)$ , that is, that the numbers have not changed.

$$\begin{aligned}
N'_g(R') &= N_0 \exp(-R e^{At}/R_1) \\
&= N_g(R) = N_0 \exp(-R/R_{10})
\end{aligned}
\tag{14}$$

Solving for  $R_1$ , we find that

$$R_1 = R_{10} e^{At} \tag{15}$$

Hence, the radius parameter is independent of  $R$  and grows at the same rate as other radii. Therefore, the new distribution has the same form as the old. In fact, it can be shown that for any distribution of the form

$$N_g = N_0 \sum_n a_n \left(\frac{R}{R_1}\right)^n \tag{16}$$

the distribution function and parameters  $a_n$  after growth are the same as the function and parameters before growth, and  $R_1$  is altered as in Eq. (15).

If only nucleation occurs, it is clear that the distribution function does not change with time; only  $N_0$  varies with time:

$$N_g(R, t) = N_0(t) \exp(-R/R_{10}) \tag{17}$$

Now consider that both nucleation and growth occur under a square wave of duration  $t$ . Then a number of voids nucleated at time  $\tau$  in the time increment  $d\tau$  and with a distribution

$$dN_g(R, t) = Nd\tau \exp(-R/R_{10}) \tag{18}$$

will grow to

$$dN_g(R,t) = \dot{N} d\tau \exp \left\{ -R / \left[ R_{10} e^{A(t-\tau)} \right] \right\} \quad (19)$$

at time  $t$ . ( $\dot{N}$  is the constant nucleation rate.) The total distribution of voids is obtained by summing all the increments  $dN_g$  nucleated between 0 and  $t$ ,

$$N_g(R,t) = \dot{N} \int_0^t \exp \left\{ -R / \left[ R_{10} e^{A(t-\tau)} \right] \right\} d\tau \quad (20)$$

With the substitutions

$$\xi = \frac{R}{R_{10}} e^{-A(t-\tau)}$$

and

$$N_0 = \dot{N} t$$

in Eq. (20), the exponential integral (Ei) form is obtained:

$$\frac{N_g(R,t)}{N_0(t)} = \frac{1}{At} \left[ -\text{Ei} \left( -\frac{R}{R_{10}} e^{-At} \right) + \text{Ei} \left( -\frac{R}{R_{10}} \right) \right] \quad (21)$$

The Ei functions are evaluated from standard tables.

The preceding distribution can be compared with that obtained with a constant distribution. The number nucleated is simply  $\dot{N}_0 t$  as above. The relative volume nucleated at time  $\tau$  is, from Eq. (8),

$$dV_{vr} = 8\pi N_0 d\tau R_{10}^3 \quad (22)$$

At time  $t$ , this volume is

$$dV_{vr} = 8\pi \dot{N}_0 d\tau \left[ R_{10} e^{A(t-\tau)} \right]^3 \quad (23)$$

The total volume is found by summing from 0 to  $t$ ,

$$V_{vr} = 8\pi \int_0^t \dot{N}_0 \left[ R_{10} e^{A(t-\tau)} \right]^3 d\tau = \left( \frac{8\pi \dot{N}_0 R_{10}^3}{3A} \right) (e^{3At} - 1) \quad (24)$$

But if the distribution is not altered, then

$$N_g = \dot{N}_t \exp(-R/R_2) \quad (25)$$

and the volume is  $8\pi \dot{N}_0 t R_2^3$  according to Eq. (8). Equating this expression for volume to Eq. (24) allows  $R_2$  to be evaluated.

$$R_2 = R_1 \left[ \frac{e^{3At} - 1}{3At} \right]^{1/3} \quad (26)$$

A comparison of the distributions obtained with Eqs. (21) and (26) is shown in Figure 22. Evidently the distribution of Eq. (21) shows a lesser number of voids at intermediate radii but more at the large radii.

The change in shape of the distribution does not alter the accuracy of the volume calculation. Each nucleated distribution of voids retains its distribution during growth as noted earlier, and its volume



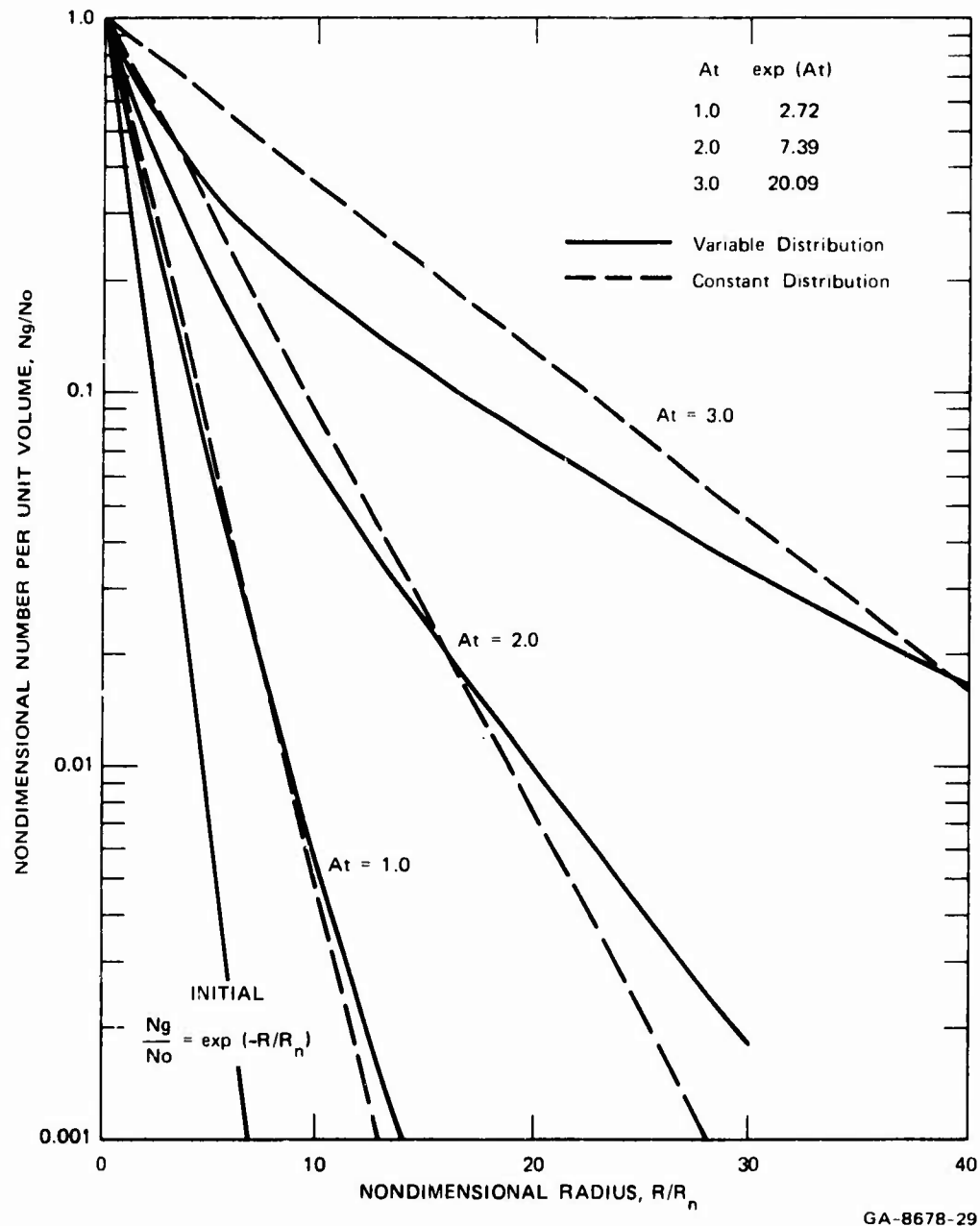


FIGURE 22 COMPARISON OF VOID SIZE DISTRIBUTIONS WITH A CONSTANT AND A VARIABLE FORM

is represented correctly by Eq. (23). Hence, the total volume given by Eq. (24) must be correct. Therefore, we conclude that the present procedure has the following properties:

- The total number of voids is correctly represented.
- The void volume is correct within the limits of the viscous growth law.
- The distribution of the form of Eq. (12) [or Eq. (25)] with the radius parameter of

$$R_2 = \left( \frac{V}{8\pi N_0} \right)^{1/3} \quad (27)$$

only crudely indicates the general shape of the actual distribution.

The present nucleation and growth procedure is adequate for our purposes.

#### c. Constitutive Relations

The presence of voids alters the constitutive relations of the material. As usual, these relations have been separated into equations for pressure and deviator stress. In the formulation we assumed that the average pressure is proportional to the change in specific volume of the solid material, i.e.,

$$P_s = P_{0s} - K \frac{\Delta V_s}{V_s} \quad (28)$$

where

$P_{0s}, P_s$  = pressures before and after the time increment

$K$  = the bulk modulus

$V_s$  = the specific volume of the solid

The specific volume of the solid,  $V_s$ , is obtained by subtracting the specific void volume from the gross specific volume. Equation (28) is the usual mechanical pressure-volume relation appropriate for low pressures. The average pressure in the solid,  $P_s$ , is related to the average pressure on a gross section through the ratio of the solid area to the gross area of a section. This ratio of areas was assumed to be related to the relative void volume,  $V_v D$ , where

$$V_v = \text{the specific volume of voids}$$

$$D = \text{the gross density}$$

The average pressure on the gross section was then presumed to be

$$p_a = P_s (1 - \alpha_c V_v D) \quad (29)$$

where  $\alpha_c$  is a constant. When Eq. (28) is expressed in terms of average pressures on the gross section, it becomes

$$\frac{p_a}{1 - \alpha_c V_v D} = \frac{p_0}{1 - \alpha_c V_{v0} D_0} - K \frac{V_s - V_{s0}}{V_{s0}} \quad (30)$$

where the subscript 0 refers to the values at the beginning of a time increment. Equation (30) was compared with the results of the two-dimensional calculations in Appendix V; the equation fits those results very well for an  $\alpha_c$  of about 2.0.

The deviator stress was assumed to be a function of the overall distortion of the material and to follow a viscoplastic law as follows:

$$\Delta\sigma' = \frac{4}{3} \mu \frac{\Delta V}{V} \quad \sigma' < \frac{2}{3} Y \frac{V_s}{V}$$

(elastic)

$$= \frac{2}{3} Y \frac{V_s}{V_0} + \frac{4\eta\Delta V}{3V\Delta t} \left(1 - \frac{4V_s}{V}\right)$$

(viscoplastic) (31)

where

- $\sigma'$  = the deviator stress
- $\mu$  = the shear modulus
- $V$  = the gross specific volume
- $Y$  = the yield strength
- $\eta$  = the material viscosity
- $\Delta t$  = the time increment

In Eq. (31) the yield strength is reduced gradually as the void volume increases. Also the viscous contribution (second term of the second equation) is reduced as the void volume increases. The latter reduction factor was derived from the results in Appendix V. Equation (31) is felt to be a reasonable form for the deviator stress, but more detailed calculations, such as those in Appendix V, have not been completed to verify it fully.

The preceding constitutive relations form a mechanical equation of state; temperature and internal energy are neglected. Initially this was assumed to be adequate. However, as shown in some of our two-dimensional calculations, internal energies can become large at the void boundary under these high loading rates. The following approximate analysis indicates that melting probably occurs at the free surface of

the void. The strain rate in the circumferential direction at the void surface,  $\dot{\epsilon}_\theta$ , is

$$\dot{\epsilon}_\theta = \frac{1}{R} \frac{dR}{dt} \quad (32)$$

Then, for no volume change in the material at the free surface, the radial strain is  $\dot{\epsilon}_r = -2\dot{\epsilon}_\theta$ . The deviator stresses in the circumferential and radial directions ( $\sigma'_\theta$  and  $\sigma'_r$ ) are obtained in Appendix V under the assumption that there is no volume change.

$$\begin{aligned} \sigma'_\theta &= \frac{1}{3} Y + 2\eta\dot{\epsilon}_\theta \\ \sigma'_r &= -\frac{2}{3} Y - 4\eta\dot{\epsilon}_\theta \end{aligned} \quad (33)$$

Since the radial stress is zero at the surface, the local pressure,  $p_\ell$ , must be the negative of  $\sigma'_r$ . Therefore, the circumferential stress is

$$\sigma_\theta = p_\ell + \sigma'_\theta = Y + 6\eta\dot{\epsilon}_\theta \quad (34)$$

An expression for internal energy at the surface of the void is obtained from

$$E = \int 2\sigma_\theta \dot{\epsilon}_\theta dt = 2 \int (Y + 6\eta\dot{\epsilon}_\theta) \dot{\epsilon}_\theta dt \quad (35)$$

We note that

$$\dot{\epsilon}_\theta = \frac{1}{R} \frac{dR}{dt} = \frac{p - p_0}{4\eta}$$

according to Eq. (9), where R is the void radius. With a square wave tensile pulse, the internal energy is then

$$E = 2 \left[ Y + \frac{3}{2} (p - p_0) \right] \frac{p - p_0}{4\eta} \Delta t \quad (36)$$

In aluminum, with a yield of 1 kbar, applied pressure of 10 kbar,  $p_0$  of 2 kbar,  $\eta$  of 200 poise, and  $\Delta t$  of 0.4  $\mu$ sec, the internal energy is  $4 \times 10^{10}$  erg/gm. The internal energy needed to cause complete melting in aluminum is about  $10^{10}$  erg/gm. Hence, it appears likely that some melting occurs at the void surface, at least for impacts causing intermediate to high damage. The preceding analysis of melting has not yet been completed or implemented in any fracturing calculations.

The mechanical constitutive relations, together with the growth and nucleation laws, are incorporated into a subroutine called DFRACT and procedures for inserting it into finite-difference (PUFF-type) computer codes are given in Appendix VII.

#### d. Wave Propagation Results

From the wave propagation calculations we obtain stress histories at selected points, void concentrations (number/cm<sup>3</sup>), and relative void volumes. Since each of these three can be obtained at any depth into the target, we can determine the variation of void concentration or volume as a function of position. The following discussion shows such variations of damage in 1145 aluminum and OFHC copper.

Calculations for 1145 aluminum are reported in references 1 and 12. These computations were repeated with the improved nucleation function (exponential, instead of linear) and with the equation of state modified to reflect the VOID calculations of Appendix V. The impacts

in aluminum, which were all uninstrumented, are listed in Table VI. The parameters used in the impact calculations are listed in Table VII. The damage distributions (void concentration and void volume as a function of depth) are shown in Figures 23 to 27. These calculated distributions are considerably closer to the experimental ones than those exhibited previously. The void concentration is represented fairly well by the computations at all impact levels; the major difference is that the computed distributions are steeper than the experimental ones. Only Shot 873 shows poor correlation between computed and experimental concentrations. The void volume distributions are satisfactory at low damage levels but are too low at high damage. These values have shallower slopes on either side of the spall plane than the experimental data, especially at high damage. This difference in slope is an indication that the damage at the spall plane is not having a sufficient effect on the nearby stress fields. It appears, therefore, that the current fracturing procedure is not able to correctly compute relative void volume above a few percent.

The two copper impacts that were studied in detail are listed in Table VIII and the fracturing parameters used in the corresponding calculations are in Table VII. The experimental and computed damage distributions are compared in Figures 28 and 29. The computed void volumes for these impacts are too low at the spall plane and on the free surface side (on the right) of the spall plane, and they are too high on the impact side. All these differences come from the same source: underproduction of void volume. In the experiment and calculations, the damage occurs first at the spall plane and to the right of it. The high damage reduces the tensile stresses propagating to the left and therefore reduces the damage on the left of the spall plane. Unfortunately, the two targets selected for study both contain fairly high damage, although it is evident now that lower-damage targets would give more assistance in model development.

Table VI

## IMPACT CONDITIONS FOR EXPERIMENTS IN 1145 ALUMINUM

Shot Number	Flyer		Target Thickness (cm)	Impact Stress (kbar)
	Thickness (cm)	Velocity (cm/sec)		
847	0.236	$1.289 \times 10^4$	0.635	10.0
873	0.236	$1.32 \times 10^4$	0.617	10.3
849	0.236	$1.426 \times 10^4$	0.635	11.0
872	0.236	$1.542 \times 10^4$	0.635	12.0
939	0.114	$1.856 \times 10^4$	0.318	14.3

Table VII

## DUCTILE FRACTURE PARAMETERS FOR 1145 ALUMINUM AND OFHC COPPER

Parameter	Units	Description	Al (1145)	Cu (OFHC)
T1 ( $3/4\eta$ )	$\frac{\text{cm}^2}{\text{dyn-sec}}$	Growth parameter	-0.01	-0.01
$\eta$	$\frac{\text{dyn-sec}}{\text{cm}^2}$	Material viscosity	75	75
T2 ( $\sigma_{g0}$ )	dyn/cm <sup>2</sup>	Growth threshold	$-4 \times 10^9$	$-5 \times 10^9$
T3 ( $R_0$ )	cm	Nucleation void radius	$1 \times 10^{-4}$	$1 \times 10^{-4}$
T4 ( $\dot{n}_0$ )	$\frac{\text{no.}}{\text{cm}^3\text{-sec}}$	Nucleation coefficient	$3 \times 10^9$	$2.8 \times 10^{12}$
T5 ( $p_{n0}$ )	dyn/cm <sup>2</sup>	Nucleation threshold	$-3 \times 10^9$	$-5 \times 10^9$
T6 ( $p_1$ )	dyn/cm <sup>2</sup>	Nucleation parameter	$-4 \times 10^8$	$-2 \times 10^9$



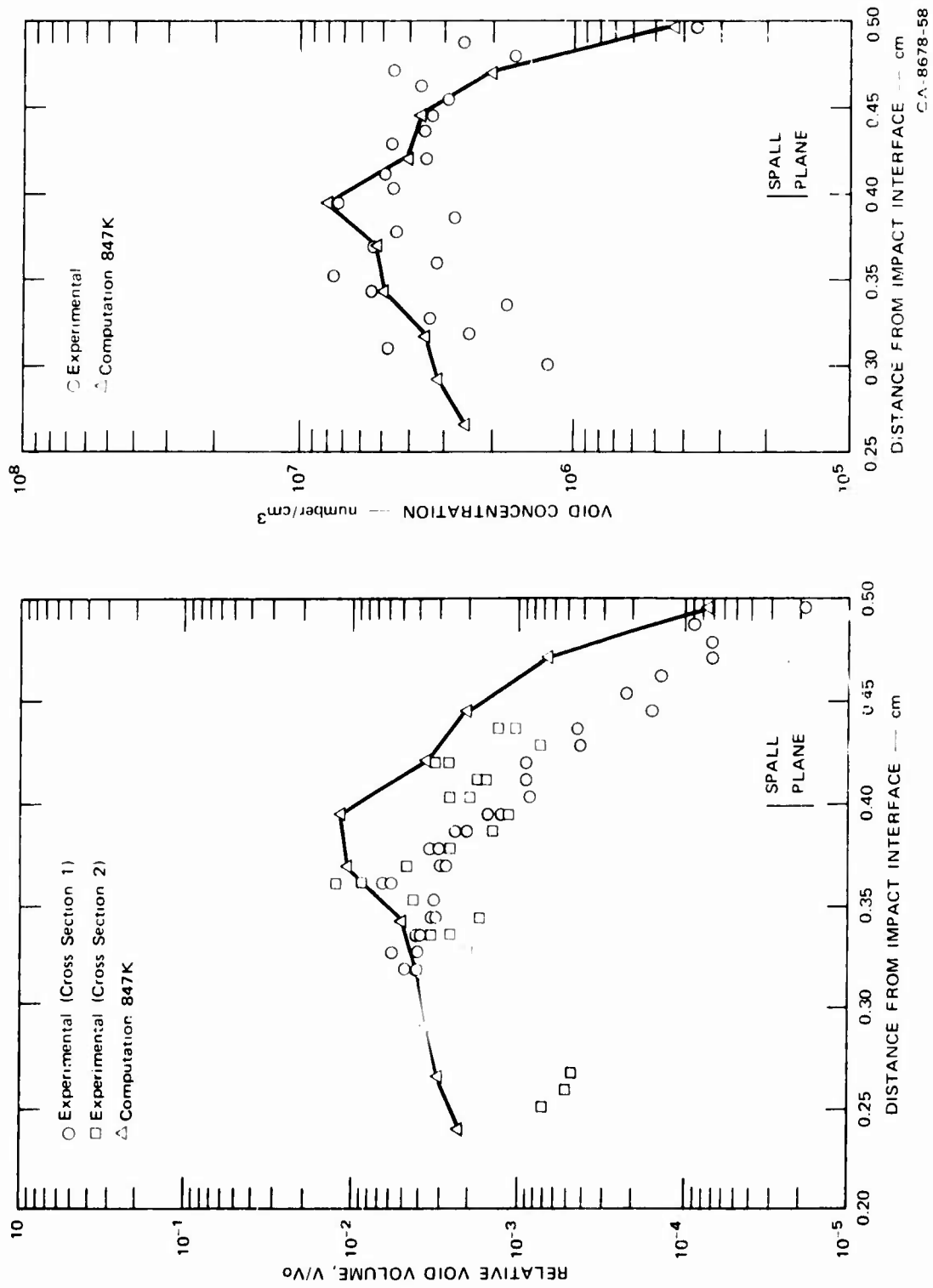


FIGURE 23 COMPUTED AND OBSERVED DAMAGE IN 1145 ALUMINUM: SHOT 847

CA-8678-58

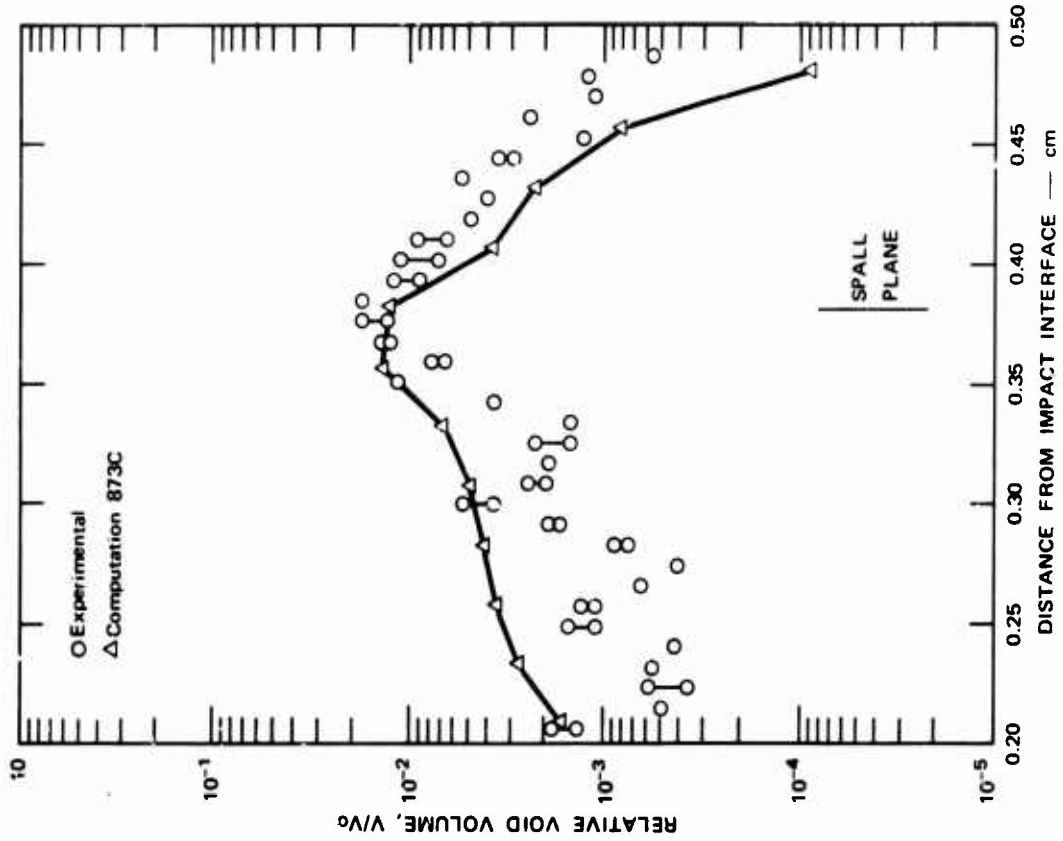
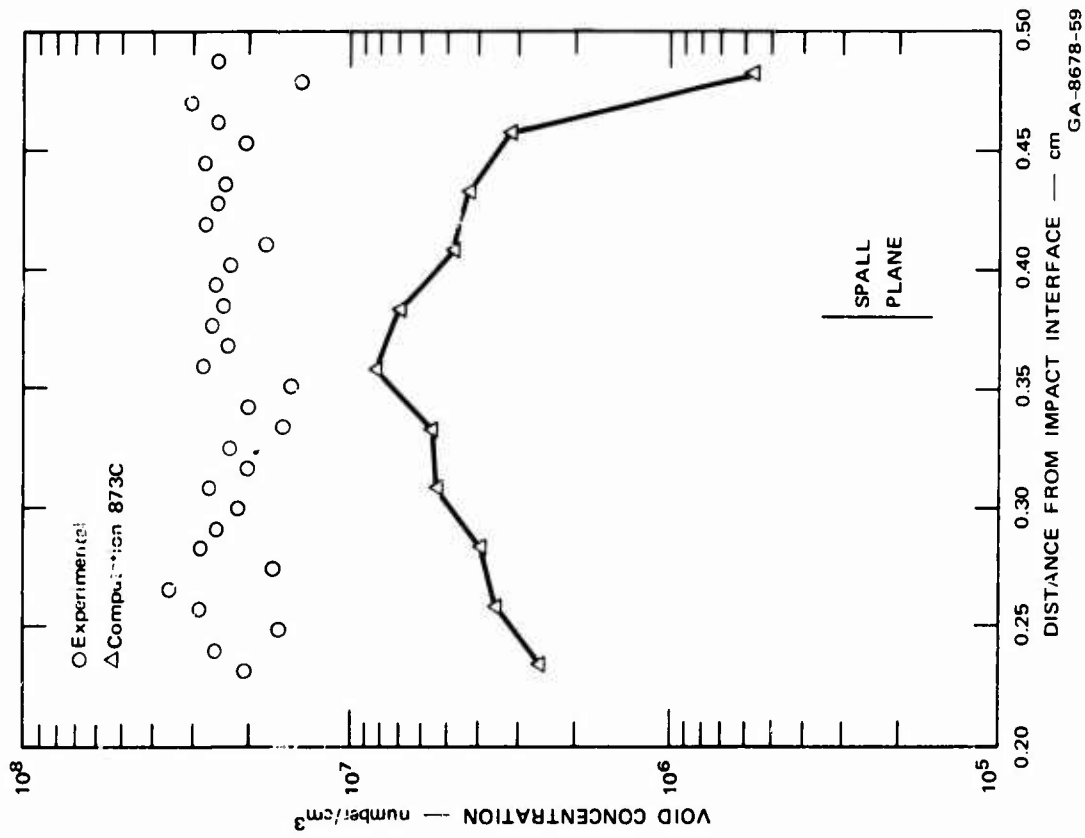


FIGURE 24 COMPUTED AND OBSERVED DAMAGE IN 1145 ALUMINUM: SHOT 873

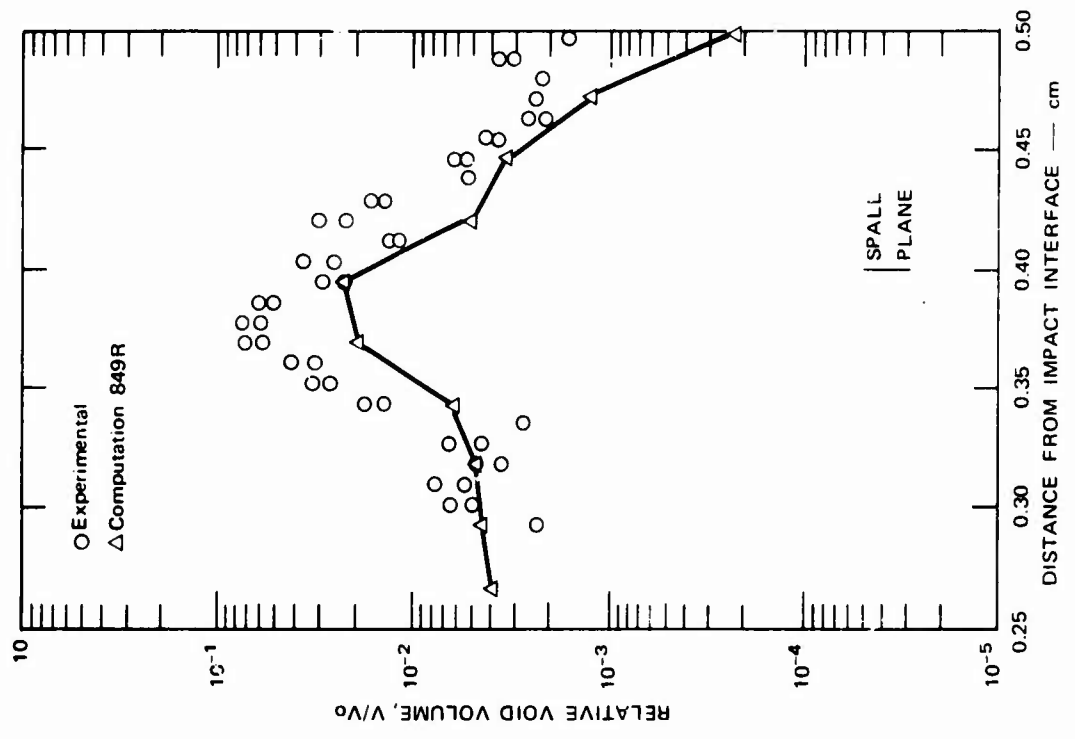
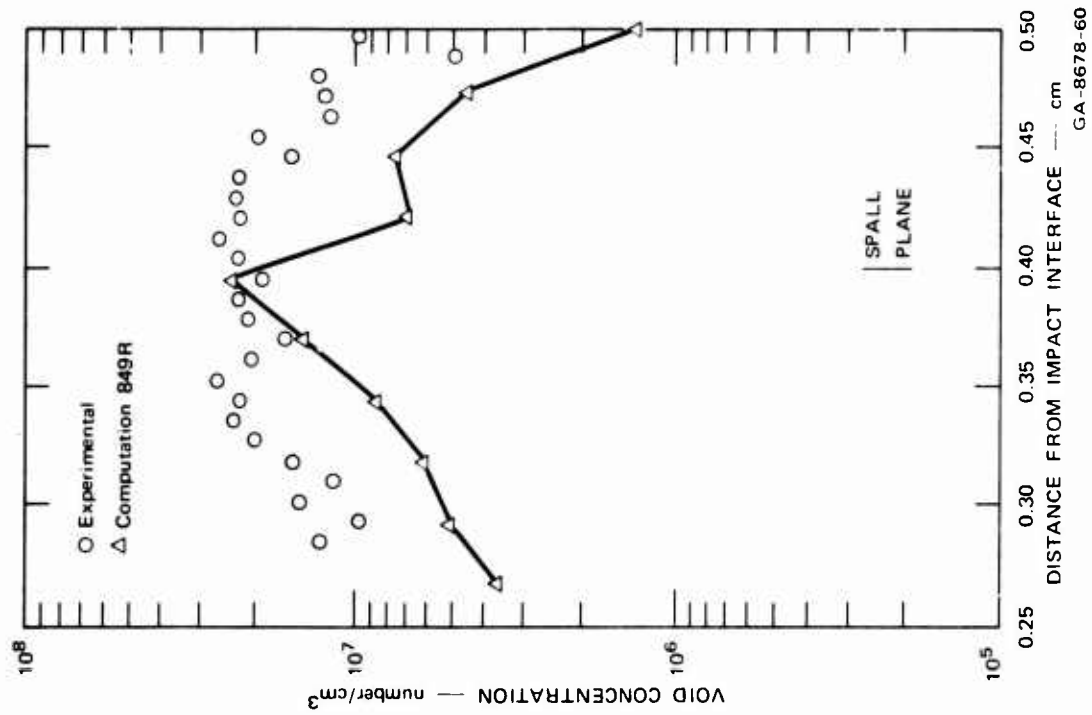
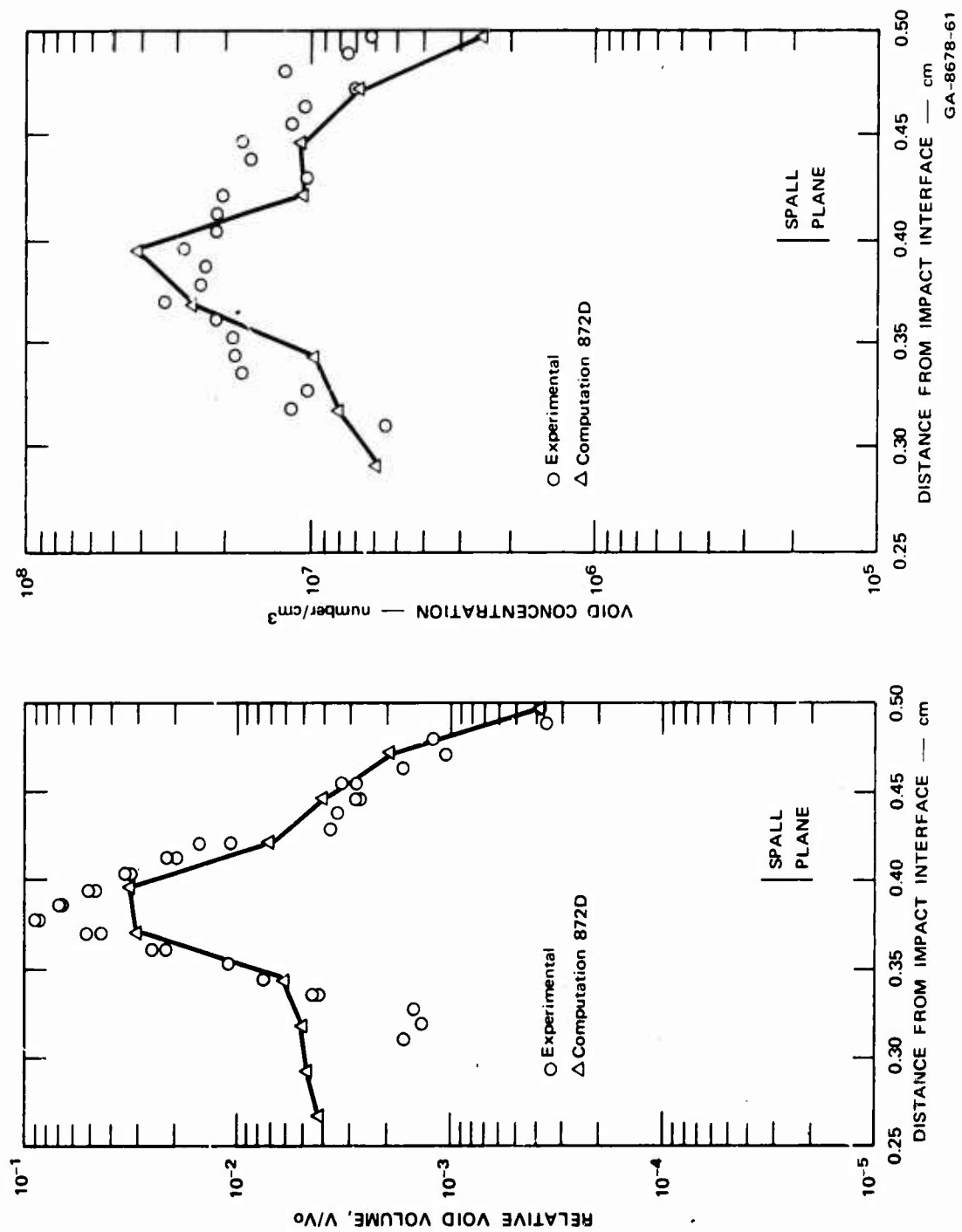


FIGURE 25 COMPUTED AND OBSERVED DAMAGE IN 1145 ALUMINUM: SHOT 849



GA-8678-61

FIGURE 26 COMPUTED AND OBSERVED DAMAGE IN 1145 ALUMINUM: SHOT 872

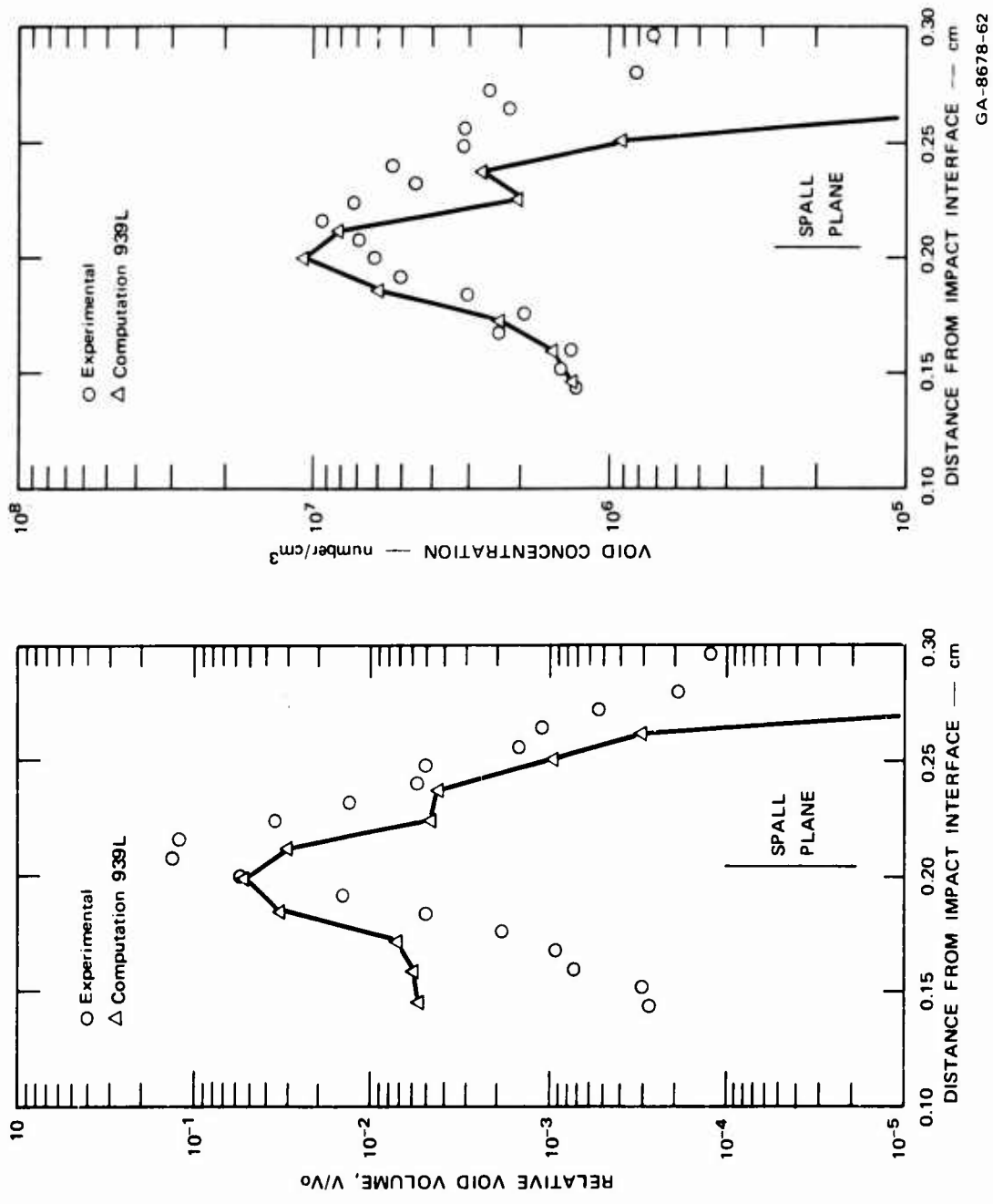


FIGURE 27 COMPUTED AND OBSERVED DAMAGE IN 1145 ALUMINUM: SHOT 939

GA-8678-62

Table VIII

IMPACT CONDITIONS FOR EXPERIMENTS IN OFHC COPPER

<u>Shot Number</u>	<u>Flyer</u>		<u>Target</u>	<u>Backing Plate</u>	<u>Impact Stress (kbar)</u>
	<u>Thickness (cm)</u>	<u>Velocity (cm/sec)</u>	<u>Thickness (cm)</u>		
S24	0.0622	$1.585 \times 10^4$	0.1587	PMMA ..	29.3
S27	0.1143	$1.286 \times 10^4$	0.3175	PMMA	23.7

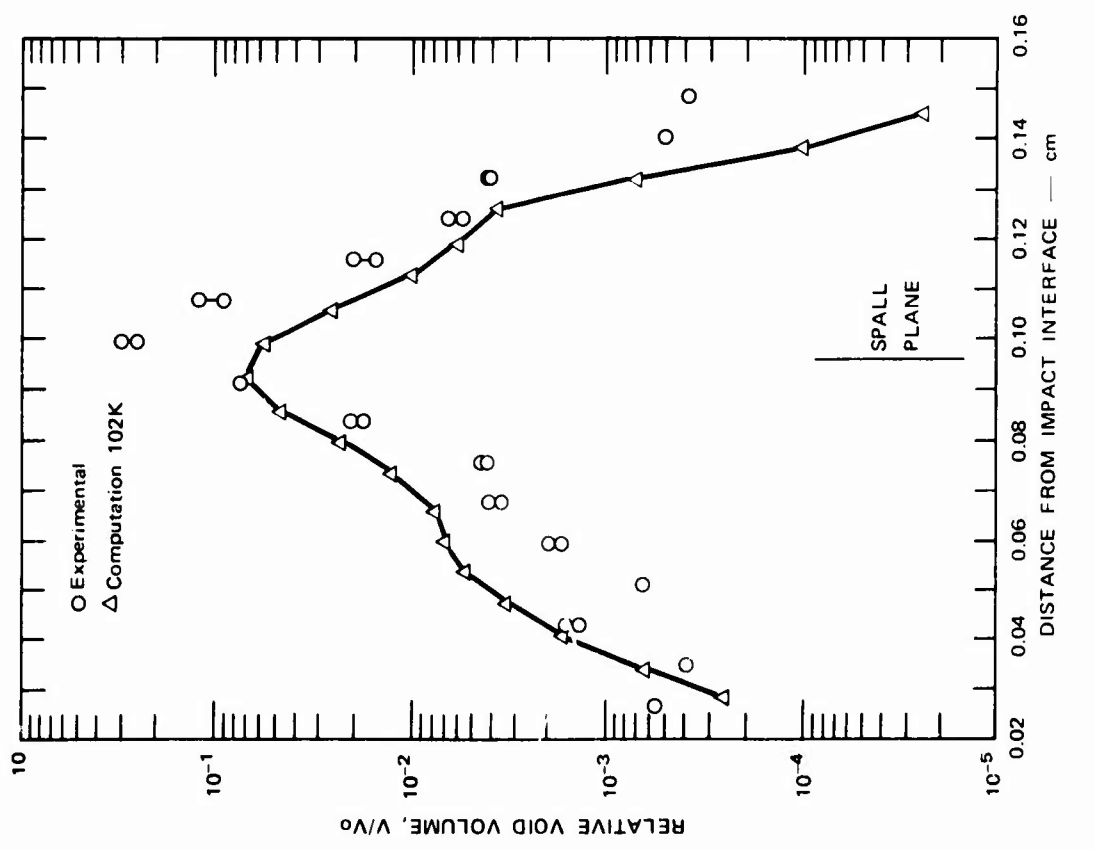
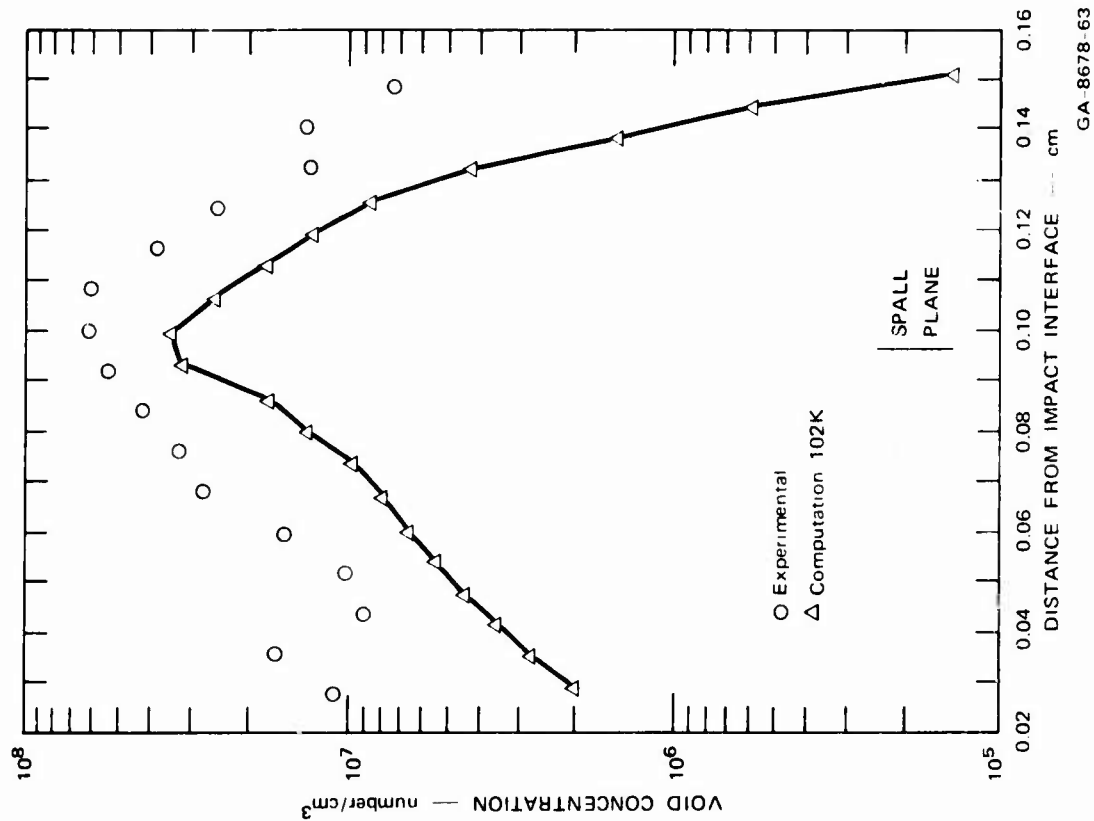
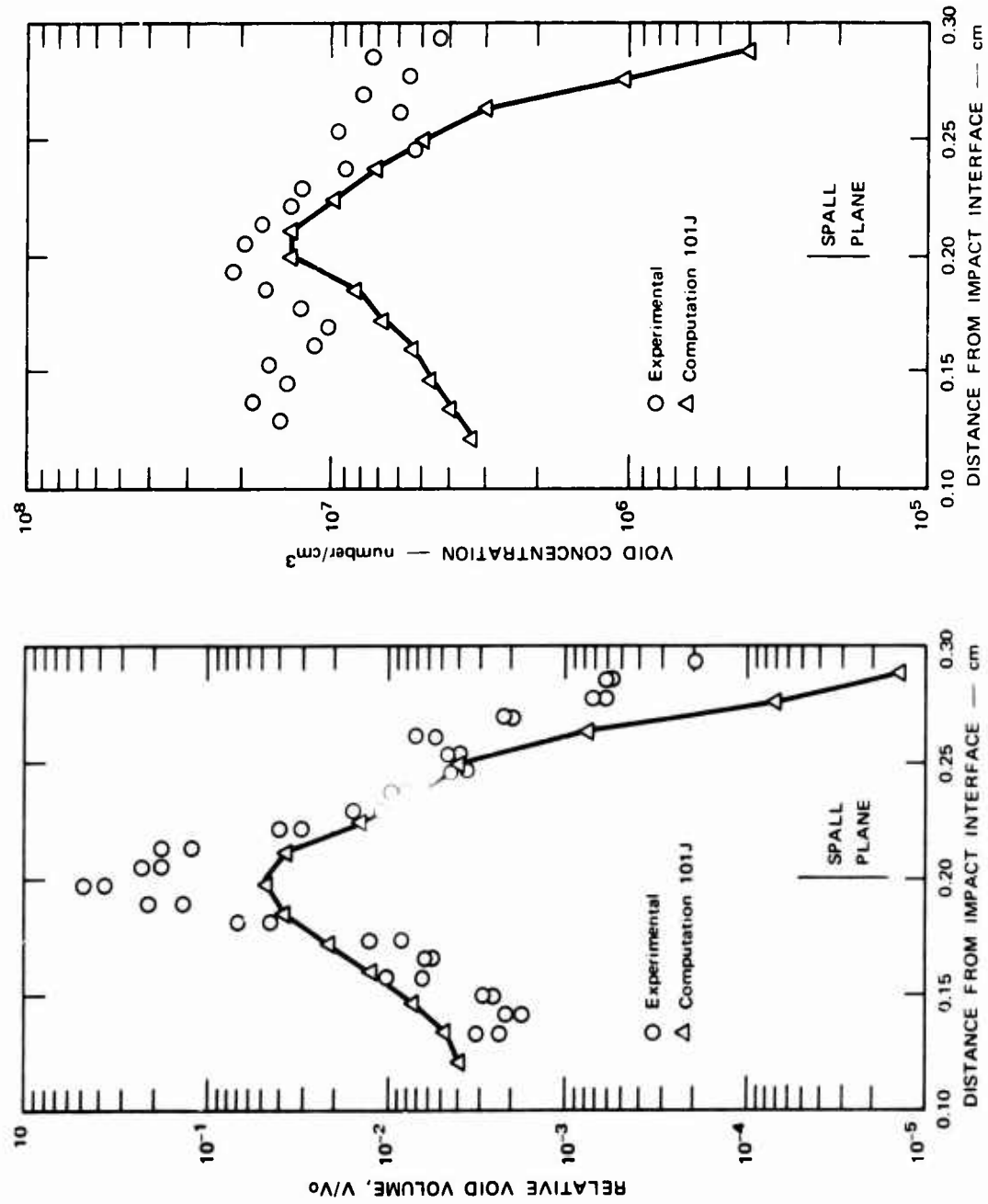


FIGURE 28 COMPUTED AND OBSERVED DAMAGE IN OFHC COPPER: SHOT S24

GA-8678-63



GA-8678-64

FIGURE 29 COMPUTED AND OBSERVED DAMAGE IN OFHC COPPER: SHOT S27



For the copper impacts, manganin gages in blocks of PMMA were placed behind the targets. The gage records and computed stress histories are given in Figures 30 and 31. The Hugoniot equation-of-state parameters of Walsh et al. (Ref. 13) was used for copper, and the data of Barker and Hollenbach (Ref. 14) were used for PMMA. The peak compressive stress is not well-represented by the calculations, indicating that the Hugoniots of one or both materials are not correct in the relevant stress range. The spall signal, the hump following the main compression pulse, is of the correct amplitude in both figures but arrives much too early. This later arrival of the experimental spall signal may indicate either that the actual damage develops more slowly than expected or that the propagation velocity is lower than that given by the calculations.

Several calculations were made with different fracture parameters to get the best correlation with experimental damage distributions and stress records. We noted that the computed amplitude of the spall signal was larger for calculations showing higher damage. The variation of the stress minimum preceding the spall peak was also studied. This minimum also increased with damage. An increase in the growth threshold decreased the difference between the minimum and the spall peak.

It should be noted that the viscosity given in Table VII is 75 poise for both aluminum and copper although previous estimates were based on viscosities of about 200 poise. We believe that 200 poise is about right for both materials at very low damage levels. The lower value of viscosity used here reflects our attempt to reach intermediate and high damage levels. At such levels, the viscosity may be reduced sharply by the internal energy or heating associated with void growth (see preceding subsection). Considering this hypothesized heating effect, the value of viscosity used here represents some average of the range of viscosities actually governing growth.

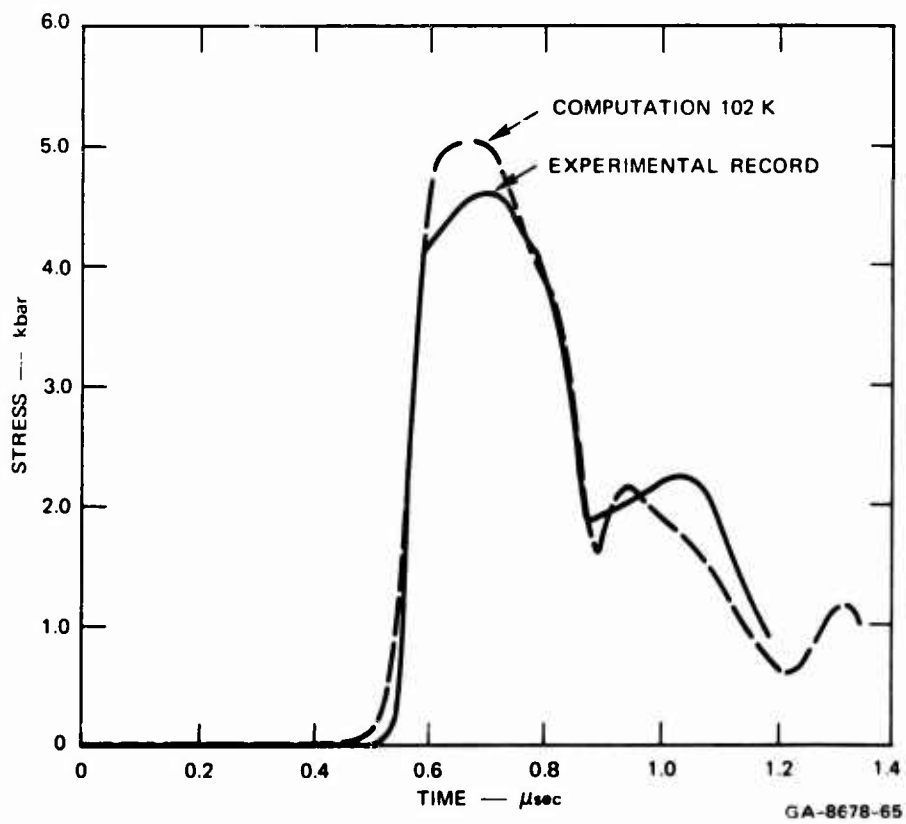
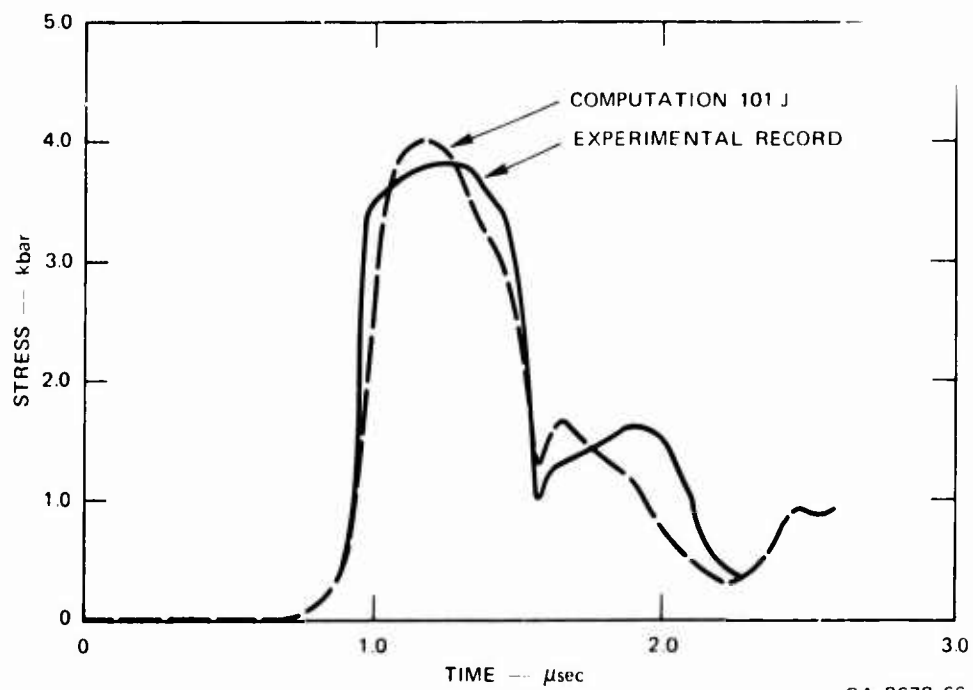


FIGURE 30 COMPARISON OF STRESS RECORD FROM MANGANIN GAGE IN PMMA BEHIND OFHC COPPER WITH COMPUTED STRESS: SHOT S24



GA 8678-66

FIGURE 31 COMPARISON OF STRESS RECORD FROM MANGANIN GAGE IN PMMA BEHIND OFHC COPPER WITH COMPUTED STRESS: SHOT S27

The present computational procedure for ductile fracture appears to provide the following results:

- The stress history is fairly well represented, indicating that some gross features of the damage are correct.
- Void volume and void concentration are correctly given for low damage.
- The void volume is underestimated at high damage.

Besides providing these direct results for prediction of fracture, the procedure has helped to indicate the kinds of nucleation functions that fit the data and the need for a new physical mechanism to handle high damage.

## 6. SIMPLIFIED DAMAGE CRITERIA

In the previous subsection we described our method for predicting the detailed damage distribution functions caused by known stress histories. These detailed damage distribution functions must form the input for future detailed calculations of the effect of shock damage on structural properties. However, for some cases these distribution functions are unnecessarily detailed; simpler rule-of-thumb descriptions of the expected levels of damage may be sufficient for many practical applications.

In this subsection we discuss two such simplified damage criteria for ductile metals: a void growth criterion and a void volume criterion. For the void growth criterion, we assume that a certain change in void radius is characteristic of a given damage level. The stress history necessary to cause this void growth is then calculated and used to explain already available data or to design new experiments. For the void volume criterion, a specific volume of voids is assumed to be characteristic of a given damage level. Under this assumption, the stress history necessary to generate this volume of voids is calculated from a knowledge of the growth characteristics of voids and the nucleation rate of voids in the material of interest. The void growth criterion requires that the material viscosity  $\eta$  and the threshold stress for void growth must be known so that the stress-time history required to cause a specified void growth can be predicted. All the information required by the growth criterion is also necessary for the void volume criterion. In addition, the stress and time dependence of the nucleation rate must be known. It is not possible, at the present time, to make a priori predictions of the stress and time dependence of the nucleation rate, as it is inherently dependent on material structure and initial defect distribution. Therefore, this information can at present be derived only from experiments.

Several generalizations can be made, though, concerning this nucleation rate. First, it is stress dependent, increasing with increasing stress. Second, it may or may not be time dependent. Third, it may be controlling if a sufficient number of nucleation sites are available. Therefore, because of a lack of information concerning the void nucleation rates, the void volume criterion is the less desirable of the two.

a. Void Growth Criterion

This method is based on Eq. (9) which, upon integration, states

$$R = R_0 \exp (At) \quad (37)$$

where

$$A = \frac{p - p_0}{4\eta}$$

The general criterion is that a void must reach a certain size  $R_1$  after a pressure of magnitude  $p_0$  has been applied for a time  $t$ . For the case of a nonsquare tensile wave, this equation becomes

$$R = R_0 \exp \left[ \int_0^t A(t) dt \right] \quad (38)$$

where

$$\int_0^t A(t) dt = \int \left( \frac{p(t) - p_0}{4\eta} \right) dt$$

Therefore, only pressures larger than  $p_0$  will contribute to the growth, and the effects of time-dependent loading, such as a simple exponentially attenuating wave, can be determined.

The method of application is to select a reasonable ratio of the void final radius to the void initial radius. The initial radius of the void is empirically determined and taken as the limit of resolution of the observational technique ( $\sim 1 \mu$ ). This size for  $R_0$  is chosen because experiments on 1145 A show that consistent results are obtained through this assumption. It may be that microstructural observations in other materials as to the size of inclusions would allow an estimation of  $R_0$  for those materials. The final radius is typically taken to have a value such that the logarithm of the ratio ( $R/R_0$ ) is an integer. The ratio taken for copper and aluminum is typically 7.4, which has a natural logarithm of two. For the case of a simple square wave, the parameters necessary to evaluate the growth function are best described by examining the growth equation in which the expression for A has been included:

$$(p - p_0)t = 4\eta \ln(R/R_0) \quad (39)$$

The tensile stress and time at stress cannot be measured directly and must therefore be calculated, most simply by applying SRI PUFF and by allowing no fracturing. The tensile stress history is then directly available for use in these calculations. The stress histories sufficient to produce a given damage level can be specified by application of Eq. (39) if the material viscosity and the threshold stress are known, assuming a value for  $\ln(R/R_0)$ .

The material viscosity can be estimated in several ways and can also be inferred directly from shock experiments. It is necessary first

to understand the nature of the viscosity and its relation to material properties.

Metals deform by the motion of dislocations. At high strain rates this motion is typically linear viscous over a wide range of stress. The observed relationship is

$$(\sigma - \sigma_0) = \eta \dot{\gamma} \quad (40)$$

where

$\sigma$  = the applied uniaxial stress

$\sigma_0$  = threshold stress for linear viscous behavior

$\eta$  = the material viscosity

$\dot{\gamma}$  = plastic strain rate

In general

$$\dot{\gamma} = \rho_m \bar{b} V_D(\sigma) \quad (41)$$

where

$\rho_m$  = the density of mobile dislocations

$\bar{b}$  = the dislocation Burger's vector

$V_D$  = the dislocation velocity

The dislocation velocity is related to the applied stress by

$$(\sigma - \sigma_0) \bar{b} = B V_D \quad (42)$$



where B is the viscous drag coefficient for individual dislocation motion.

Manipulation of Eqs. (41) and (42) gives the material viscosity as

$$\eta = \frac{B}{\rho_m b^2} \quad (43)$$

Therefore, the two variables for defining the material viscosity are the viscous drag coefficient for dislocations B and the mobile dislocation density  $\rho_m$ .

The values of B vary from material to material and can be experimentally measured. The techniques usually applied are (1) etch stress pulse method (Ref. 15) and (2) internal friction measurements (Ref. 16). The stress pulse method is most direct, although it requires the assumption of small dislocation inertia and uniform motion during the time of stress application. Internal friction measurements require detailed interpretation based on dislocation damping induced losses, the density of moving dislocation, and other material parameters. The first is most likely to give measurements of the most significance.

A third technique is to evaluate the stress dependence of the strain rate using the split Hopkinson bar (Refs. 17, 18). The major problem in this technique is that detailed analysis is necessary to determine the strain rate dependence of the yield stress. Further, experimental difficulties in the high strain rate region limit the accuracy of this technique.

These methods of analyses allow us to determine an upper bound on the material viscosity. However, a complete ignorance of the density of mobile dislocations precludes an accurate determination of the material

viscosity from a knowledge of the viscous drag coefficient  $B$ . There are also questions concerning using the values observed at low stresses for the coefficient  $B$  at high stresses, i.e., relativistic effects.

Probably the best method that can be used to determine experimentally the mechanical viscosity of material under shock conditions is the measurement of shock front thicknesses of steady state shock waves (Refs. 19, 20). Recent advances in measurement techniques make this method attractive (Refs. 21, 22). An analysis for the relationship of shock front thickness and material viscosity has been carried out on this program; the details are presented in Appendix VI. Several methods can be used to obtain the desired stress histories. They vary from interpretation of surface motion observed by optical or electrical methods, or both, to piezoelectric or piezoresistive stress gage measurements. Measurements of surface motion are, to a major extent, more accurate representations of the shock profile, since they have inherently better time resolution than either piezoelectric or piezoresistive stress gage measurements, because surface motion measurements are not limited by the size of the sensing element but detect only a small portion of the sample surface.

In general, high material viscosity results in broad steady state shock waves. Therefore, less accurate measurement techniques can lead to reasonable measurements for high-viscosity materials, which include iron, tungsten, and molybdenum. Materials such as aluminum and copper have much smaller viscosities, and meaningful data can be derived only from measurements made using high-resolution techniques.

To determine the threshold stress necessary to initiate and maintain void growth, a solution has been derived for the quasi-static growth of a void in a zero strength, viscous medium and in an elastic,

perfectly plastic medium. The detailed calculations are presented in Appendices III, IV, and V.

The results of the static elastic, perfectly plastic solution (Appendix IV) show that yielding starts around a void when the shear stress resulting from hydrostatic tension at large distances from the void reaches the yield stress. The stress needed to continue growth increases to a limiting value as the plastic zone formed about the void reaches a limiting ratio with respect to the void radius. As long as this stress is applied, void growth can occur.

The dynamic analysis of a void in viscous material (Appendix III) shows that viscous stresses dominate over the small void radius range (1 to 10  $\mu$ ) and that a threshold stress such as that derivable from simple elastic-plastic models is valid for void growth.

The elastic-plastic solution for the external, spherically symmetric, hydrostatic tensile stress necessary to maintain void growth is

$$\sigma_0 = \frac{2}{3} Y \left\{ 1 - \ln \left[ 2Y \left( \frac{1}{3K} + \frac{1}{4\mu} \right) \right] \right\} \quad (44)$$

where

Y = the uniaxial yield stress

$\mu$  = the shear modulus

K = bulk modulus for the material of interest.

The yield strength Y includes several components:

- The quasi-static yield strength of the material.
- The increase in the quasi-static yield strength caused by strain hardening occurring during the prestraining of the material by the compression phase of shock loading.

The increase in the yield strength necessary to account for the effect of strain rate on the transition to linear viscous behavior.

This calculation of the threshold stress is accurate only for materials in which the tensile stress field is nearly hydrostatic. As discussed in the previous section (III, 5), under conditions of macroscopic uniaxial strain, a lower threshold stress about equal to  $2Y$  may be appropriate. Irrespective of this, the growth equation will hold with a modified threshold stress, even for materials in which a nonhydrostatic tensile stress field is present.

b. Void Volume Criterion

The simple equation describing the development of void volume in a sample during dynamic tensile loading (particularly at low damage levels) is, from Eq. (24)

$$V = \frac{8\pi_0^3 R^3}{3A} \left( e^{3At} - 1 \right)$$

As previously stated, this criterion requires the a priori knowledge of the stress and time dependences of the void nucleation rates. These are available only from experiments. Therefore, at the present time, this criterion appears to be the less desirable of the two described.

The void radius criterion can be related to the specific void growth criterion by assuming an average void radius that is characteristic of a given damage level. This average void radius is given as

$$\bar{R} = \left[ \left( \frac{3}{4\pi} \right) \frac{V_{VR}}{N_t} \right]^{1/3} \quad (45)$$

where  $N_t$  is the total number of voids and  $V_{vr}$  the void volume resulting from a specific loading history. It is likely that this quantity is a more reasonable parameter to choose than that used in the simple growth criterion in the determination of a damage criterion. It has the complication, however, that at present it requires a detailed analysis of the damage distribution so that the volume of voids and the total number of voids can be determined. If an ability to predict nucleation rates can be developed for this criterion, the average void radius will probably be more reasonable, since it will allow estimates of full separation to be made on the basis of void coalescence considerations.

c. Example of the Use of Simplified Damage Criteria: OFHC Copper

The simplified predictive technique discussed above was actually used to predict damage levels in OFHC copper before our copper experiments were performed. It was assumed that copper would fracture in a manner similar to aluminum, and our experience with 1145 aluminum was used to help select the fracture parameters for the predictions. This successful effort is described in the following paragraphs.

The two parameters necessary for damage prediction are the material viscosity  $\eta$  and the stress threshold for void growth  $\sigma_0$ . The material viscosity measured by various techniques and the viscous drag coefficients on individual dislocations in aluminum and copper are given in Table IX.

The viscosity of copper is seen to vary by over a factor of 60 depending on the method of measurement, although the viscous damping coefficient varies by only a factor of two. Analysis of shock front widths indicates that the viscosity should be less than 600 poise, since the rise time of the shock wave fronts analyzed was determined primarily by the characteristics of the measurement technique. The aluminum viscosity is also seen to vary over a factor of 60, depending on the method of measurement. The Kolsky thin wafer technique appears to give values larger

than those from other techniques by over an order of magnitude. The value of the material viscosity is therefore best determined from the most consistent set of measurements, the etch-stress pulse technique for measuring B, the viscous drag coefficient of dislocations. A law of common states was assumed to apply and the ratio of the viscosity of copper to that of aluminum was assumed to be equal to that of their viscous drag coefficients for dislocation motion. This ratio was used with the viscosity for aluminum determined from the void growth constants to estimate the viscosity of copper under shock conditions.

Table IX

MECHANICAL VISCOSITIES OF COPPER AND ALUMINUM AT HIGH STRAIN RATES

<u>Material</u>	<u>Material Viscosity (poise)</u>	<u>Experimental Technique</u>	<u>Viscous Drag on Dislocations (poise)</u>	<u>Experimental Technique</u>
Copper	$3.7 \times 10^4$	Kolsky thin wafer (Ref. 23)	$1.7 \times 10^{-4}$	Etch-stress pulse (Refs. 24, 25)
	$1.15 \times 10^3$	Hopkinson Bar (Ref. 26)	$7.5 \times 10^{-5}$	Acoustical attenuation (Ref. 20)
	$< 6 \times 10^2$	Shock front thickness		
Aluminum	$1.1 \times 10^4$	Kolsky thin wafer (Refs. 17, 18)	$2.5 \times 10^{-4}$	Etch-stress pulse (Ref. 27)
			$2 \times 10^{-3}$	Internal friction (Ref. 28)
6061 T6	$1.8-4.8 \times 10^2$	Shock front thickness		
1145 Al	$3.6 \times 10^2$	Void growth (Ref. 12)		

The ratio of these quantities for aluminum and copper is

$$\frac{B(\text{Cu})}{B(\text{Al})} = \frac{1.7 \times 10^{-4}}{2.5 \times 10^{-4}} = 0.68$$

Therefore, the viscosity of copper under shock conditions is approximately 0.6 to 0.7 of that of aluminum and is therefore estimated as  $\eta(\text{Cu}) \simeq 250$  poise.

The threshold stress  $\sigma_0$  can be calculated by using Eq. (44) and the correct values for the uniaxial yield stress  $Y$ . The static yield strength for OFHC copper is approximately 7000 psi ( $\sim 0.5$  kbar). The increase in yield strength necessary to account for the strain rate effect in reaching the viscous threshold is of the order of 0.5 kbar. Further, from the work of Grace (Ref. 29), the increase in static yield strength due to shock compression hardness is approximately 1.5 kbar per 100 kbar peak compression pressure for stresses up to 100 kbar. Therefore, assuming a typical compressive stress of 20 kbar, the yield strength to be used with Eq. (44) is 1.3 kbar. The resulting threshold stress is 6.5 kbar.

Table X gives the results of calculations based on this criterion assuming a threshold stress of  $6.5 \times 10^9$  dynes/cm<sup>2</sup> and material viscosities of 200 and 250 poise for times at stress of 0.5, 0.25, and 0.125  $\mu$ sec.

The experiments to be described were designed on the basis of the stresses and times at stress shown in Table X, and some of the results were shown in Fig. 17.

Table X

## PREDICTED DAMAGE THRESHOLD CONDITIONS FOR OFHC COPPER

<u>Time at Stress (sec)</u>	<u>Stress (kbar) for <math>\eta = 200</math> poise</u>	<u>Stress (kbar) for <math>\eta = 250</math> poise</u>
$5 \times 10^{-7}$	11.2	12.0
$2.5 \times 10^{-7}$	14.4	16.0
$1.25 \times 10^{-7}$	20.8	24.0

The times at stress for the regions shown in Figures 17(a), 17(b), and 17(c) are 0.32  $\mu\text{sec}$ , 0.64  $\mu\text{sec}$ , and 1.2  $\mu\text{sec}$ , respectively. Using these times at stress and calculated values of tensile stress, we calculated the damage level factor  $\ln R/R_0$  to be 4.8, 3.9, and 3.2 for the experiments shown in Figures 17(a), 17(b), and 17(c), respectively. Examination of the micrographs shows that the experimental values of  $\ln R/R_0$  are 4.4, 3.4, and 3.1 for the damage shown in Figures 17(a), 17(b), and 17(c), respectively. The agreement with the predictions is excellent on this basis and shows that a range of damage levels are amenable to prediction.

A further verification of the predictions has been gained by detailed analysis of Shot S24 (sample thickness 1.578 mm, projectile thickness 0.619 mm, impact velocity 0.158 mm/ $\mu\text{sec}$ ), which was instrumented with back surface manganin piezoresistance pressure transducer mounted in PMMA. Interpretation of this analysis indicates that the peak tensile stress imposed on the sample was 17.5 kbar. The derived growth constant, A, was  $1.08 \times 10^7 \text{ sec}^{-1}$  for the volume analysis and  $1.07 \times 10^7 \text{ sec}^{-1}$  for the radii analyses procedures. The growth constant is given as  $A = (\sigma - \sigma_0)/4\eta$ . A viscosity of approximately 260 poise is predicted when the tensile stress is assumed as 17.5 kbar and the threshold stress as 6.5 kbar,



in agreement with the original value chosen. The observed void nucleation rate is of the order of  $4 \times 10^{14} (\text{cm}^3 \text{ sec})^{-1}$ , a value similar to those observed in 1145 aluminum.

The experimental results and their consistency with the dynamic fracture criterion indicate that other fracture data on OFHC copper should be explainable in terms of this model. In the description of the calculation of the threshold stress for the formation of damage in a material under the action of a dynamic tensile load, it was stated that the effects of strain hardening during the compressive phase of the shock process must be included. The method shown was to include this as an increase in the yield stress used in the calculation of the stress necessary to cause unbounded void growth. This method of accounting for the effects of strain hardening resulting from shock loading can also be used to evaluate the influence of cold working on material before shock loading. This is best demonstrated by considering the dynamic fracture thresholds observed in 3/4 hard OFHC copper (Ref. 26). The static yield stress at a strain rate of  $10^3$ /sec in this material was reported as 3 kbar. Further, at this hardness level, essentially no increase in the yield strength resulting from the compressive phase of shock loading is expected. From Eq. (44) the threshold stress is calculated to be 13.5 kbar, assuming a yield stress of 3 kbar. Dynamic fracture thresholds can then be calculated from the growth criterion, assuming a viscosity of 200 poise if the times at stress are shown. The times at stress are defined by the ratio of the projectile-to-target thicknesses as well as by the absolute value of the target thickness. In this material, the magnitude of the elastic precursor was about 3 kbar, and it is necessary to consider only the duration of the tensile plastic wave unaffected by the elastic precursor rarefactions. The results of such calculations are presented in Table XI and compared with the reported results. The general agreement is excellent; the greatest error is apparent at the shorter times at stress.

Table XI

PREDICTED AND EXPERIMENTALLY OBSERVED DAMAGE THRESHOLD CONDITIONS  
FOR 3/4 HARD OFHC COPPER

<u>Time at Stress (sec)</u>	<u>Experimental Damage Threshold (kbar tension)</u>	<u>Calculated Damage Threshold (kbar tension)</u>
$7 \times 10^{-7}$	15.5	15-16
$3.5 \times 10^{-7}$	18.5	19-20
$1.2 \times 10^{-7}$	23	24-25

The main result of this discussion is that the apparent disagreement in the dynamic fracture threshold conditions observed for these two samples of OFHC copper is resolved by the understanding of the influence of strain hardening on the hydrostatic tensile threshold stress for unbounded void growth. Further, the fact that dynamic fracture thresholds observed by separate investigators have been correlated through a simple theory is unique.

The void growth criterion presented in this report can be directly related to other phenomenological models for dynamic fracture. All previous models were relevant only to the material studied, and any constants were characteristic of only one material. Using the void growth criterion, the constants in these other models can be directly related to the material viscosity  $\eta$ , the threshold stress for void growth, and the damage parameter (i.e., the ratio of final to initial voids radii).

The ability to predict the damage in a material with some accuracy when the applied stress history is known implies that observation of given damage level should allow an estimate of the local tensile stress history to be made. Such an estimate would be only of an integrated nature. For the case of the viscous void growth, the model described

here, a tensile impulse could be estimated. This could provide a check on any stress gaging of the samples and would be an extremely stable measuring device.

## 7. SUMMARY OF DUCTILE FRACTURE

The results of a study of the dynamic fracture of ductile metals have been reported. They include the development of techniques for quantitatively measuring the nucleation and growth rates of voids (the observed damage mode) and for finding their dependence on stress, time, material viscosity, and yield strength. These results were used to formulate a model describing the fracture process in ductile metals in which the effects of damage on the local stress are considered. A simple damage threshold criterion based on the void growth mechanism was also formulated and predictions were made for OFHC copper. Experimental data were in agreement with these predictions, verifying the model.

The basic result has been the demonstration of a capability for predicting damage levels and distributions for an arbitrary stress history. We have shown that the correlation of predicted damage with experimentally observed damage is good, but not exact. The uncertainty is believed to be related to the model used to include the effect of developing damage on the local stress. Even with this error the results are very encouraging since at no previous time has such agreement been obtained.

## SECTION IV

### BRITTLE FRACTURE

In this section we discuss the work performed on the materials that, under dynamic conditions, fracture by nucleation and growth of brittle microcracks. We discuss our experimental observations and our methods of analysis, followed by a description of our stress history calculations and of the results of these computations. Finally, a summary of our results and conclusions regarding dynamic brittle fracture is given.

#### 1. BRITTLE FRACTURE MODEL

##### a. Nature of the Model

The brittle fracture model was patterned after the ductile model and based on observations of damage in Armco iron. An example of this damage is shown for a tapered flyer experiment in Figure 32. The sections are from four positions across the target parallel to the impact plane and show, in descending order, the effect of impacts with increasing flyer thickness. The tapered flyer induces the same peak tensile stress at the (expected) spall plane all across the target, but the duration of that stress varies as described in Appendix I. These nominal durations of the peak tensile stress are listed in the figure. Clearly the number and length of cracks appear to increase with duration of loading. These observations indicate that nucleation and growth of cracks must be included in a model to represent the damage correctly. A quantitative picture of the damage is obtained by counting the surface area of damage and sorting into groups by crack length and angle with

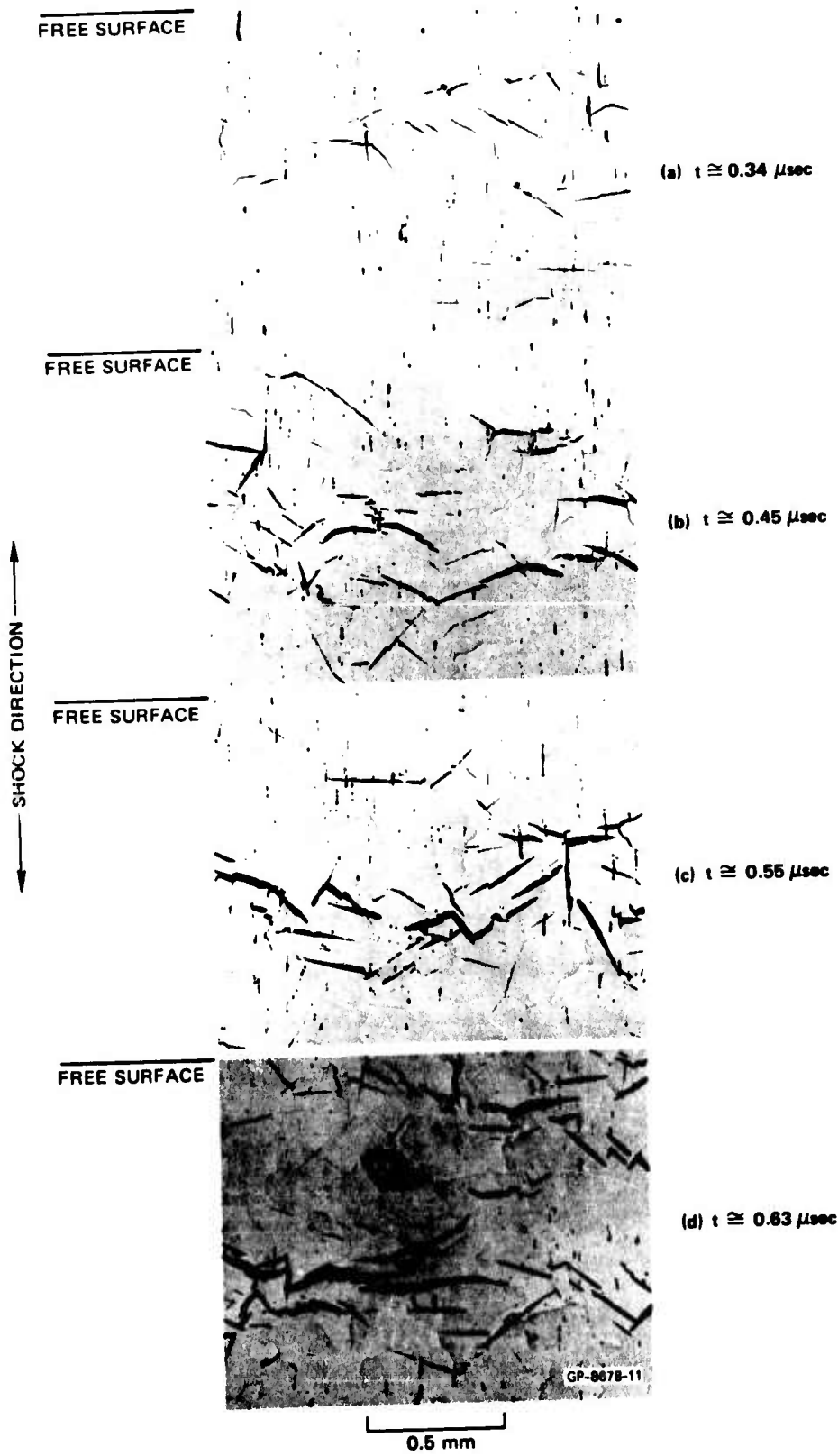


FIGURE 32 DAMAGE DISTRIBUTION OBSERVED IN A TAPERED FLYER SHOT ON ARMCO IRON (Shot S1)

respect to the direction of impact. A statistical transformation of the observed cracks, similar to that of Kaechele and Tetelman (Ref. 30), is made to determine the volume distribution of cracks (number/cm<sup>3</sup> in each length and angle group). These distributions in angle, length, and position in the target, as well as stress gage records, should be simulated approximately by the fracture model. Because of the wealth of information provided by the crack distributions, a model that fits these distributions must have considerable fidelity to the actual processes occurring.

The model provides for the nucleation of cracks as a function of stress level, for the growth of the cracks while the stress intensity factor exceeds the fracture toughness, and for the relaxation of stress as a function of the developing damage. The growth and stress relaxation aspects are based on classical fracture mechanics and fracture dynamics.

The material information required for using the model to calculate fracture includes fracture toughness, an initial crack size, limiting growth velocity, and nucleation rate parameters. The output from the calculation includes number and size of cracks as a function of position in the damaged target, and stress histories at any point in the target. This output is somewhat more detailed than that for ductile fracture, because the crack size distribution is not forced to fit a particular analytical form. The distribution is given in ten increments. As in the ductile fracture calculations, the computed results indicate a plane of very high damage with regions of lesser damage on either side.

b. Nucleation Rate

As with ductile fracture, experimentally obtained numbers of nuclei refer to observed cracks. Hence, some permanent set (plastic flow) must occur, and the crack length and opening must be large enough for detection. Generally our observable crack length is a few microns. In

Armco iron the nucleated cracks appear to be randomly or homogeneously located; a homogeneous model has been used for nucleation. Also the orientation of the cracks with respect to the plane of impact appears to be random, but for simplicity, our initial brittle fracture model considers all cracks parallel to the plane of impact. The nucleation size is not known but is presumed to be about 1 micron.

The nucleation rate could not be obtained directly from the observed damage as it could for incipient ductile fractures. The effect of damage on the stress was so great that the stress histories could not be approximated as square waves for any cases considered. Hence, for our calculations of brittle fracture, a very strong interaction exists between the nucleation and the other factors governing the stress history.

c. Growth Rate and Growth Threshold

The growth of cracks as a function of stress level has been treated for many years by workers in fracture mechanics and fracture dynamics, such as Griffith (Ref. 31), Irwin (Ref. 32), Mott (Ref. 33), Sneddon (Ref. 34), Dulaney and Brace (Ref. 35), Neuber (Ref. 36), and Barenblatt (Ref. 37). Where applicable, their work has been used to develop the growth model. Growth is presumed to occur when the stress intensity factor  $K_I$  reaches the critical value or fracture toughness  $K_{IC}$ . In turn,  $K_{IC}$  determines the critical or threshold stress for any crack length. The velocity of growth for stresses above the critical level is presumed to be a function of stress and to reach a limiting value for high stresses.

We assume that the crack is penny-shaped, in an elastic stress field, and its opening is given by Sneddon's analysis (Ref. 34) for a unidirectional tensile field. Clearly we are neglecting the orientation of the cracks, the interaction of adjacent cracks, and the occurrence of

considerable plastic flow at these high stresses. We have also selected the simple relation of Mott (Ref. 33) for velocity, although that relation is known to be approximate even for planar (not penny-shaped) cracks. In spite of these shortcomings, the functional relationships are expected to have the correct form. The computed crack growth (exhibited later) shows reasonable agreement with the observed crack sizes.

#### d. Constitutive Relations

The presence of cracks in the material causes some change in the stress-strain or constitutive relations. The propagation of waves through the partly fractured material depends entirely on these constitutive relations. Therefore, to perform stress propagation calculations that proceed through fracturing, constitutive relations must be developed.

The current constitutive relations have been separated into relations for pressure and deviator stress. They are continuous with the relations for undamaged material and very similar to those for ductile fracture. The primary mechanism for stress reduction in our model is the elastic opening of the cracks. This crack volume permits the specific volume of the remaining solid to reduce and thus reduces the stress in the solid. Within each one-dimensional cell of the SRI PUFF computer code, a state of static equilibrium is presumed. Hence, cracks may send recompression waves to adjacent cells, but they are in a state of equilibrium with the material in their own cell. This static requirement may be serious if growth velocities approach wave velocities but is probably unimportant for the crack velocities in Armco iron (1/20 of longitudinal sound speed).



## 2. EXPERIMENTAL PHASE

The dynamic fracture of brittle solids must include investigations of several types of materials if a generalized understanding of the fracture process is to be gained. Further, truly brittle solids, if they can be reproducibly manufactured, have the possibility of being used as standards since their fracture behavior is generally well understood under quasi-static conditions. Therefore, in this study of brittle materials fractured under dynamic conditions two classes of materials were investigated.

The first material is an isotropic graphite specially prepared by Los Alamos Scientific Laboratory (LASL). This material is unique in that the grain size, grain orientation, and material properties are extremely reproducible from sample to sample and from manufacturing batch to manufacturing batch. This high density graphite ( $\rho \approx 1.79 \text{ gm/cm}^3$ ) is isotropic and uniformly porous on a macroscopic scale. It exhibits nearly ideal brittle behavior, which is strongly affected by the material microstructure.

The second material is Armco iron, a classic rate-dependent, body-centered, cubic metal exhibiting a ductile-brittle transition with both decreasing temperature and increasing strain rate. This material is of interest because its fracture mode is typical of most high strength materials exhibiting a ductile-brittle transition.

In this section we give a short description of the experimental observations for the above materials. Detailed descriptions of the experimental techniques are given in Appendices I and II.

The experimental program consisted of two main elements:

- Instrumented and uninstrumented impact experiments to produce known stress histories in samples under conditions of uniaxial strain.
- Metallurgical examination of impacted specimens.

Both procedures are the same for the brittle materials as for the previously described ductile materials.

a. Graphite

(1) Objective

The dynamic fracture of the LASL high density graphite was studied experimentally. The purpose of this work was to define the dynamic fracture characteristics of this material under plate impact conditions so that comparison could be made with results attained by other dynamic loading methods. The program consisted of the components given in the introduction (Section I) which are necessary to carry out a dynamic fracture study.

The first step in this process is to develop methods for recovering samples in a condition suitable for analysis. New recovery methods had to be developed for this material because of its low strength; these will be described first. The second step is to calculate relevant stress histories for the material. This requires a knowledge of the dynamic equation of state, which was not available for graphite. Therefore, static uniaxial strain compression tests were carried out to define an equation of state to be used as an initial estimate of the dynamic equation of state. These results are discussed with other data including sound velocities, density, and yield strength. The third step is to characterize the damage metallographically. The results of the fracture experiments are presented, and the observed fracture structures are

described. A discussion of these results and the relation to standard experimental techniques for measuring high rate fracture behavior are then discussed. The results are then summarized and possible future work described.

## (2) Recovery System

Graphite is, in tension, a low strength material exhibiting essentially completely brittle behavior. Typical strengths in tension are 2 to  $2.5 \times 10^3$  psi (0.14 to 0.17 kbar) for ATJ graphite, which has a density of  $1.73 \text{ gm/cm}^3$ . The flexural strength of this material, which is often used as a measure of impact strength, is from  $3.5$  to  $4.0 \times 10^3$  psi (0.24 to 0.28 kbar). Compressive strengths in uniaxial strain loading are about  $8.5 \times 10^3$  psi (0.59 kbar), and the crush strength is approximately twice that. Since all these strengths are low, extreme care is necessary in the design of the recovery system used in dynamic fracture experiments.

Two specific recovery systems were used. In each the sample was mounted in the manner described in Appendix II, and the energy absorbing recovery system (EARS) was used. The two systems of sample mounting were designed to provide added strength and proper impedance matching to the graphite. In the first system the graphite sample, a disc 0.250-inch thick by 1.5-inch diameter, was mounted in a tapered poly methylmethacrylate (PMMA) ring using a thin layer of C-7 epoxy. PMMA was chosen since the impedance match at low stresses is good and its fracture strength is approximately 1 kbar, which is over twice that of the graphite. This sample assembly was then sandwiched between two 0.0625-inch-thick PMMA discs to provide support during recovery. The whole assembly was then press fit into a PMMA plate so that the sample was ejected into the EARS following impact. In this system the sample was impacted by a 0.1875-inch-thick PMMA projectile, the rear surface of which was free so that

full stress release was achieved. Four shots were carried out using this technique. The system was modified after three shots because parting of the PMMA cover was observed, and the graphite sample proved to be easily recoverable at the low impact velocities used (less than 100 fps).

The second system was similar to that described above in that the sample and its mounting ring were identical. No covers were placed on the sample, and it was mounted in a 0.250-inch-thick PMMA plate in a tapered hole allowing ejection and recovery. The projectiles were graphite in this system. They were designed to allow recovery of the projectile heads intact. The projectile heads experience only compressive loading and can be examined to determine the effects of the compressive phase during shock loading.

In almost all cases the samples were recovered intact with no obvious surface damage. The few cases where surface damage was observed occurred at high impact velocities, i.e., at high tensile stresses where full separation was observed. This breakup of the sample occurred in a manner defined by the grain structure of the material and might be expected during any full dynamic fracture occurrence.

### (3) Quasi-static Measurement of Stress Volume Paths

Quasi-static, one-dimensional, compression tests were performed on samples of the porous LASL graphite. The purpose of these tests was to measure a loading isotherm and unloading and reloading curves for this material. It was hoped that these measured curves would aid in the formation of constitutive relations for describing the behavior of the porous materials in the "partially compacted region," particularly just above the "elastic" limit where accurate dynamic measurements are difficult to obtain and are not available for this material. A major question of interest was whether the quasi-static pressure-volume (P-V) data could

be used to approximate the dynamic data in the "partial compaction" region, despite the drastic differences in loading rate.

The testing apparatus, shown schematically in Figure 33, was made of high strength steel and the capacity limited to about 10 kbar. The porous samples used were 1 inch in diameter and either 1-inch or 1/2-inch long. They were inserted in the die inside a 1-mil-thick sleeve of indium--the indium being required for lubrication to reduce wall friction. Pressure was applied with a hydraulic jack acting on the plunger above the sample. Tests were performed by loading to a certain pressure and reading the length of the plungers and sample with a gage recording to 0.0001 inch. Then the pressure was released until the gage reading began to change. The "true" pressure was then taken as the average of the upper and lower pressures. This double-reading procedure was used to reduce errors associated with friction between the sample and the body of the die.

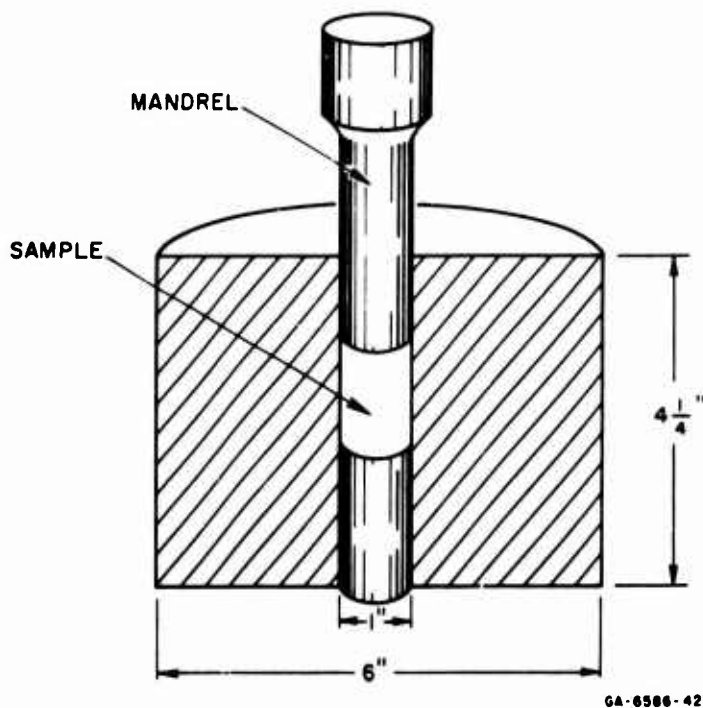


FIGURE 33 CUTAWAY VIEW OF QUASI-STATIC COMPRESSION DEVICE

To determine both the loading isotherm and the unload-reload behavior, two testing plans were adopted. In the first, the loading was increased monotonically to 6 kbar. In the second plan, the loading proceeded only to some fraction of 6 kbar and then the sample was unloaded and reloaded to a higher pressure. This load-unload cycle was repeated until 6 kbar was reached.

Compression of the sample was deduced from the recorded overall shortening of the combination of the sample and two plungers. In determining the total volume change of the sample, an allowance was also made for the lateral expansion of the die. This lateral expansion (which necessitated a small correction to the longitudinal volume change) was deduced from calibration tests with lead as a sample with a known compression isotherm.

The loading, unloading, and reloading curves obtained are shown in Figure 34.

#### (4) Elastic Constants from Acoustic Velocity Measurements

Acoustic velocity measurements were made with samples of the LASL graphite to determine the elastic constants of the materials at nominally zero stress levels. The tests were conducted by transmitting longitudinal (compressional) and shear pulses through thin specimens and measuring the transit times. These transit times were then used to compute Young's modulus  $E$  and Poisson's ratio  $\nu$  for each material.

The equations used to determine the elastic constants are the usual ones for linearly elastic, homogeneous, isotropic materials. The samples did not qualify as isotropic on a microscopic scale because of their porosity. However, with the assumption of macroscopic isotropy we can compute longitudinal and shear acoustic velocities  $C_L$  and  $C_S$  from

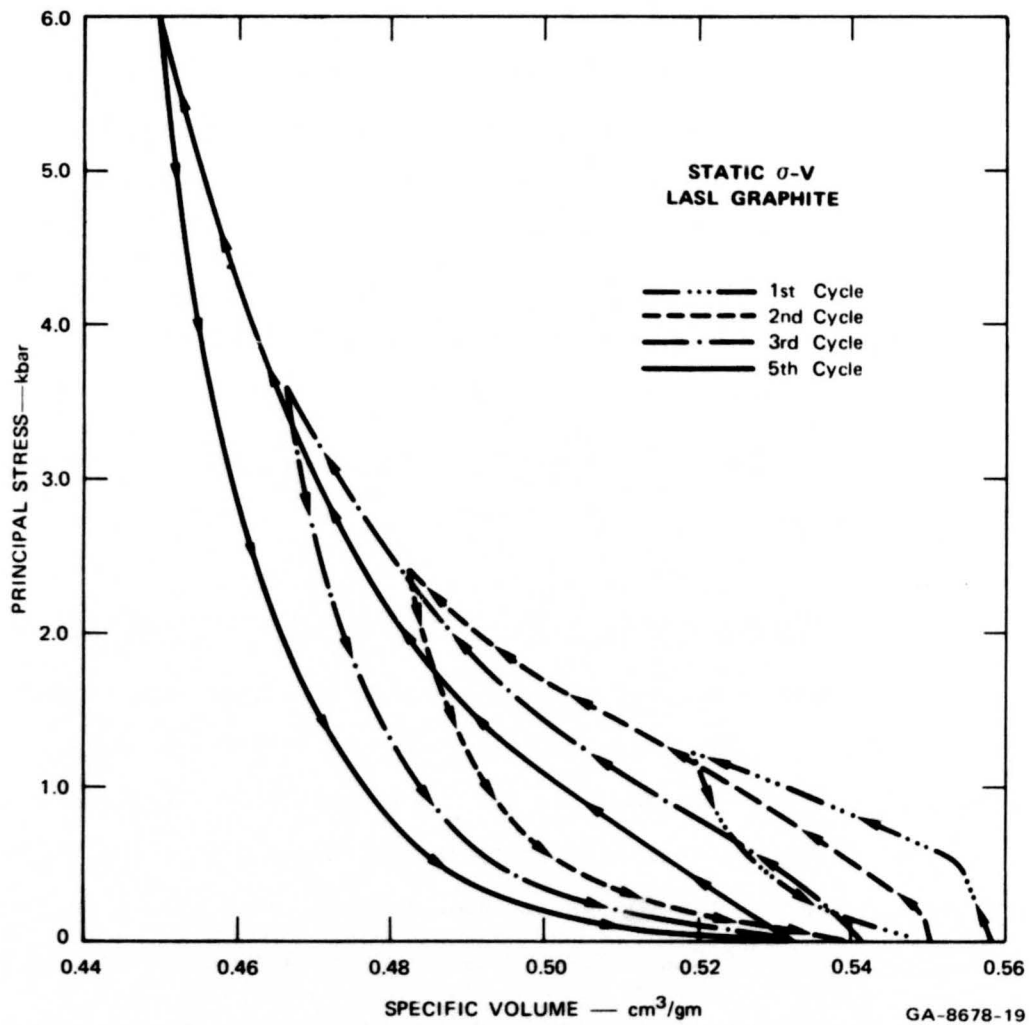


FIGURE 34 STATIC COMPRESSION AND UNLOADING CURVES FOR LASL GRAPHITE

the travel times of the waves through the samples. These sound velocities are related to the elastic constants as follows:

$$C_L = \frac{E}{\rho} \left[ \frac{(1 - \nu)}{(1 - 2\nu)(1 + \nu)} \right]^{1/2} \quad (46)$$

$$C_S = \left[ \frac{E}{\rho} \frac{1}{2(1 + \nu)} \right]^{1/2} \quad (47)$$

where

$\rho$  = the material density

Equations (46) and (47) can be solved for E and  $\nu$ , obtaining

$$\nu = \frac{(C_L/C_S)^2 - 2}{2(C_L/C_S)^2 - 2} \quad (48)$$

$$E = 2(1 + \nu)C_S^2\rho \quad (49)$$

$$E = \frac{(1 - 2\nu)(1 + \nu)}{(1 - \nu)} C_L^2\rho \quad (50)$$

The measured acoustic velocities and the elastic constants derived therefrom are exhibited in Table XII.

Two features are apparent in these results. First, Poisson's ratio is decreased by compressing to a pressure of 6 kbar and is essentially zero after compression and release. Second, Young's modulus is halved, indicating a decrease in the effective strength of the



Table XII

## MEASURED WAVE VELOCITIES AND CALCULATED ELASTIC CONSTANTS FOR G

Sample	$\rho$ (gm/cm <sup>3</sup> )	$C_L$ (mm/ $\mu$ sec)	$C_S$ (mm/ $\mu$ sec)	$\nu$	$E$ (dyn/cm <sup>2</sup> $\times 10^{10}$ )	Comments
02	1.79	2.42	1.55	0.16	9.9	As received
04	1.78	2.45	1.54	0.18	9.9	As received
01	1.83	1.44	1.06	(-0.08)	4.06	Compressed (static) ~6 kbar
03	1.84	1.53	1.08	0	4.29	Compressed (static) ~6 kbar
S36 (projectile head)	--	2.02	--	--	--	Compressed (shock) ~0.3 kbar

material. Since the samples are only 85 percent of full density, the measured modulus is only an effective modulus reflecting the effects of porosity. Hence, it is likely that fracturing on the basal plane of the graphite occurs and leads to a large decrease in the strength upon subsequent loading, and also causes a decrease in the measured shear and longitudinal wave velocities.

(5) Comparison of Static and Dynamic Loading Curves

If the response of graphite is rate-independent, it should be possible to get good agreement between the statically measured loading curves and dynamically measured curves. Little information is currently available for dynamic measurements of LASL graphite. However, Lockheed Missiles and Space Company has made some of its data for ATJ-S graphite available to us. Figure 35 compares the SRI static data with Lockheed's Hugoniot data. The initial densities are different, but if the SRI curve were displaced to the same initial density as the Lockheed material, good agreement would result. In addition, a loading curve from shot 844 on  $1.76 \text{ gm/cm}^3$  graphite by Charest (Ref. 38) is shown. The curve, which we obtained from a Lagrangian analysis of records from two embedded manganese gages, show good correspondence with our static data. If the SRI static curve is assumed to define a Hugoniot curve, the data can be presented in the form of a shock velocity-particle velocity curve, or alternatively, as a stress-particle velocity curve. This has been done, and the results are shown in Figures 36 and 37. We have also recently received dynamic Hugoniot data for LASL graphite generated by J. A. Charest at EG&G Inc., and these data are also in good agreement with the SRI static results. This good agreement with the dynamic data indicates that the graphite behaves in a rate-independent manner and that static uniaxial strain compressive tests are useful in predicting Hugoniot curves for this material and other similar materials.

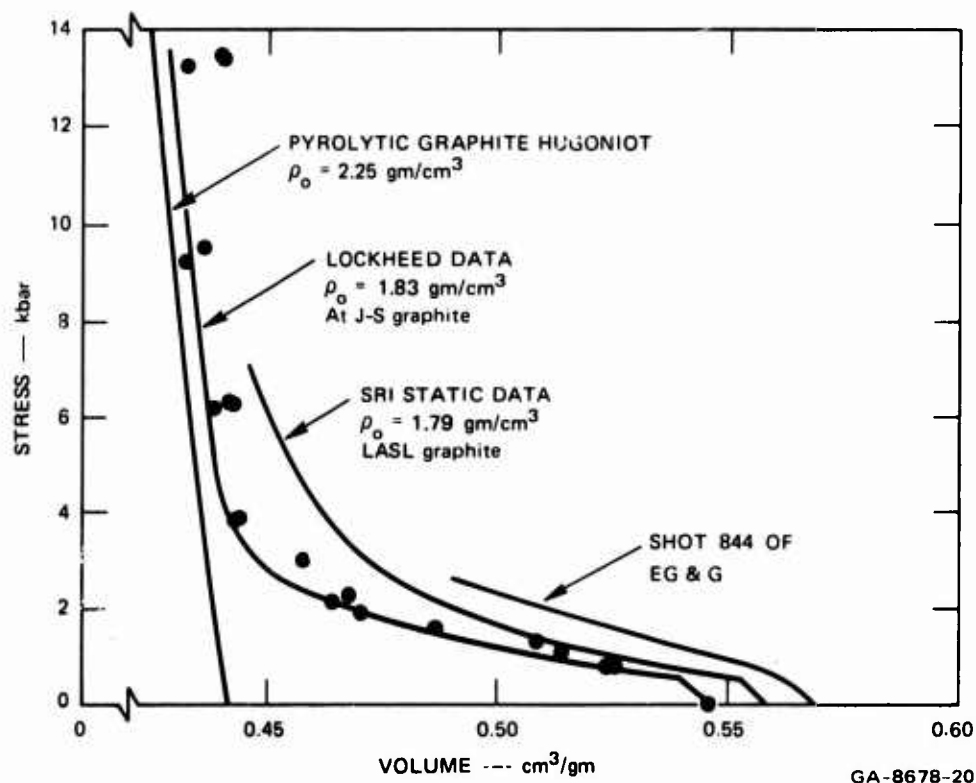


FIGURE 35 COMPARISON OF STATIC AND DYNAMIC COMPRESSION CURVES FOR SEVERAL GRAPHITES

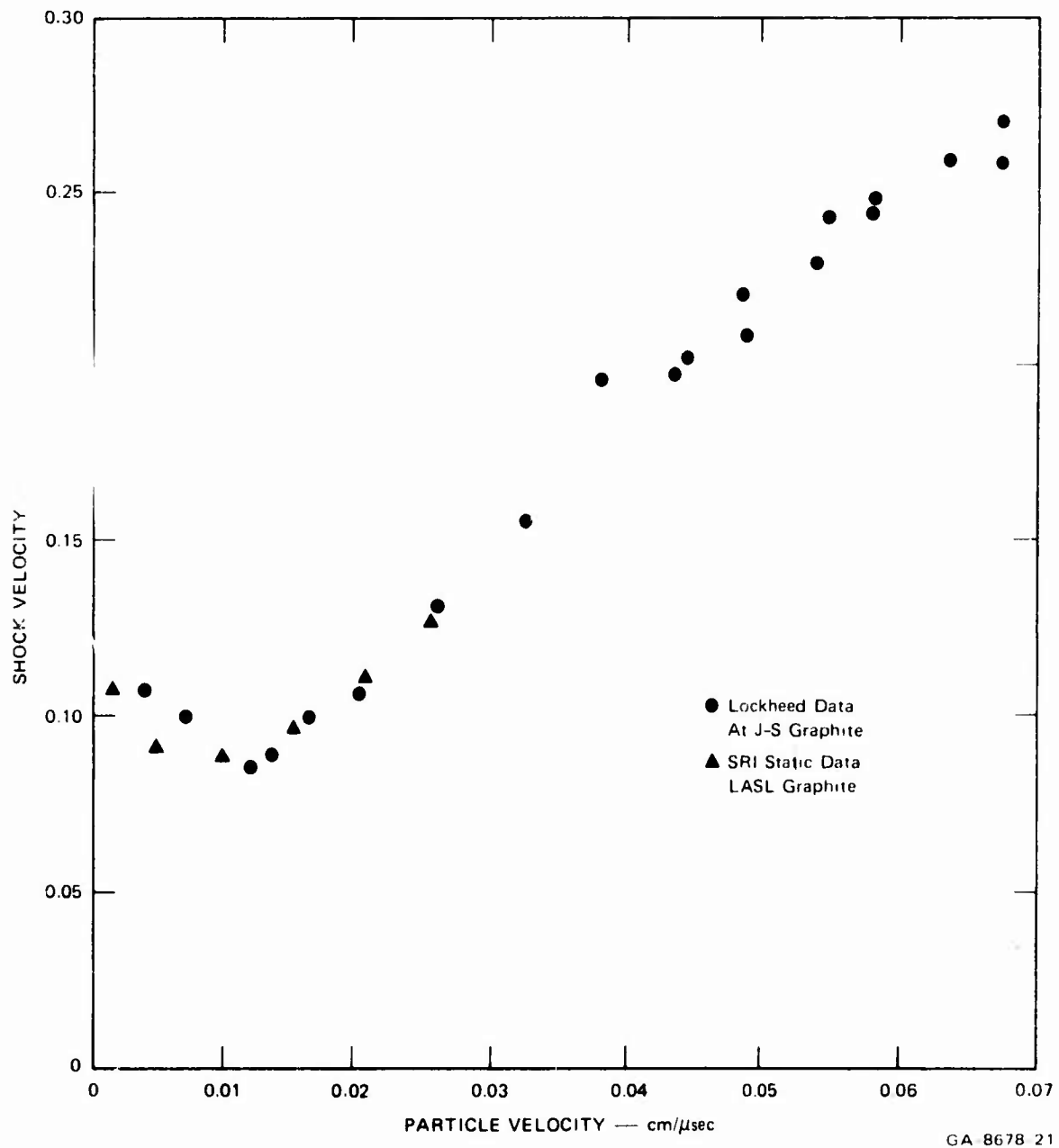


FIGURE 36 COMPARISON OF SHOCK VELOCITY-PARTICLE VELOCITY DATA GENERATED FROM STATIC AND DYNAMIC EXPERIMENTS ON GRAPHITE

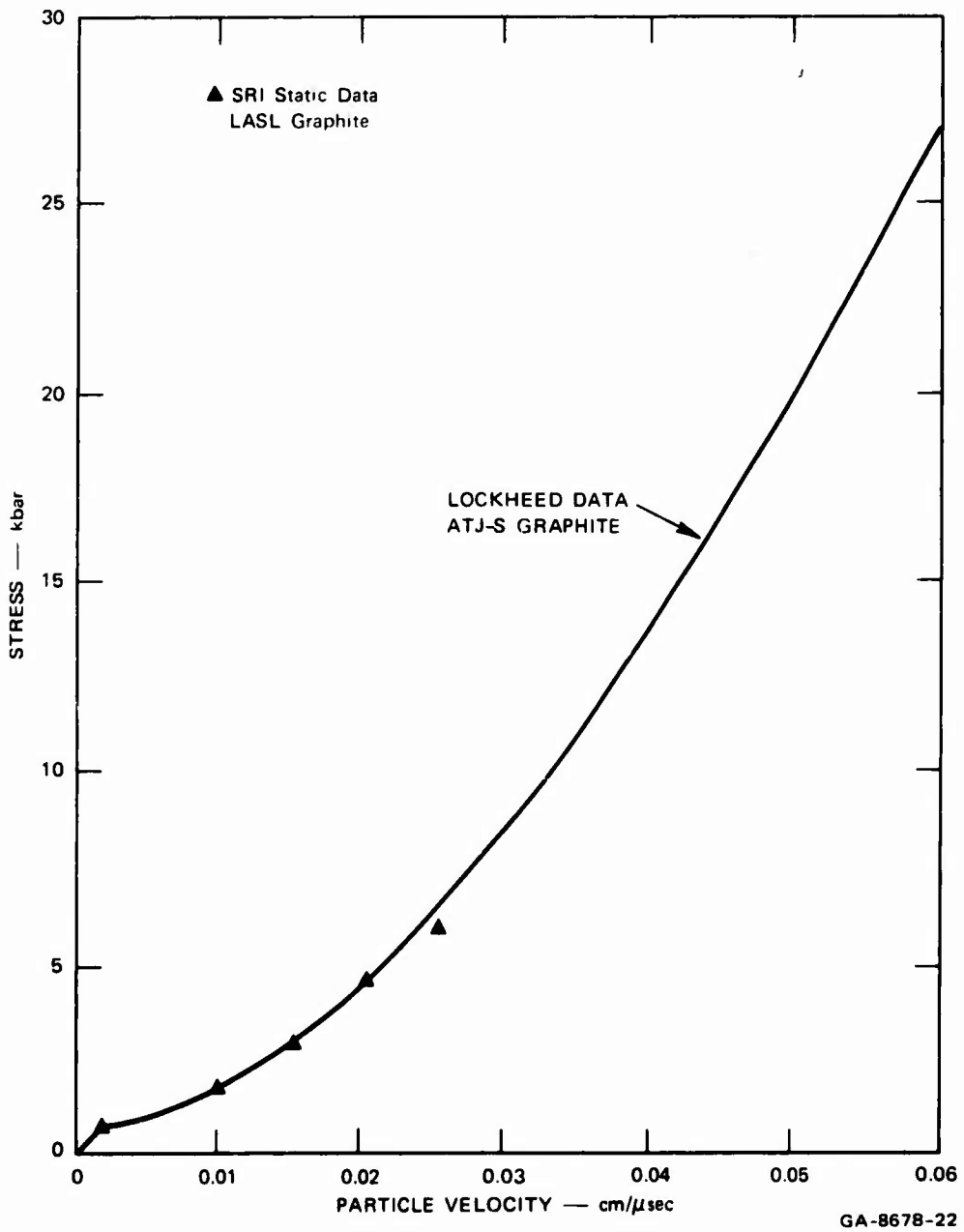


FIGURE 37 COMPARISON OF STRESS-PARTICLE VELOCITY DATA GENERATED FROM STATIC AND DYNAMIC EXPERIMENTS ON GRAPHITE

(6) Dynamic Fracturing Experiments

Twelve recovery shots were fired on the SRI 2-1/2-inch diameter light gas gun. These shots are summarized in Table XIII.

Metallographic examination of the as-received LASL graphite revealed that the microstructure consisted of large, roughly spherical grains (~1-mm diameter), which in turn consisted of smaller grains (~0.1-mm diameter). The smaller grains consisted of crystallographically oriented material. However, since the orientations of the smaller grains varied randomly, the material can be considered isotropic on the scale of the larger grains.

The microcracks observed in the dynamically loaded samples traveled mostly on the boundaries between the larger grains. In the cases in which the cracks traversed a large grain, the fracture path followed the smaller grain boundaries. Figure 38 shows micrographs of intermediate damage in Shot S36; note that the fracture path lies mostly between the large grains. Figure 38(c) shows a crack that lies on the boundaries between the smaller grains. In this sample no separation occurred, and the sample appeared undamaged before sectioning. However, X-ray radiographs of the unsectioned sample revealed the presence and location of the damage. Figure 39 shows the X-ray picture of the shock damage in Shot S36, and Figure 40 shows a similar X-ray radiograph of the heavier damage in Shot S49.

At high damage levels, where complete separation occurs, the main mode of damage is decohesion of the large grains. This can be seen in Figure 41, which shows the recovered specimen from Shot S35.

The other extreme, incipient damage, is shown in Figure 42, where a few incipient cracks may be discerned on the large grain boundaries.

Table XIII

## DYNAMIC FRACTURE EXPERIMENTS FOR GRAPHITE

 $(\rho_0 = 1.79 \text{ gm/cm}^3)$ 

Shot No.	Flyer Material and Thickness (mm)	Impact Velocity (mm/ $\mu$ sec)	Target Thickness (mm)	Peak Tensile Stress (kbar)	Stress Duration ( $\mu$ sec)	Comments
S35	PMMA; 4.73	0.0442	6.313 1.578 PMMA(2) <sup>a</sup>	~0.4	~3.5	Full separation
S36	PMMA; 4.73	0.0248	6.313 1.578 PMMA(2) <sup>a</sup>	~0.4	~3.5	Intermediate damage
S39	PMMA; 4.73	0.0224	6.313 1.578 PMMA(2) <sup>a</sup>	~0.4	~3.5	Intermediate damage
S40	PMMA; 4.73	0.0392	6.313 1.578 PMMA(2) <sup>a</sup>	~0.4	~3.5	Full separation
S41	Graphite; 2.27	0.0143	6.313	0.31	2.0	Light damage
S42	Graphite; 2.27	0.0248	6.313	0.53	2.0	Intermediate damage
S45	Graphite; Tapered Flyer	0.0128	6.313	0.28	1.0-2.5	Light damage
S46	Graphite; Tapered Flyer	0.0211	3.156	0.45	0.5-1.5	Incipient damage
S47	Graphite; Tapered Flyer	0.0278	6.0	0.60	1.0-2.5	No damage to heavy damage
S48	Graphite; Tapered Flyer	0.0311	3.04	0.67	0.5-1.5	Full separation
S49	Graphite; 2.02	0.0335	5.98	0.72	1.7	Heavy damage
S50	Graphite; 2.27	0.0277	5.93	0.60	2.0	Intermediate damage

<sup>a</sup> Target is a sandwich with 1.578-mm PMMA discs before and after the 6.313-mm graphite sample.

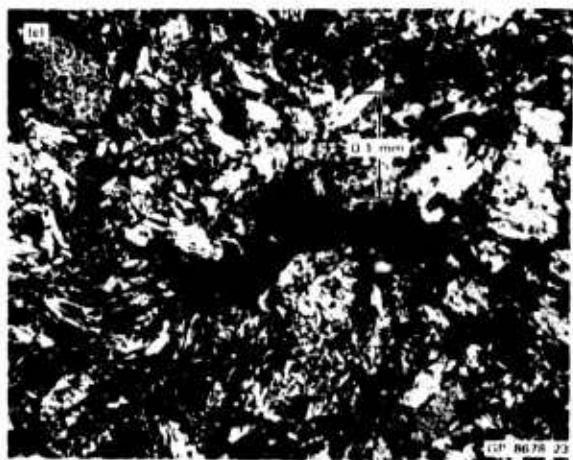
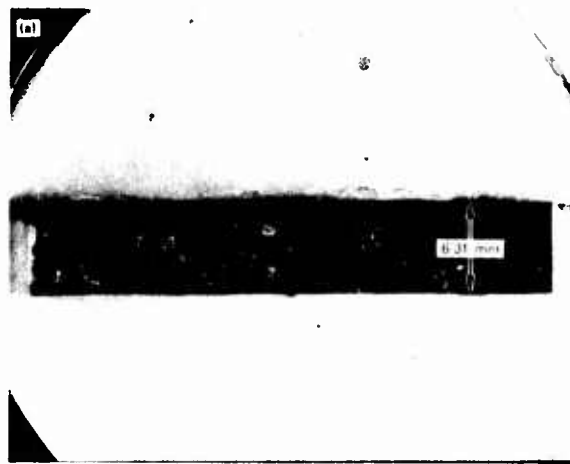


FIGURE 38 INTERMEDIATE DAMAGE IN LASL GRAPHITE: SHOT S36



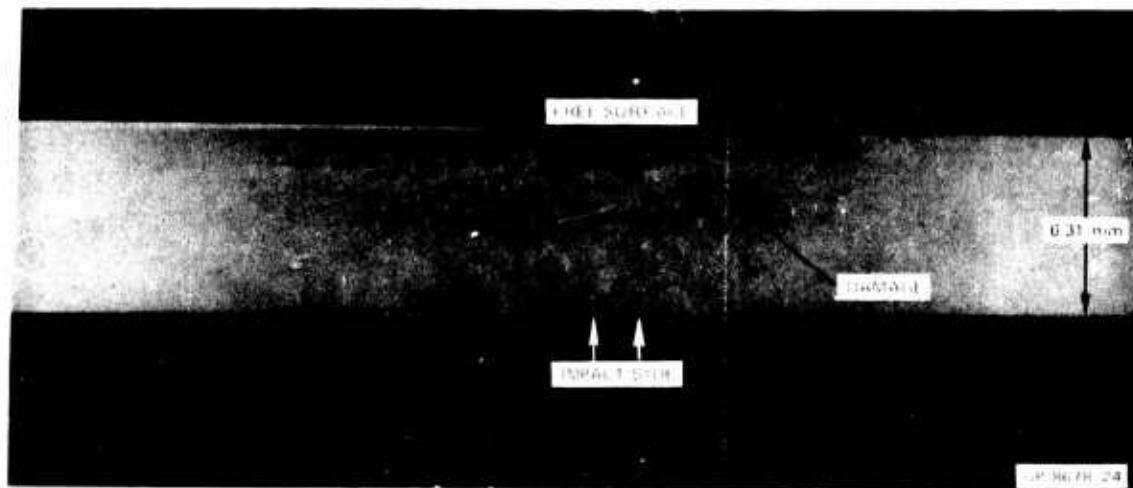


FIGURE 39 INTERMEDIATE DAMAGE IN LASL GRAPHITE: RADIOGRAPH OF SAMPLE FROM SHOT S36

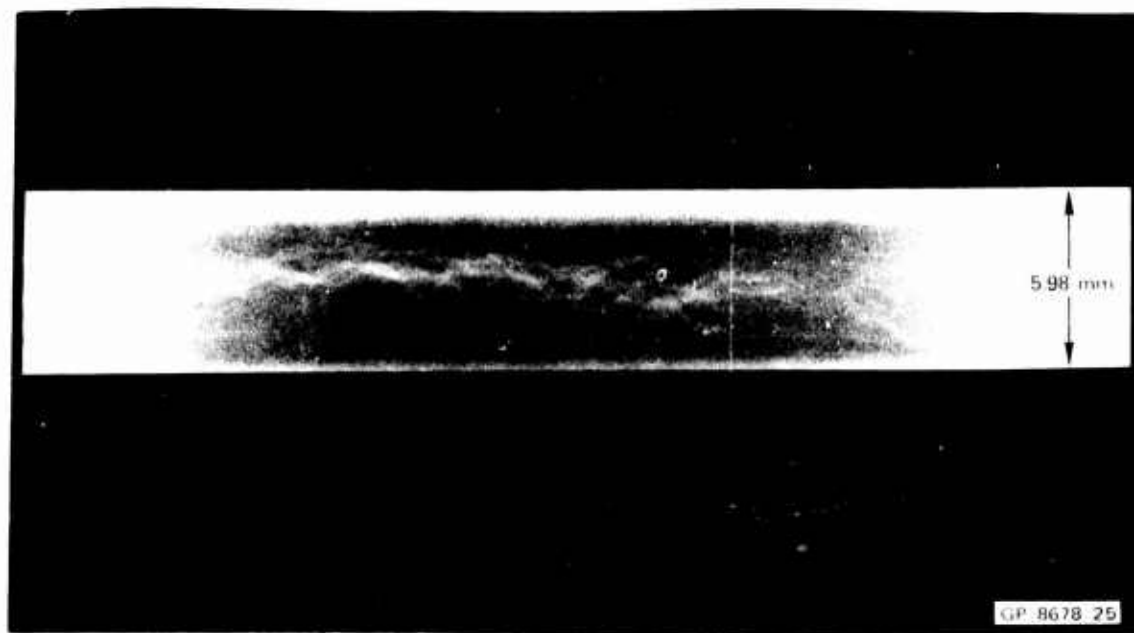


FIGURE 40 HEAVY DAMAGE IN LASL GRAPHITE: RADIOGRAPH OF SAMPLE FROM SHOT S49



GP-8678-26

FIGURE 41 FULL SEPARATION OF LASL GRAPHITE: SHOT S35

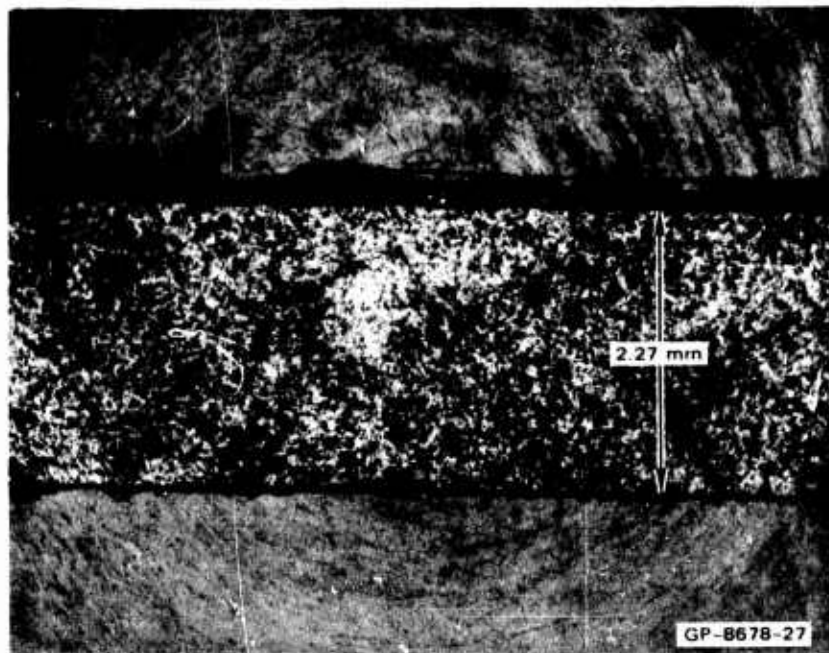


FIGURE 42 LIGHT DAMAGE IN LASL GRAPHITE: SHOT S41

(7) Effects of Precompression

As mentioned earlier, the graphite projectile heads had experienced only compression, and thus served as ideal samples for study of the effects of the compressive phase of the loading history. Unfortunately, we were not able to complete a metallurgical study of these projectile heads during the course of the project. A measurement of sound velocity in such a projectile head was made, and the result was listed in Table XII. It is seen that shock compression to about 0.3 kbar, followed by unloading to zero stress, had the effect of reducing the longitudinal sound speed by about 17 percent. This indicates that dynamic precompression to levels well below the compressive yield point nevertheless caused irreversible changes in the microstructure.

More work is obviously needed to clarify the effects of compression on this material. Any future work should clearly include detailed examination of the graphite projectile heads from these shots.

(8) Stress History Calculations

The loading and unloading paths shown in Figure 34 were used as the basis of the dynamic equation of state of the LASL graphite, and were incorporated in SWAP (Ref. 12) computer runs to calculate the stress histories in the graphite targets. For the shots in which PMMA covers were not used on the graphite targets, the calculations are especially simple because the peak compressive stress in the graphite was less than the compressive strength, and the graphite was assumed to be linearly elastic upon loading and unloading. As usual, the stress histories varied with depth into the target. However, the damage consisted of a limited number of large cracks near the plane of first tension; it was thus not easily characterized by means of the distribution functions used successfully for Armco iron. Therefore, we have, for the present, limited ourselves to characterizing the damage in the usual qualitative way, i.e., the damage is referred to as incipient, intermediate, heavy, and the like. Correspondingly, we have simplified the results of the stress history calculations by listing only the peak tensile stress and the stress duration of the plane of first tension. These data were listed in Table XIII. The information in Table XIII is partially reproduced in Figure 43, which shows isodamage curves plotted in the space defined by the peak tensile stress and the stress duration. The points furthest to the right in Figure 43 correspond to the PMMA-covered shots in Table XIII in which the compressive phase exceeded the compressive strength and presumably weakened the graphite.

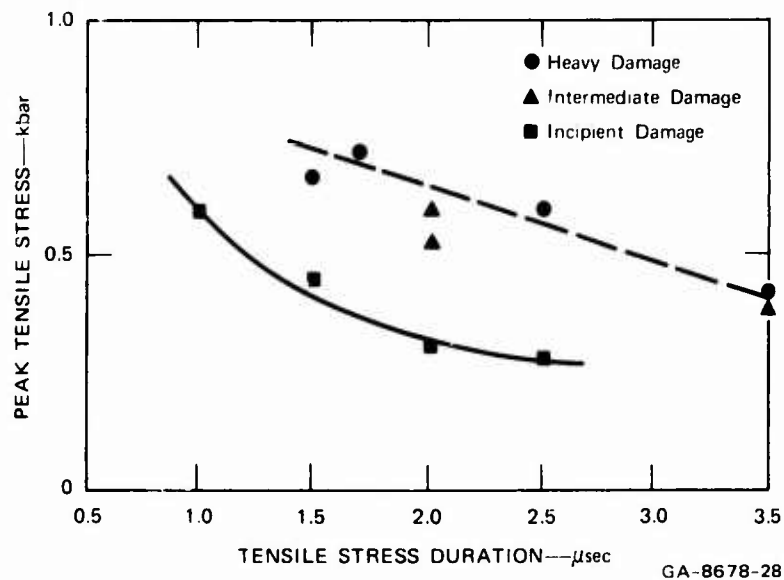


FIGURE 43 IOSDAMAGE CURVES FOR LASI GRAPHITE

(9) Interpretation of Results

The nature of the shock damage in graphite (relatively few, long cracks) made it unproductive to apply the statistical approach that was used for Armco iron to determine the growth of damage. However, the brittle nature of the damage and the apparent rate-independence of the loading curves suggest that the Griffith-Irwin criterion (Refs. 31, 32) for initiation and growth of damage should apply. This criterion, for a penny-shaped crack, can be written as

$$\sigma_F = \sqrt{\frac{\pi E \gamma_c}{4R}} \quad (51)$$

where  $\sigma_F$  is the externally applied critical fracture stress needed in plane strain loading to cause an incipient crack of radius  $R$  to propagate, providing the apparent surface energy during crack formation is given by  $\gamma_c$ .

Inspection of the as-received material shows that many voids about  $10^{-3}$  cm in diameter exist between the grains. (See Figure 38c.) If the incipient crack size is thus chosen to be about  $10^{-3}$  cm,  $E$  assumed to be about  $10^{11}$  dyn/cm<sup>2</sup> (see Table XII), and  $\gamma_c$  taken to be the theoretical surface energy of graphite, or about 120 erg/cm<sup>2</sup> for the basal plane (Ref. 39), then the order of magnitude of the critical stress can be calculated from Eq. (51) to be

$$\sigma_F \sim 0.1 \text{ kbar}$$

which is consistent with the results shown in Figure 43, as well as being in the neighborhood of the static uniaxial stress tensile strength (0.14 to 0.17 kbar).

The tentative conclusion is that crack nucleation in a very brittle material such as graphite may be expected to show little rate dependence, and the standard Griffith-Irwin (i.e., fracture toughness) criterion may be used to predict the stress at which growth of microcracks is initiated. The growth phase, however, will naturally be time dependent; the cracks will grow to greater sizes if the stress duration is increased.

A primitive model that fits the meager data currently available is the following. Assume that microcracks are activated, as discussed above, at a threshold stress  $\sigma_0$  of about 0.1 kbar in accordance with the Griffith-Irwin fracture toughness criterion. Assume further that a measure of damage is the average crack length given by the average crack velocity times the tensile stress duration. If we further assume that the average crack velocity is a linear function of excess stress  $\sigma - \sigma_0$  the damage should be proportional to the excess impulse  $(\sigma - \sigma_0)t$ , where  $t$  is the tensile stress duration. Examination of the incipient damage

curve in Figure 43 shows that this curve is indeed well described by the formula

$$(\sigma - \sigma_0)t = 0.5 \text{ kbar-}\mu\text{sec} \quad (52)$$

where

$$\sigma_0 = 0.1 \text{ kbar}$$

A more sophisticated model of crack nucleation and growth, such as that used for Armco iron and discussed in detail in Appendix VIII, could of course be used. However, the experimental results are currently too meager to justify such a procedure.

An interesting feature of the above simple model is that it predicts that the damage nucleation threshold stress is a function of pore size and suggests that the porosity of the graphite is important in determining the resistance of the material to shock damage.

The preceding discussion has been directed to explaining the damage threshold conditions. In the following, the full separation or fracture conditions will be considered on an energy basis. In the case of graphite it has been found that the dynamic fracture behavior measured by standard notched bar tests can be correlated with static bend rupture tests. For ATJ graphite the elastic energy density in the surface element in a bend rupture test necessary to cause full fracture is about  $4 \times 10^7 \text{ erg/cm}^3$ . In our tests, if we assume the volume change can be correlated with elastic strain, the elastic strain energy density under conditions for full fracture is about  $2 \times 10^7 \text{ erg/cm}^3$ . As it is difficult to ascertain the exact stress and strain in tension under dynamic conditions, this correlation is very encouraging. The inference of this correlation is that, for materials that are both brittle and essentially rate-independent, dynamic fracture behavior can be approximated by correlation with the results of static tests.

b. Armco Iron

The dynamic fracture of brittle materials occurs by the nucleation and growth of damage in the form of planar cracks. In Armco iron, dynamic fracture occurs in a brittle-ductile sequence. First, brittle cleavage cracks are nucleated and traverse individual grains, being arrested at grain boundaries. Second, cracks coalesce by ductile mechanisms through the extension of ligaments between non-coplanar cracks. This sequence of events allows the formation of a high damage level at relatively low stresses in the form of brittle cracks. Much higher stresses are necessary for full separation of the material. These observations can be described by three steps, each of which may be considered separately. These are: (1) crack nucleation--brittle, (2) crack growth--brittle, and (3) crack coalescence--ductile. We will discuss these physical phenomena in the following.

Again, as with the ductile dynamic fracture investigation, the intent of this investigation of brittle dynamic fracture is to determine the stress and time dependences of crack nucleation and growth rates to develop a description of the fracture process. First, a specimen is shocked with a known stress history and recovered. Next, the damage is described quantitatively at a position in the specimen shocked to a known stress for a specific length of time. The nucleation frequency and growth rates at a specific stress are then extracted from a comparison of crack density and size distributions at specimen locations shocked to the same stress for different times. Thus to make this approach work for a specific brittle material, we must be able to: (1) load dynamically and recover specimens, (2) achieve an experimental control so that the cracks can be stopped in different stages of growth, (3) describe the size and spatial distributions of cracks quantitatively, and (4) specify the macroscopic stress and time at stress experienced at any location in the specimen assuming either no damage formation or nucleation and growth of damage.



It is important to note any correlations that exist between specific material properties and the experimentally determined nucleation and growth laws. Such correlations are useful as guides for predicting the behavior of similar materials.

A total of seven symmetric impact experiments were carried out using the 2-1/2-inch-barrel-diameter light gas gun to investigate the dynamic fracture of Armco iron. The objectives of these experiments were to gain insight into the sequence of events leading to the brittle fracture of Armco iron, to define the important parameters in this sequence, and to measure fracture signals resulting from the dynamic fracture process. To meet these objectives, five of the experiments were tapered flyer shots (See Appendix I). This was done so that the development of damage at constant stress could be observed over a continuous range of levels caused by the variation of time at stress with position in the sample. Further, since brittle crack growth rates are extremely large, a continuous observation of the damage as a function of time at stress is necessary so that cracks can be observed at different stages of growth. The remaining two experiments were instrumented with back surface manganin piezoresistive stress gages to record fracture signals. The details of these experiments are presented in Table XIV.

Figure 44 shows the damage observed in a 6.313-mm-thick sample impacted with a flyer projectile varying in thickness from 3.156 mm to 1.578 mm at a velocity of 0.103 mm/ $\mu$ sec (Shot S1). The time at stress for this experiment varied from 0.74  $\mu$ sec at the thick end of the projectile to 0.26  $\mu$ sec at the thin end. Figure 44 shows a region at stress for approximately 0.34  $\mu$ sec. A low crack density is seen in which most of the cracks are smaller than one grain diameter. Also, the residual crack opening displacement is small, indicating that very little plastic deformation occurred at the crack tip. At a shorter time at stress, the

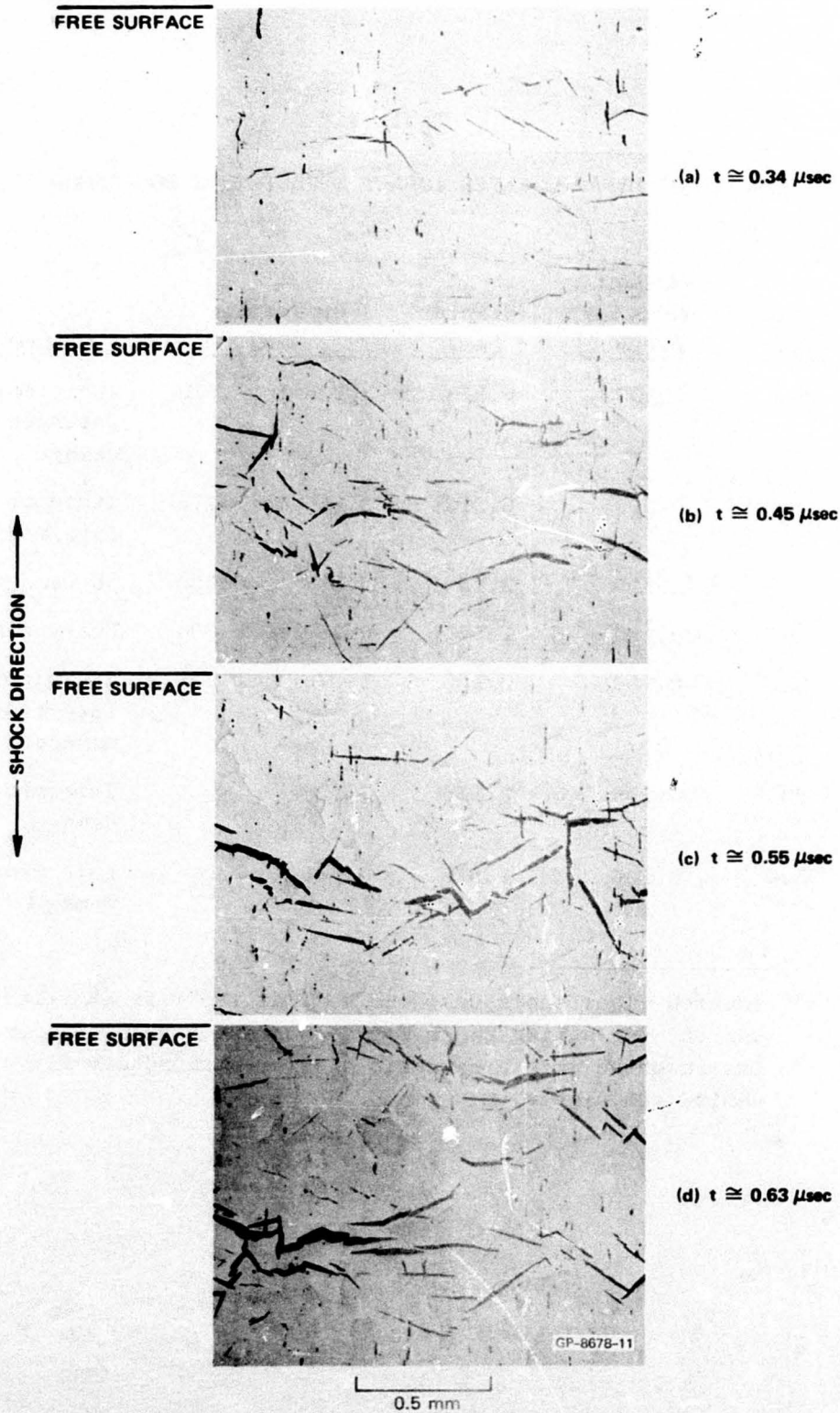
Table XIV

## SUMMARY OF DYNAMIC FLYER IMPACT EXPERIMENTS FOR ARMCO IRON

<u>Shot No.</u>	<u>Impact Velocity (mm/<math>\mu</math>sec)</u>	<u>Sample (mm)</u>	<u>Projectile (mm)</u>	<u>Comments</u>
S1 <sup>a</sup>	0.1033	6.313	3.156 to 1.578	Incipient to intermediate damage
S2 <sup>a</sup>	0.0905	6.313	3.156 to 1.578	Incipient to intermediate
S5 <sup>a</sup>	0.135	3.156	1.578 to 0.789	No damage
S8 <sup>a</sup>	0.190	1.578	0.789 to 0.394	Heavy damage
S11 <sup>a</sup>	0.154	3.156	1.578 to 0.789	Incipient to intermediate damage
S25 <sup>b</sup>	0.196	3.156	1.138	Intermediate damage
S26 <sup>b</sup>	0.236	1.578	0.568	Intermediate damage

<sup>a</sup> Tapered flyer shots designed so that the time at stress was varied over a wide range for a constant stress experiment.

<sup>b</sup> Instrumented with a manganin pressure transducer directly behind the sample.



**FIGURÉ 44** DAMAGE DISTRIBUTION OBSERVED IN A TAPERED FLYER SHOT ON ARMCO IRON (Shot S1)

crack density was essentially zero (i.e., one or two cracks were observed in the micrograph), and no cracks were longer than 50 microns. This indicates that no macroscopic crack growth occurred at the stress achieved in this experiment, approximately 11 kbar tension. Hence, an incubation time for cracks has been observed which is, at a stress of 10 kbar, approximately 0.15 to 0.2  $\mu$ sec. This incubation time is certainly stress dependent, decreasing as the applied stress is increased. This stress dependent incubation time therefore defines the no-damage threshold for the dynamic fracture of Armco iron. It is likely that similar behavior will be observed in other brittle metals and nonmetals. Figure 44, which is a micrograph of a region at stress for approximately 0.45  $\mu$ sec, shows a broader damage zone, a higher crack density and wider crack opening displacements than those shown in Figure 44a. Similar changes, particularly with respect to the crack opening displacement, are seen to occur with further increases in the time at stress in Figure 44c (0.55  $\mu$ sec) and in Figure 44d (0.67  $\mu$ sec). These observations allow construction of a mechanistic model to describe the fracture process in brittle metals, such as Armco iron.

In Armco iron and other brittle body-centered cubic materials, dynamic fracture at room temperature occurs by the nucleation and growth of brittle cleavage cracks along intragranular or intergranular paths. Intergranular fracture can be affected by concentration of oxygen, phosphorous, or other embrittling constituents at grain boundaries leading to a local increase in yield stress and, possibly, a lowering of the local surface energy. This lowering of the local surface energy allows cracks to propagate preferentially along grain boundaries. Little plastic deformation occurs during intergranular fracture, since the grain boundaries form a continuous path through the material for the growth of cracks and coplanarity is therefore not necessary.

The cracks observed in Armco iron, however, were mostly transgranular, and thus are in all likelihood initiated by microscopic plastic deformation. Several models for the dependence of crack nucleation on plastic deformation have been proposed. The one most discussed is the dislocation pile-up (Refs. 40 and 33). In this model, a stress concentration results from the impingement of an array of coplanar dislocations on an impenetrable barrier such as a grain boundary or a hard inclusion. Also, twin interactions may also nucleate cracks (Ref. 41) because of the large stress fields at the tip of a twin. In any case, such mechanisms are stress and time dependent, since the development of the stress concentration is both stress and time dependent. In the case of dislocations, it is probably the stress and time dependence of the dislocation mobility that is controlling.

The propagation of these cracks, once nucleated, is basically a brittle process. It is unlikely that appreciable plastic deformation occurs at the crack tips during this phase of crack growth. The velocity of these cracks is undoubtedly large, approaching the limiting velocity for crack growth (i.e., approximately 0.3 of the shear wave velocity). Because of the orientation dependence of the crack plane [i.e., the cleavage plane in iron is the (100) plane], the growth of cracks in adjacent grains in a coplanar manner is not likely. Therefore, a single crack is effectively stopped at a grain boundary and is limited to a single grain diameter in length. Full failure can occur only by linking these cracks through formation of brittle cracks or by ductile mechanisms. The mechanism observed is ductile failure of the ligaments connecting the cracks.

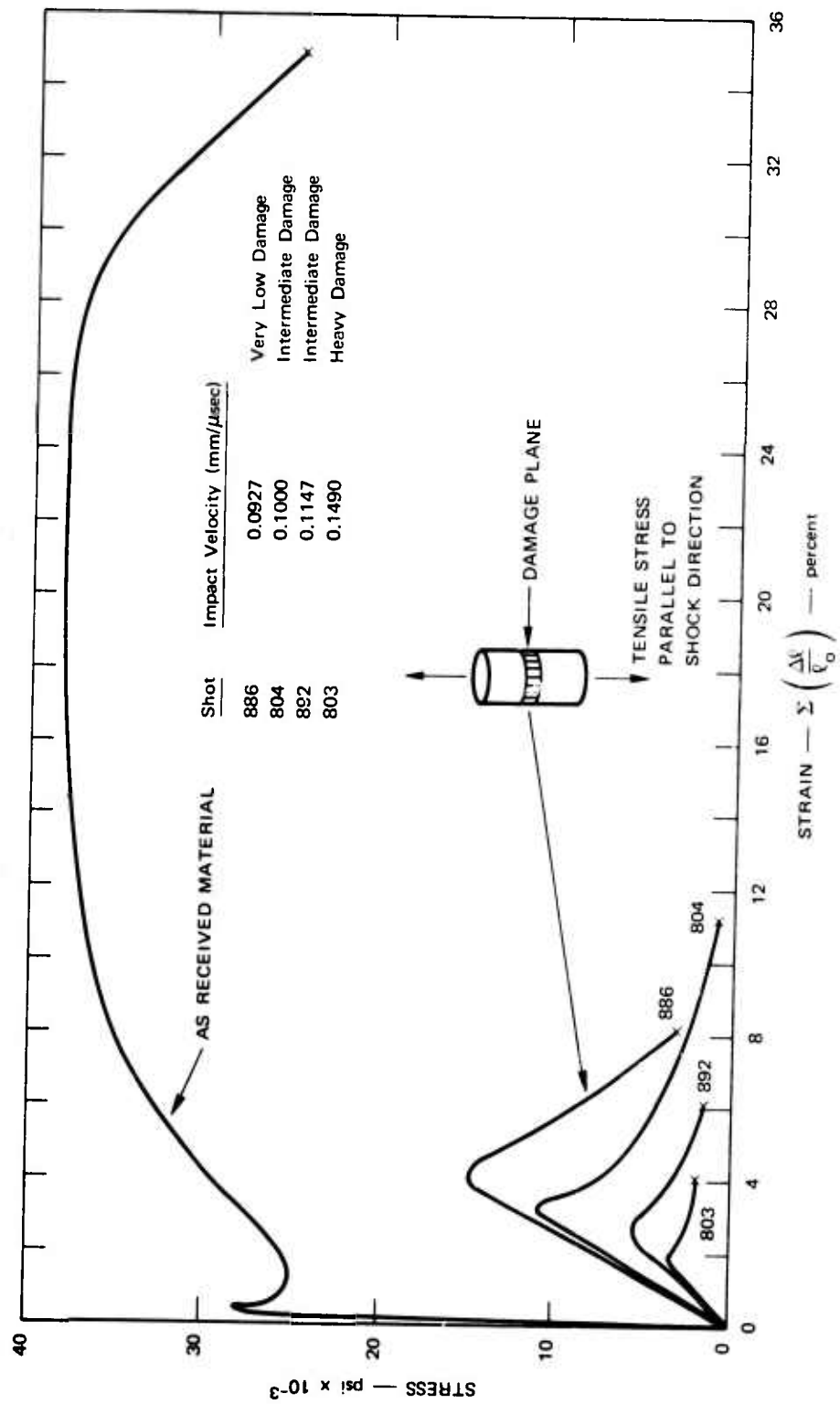
Another series of experiments were carried out to investigate the effects of the shock induced damage on the residual strength of Armco iron. In these experiments cylindrical samples 0.25-in. in diameter were

spark machined from the damaged samples with the plane of damage normal to the cylinder axis. They were then friction gripped at the ends and pulled in tension at a crosshead speed of  $2.1 \times 10^{-5}$  cm/sec. The engineering stress-strain behavior observed is shown in Figure 45 along with the behavior of as-received material.

Four points are apparent from these results. First, the yield strength and ultimate tensile strength are equal for the damage samples and are greatly reduced as shown in Figure 46. Second, the apparent strain to fracture is greatly reduced. Third the apparent modulus decreases with increasing impact velocity. Fourth, and most important, the onset of damage results in a drastic decrease in strength, indicating that for brittle materials the damage threshold essentially defines the useful limit of the material.

The first three of these effects are consistent with the increasing damage with increasing impact velocity. The higher the damage level, the lower the effective strength in the damage zone, hence the lower yield strength. The higher the damage in the damage zone, the lower the effective modulus due to both stress concentration and reduction of effective load bearing area. Also, the higher the damage, the less the work necessary to cause full failure, and the strain to failure decreases.

The fourth point is very important as it gives information necessary for engineering decisions. The drastic decrease in strength at the onset of damage indicates that this value (threshold damage level strength) is effectively an upper design limit for application of such materials. Therefore, such data are absolutely necessary for engineering design and for an understanding of the mechanisms leading to the formation of damage (i.e., nucleation) primary to evaluation of new materials and to improvements in the uses of old materials.



GA-8678-98

FIGURE 45 EFFECT OF DAMAGE ON STRESS-STRAIN CURVES OF ARMCO IRON

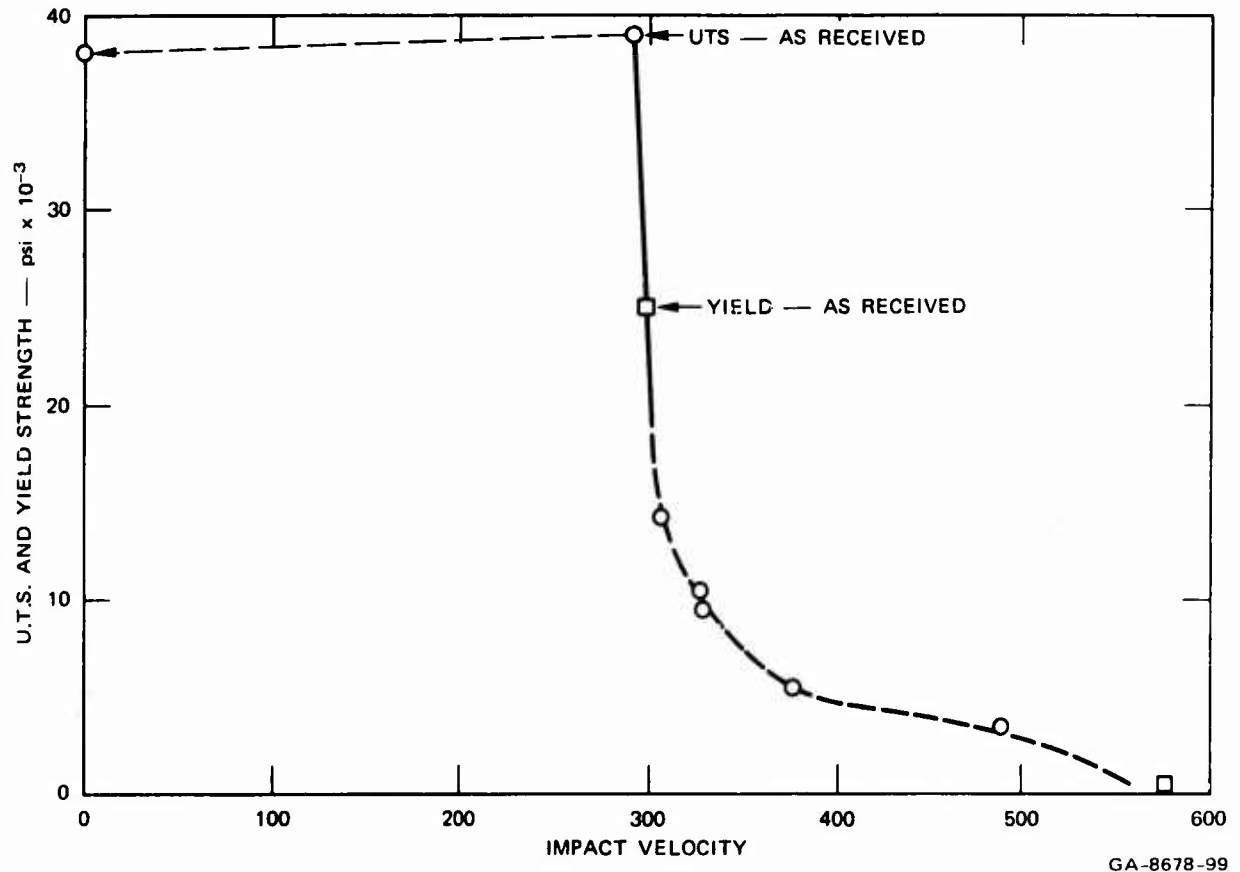


FIGURE 46 EFFECT OF DAMAGE ON THE ULTIMATE TENSILE STRENGTH AND THE YIELD STRENGTH OF ARMCO IRON

c. 99.99 Percent Pure Iron

The dynamic fracture of 99.99 percent pure iron was also experimentally investigated. Four impact experiments were carried out using the 2-1/2-in.-barrel-diameter light gas gun. The details of these experiments are listed in Table XV. These experiments required the use of Armco iron projectile heads because of the high cost of high purity material. Two types of experiments were carried out. First, uniform thickness projectile heads were used to study both damage formation and full separation of this material. Second, a tapered flyer experiment was carried out to examine, in one experiment, the general



Table XV

SUMMARY OF DYNAMIC FLYER PLATE EXPERIMENTS  
FOR 99.99% PURE IRON

Shot No.	Impact Velocity (mm/ $\mu$ sec)	Sample (mm)	Projectile (mm)	Comments
S37	0.093	2.96	1.16	No damage
S38 <sup>a</sup>	0.161	2.98	1.16 to 0.58	Heavy to light damage
S44	0.103	2.78	1.16	Light damage
S45	0.245	3.00	1.16	Full separation

<sup>a</sup> Tapered flyer shots designed so that the time at stress was varied over a wide range for a constant stress experiment.

nature of the damage development process. These data are next discussed and correlated with observations made on Armco iron.

The data in Table XV show that the damage threshold for the pure iron occurred at an impact velocity of 0.10 mm/ $\mu$ sec, which can be compared with the results shown in Table XIV for Armco iron. The threshold impact velocity in a nearly equivalent experiment was above 0.135 mm/ $\mu$ sec. Therefore the damage threshold characteristics vary widely for these materials and reflect, undoubtedly, the yield behavior. Further, since the high purity iron has a damage threshold impact velocity that is less than that for Armco iron, it is likely that the crack nucleation threshold is controlled by the plastic flow of the material. This is the conclusion in spite of the stress risers and inclusions present in the Armco iron, which should be active as crack nucleation sites. Therefore, mechanisms associated with the intrinsic material characteristics, rather than the inclusion content, seem to be controlling the damage nucleation.

Crack distributions observed at threshold and intermediate damage levels are shown in Figures 47 and 48. The observed crack distributions are broad, but nearly identical to those observed in Armco iron. In Figure 48 a single large grain is observed, somewhat removed from the region of maximum damage containing essentially isolated cracks. These cracks are apparently not associated with grain boundaries or other observable metallographic features. Therefore, nucleation probably occurred in a currently unknown manner that is an inherent property of the iron itself, and not of the impurity content.



FIG 47 THRESHOLD DAMAGE IN 99.99% PURE IRON

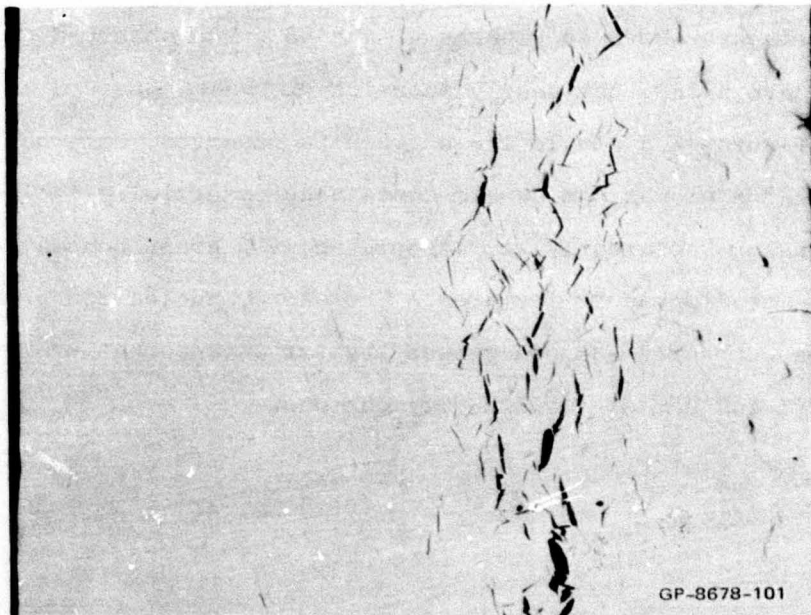


**FIGURE 48** INTERMEDIATE DAMAGE IN 99.99% PURE IRON

Scanning electron microscope micrographs of the fully fractured sample are shown in Figure 49. This figure shows, first, the cleavage facets within individual grains and, second, the plastic response leading to full failure following the formation of the cleavage planes. Specifically, nucleation sites are observed near the sample center in Figure 49(b). This is the center of the so-called river pattern observed there.

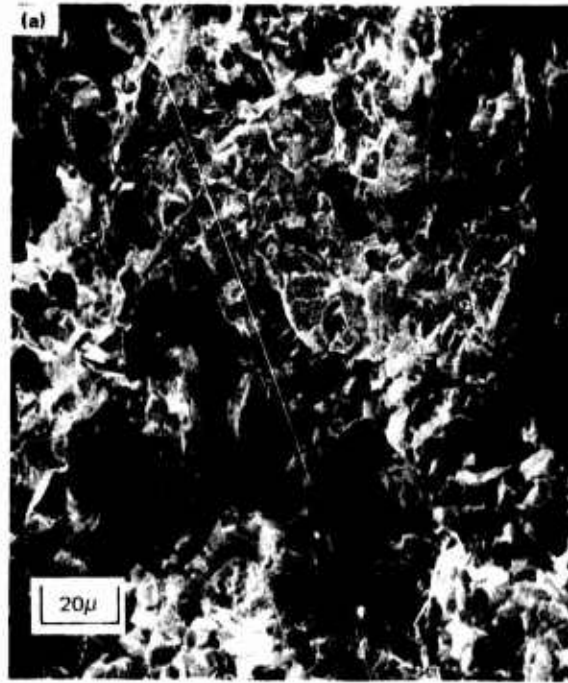


FIGURE 49 DETAILS OF FRACTURE SURFACE  
IN 99.99% PURE IRON

### 3. QUANTIFYING THE DAMAGE

The statistical treatment of the observed damage in brittle materials followed the same general approach as that described for ductile materials in Section III, 4. In brittle materials, however, the microscope damage manifests itself as brittle microcracks instead of spherical voids. These cracks vary in size, width, and orientation with respect to the axis of principal stress. Therefore, the statistical treatment of the observed damage in brittle materials must account for more variables than were necessary for the ductile damage.

As in the case of ductile materials, the shock-loaded specimen is sectioned, lapped, and polished so that the plane of polish contains the axis of principal stress. The microcracks intersect the plane of polish with varying apparent lengths, widths, and angles to the axis of principal stress. (See Figure 44 for example) The observed parameters are defined as follows:

$x, z$  = location of the apparent center of the crack in the plane of polish.  $z$  is the direction of the major stress, and  $x$  is normal to  $z$  and in the plane of polish. The origin of coordinates is arbitrary and is chosen for convenience.

$\sigma(z)$  = peak tensile stress experienced at position  $z$ ;  $\sigma$  is assumed independent of  $x$ .

$t(z)$  = duration of peak tensile stress  $\sigma(z)$  at position  $z$ . The experiments utilized stress-time histories that were approximately square waves; hence  $\sigma$  and  $t$  determine the tensile stress history.

$\alpha$  = angle between the normal to the trace of the crack in the plane of polish and the  $z$  axis.

$c$  = half the length of the crack trace in the plane of polish.

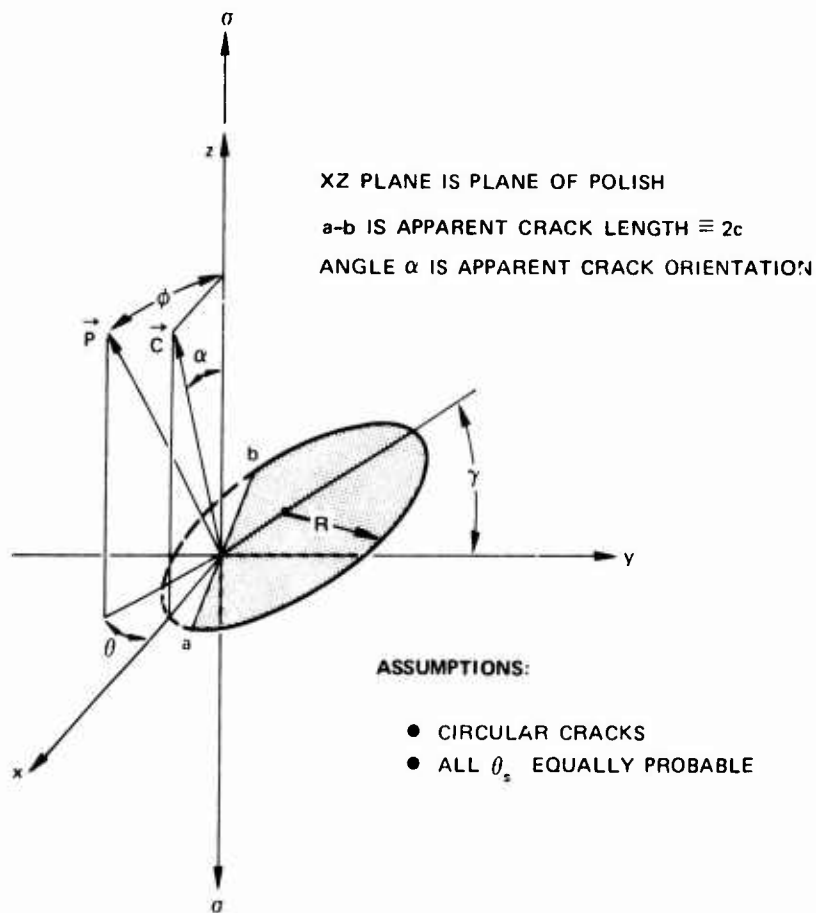
w = width of the crack trace in the plane of polish.

Photographic enlargements of the polish planes are made for each sample, and the polish plane is divided into zones corresponding to different stress durations. The Telereadex machine is used to aid in counting the cracks and in recording on punched cards the positions of the cracked ends, center, and sides. A small computer program is used to convert these numbers to the desired values of crack center position, crack width, crack length, and crack orientation. Thus, the values of  $x$ ,  $z$ ,  $w$ ,  $c$ , and  $\alpha$  for each crack are recorded. Since a stress wave analysis is used to calculate  $\sigma(z,t)$  for each experiment, the resulting data can be expressed as a distribution function

$$N(\alpha, c, w, x, z, \sigma, t)$$

where  $N$  is the number of observed cracks per unit area in the polish plane in the intervals between  $\alpha$  and  $\alpha + \Delta\alpha$ ,  $c$  and  $c + \Delta c$ ,  $w$  and  $w + \Delta w$ ,  $z$  and  $z + \Delta z$ ,  $x$  and  $x + \Delta x$ ,  $\sigma$  and  $\sigma + \Delta\sigma$ , and  $t$  and  $t + \Delta t$ .

As in the ductile analysis, however, the distribution of actual interest is the volume distribution of cracks that was present before the polish plane was interposed in the material. Specifically, we wish to ascertain  $\rho(\varphi, \theta, R, W, x, z, \sigma, t)$ , where  $\varphi$  is the angle that the normal to the actual crack surface makes with the  $z$  axis,  $\theta$  is the angle by which the normal to the crack plane is rotated around the  $z$  axis,  $R$  is the true crack radius (assuming circular cracks),  $W$  is the true crack opening displacement,  $(x,y,z)$  is the location of the crack center ( $y$  points into the plane of polish), and  $\sigma$  and  $t$  specify, as before, the tensile stress history (See Figure 50).  $\rho$  is then the number of cracks per unit volume in the appropriate intervals of  $\varphi$ ,  $\theta$ ,  $R$ ,  $W$ ,  $y$ ,  $z$ ,  $x$ ,  $\sigma$ , and  $t$ .



GA-8678-16

FIGURE 50 CIRCULAR CRACK INTERSECTING THE PLANE OF POLISH

The main statistical problem is thus to transform the observed surface distribution  $N$  into the desired volume distribution  $\rho$ . The procedure for doing this in the ductile case was incorporated into the computer program BABS 1 described earlier (Ref. 12). What is needed is thus a more comprehensive form of BABS to perform the same function for brittle damage. The procedure for doing this was worked out and incorporated into a computer program called BABS 2. The method is similar to that developed by Kaechele and Tetelman (Ref. 30) but is appreciably more complex since Kaechele and Tetelman did not treat the crack size or

width distribution. Complete descriptions of the analysis and the computer program are given in Appendices IX and X. To make the treatment tractable, the following simplifications were made:

- The cracks were assumed to be penny-shaped.
- The distributions were assumed to be independent of  $\theta$  (the angle of rotation around the direction of principal stress).
- The distributions were assumed to be independent of  $x$  and  $y$ . (This is, in fact, an experimental condition if the material is reasonably homogeneous.)
- The crack length and crack width distributions were handled separately; i.e., we may solve either for  $\rho(\varphi, R, z, \sigma, t)$  or for  $\rho(\varphi, W, z, \sigma, t)$ .

Once the volume distributions  $\rho(\varphi, R$  or  $W, z, \sigma, t)$  are obtained, the nucleation and growth functions are found from the relations:

$$\frac{\partial \rho}{\partial t} \bigg|_{\sigma, R_0, \varphi, \sigma} = \text{nucleation rate}$$

where  $R_0$  is the incipient crack radius, and

$$\frac{\partial R}{\partial t} \bigg|_{\rho, \varphi, z, \sigma, t} \quad \text{and} \quad \frac{\partial W}{\partial t} \bigg|_{\rho, \varphi, z, \sigma, t} = \text{growth rates}$$

Examples of the observed brittle crack surface distribution in the plane of polish and the corresponding computed volume distribution are given in Figures 51 and 52, where we show our results for Amco iron shot number S25. Another example is given in the next subsection. In addition, examples of computations performed on assumed test distributions are given in Appendix IX, where a complete description of the statistical analysis procedures is also given.



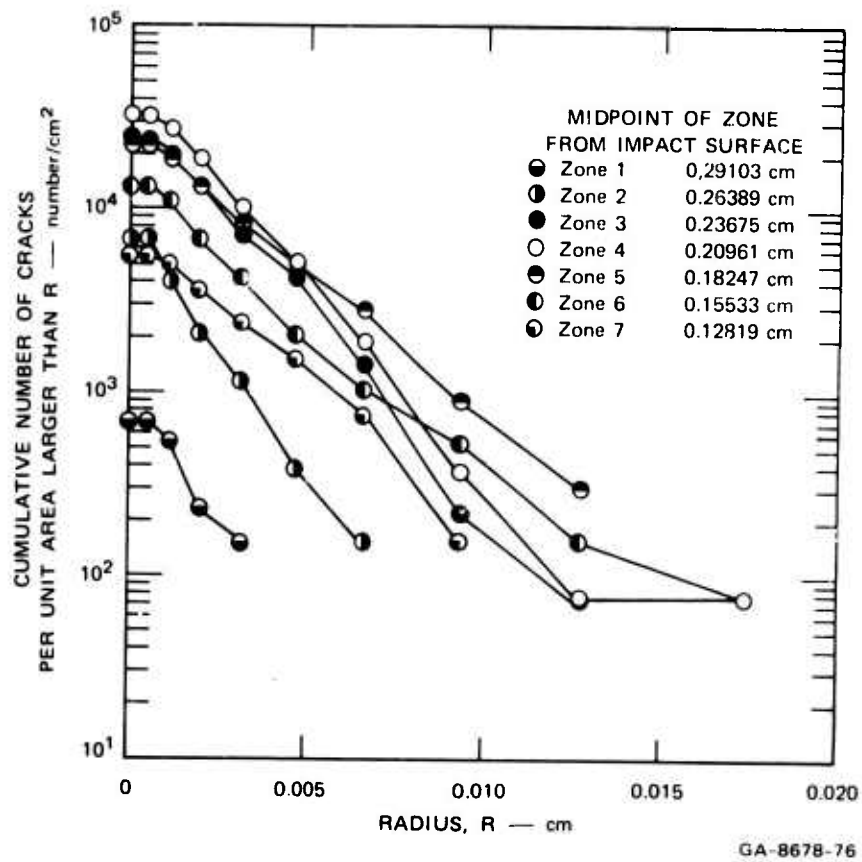


FIGURE 51 CUMULATIVE CRACK SURFACE CONCENTRATION FOR ARMCO IRON: SHOT S25

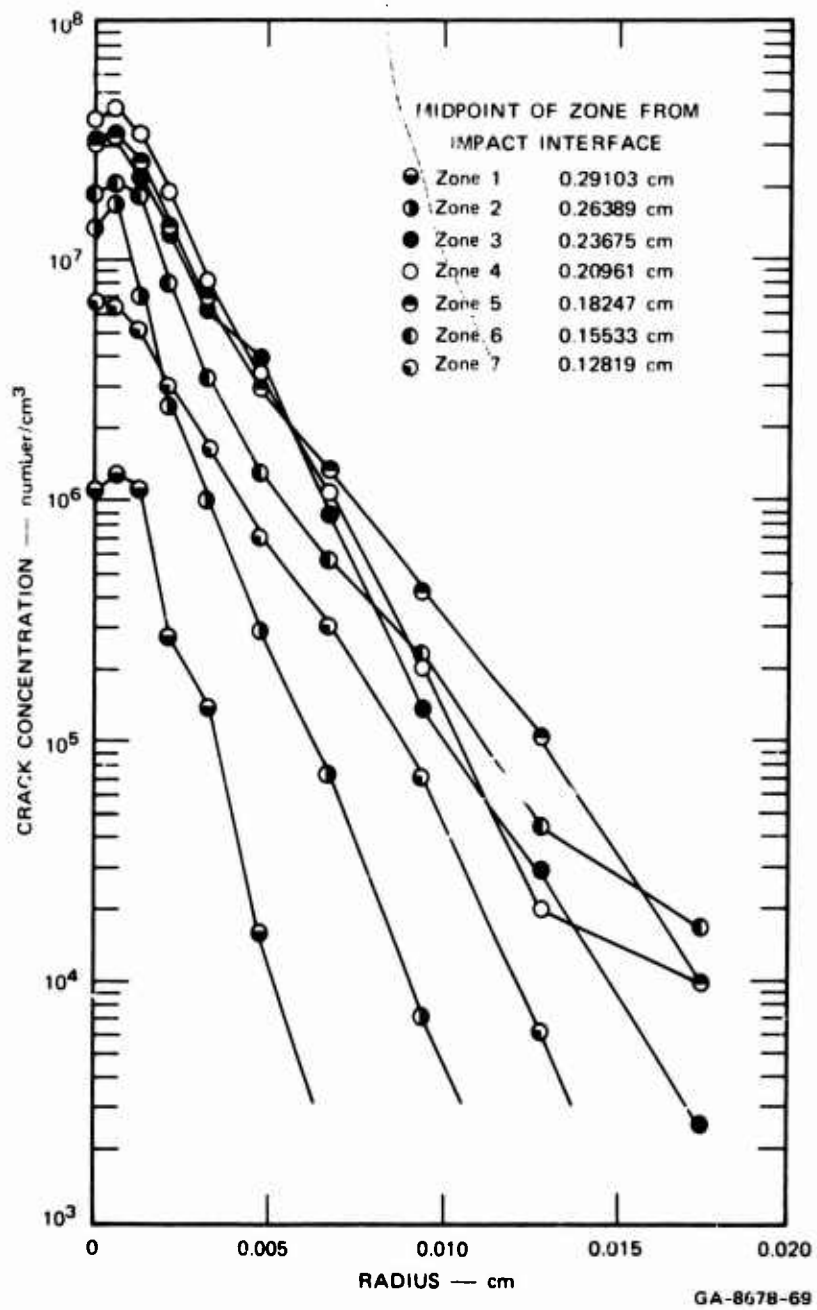


FIGURE 52 COMPUTED CUMULATIVE CRACK VOLUME CONCENTRATION FOR ARMCO IRON: SHOT S25

#### 4. WAVE PROPAGATION CALCULATIONS AND COMPARISON WITH DATA

The equations used for nucleation and growth of cracks and the constitutive relations for damaged material are derived in this section. These equations were used in wave propagation calculations to compute the damage from impacts in Armco iron plates.

##### a. Nucleation Rate

The nucleation rate was assumed to have the form

$$\dot{N} = \dot{n}_0 \exp\left(\frac{\sigma - \sigma_{n0}}{\sigma_1}\right) \quad (55)$$

where

$\sigma_{n0}$  = a threshold stress for nucleation

$\dot{n}_0, \sigma_1$  = constants

This nucleation rate is similar to that derived from the ductile fracture experimental data. The form also resembles the form given by Zhurkov (Ref. 42) for rate of breakage of atomic bonds.

All the cracks are assumed to be nucleated at the same radius (half-length) and to lie in a plane perpendicular to the direction of propagation. A radius of about one micron was chosen for our calculations.

##### b. Crack Growth

Traditional fracture mechanics has been called upon to determine whether growth occurs under a given tensile stress. According to Sneddon (Ref. 34), the critical crack radius for a penny-shaped crack in a one-directional, elastic, tensile field is

$$R^* = \frac{\pi E \gamma}{4\sigma^2 (1 - \nu^2)} = \frac{\pi K_{IC}^2}{4\sigma^2} \quad (56)$$

where

$E$  = the elastic modulus

$\gamma$  = the surface energy

$\sigma$  = the one-directional tensile stress applied at infinity

$\nu$  = Poisson's ratio

$K_{IC}$  = the plane strain fracture toughness in the opening mode.

If the crack radius is less than  $R^*$ , no growth occurs. If the radius is larger, growth is presumed to occur with a velocity given by the relation of Dulaney and Brace (Ref. 35) for the propagation of a planar crack in elastic material.

$$\frac{V_c}{V_t} = 1 - \frac{R^*}{R} \quad R > R^* \quad (57)$$

where

$V_c$  = the growth velocity

$V_t$  = the terminal velocity

$R$  = the crack radius

### c. Constitutive Relations

The form of the constitutive relations for material with voids was used also for material with cracks. These relations provide for separate expressions for pressure and deviator stress. Instead of

a void volume, the damage is measured by the total volume of the cracks. This volume is computed from the expression of Irwin (Ref. 32) for the volume of a penny-shaped crack in an elastic medium

$$v = \frac{4\pi R^3 \sigma}{3E}$$

Because no plastic flow is provided for in this expression, the volume so obtained is a lower-bound estimate of the actual volume. Because the crack volume is elastic, it becomes zero when tensile stresses are removed. Plastic flow at the crack tips can be included in our calculations in a straightforward manner, and this may be done in future work. A more complete description of the constitutive relations is presented in Section III 5c and in Appendix VIII.

d. Wave Propagation Results

From the wave propagation calculations we obtain stress histories at selected points, total crack concentrations (number/cm<sup>3</sup>), number of cracks at each crack radius (a size distribution), and relative crack volume. Since each of these can be obtained at any depth in the target, we can study the variation of crack concentration or volume as a function of position.

The calculations made for Armco iron are based on the fracture parameters listed in Table XVI and the shot conditions in Table XVII. Note that the fracture toughness, threshold stress for nucleation, and nucleation radius are coordinated so that growth begins at the nucleation stress level. The limiting velocity is only  $3 \times 10^4$  cm/sec, or about 5 percent of longitudinal sound speed; this low velocity probably indicates that considerable plastic flow is occurring at the crack tip during propagation.

Table XVI

## BRITTLE FRACTURE PARAMETERS

<u>Parameter</u>	<u>Units</u>	<u>Description</u>	<u>Armco Iron</u>
T1( $v_t$ )	cm/sec	Limiting crack velocity	$3 \times 10^4$
T2( $K_{IC}$ )	dyn/cm <sup>3/2</sup>	Fracture toughness	$3.4 \times 10^7$
T3	cm	Nucleation crack radius	$1 \times 10^{-4}$
T4( $\dot{n}_0$ )	$\frac{\text{no.}}{\text{cm}^3/\text{sec}}$	Nucleation rate coefficient	$1 \times 10^{13}$
T5( $\sigma_{n0}$ )	dyn/cm <sup>2</sup>	Nucleation threshold	$-3 \times 10^9$
T6( $\sigma_1$ )	dyn/cm <sup>2</sup>	Nucleation parameter	$-9.5 \times 10^9$

Table XVII

## IMPACT CONDITIONS FOR EXPERIMENTS IN ARMCO IRON

<u>Shot Number</u>	<u>Flyer</u>		<u>Target</u>	<u>Impact</u>	<u>Backing Material</u>
	<u>Thickness (cm)</u>	<u>Velocity (cm/sec)</u>	<u>Thickness (cm)</u>	<u>Stress (kbar)</u>	
886	0.236	$9.15 \times 10^3$	0.635	18.5	none
S25	0.1138	$1.96 \times 10^4$	0.3156	38.3	PMMA

The observed and computed damage are compared in Figures 53 to 56. The observed distributions appear to be essentially linear on the semilog scale. They depart from linearity only for small cracks; this departure may be caused by our inability to see very small cracks that close after the passage of the tensile wave. The computed distributions are not linear, and they tend to have less slope than the observed distributions. Since the observed damage curves are nearly parallel to each other, there is little tendency for adjacent curves to cross. However, the computed curves have dissimilar slopes and do cross in some instances. These observations indicate that some changes are probably needed in the nucleation and growth functions and that it would be desirable to nucleate a distribution of cracks, rather than a single size crack.

The comparison of observed and computed damage should be made on the basis of the portion of the distribution that contributes most strongly to stress and modulus reduction. According to Eq. (58), the total crack volume is proportional to number times radius cubed. If this volume is the correct measure of damage, then the maximum contribution to damage is from a central portion of the distribution; at the large radius end there are too few cracks and at the small radius end, individual volumes are too small. Hence, it is this central portion of the distribution curves that should be matched. An attempt to compare crack concentrations in this middle range is shown in Figures 57 and 58. The observed distributions show a considerably sharper peak at the spall plane than the computed distributions; this indicates that insufficient damage is accounted for in the computations. Higher damage might be produced by:

- Increasing the volume of each crack (by permitting plastic deformation).

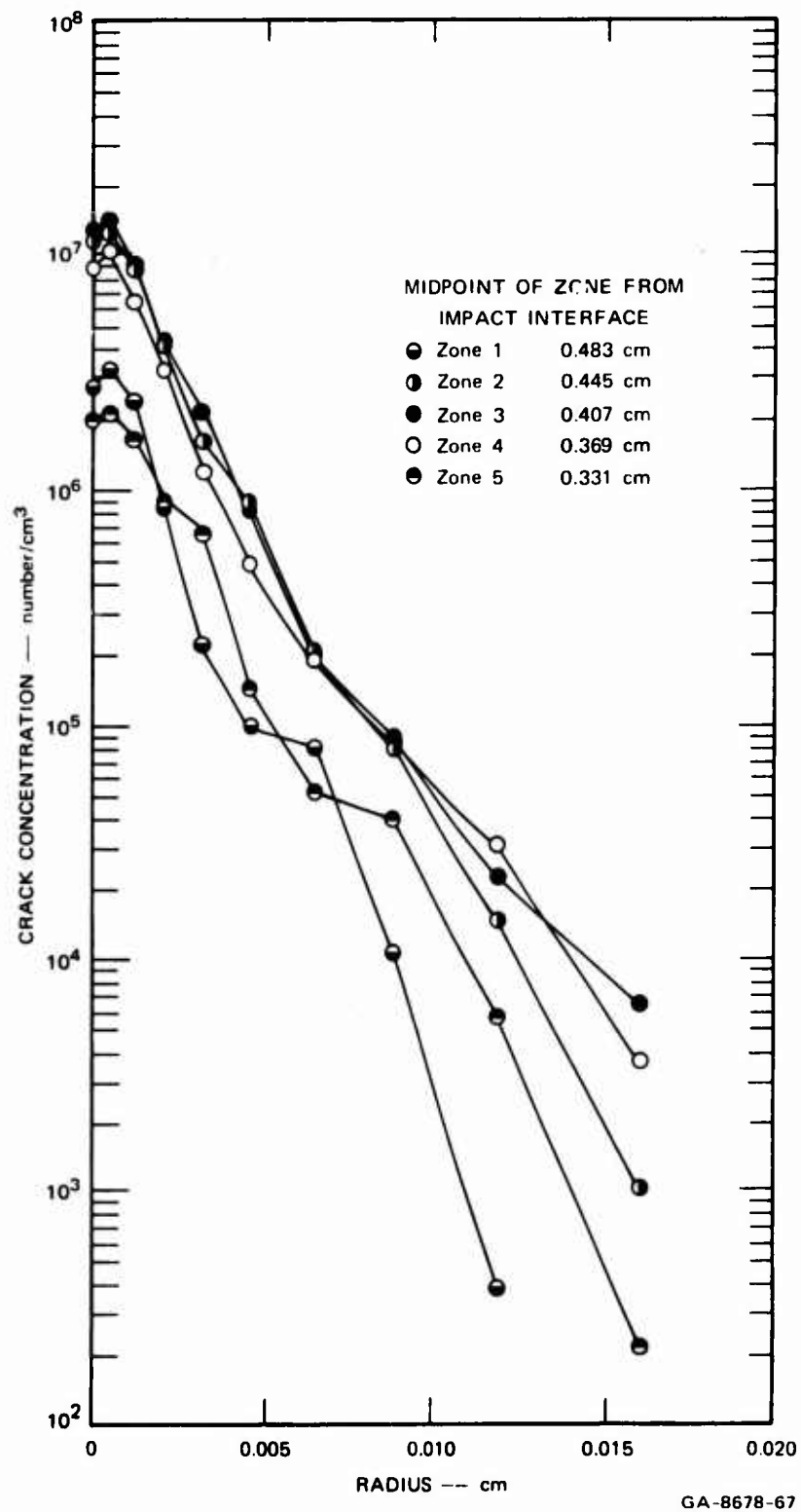


FIGURE 53 CRACK SIZE DISTRIBUTIONS IN ZONES NEAR THE SPALL PLANE IN ARMCO IRON: SHOT 886



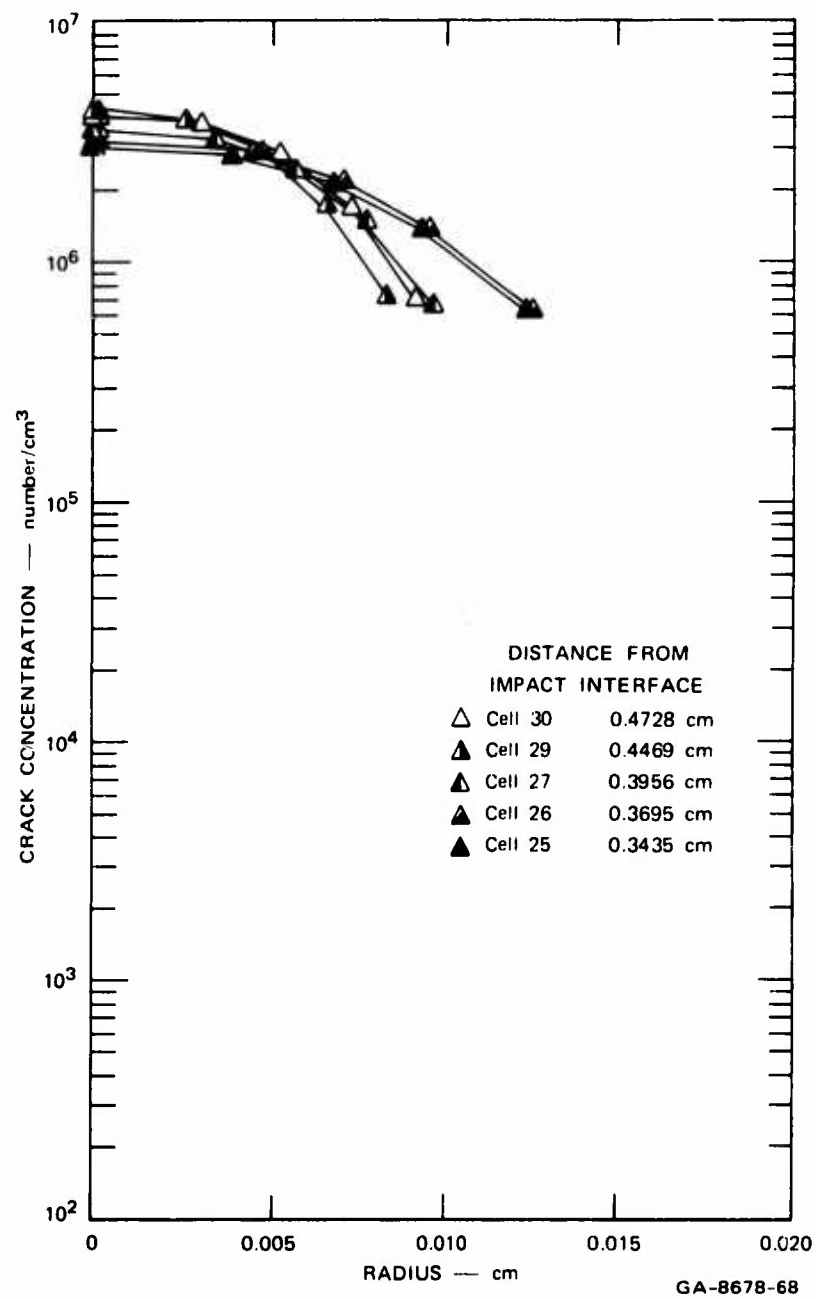


FIGURE 54 COMPUTED CRACK SIZE DISTRIBUTIONS FOR  
ARMCO IRON: SHOT 886

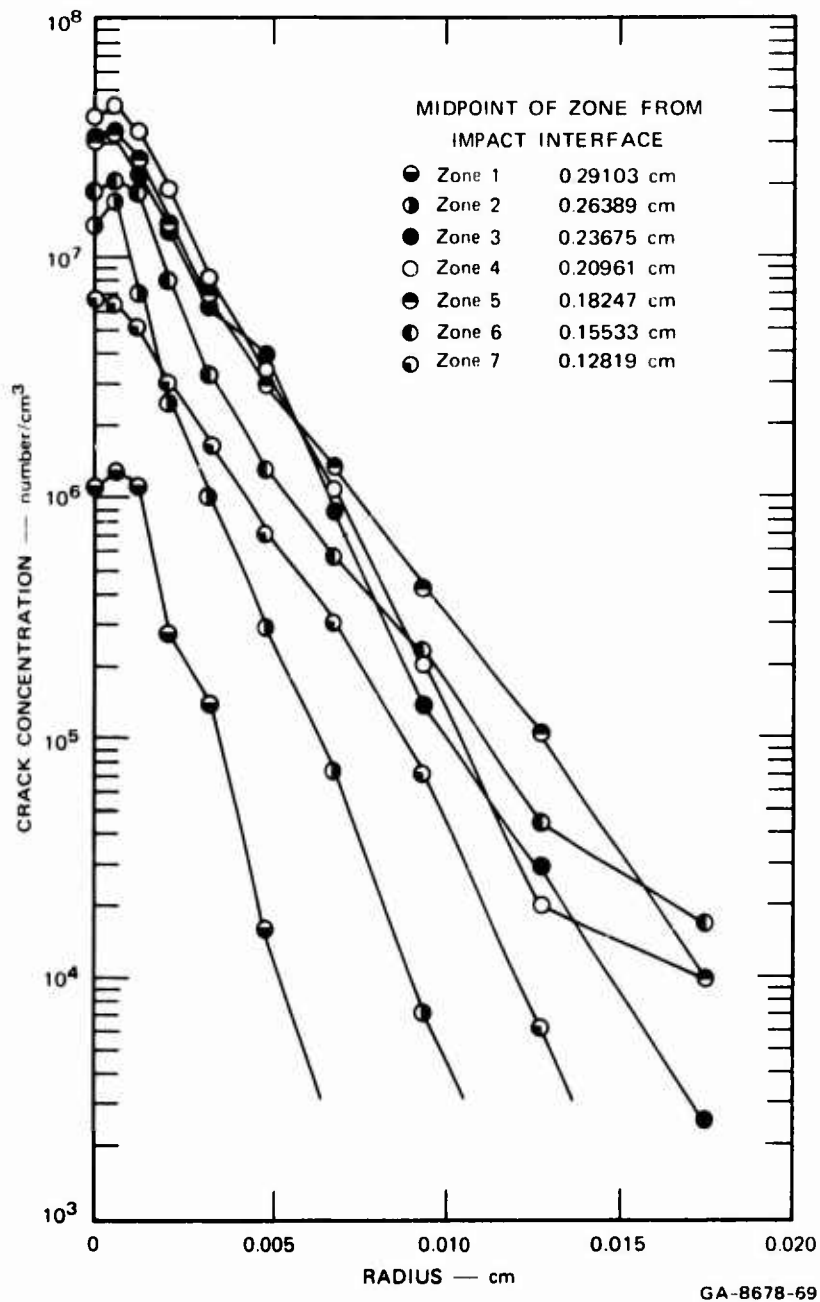


FIGURE 55 CRACK SIZE DISTRIBUTIONS IN ZONES NEAR THE SPALL PLANE IN ARMCO IRON: SHOT S25

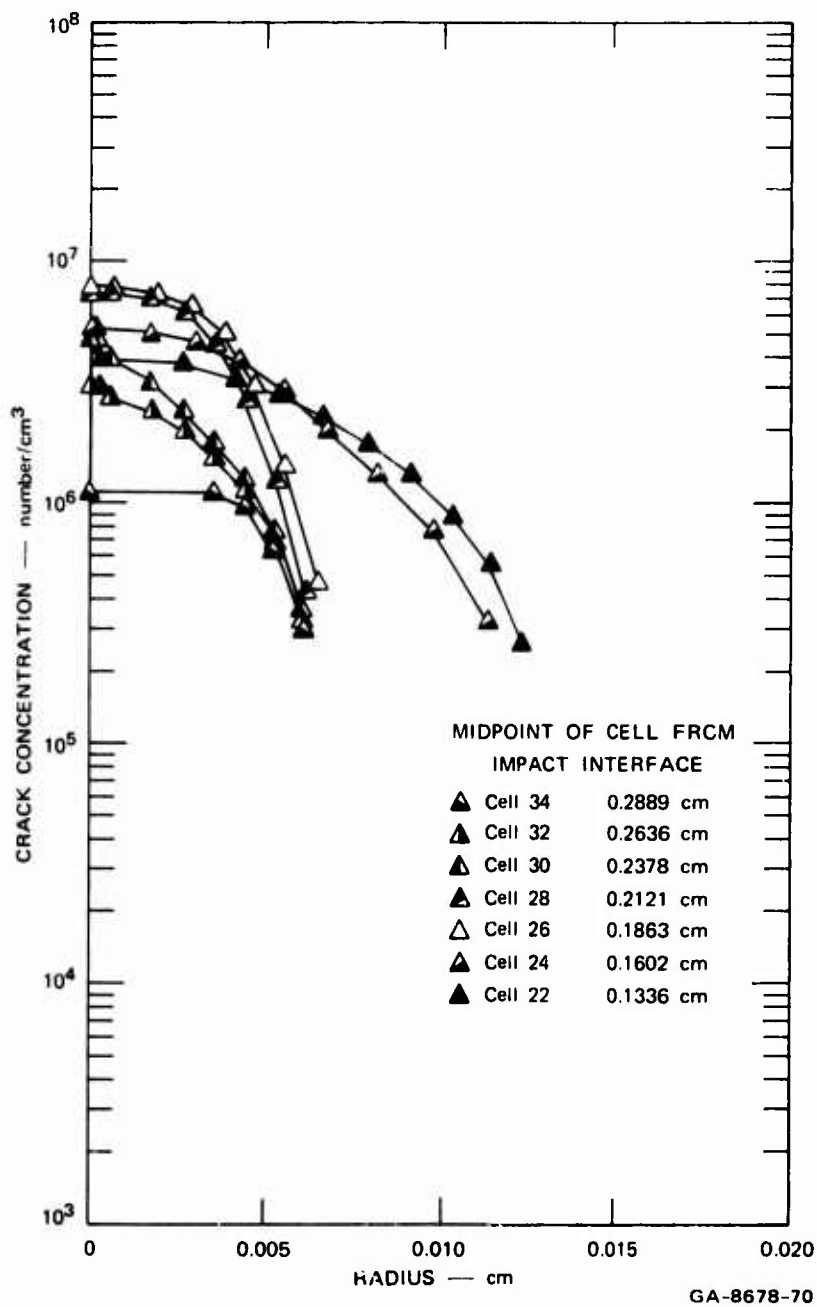


FIGURE 56 COMPUTED CRACK SIZE DISTRIBUTIONS FOR ARMCO IRON:  
SHOT S25

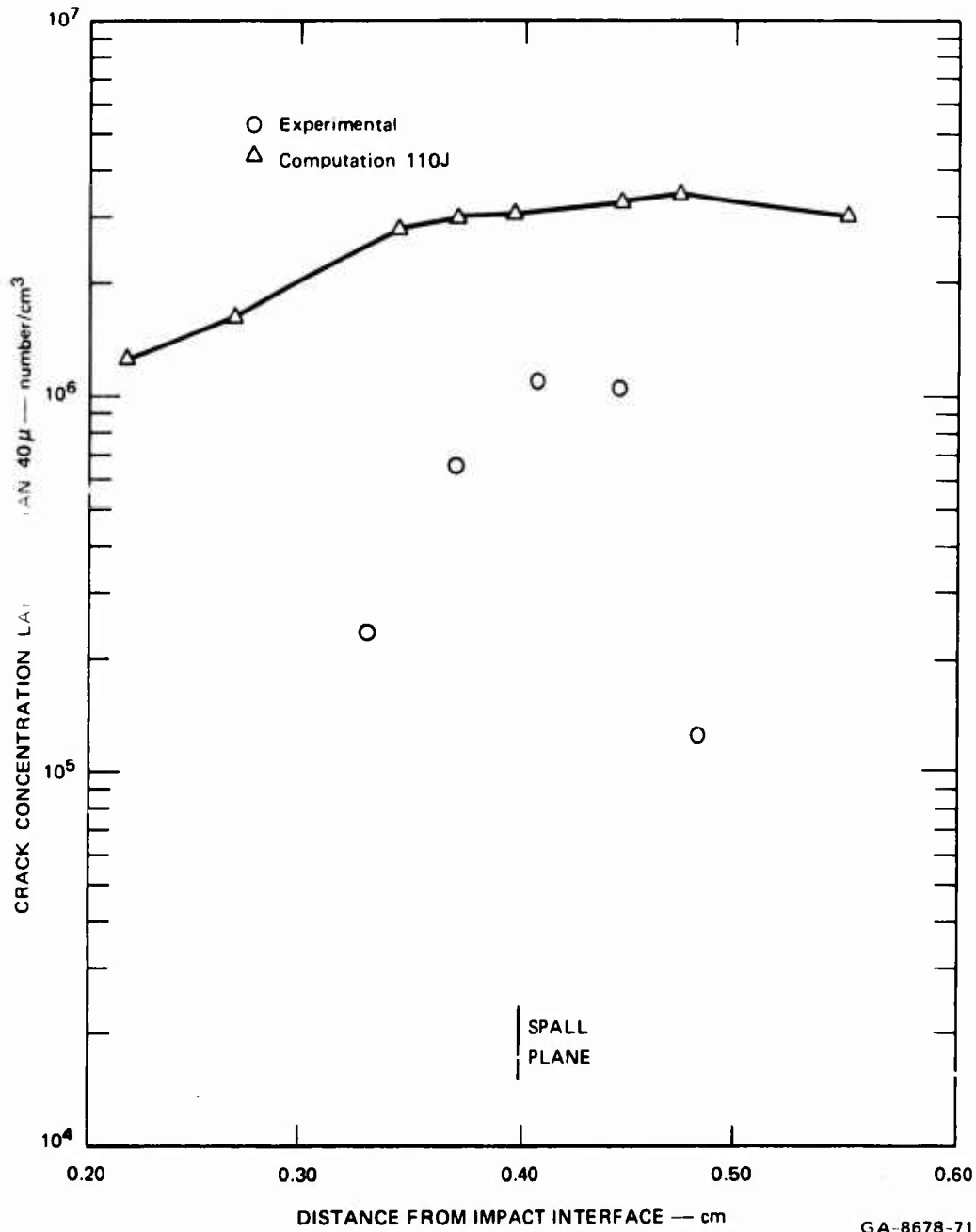
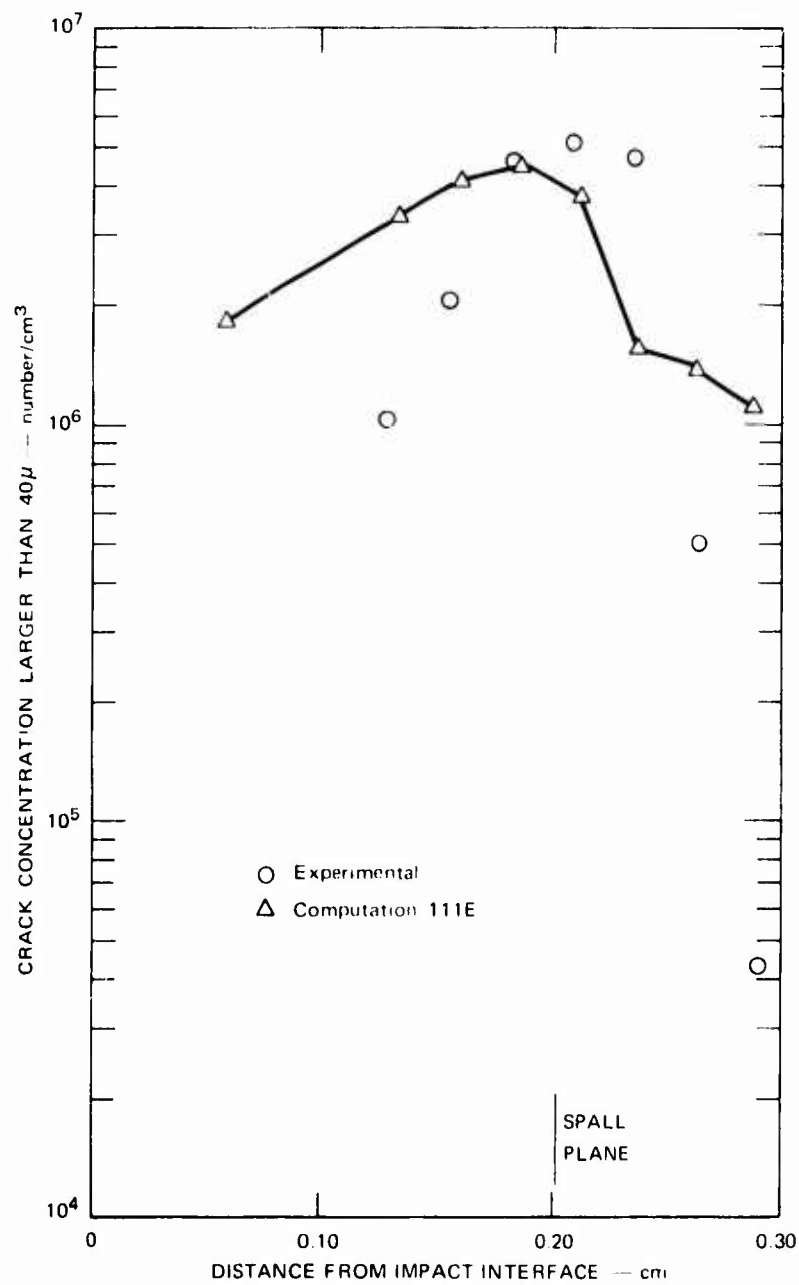


FIGURE 57 COMPARISON OF COMPUTED AND EXPERIMENTAL CONCENTRATIONS OF CRACKS LARGER THAN 40 MICRONS IN ARMCO IRON: SHOT 886



GA 8678-72

FIGURE 58 COMPARISON OF COMPUTED AND EXPERIMENTAL CONCENTRATIONS OF CRACKS LARGER THAN 40 MICRONS IN ARMCO IRON: SHOT S25

- Providing for interaction of cracks and thereby an increase in the effect on stress reduction.
- Modifying the constitutive relations to show more stress reduction for a given crack volume.

All these three are possible mechanisms for improving the fracture calculations.

A stress record was obtained from a manganin gage in a block of PMMA behind the Armco iron target on Shot S25. This record is compared in Figure 59 with stress histories from two computations. The poor comparison of the compressive pulses indicates possible inaccuracy

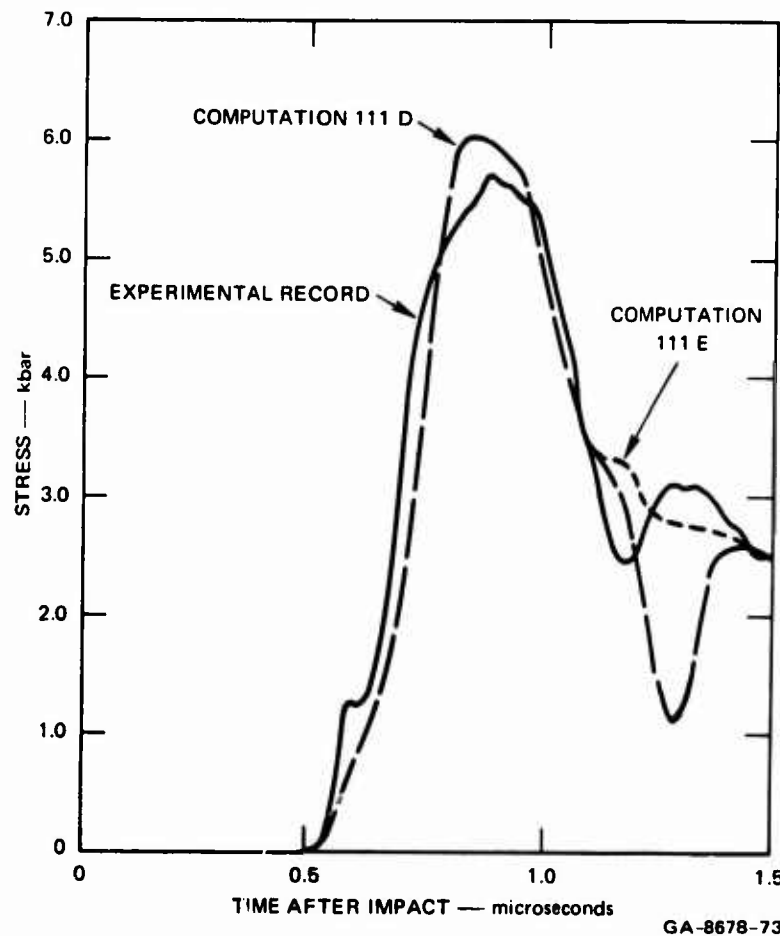


FIGURE 59 COMPARISON OF STRESS RECORD FROM MANGANIN GAGE WITH THE COMPUTED STRESS HISTORY FOR ARMCO IRON: SHOT S25

in the equation of state of the Armco iron and also in that of the PMMA. The region of interest in the figure is the so-called "spall signal," the hump following the main compressive pulse. Although the computed damage from the two calculations shown was similar, the stress histories appear different. Furthermore, these histories appear to bracket the experimental record, suggesting that with a few more trials good agreement could be obtained between computed and experimental stresses.

The foregoing initial results with the brittle fracture calculations have been encouraging. They give some hope of providing a means for gaining a detailed understanding of nucleation and growth. The nucleation function appears to have an appropriate form.

A study of the computed distributions has already led to more understanding of the nucleation and growth process. In our trial calculations it was noticed that the shape of the distribution was at least somewhat dependent on the shape of the rising portion of the tensile wave. New groups of cracks are nucleated at each time increment after the threshold stress is exceeded. Thus the number of all the larger cracks is determined early in the fracture process. The subsequent stress history merely allows the cracks to grow. To make the crack size distribution less dependent on the rise of the stress wave, it may be advisable to allow for nucleation of a distribution of cracks. Thus at each time step, cracks of various sizes would be nucleated.

A residual crack volume associated with plastic flow about the crack should be provided in the calculations. This will require a minor change in the present volume formula and the addition of an array to store the residual crack opening.

From the comparisons of computed and experimental results, we conclude that an acceptable initial model has been developed. Modifications to the model--nucleation of a distribution of cracks, computation

of the contribution of plastic flow to crack volume, and improvements in the constitutive relations--will lead to more accurate results.

#### 5. SUMMARY OF BRITTLE FRACTURE

The results of a study of the dynamic fracture of brittle materials have been presented. As described in the introduction, the main components of this approach are:

- To load dynamically and recover usable specimens.
- To achieve experimental control so that damage can be arrested in different stages of growth.
- To measure quantitatively the size and spatial distribution of damage in the volume of the material.
- To specify the macroscopic stress and its duration at any point in the sample under conditions of damage nucleation and growth.
- To use the results of these steps to develop a dynamic fracture model that includes the effects of developing damage on the local stress states.

The first two of these steps have been fully developed and applied to Armco iron and LASL graphite. The third step has been developed to the state where it can be applied to the brittle metals in which statistical distributions of cracks are formed. Step four has been attempted, but the results are considered as only a first approximation and further work is necessary. Step five has also been carried through and a computer program developed (BFRACT), which yields prediction of brittle damage which can be compared with experimental results.

The basic result of this effort is that a predictive capability for the dynamic fracture of brittle materials has been developed and compared with experiment. The agreement between theory and experiment is encouraging, but further work is necessary before a fully verified

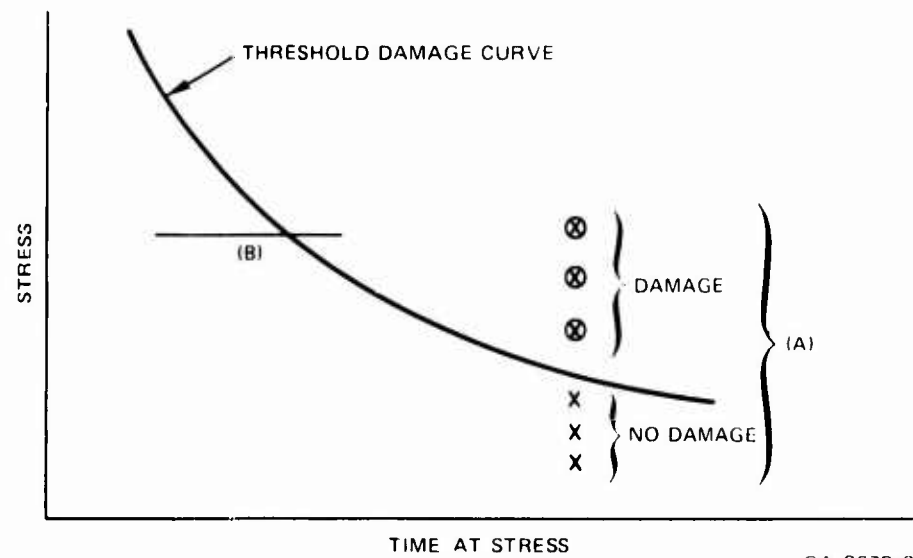


model is formulated. The primary problem, at present, is in describing the effects of developing damage on the local stress and the subsequently formed damage. Further, more complete data on the dependence of the nucleation and growth functions on material properties are necessary before any systematic evaluation of the important material parameters can be developed.

APPENDIX I

TAPERED FLYER TECHNIQUE

The study of the dynamic fracture of metals has shown that the damage level achieved in a given material is a function of both the tensile stress and its time duration. This is best seen in Figure 60, which is a schematic representation of the time dependence of the stress threshold for dynamic fracture.



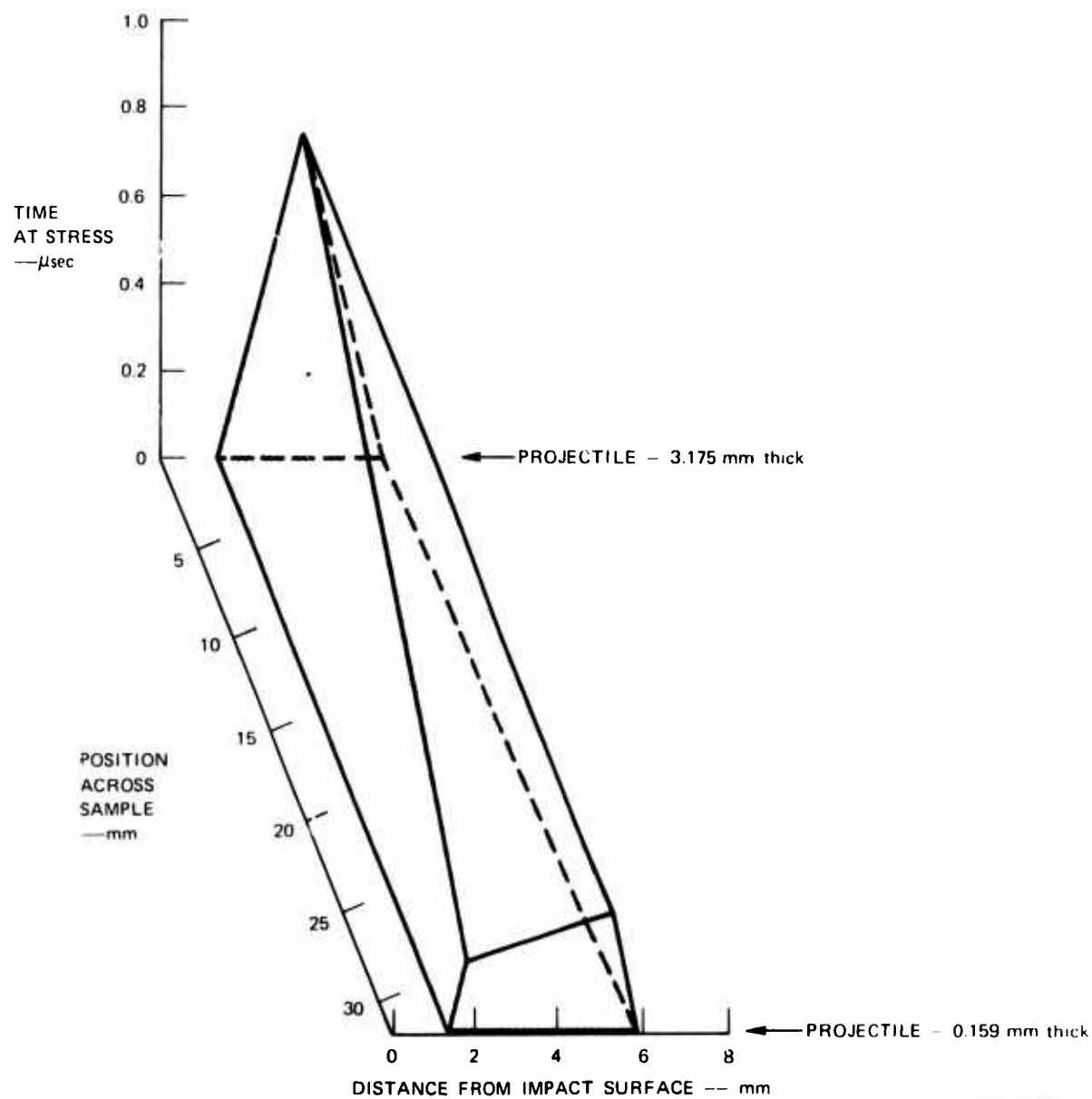
GA 8678 9

FIGURE 60 SCHEMATIC CURVE SHOWING THE TIME DEPENDENCE OF THE STRESS FOR THRESHOLD DAMAGE. Region A shows the number of experiments necessary to define a damage threshold if standard techniques are used. Region B shows that in a single experiment using a tapered flyer, the no-damage to damage transition can be spanned in a single experiment.

The points at (A) in this figure are representative of the typical method for determining dynamic fracture thresholds. Each point represents a separate experiment in which each sample must be sectioned and examined to determine whether fracture occurred. As one might suspect, the probability of achieving a given level of damage in an exploratory investigation is small. The line at (B) represents the conditions that can be achieved in a single experiment using a tapered projectile with a planar impact, a technique proposed by Butcher, et al (Ref. 59). The time at stress is controlled by the variation in the projectile thickness with position, resulting in a continuous variation in damage across the sample.

There are two problems in the use of this technique. First, reflection of a dilational shock wave at non-normal incidence from a planar surface causes the formation of a shear wave. The magnitude of this shear wave is small at small angles and has little or no effect on the experimental result if the yield strength of the material is large enough. This is apparently the case for all the material studied in this work. The second problem is that the magnitude of the principal stress is decreased upon reflection from a tilted surface. This effect is also small for small-tilt angles and has no effect in the experiments carried out on this program.

Figure 61 shows the time at stress in an Armco iron sample 6.313 mm thick, impacted with a projectile varying in thickness from 3.156 mm to 1.578 mm. The time at stress varies from approximately 0.74  $\mu$ sec at the thick end of the projectile to approximately 0.26  $\mu$ sec at the thin end of the projectile. The damage produced in such an experiment is shown in Figure 62. The damage plane is seen to follow the plane of maximum time at stress and to increase with increasing time at stress. As is obvious, essentially any damage level can be observed by this method, and accurate damage curves can be determined.



GA-8678 10

FIGURE 61 TIME AT STRESS AS A FUNCTION OF POSITION IN A SAMPLE IMPACTED WITH A TAPERED FLYER: SHOT S1. The time at stress is vertical; the position in the sample thickness is given on the horizontal axis. The position across the sample is given by the third axis.



FIGURE 62 DAMAGE OBSERVED IN SHOT S1, A TAPERED FLYER SHOT ON ARMCO IRON

## APPENDIX II

### OTHER EXPERIMENTAL TECHNIQUES

Spallation experiments were performed on the selected materials in the as-received condition. Projectile and target plates of each material were usually machined out of large samples (~48 in. x ~48 in. x ~1-1/2 in.) obtained from suppliers. Care was taken during machining to prevent local heating from occurring in the specimens. Projectile plates were commonly 2-7/16-in.-diameter flat plates of different thicknesses and with a surface finish of 0.0002-in. rms and parallel to within 0.0005 in. Flatness and parallelism of targets were maintained to 0.0005 in. The experimental arrangement is shown in Figure 63. The usable target area for spall observations equals the projectile area less the area influenced by edge effects.

The experiments were designed in such a way that the projectile was stopped at impact. This eliminated any secondary impacts that might have occurred between the target plate and the ensuing projectile. (Secondary impacts of the target specimen are undesirable since they might alter the damage caused by the primary impact.) The average tilt at impact using the experimental system shown in Figure 63 was 750  $\mu$ rad, as determined by a set of tilt pins installed in each target plate.

To minimize the edge effects and to facilitate the recovery of the target specimen, we used a tapered plug design. For uninstrumented recovery experiments the center region (covering an area of 1-1/2 in. diameter) of the 4-in.-diameter target plate was cut out at an angle of about  $8^\circ$  with the normal in such a way that the smaller diameter was on the impact side of the target (Figure 63). Only the outer portion or

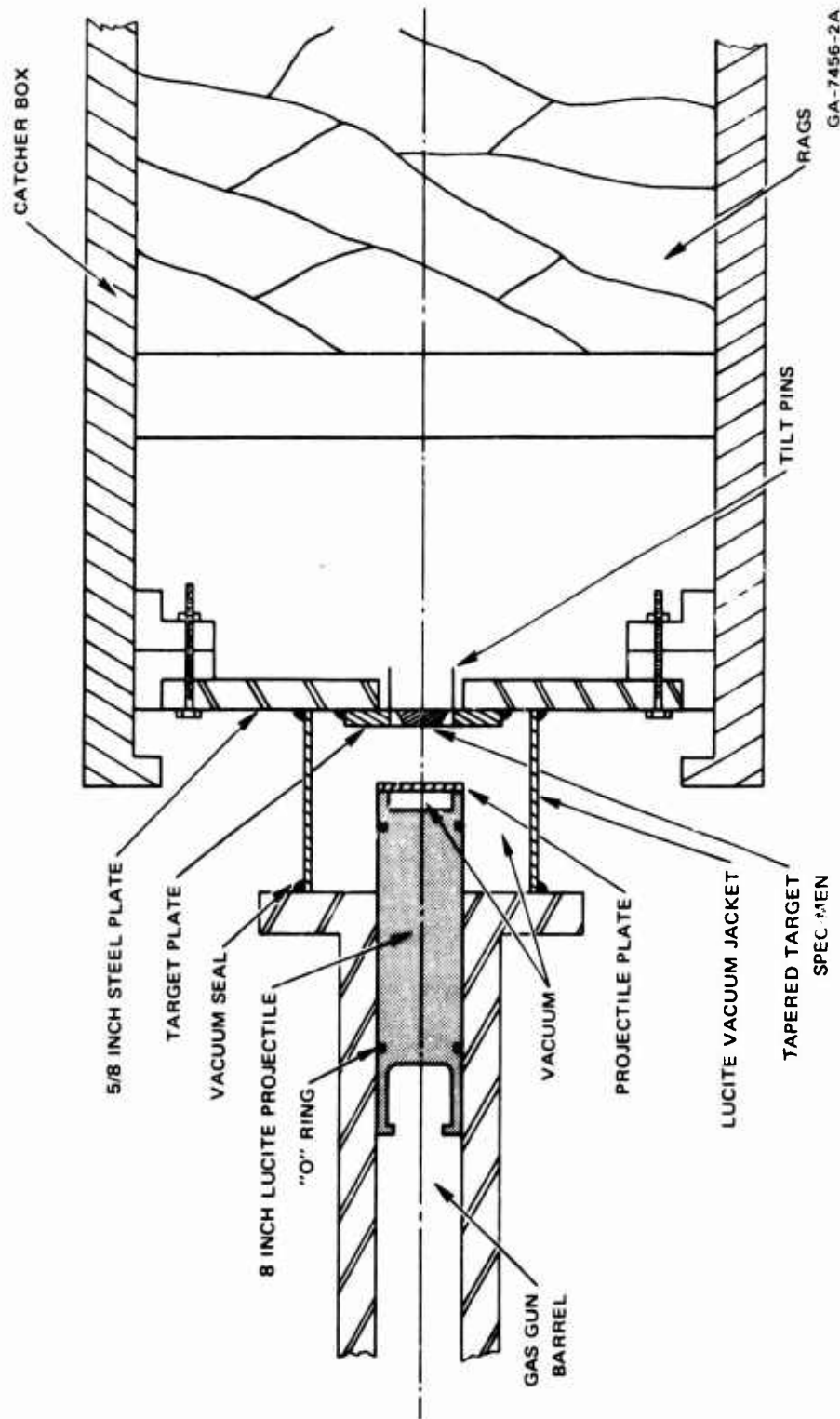


FIGURE 63 EXPERIMENTAL SYSTEM FOR DYNAMIC FLYER PLATE EXPERIMENTS

retaining ring was kept, and a new tapered plug was machined to fit precisely into the center of the retaining ring (see Figure 64). Two configurations were used for instrumented recovery experiments. In the earlier recovery experiments the 4-in.-diameter target plate contained a 1-in.-diameter tapered plug on one side of its center and a manganin-in-C7-epoxy<sup>\*</sup> pressure transducer on optical prism on the other (see Figure 64). During the shock experiment only the plug was recovered for subsequent metallographic observations. For later experiments it was realized that the stress record should correspond with the damage in the plug. Therefore the manganin-in-C7-epoxy gage was mounted directly behind the 1½-in-diameter plug.

For those experiments instrumented with the manganin pressure transducer, a manganin-in-C7-epoxy gage was mounted to the back of the 4-in.-diameter target plate. The manganin wire element (~0.6%) was situated approximately 0.080 in. from the target-plate/C7-epoxy interface. Since the Hugoniot of the target plate materials and the C7 epoxy are known, the shock wave profile at the target-C7 interface can be obtained from that recorded by the manganin-in-C7 gage behind the target. However, the effect of wave interactions must be taken into consideration if the exact wave shape at the target-C7 interface is to be obtained. For the present study, it was found that the manganin-in-C7 gage could detect reliably the spall signal originating within the target plate.

All samples recovered from these dynamic flyer plate experiments were sectioned in half. One of the exposed surfaces was then ground to remove the layer of material influenced by the sectioning process. The surface was polished and in some cases chemically etched with suitable etchants and then examined at various magnifications from 8x to 1000x.

---

\* Trademark, Acrylic resin produced by Du Pont.



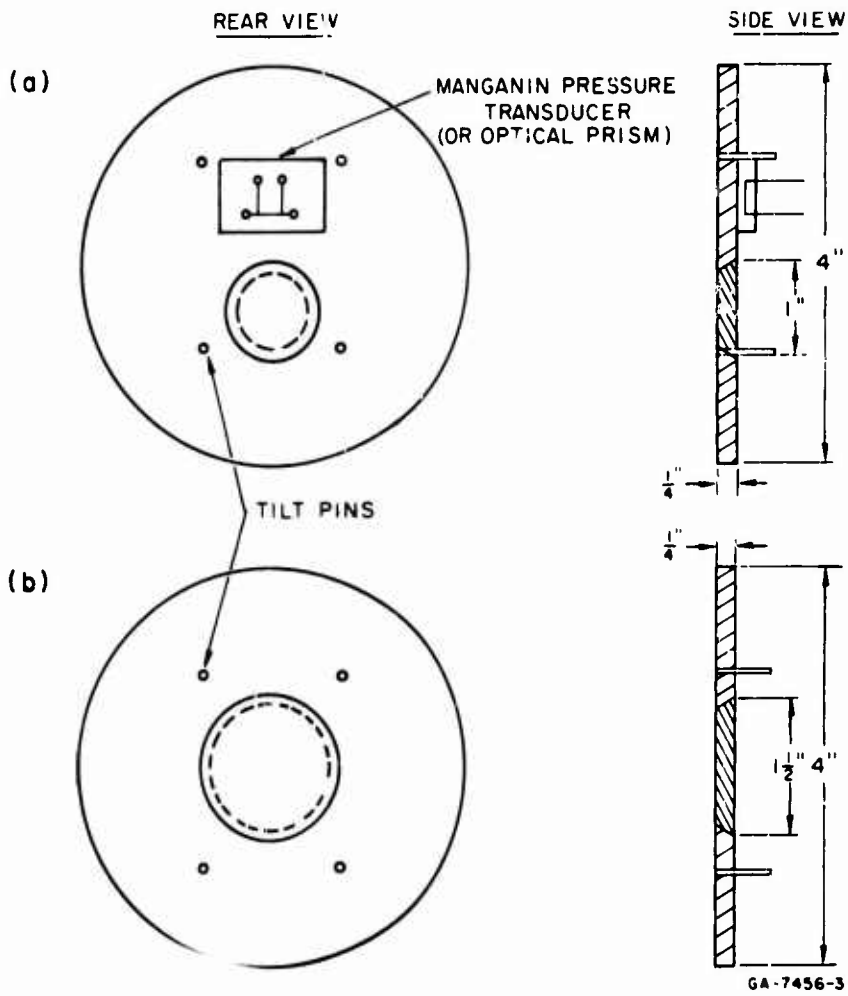


FIGURE 64

PLATE ASSEMBLY SHOWING TAPERED SPECIMEN

(a) Instrumented assembly; (b) Uninstrumented assembly.

### APPENDIX III

#### DYNAMIC SPHERICAL BUBBLE GROWTH

As a guide in measuring the growth rate of voids in ductile material undergoing fracture, a study was made of the growth of a bubble in a spherically-symmetric stress field. The material is assumed to be viscous above the yield strength, elastic below. First, a general equation for bubble growth is derived. Then this equation is solved approximately in several ranges of  $R$ , the bubble radius. A numerical solution is then introduced for the full range of  $R$ . These numerical results lead to appropriate forms for the growth rate relationship.

#### 1. DERIVATION OF DIFFERENTIAL EQUATION GOVERNING GROWTH

The equation for the expansion of a cavity in a plastic-viscous material is derived by the method of Poritsky (Ref. 43). At the boundary of the cavity the radial stress is

$$\sigma_r = -p - \frac{2}{3} Y + 2\eta \dot{e}_r \quad (59)$$

where

- $p$  = pressure (positive in compression)
- $Y$  = yield strength (positive in tension)
- $\dot{e}_r$  = the radial strain rate and is equal to the plastic strain rate by assumption.
- $\eta$  = the coefficient of viscosity

Here we have assumed that sufficient deformation has occurred that the yield strength was exceeded.

In Poritsky's approach the equations of motion are reduced to an equation at the cavity boundary. Therefore, the behavior of the entire flow field must be represented by the behavior at this boundary. For this reason the threshold pressure  $2Y/3$  should be reinterpreted. This threshold is the pressure at which yielding occurs. True, it does occur at the boundary at  $2Y/3$  but not throughout the material surrounding the void (See Appendix IV for the threshold pressure in spherical flow). Therefore, the threshold pressure is taken here as  $p_0$ , which is a function of the yield strength. Equation (59) is then

$$\sigma_r = -p - p_0 + 2\eta \dot{e}_r \quad (59')$$

According to Poritsky's derivation,

$$\dot{e}_r = -2 \frac{\dot{R}}{R} \quad (60)$$

Then

$$\sigma_r = -p - p_0 - 4\eta \frac{\dot{R}}{R} \quad (61)$$

However, since there is no internal pressure in the bubble,

$$p = -p_0 - 4\eta \frac{\dot{R}}{R} \quad (62)$$

This expression for  $p$  is then inserted in the general expression for void growth,

$$\frac{p}{\rho} = \frac{p_{\infty}}{\rho} + R \ddot{R} + \frac{3}{2} (\dot{R})^2 + \frac{2\sigma_s}{R\rho} \quad (63)$$

where

$\sigma_s$  = surface tension

$p_{\infty}$  = the pressure at infinity

Equation (63) was obtained from a comparison of Eq. (6) of Bornhorst and Hatsopoulos (Ref. 44) with Eqs. (23) and (25) of Poritsky. With the value of  $p$  from Eq. (62) in Eq. (63), the growth equation becomes

$$\ddot{R} + \frac{4\eta}{\rho R^2} \dot{R} + \frac{3}{2R} (\dot{R})^2 + \frac{2\sigma_s}{R^2 \rho} = \frac{T - p_0}{\rho R} \quad (64)$$

where  $T$ , the applied tension, has replaced  $-p_{\infty}$ . For discussion and the numerical solution, the differential equation is rewritten as

$$\ddot{R} + B\dot{R} + D\dot{R}^2 = C \quad (65)$$

where

$$B = \frac{4\eta}{\rho R^2}$$

$$C = \frac{T - p_0}{\rho R} - \frac{2\sigma_s}{\rho R^2}$$

$$D = \frac{3}{2R}$$

For consistency with the assumptions used in setting up the equation,  $T$  cannot be allowed to decrease below  $p_0$  for tensile loading. For

smaller tensile loads, the behavior is elastic and therefore not accounted for in our basic differential equation. To account for compressive loading, the sign of the yield strength must be changed, and T must again exceed  $p_0$ .

## 2. ANALYTICAL SOLUTION FOR SMALL RADIUS

For small radii, the inertial terms,  $\ddot{R}$  and  $\dot{R}^2$ , may be approximated. The growth rate  $\dot{R}$  is expanded in a series in R as follows

$$\dot{R} = A_0 + A_1 R + A_2 R^2 \dots \quad (66)$$

Then the inertial terms are derived from the expansion.

$$\ddot{R} = (A_1 + 2A_2 R \dots) \dot{R}$$

$$\dot{R}^2 = (A_0 + A_1 R + A_2 R^2 \dots) \dot{R}$$

Then let  $A = (T - p_0)/4\eta$  and the  $\dot{R}$  is given by Eq. (64) as

$$\dot{R} \left[ 1 + \frac{\rho R^2}{4\eta} (A_1 + 2A_2 R \dots) + \frac{3\rho}{8\eta} R (A_0 + A_1 R \dots) \right] = A_0 + AR$$

When  $\dot{R}$  is replaced by its expansion in R, and coefficients of each term in R equated to zero, the coefficients are determined as follows:

$$A_0 = -\frac{\sigma}{2\eta}$$

$$A_1 = A - \frac{3\rho}{8\eta} A_0^2$$

$$\begin{aligned}
A_2 &= -\frac{\rho}{\eta} A_0 A_1 \\
A_3 &= -\frac{5\rho}{4\eta} (A_0 A_2 + \frac{1}{2} A_1^2) \\
A_4 &= -\frac{3\rho}{2\eta} (A_0 A_3 + A_1 A_2) \\
A_5 &= -\frac{7\rho}{4\eta} (A_0 A_4 + A_1 A_3 + \frac{1}{2} A_2^2)
\end{aligned}
\tag{67}$$

Usually the surface tension will provide a very small effect so that only odd powers of  $R$  will contribute significantly. If we neglect  $A_0$ , these terms are

$$\begin{aligned}
A_1 &= A \\
A_3 &= -\frac{5\rho}{8\eta} A^2 \\
A_5 &= \frac{35}{32} \frac{\sigma^2}{\eta^2} A^3
\end{aligned}$$

From these coefficients we can estimate the point where the growth rate can no longer be approximated by  $A_0 + A_1 R$ . That point will occur when

$$r = \frac{A_3 R^3}{A_1 R} = -\frac{5\rho}{8\eta} AR^2$$

is no longer negligible. Then the critical radius is

$$R_{cr}^2 = \frac{1.6r\eta}{\rho A} = \frac{6.4r\eta^2}{\rho(T - p_0)} \quad (68)$$

Then  $R_{cr}$  is about 5 microns for aluminum for which  $\eta = 200$  poise,  $\rho = 2.7 \text{ gm/cm}^3$ ,  $T = 10 \text{ kbar}$ ,  $p = 2 \text{ kbar}$ , and  $r = 0.02$ .

### 3. ANALYTICAL SOLUTION FOR LARGE RADIUS

Equation (64) can also be solved for large  $R$  by treating the viscous term approximately. The equation becomes

$$\dot{R} + \frac{3}{2R} \dot{R}^2 = \frac{T - p_0}{\rho R} - \frac{4\eta}{\rho R^2} \dot{R} \quad (69)$$

Multiply each term by  $2R^3 \dot{R}$ , and combine the first two:

$$\frac{d}{dt} (R^3 \dot{R}) = \frac{2}{3} \frac{T - p_0}{\rho} 3R^2 \dot{R} - \frac{8\eta}{\rho} R \dot{R}^2$$

Then we seek a solution of the form

$$\dot{R} = \beta + \frac{a_1}{R} + \frac{a_2}{R^2} \quad (70)$$

where

$$\beta^2 = \frac{2}{3} \frac{T - p_0}{\rho}$$

For the integration of Eq. (69), replace one of the  $\dot{R}$  values of the last term by the series, Eq. (70). Then integrate and divide by  $R^3$  obtaining

$$\dot{R}^2 = \beta^2 - \frac{4\eta\beta}{\rho R} - \frac{8\eta a_1}{\rho R^2} - \frac{8\eta a_2}{\rho R^3} \ln R \dots$$

The terms in this series are compared with those in the square of Eq. (70) to evaluate  $a_1$  and  $a_2$ .

Then

$$a_1 = -\frac{2\eta}{\rho}$$

$$a_2 = \frac{6\eta^2}{\beta\rho^2}$$

The alternating signs suggest an exponential series that may be approximated as

$$\dot{R} = \beta e^{-2\eta/(\rho R\beta)} \quad (71)$$

Comparison of the third term in the exponential,  $2\eta^2/(\rho^2 R^2 \beta^2)$ , with the second term indicates the range of validity of this solution. Let the ratio of successive terms be as before. Then

$$r = \frac{2\eta^2/(\rho^2 R^2 \beta^2)}{2\eta/(\rho R\beta)} = \frac{\eta}{\rho R\beta}$$

Thus the critical radius is, for  $r = 0.02$



$$R_{cr} = \frac{\eta}{0.02\rho\beta} \quad (72)$$

For the aluminum with  $\eta = 200$  poise,  $T = 10$  kbar,  $p_0 = 2$  kbar,  $Y = 3$  kbar, the minimum radius should be about 800 microns. Actually, as demonstrated later, Eq. (71) appears to be correct down to about 100 microns.

#### 4. NUMERICAL SOLUTION

Returning to Eq. (65), we rewrite it as

$$\frac{dV}{DV^2 + BV - C} = -dt \quad (73)$$

where  $V$  replaces  $\dot{R}$ . This equation will now be integrated analytically for a short time increment  $\Delta t$  in which the radius will undergo only a slight change.

$$V = \frac{(B + \delta) C_0 e^{-\delta\Delta t} + \delta - B}{2D(1 - C_0 e^{-\delta\Delta t})} \quad (74)$$

where

$$C_0 = \frac{2DV_0 + B - \delta}{2DV_0 + B + \delta}$$

$$\delta = (B^2 + 4CD)^{1/2}$$

and  $V_0$  is the velocity at the beginning of the time increment. The velocity is evaluated at the end of the increment so that the appropriate radius to use in evaluating A, B, and D is the final radius. Since the final radius depends on the velocity, the coefficients and the velocity are determined by iteration.

A small time-share computer program was written to integrate Eq. (73). It was found that three or four iterations were required to make successive velocities agree to 0.1 percent and that time increments must be controlled so that the radius does not increase more than 10 percent in each step. With these controls the velocity and radius were computed to 0.02 percent.

A sample of the velocity computations is shown in Figure 65 for aluminum at 10 kbar. The results of the analytical expressions, Eqs. (67) and (70) are shown for comparison.

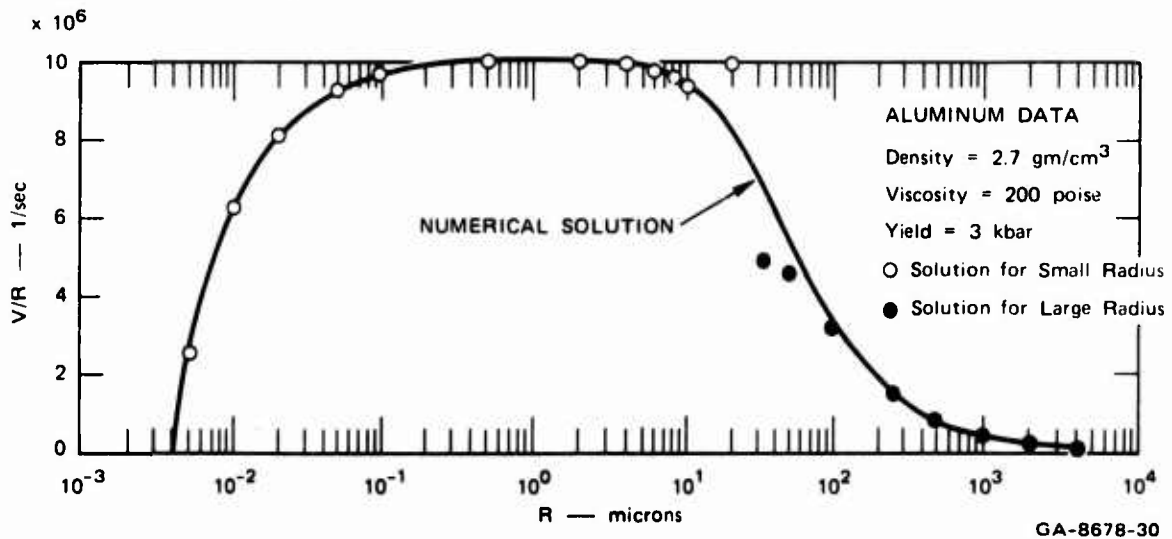
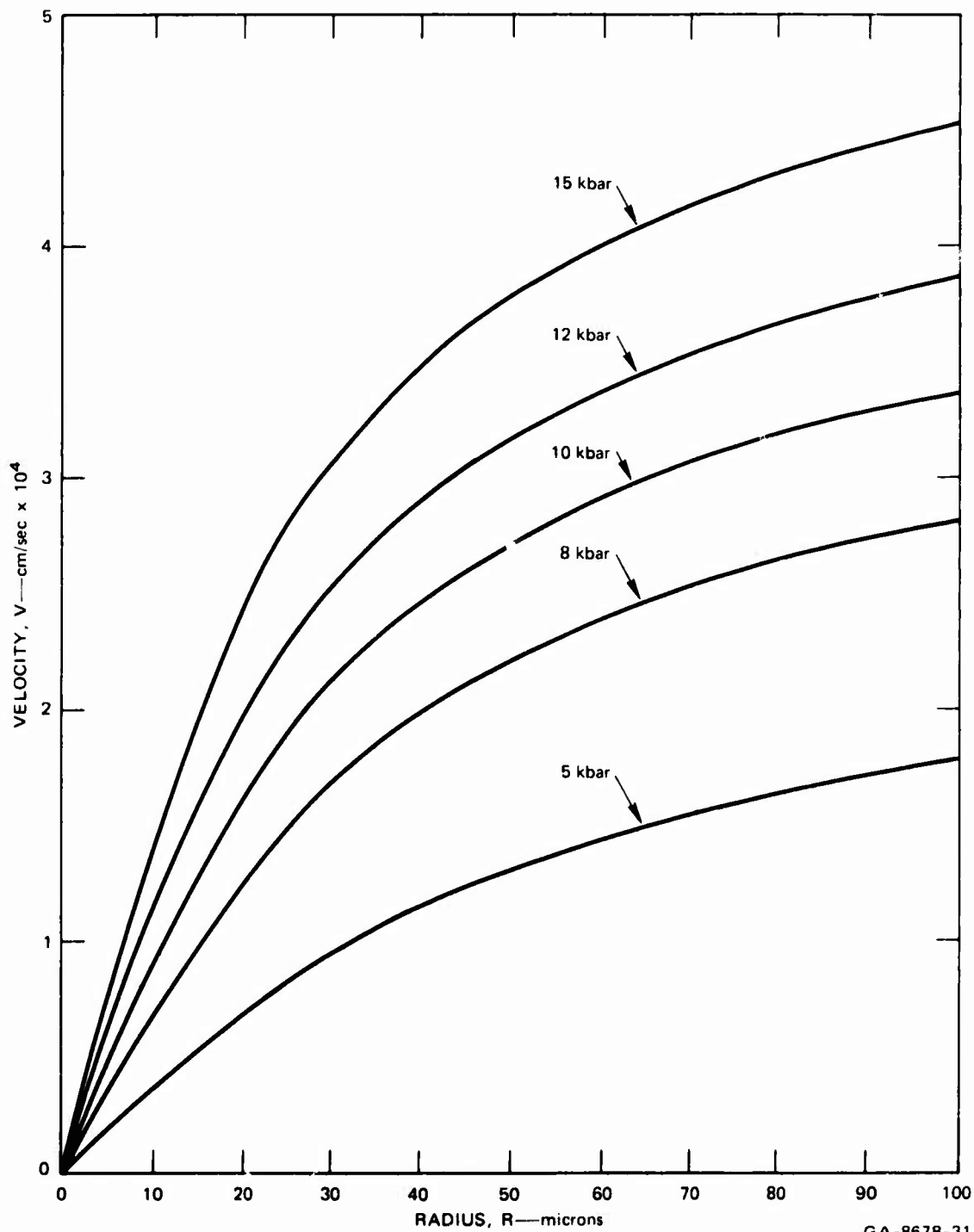


FIGURE 65 GROWTH VELOCITY OF A VOID AS A FUNCTION OF VOID RADIUS: COMPARISON OF NUMERICAL AND ANALYTICAL RESULTS FOR A TENSILE STRESS OF 10 kbar

A series of computations at different stress levels led to the curves in Figure 66. Here it is apparent that at small R the velocity is linearly related to R. Because of the general appearance of the curves, they were fitted with a parabola of the form  $V = A_1 R + A_2 R^2$ . It was found that both  $A_1$  and  $A_2$  were linear in stress so that the velocity is related to stress as

$$V = (a_1 R + a_2 R^2) (T - p_0) \quad (75)$$

where  $a_1$  and  $a_2$  are functions of viscosity and density only. This form appears to be appropriate for some range of radius beyond the solution for small radius (Eq. 67). The upper limit of applicability was not investigated.



GA-8678-31

FIGURE 66 RELATIONSHIP BETWEEN VELOCITY AND VOID RADIUS AS A FUNCTION OF STRESS LEVEL

NOMENCLATURE FOR APPENDIX III

- A  $(T - \frac{2}{3} Y)/4\eta$ , 1/sec
- $A_i$  coefficients in an expansion for  $\dot{R}$ ,  $\text{cm}^{1-i}/\text{sec}$
- B  $4\eta/\rho R^2$ , 1/sec
- C  $(T - \frac{2}{3} Y)/\rho R - 2\sigma_s/\rho R^2$ ,  $\text{cm}/\text{sec}^2$
- $C_0$   $(2DV_0 + B - \delta)/(2DV_0 + B + \delta)$
- D  $3/2R$ , 1/cm
- R radius of void, cm
- T applied tension,  $\text{dyn}/\text{cm}^2$
- V velocity of void growth, cm/sec
- $V_0$  initial velocity of void growth, cm/sec
- Y yield strength,  $\text{dyn}/\text{cm}^2$
- $a_i$  coefficients in expansions for  $\dot{R}$
- $\dot{\epsilon}_r$  radial strain rate, 1/sec
- p pressure,  $\text{dyn}/\text{cm}^2$
- $p_0$  threshold pressure,  $\text{dyn}/\text{cm}^2$
- $p_\infty$  pressure at infinity,  $\text{dyn}/\text{cm}^2$
- r ratio of successive terms in expansion for  $\dot{R}$
- $\beta$   $\left[ \frac{2}{3} \cdot \left( T - \frac{2}{3} Y \right) / \rho \right]^{1/2}$ , a loading parameter, cm/sec
- $\delta$   $(B^2 + 4CD)^{1/2}$ ,  $1/\text{sec}^2$

$\eta$  material viscosity, dyn-sec/cm<sup>2</sup>

$\rho$  density, gm/cm<sup>3</sup>

$\sigma_r$  radial stress, dyn/cm<sup>2</sup>

$\sigma_s$  surface tension, dyn/cm

## APPENDIX IV

### STATIC SPHERICAL GROWTH OF VOIDS

To aid in understanding the fracture of ductile materials by void growth, a brief investigation was made of the growth of a spherical cavity in a spherically symmetric tensile field. By a reversal of the sign of loading, the solution describes the collapse of voids in a porous material in a compressive field. This appendix provides an estimate of the threshold stress for rapid growth of voids in tension, and stress-volume paths for porous material in tension or compression.

The stress-strain relationship of a material containing spherical voids has been recognized as important in estimating the behavior of porous material, although the pores may only roughly approximate spheres. The decreased elastic stiffness of material with voids has been studied by MacKenzie (Ref. 5), by Hashin (Ref. 45), and by many others. The growth of the void in plastic material has been considered by Hill (Ref. 46). Recently it was realized (Refs. 4 and 12) that ductile materials fail by a process of void growth; hence they behave as porous materials during fracturing.

Three static analyses are conducted to study the behavior of porous material: (1) void growth under external tension, (2) void collapse under external compression, and (3) void growth under internal pressure. For all three analyses, the material is assumed to be elastic and perfectly plastic, the loading is quasi-static, and the geometry is spherically symmetric.

## 1. EXTERNAL TENSION PROBLEM

An external tension is gradually applied symmetrically to a medium with a spherical void of initial radius  $a_0$ . Before yielding begins, there is some displacement of the void boundary. This void displacement is derived from the general elastic expression (Ref. 47) for displacement  $u$  at any radius.

$$u = \frac{r\sigma_0}{3K} + \frac{\sigma_0 - \sigma_i}{4\mu r^2} r_i^3 \quad (76)$$

where

$\sigma_0$  = external applied stress (positive in tension)

$\sigma_i$  = internal stress

$r_i$  = internal radius

$K, \mu$  = bulk and shear moduli of the solid material

Then at  $r = a$ ,  $u$  is  $da$ , and Eq. (76) is rewritten on a differential basis.

$$\frac{da}{a} = d\sigma_0 \left( \frac{1}{3K} + \frac{1}{4\mu} \right) = \frac{\Gamma}{3K} d\sigma_0 \quad (77)$$

where  $\Gamma = 1 + 3K/(4\mu)$ . On integrating, this expression becomes

$$a = a_0 \exp [\Gamma\sigma_0/(3K)] \quad (78)$$

Yielding first occurs at the void surface and then continues outward with increasing load; the phenomena are similar to those following loading



with an internal pressure. In the elastic region ( $r > c$ ,  $c$  = elastic-plastic interface as in Figure 67), the radial and circumferential stresses are

$$\sigma_r = \sigma_c c^3/r^3 + \sigma_0(1 - c^3/r^3) \quad (79)$$

$$\sigma_\theta = -\frac{1}{2} \sigma_c c^3/r^3 + \frac{1}{2} \sigma_0(2 + c^3/r^3) \quad (79')$$

where  $\sigma_c$  is the radial stress at  $r = c$ .

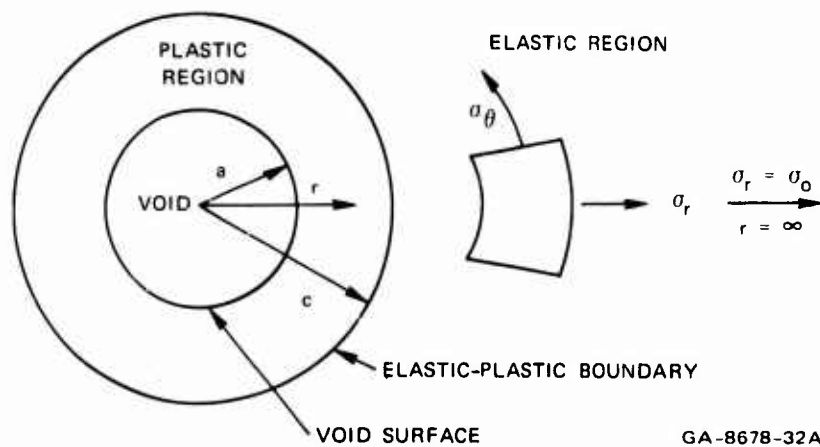


FIGURE 67 GEOMETRY AND NOMENCLATURE FOR SPHERICAL VOID

For yielding to occur at  $r = c$ , it is necessary that  $\sigma_\theta - \sigma_r = Y$  and hence that

$$\sigma_c = \sigma_0 - \frac{2}{3} Y \quad (80)$$

Evidently  $\sigma_0 = 2Y/3$  at first yielding when  $\sigma_c = \sigma_a = 0$ . In the plastic region, the equation of equilibrium for the radial direction is

$$\frac{\partial \sigma_r}{\partial r} = 2 \frac{\sigma_\theta - \sigma_r}{r} = \frac{2Y}{r} \quad (81)$$

The integral of this expression leads to

$$\sigma_r = 2Y \ln \left( \frac{r}{a} \right) \quad (82)$$

$$\sigma_\theta = 2Y \ln \left( \frac{r}{a} \right) + Y \quad (83)$$

where  $a$  is the current void radius. Equating Eqs. (80) and (82) to find the radial stress on the elastic-plastic boundary, we find a relation between  $\sigma_0$  and variables in the plastic zone

$$\sigma_0 = \frac{2}{3} Y + 2Y \ln \left( \frac{c}{a} \right) \quad (84)$$

Determination of the motion of the void surface requires a solution of displacements in the plastic and elastic regions. From the elastic solution [Eqs. (76) and (80)], the outward displacement in the elastic region is

$$u = \frac{\sigma_0 r}{3K} + \frac{Yc^3}{6\mu r} \quad (85)$$

The displacements in the plastic region, and hence of the void surface, are determined in two steps, following the method of Hill (Ref. 46). First a relation is found between the displacement at any point in the plastic region and the displacement of the void boundary. Differential motion is considered so that large deformations can be followed. Let

a differential displacement at any point,  $du$ , be proportional to  $da$ , the motion of the void.

$$du = v da \quad (86)$$

where  $v$  is a proportionality factor. Following Hill (Ref. 46), this relation is inserted into the expression relating compressibility and average stress. The three principal strains and stresses are:

$$d\epsilon_r = \frac{\lambda}{\partial r} (du) = \frac{\lambda v}{\partial r} da \quad (87)$$

$$d\epsilon_\theta = d\epsilon_\varphi = \frac{du}{r} = \frac{v da}{r} \quad (88)$$

$$d\sigma_r = \frac{\partial \sigma_r}{\partial a} da + \frac{\partial \sigma_r}{\partial r} dr = \left( \frac{\partial \sigma_r}{\partial a} + v \frac{\partial \sigma_r}{\partial r} \right) da \quad (89)$$

$$d\sigma_\theta = d\sigma_\varphi = \left( \frac{\partial \sigma_\theta}{\partial a} + v \frac{\partial \sigma_\theta}{\partial r} \right) da \quad (90)$$

With these values for stress and strain the compressibility relation is:

$$\frac{\partial v}{\partial r} + \frac{2v}{r} = \frac{1}{3K} \left( \frac{\partial}{\partial a} + \frac{v \partial}{\partial r} \right) (\sigma_r + 2\sigma_\theta) \quad (91)$$

When Eqs. (82) and (83) are inserted in Eq. (91), the following differential equation for  $v$  is found:

$$\frac{\partial v}{\partial r} + (2 - 3\delta) \frac{v}{r} = - \frac{3\delta}{a} \quad (92)$$

where  $\delta = 2Y/3K$ .

With the condition that  $v = 1$  at  $r = a$ , the solution of Eq. (92) is

$$v = - \frac{\delta}{1 - \delta} \left( \frac{r}{a} \right) + \frac{1}{1 - \delta} \left( \frac{a}{r} \right)^{2-3\delta} \quad (93)$$

The second step in deriving the expression for displacement throughout the plastic region ( $a \leq r \leq c$ ) is to express that displacement as a function of the applied stress, the motion of the elastic-plastic boundary, and the radius, as follows:

$$du = \frac{\partial u}{\partial \sigma_0} d\sigma_0 + \frac{\partial u}{\partial c} dc + \frac{\partial u}{\partial r} dr = dr \quad (94)$$

At  $r = c$ , this expression is derived from Eq. (85):

$$du_c = dr_c = v_c da = \frac{c}{3K} d\sigma_0 + \frac{Y}{2\mu} dc + \left( \frac{\sigma_0}{3K} - \frac{Y}{3\mu} \right) dr_c \quad (95)$$

Then  $dr_c$ , the particle motion at  $r = c$ , is replaced by  $v_c da$ ;  $v_c$  is determined from Eq. (94) and  $c$  is eliminated with the aid of Eq. (84). The differential of  $c$  is also found from Eq. (84)

$$dc = \left( da + \frac{a}{2Y} d\sigma_0 \right) \exp \left[ \frac{\sigma_0}{2Y} - \frac{1}{3} \right] \quad (96)$$

For convenience the stress variable  $\sigma_0$  is replaced by  $\alpha$  where

$$\alpha = \frac{3\sigma_0}{2Y} - 1 \quad (97)$$

Then Eqs. (84) and (96) become

$$c = ae^{\alpha/3} \quad (84')$$

$$dc = \left( da + \frac{a}{3} d\alpha \right) e^{\alpha/3} \quad (96')$$

With these values for  $c$ ,  $dc$ , and  $\alpha$ , Eq. (95) becomes, after some rearranging

$$\frac{da}{a} = \frac{\frac{1}{3} \delta \Gamma (1 - \delta) e^{\alpha(1-\delta)} d\alpha}{\left[ 1 - \frac{\delta}{3} (\alpha + 3 - 2\Gamma) \right] - \delta \left[ \Gamma - \frac{\delta}{3} (\alpha + \Gamma) \right] e^{\alpha(1-\delta)}} \quad (98)$$

where  $\Gamma = 1 + 3K/(4\mu)$ . Equation (98) can be integrated approximately by neglecting the variations of the  $\alpha$ 's which are not in the arguments of the exponentials. Because each of these  $\alpha$ 's is multiplied by  $\delta$ , a small number, this approximate integration is satisfactory. To simplify the algebra of the integration, replace the denominator of the integrand on the right side of Eq. (98) by  $B - Ce^{\alpha(1-\delta)}$ . Then the integrated form is

$$\ln a \Big|_{a_1}^{a_2} = \frac{-\frac{1}{3} \Gamma}{\left[ \Gamma - \frac{\delta}{3} (\alpha + \Gamma) \right]} \ln \left[ B - Ce^{\alpha(1-\delta)} \right] \Big|_{\alpha_1}^{\alpha_2} \quad (99)$$

Let F be the coefficient of the logarithm. Then

$$\frac{a_2}{a_1} = \left[ \frac{B - Ce^{\alpha_2(1-\delta)}}{B - Ce^{\alpha_1(1-\delta)}} \right]^F \quad (100)$$

where

$$F = -\frac{1}{3} \frac{1}{1 - \frac{\delta}{3} (1 + \alpha/\Gamma)} = -[3 - \delta(1 + \alpha/\Gamma)]^{-1}$$

$$C = \delta \left[ \Gamma - \frac{\delta}{3} (\alpha + \Gamma) \right]$$

$$B = 1 - \frac{\delta}{3} (\alpha + 3 - 2\Gamma)$$

Equation (100) provides a relation between steps in stress  $\alpha$  and steps in the void radius during plastic flow. The displacement of the void boundary at the point of initial yielding is found from Eq. (76) for  $\sigma_0 = 2Y/3$

$$a_y = a_0 \exp [2\Gamma Y/(9K)] = a_0 \exp (\delta\Gamma/3) \quad (101)$$

The complete solution for the motion of the void boundary is obtained from the use of Eq. (101) once and then Eq. (100) for a large number of steps in stress. A void growth curve for aluminum calculated from these equations is shown in Figure 68 for a yield strength of 2 kbar. In addition, the trajectories of the elastic-plastic boundary and several initial radii are shown. There appears to be very little growth of the void until the stress reaches four or five times the yield strength. The response is reminiscent of an elastic-perfectly-plastic stress-strain curve. The

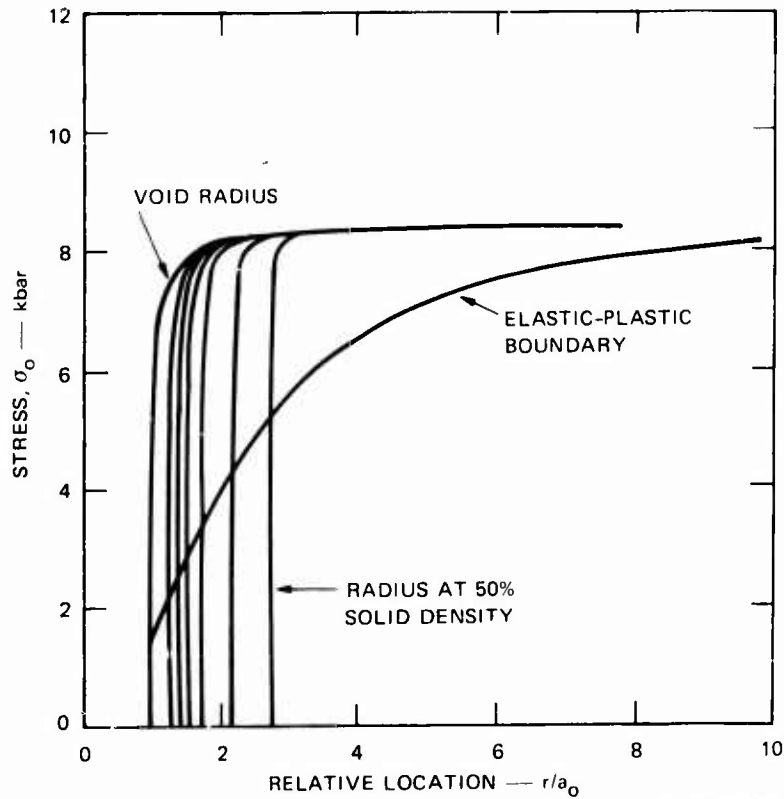


FIGURE 68 TRAJECTORY OF THE VOID RADIUS, ELASTIC-PLASTIC BOUNDARY, AND SELECTED RADII FOR TENSILE LOADING WHERE YIELD = 2 kbar

stress for which the void radius becomes infinite is found by equating the numerator of Eq. (100) to zero, that is,

$$B = C e^{\alpha_m (1-\delta)} \quad (102)$$

or,

$$\alpha_m = \frac{1}{1-\delta} \ln \frac{B}{C} = -\frac{1}{1-\delta} \ln \left\{ \frac{\Gamma \delta \left[ 1 - \frac{\delta}{3} \left( 1 + \frac{\alpha}{\Gamma} \right) \right]}{1 - \frac{\delta}{3} (\alpha + 3 - 2\Gamma)} \right\} \quad (103)$$

$$W = -\frac{1}{1-\delta} \ln (\Gamma \delta) \quad (103')$$

Because B and C are weak functions of  $\alpha_m$ , Eq. (103) is solved iteratively for  $\alpha_m$ . The limiting stress is then

$$\sigma_m = \frac{2}{3} Y(\alpha_m + 1) \quad (104)$$

The limiting stress for aluminum is graphed in Figure 69 as a function of the yield strength. If a stress larger than the limiting stress is applied, the response will be dynamic. The void size will be limited by rate-dependent mechanisms: viscosity, stress relaxation, inertia.

In a porous material under tension or compression, the flow around the void is not spherically symmetric. However, we expect that the bulk

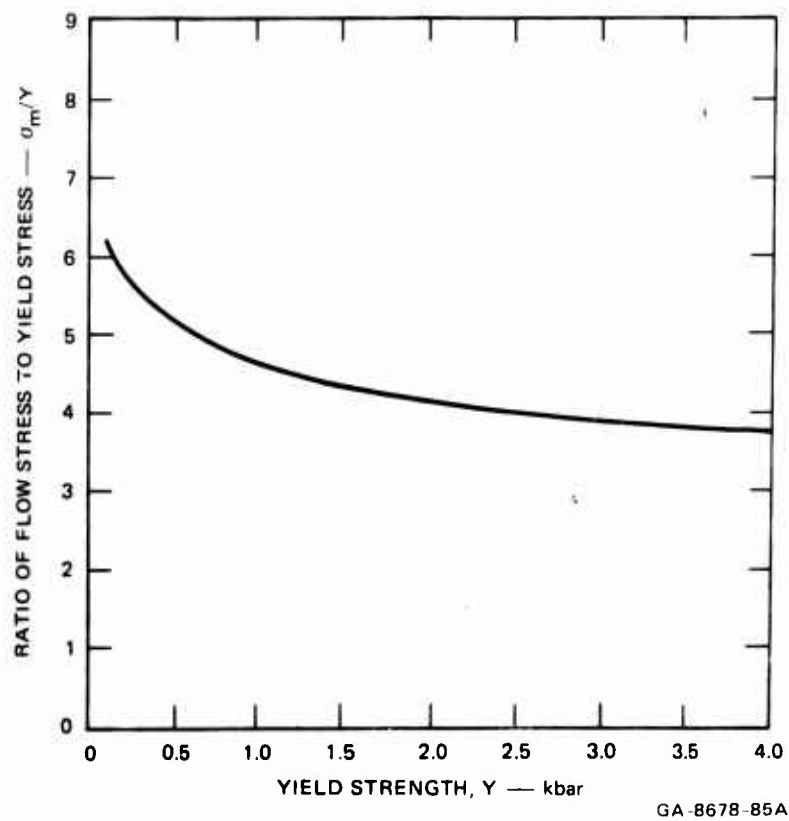


FIGURE 69 RELATIONSHIP BETWEEN FLOW STRESS AND YIELD STRENGTH IN TENSION



modulus for the spherically symmetric problem varies qualitatively similarly to the bulk modulus for the porous material. To determine the gross bulk modulus for a porous material, we selected for study a sphere of material containing a spherical void, that is, a sphere of known porosity. Then the coordinates of the sphere of material and the void were followed during the loading calculations to determine the variation of the bulk modulus. The bulk modulus, defined as the ratio of the change in stress to the volumetric strain, decreases when yielding occurs around the void; therefore the modulus is a function of yield strength. The modulus also varies as the void grows or diminishes and varies with porosity.

The displacements of the radii  $r$  were found from the following three equations, which were derived earlier:

Elastic at  $r$  and  $a$ :

$$du = \frac{rd\sigma_0}{3K} + \frac{a^3 d\sigma_0}{4\mu r^2} \quad (105)$$

Elastic at  $r$ , plastic at  $a$ :

$$du = \frac{rd\sigma_0}{3K} + \frac{Y_c^2 dc}{2\mu r^2} \quad (106)$$

Plastic at  $r$  and  $a$ :

$$du = - \left[ \frac{\delta}{1-\delta} \frac{r}{a} + \frac{1}{1-\delta} \left( \frac{a}{r} \right)^{2-3\delta} \right] da \quad (107)$$

The motion of these selected radii were followed during the loading calculation, so that  $a$ ,  $c$ ,  $d\sigma_0$  are known.

A sample of the trajectories of the radii is shown in Figure 68 for a yield strength of 2 kbar and an applied tensile stress. The initial radii are the radii of spheres with an initial gross density of 50%, 60%, 70%, 80%, 90%, and 95% of the solid. Evidently very little displacement of the radii occurs until the flow stress of four to five times the yield is reached. Then the flow is unlimited. Figure 70, the stress-specific-volume plot for the same calculation as Figure 68, shows a similar result.

The variations of bulk modulus with stress are shown in Figure 71 for a yield strength of 2 kbar. This clearly shows the rapid drop in modulus that accompanies yielding, although this change is not nearly so apparent in Figure 68. The elastic values of bulk modulus at zero stress

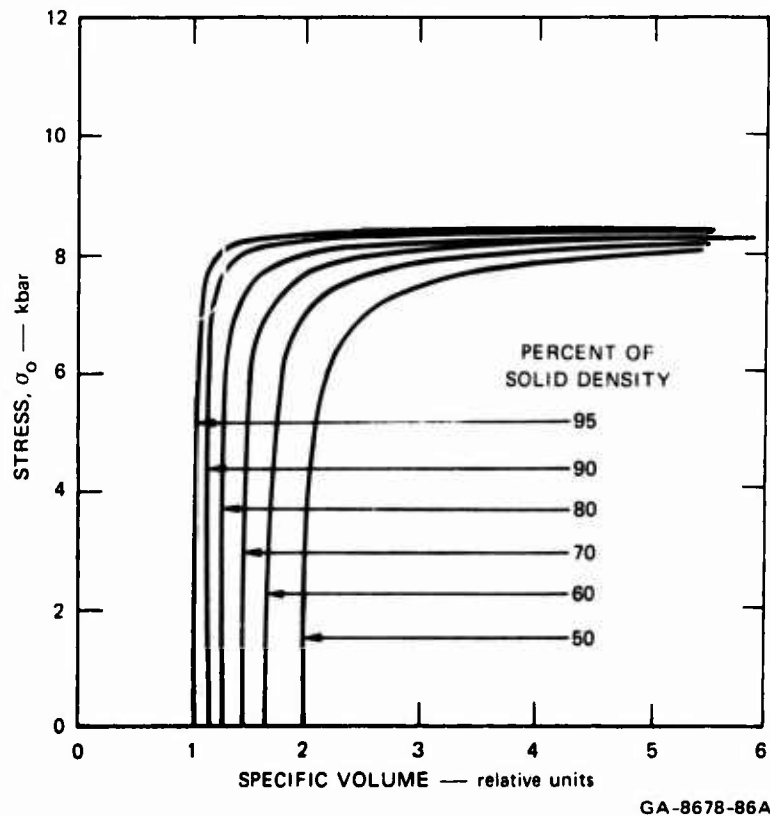


FIGURE 70 RELATION BETWEEN STRESS AND SPECIFIC VOLUME FOR POROUS MATERIAL UNDER TENSION WHERE YIELD = 2 kbar

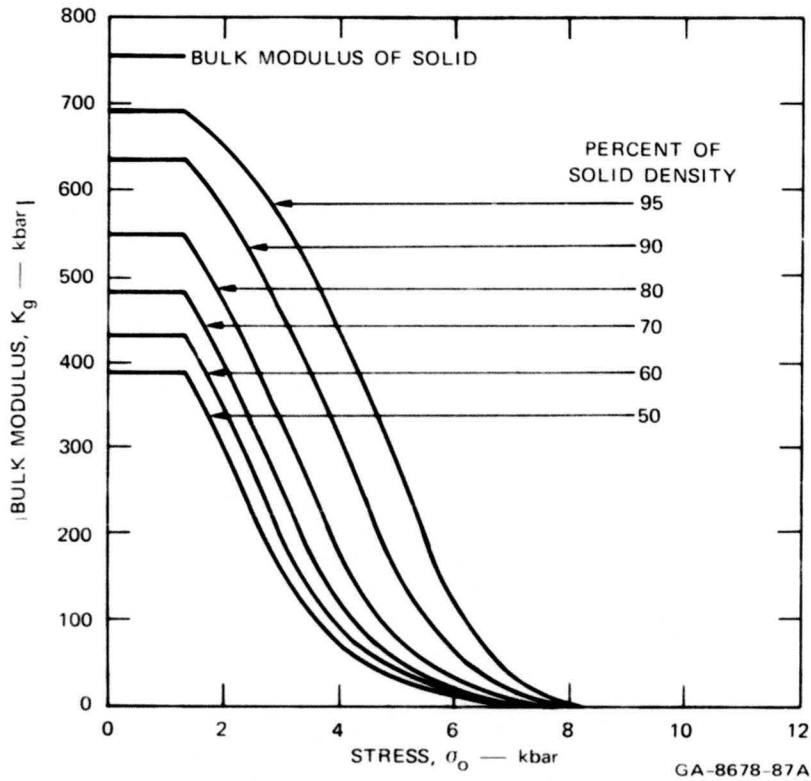


FIGURE 71 VARIATION OF BULK MODULUS WITH TENSILE LOAD ON A POROUS MATERIAL

may be compared with the results of MacKenzie (Ref. 5), and of Hashin (Ref. 45). The present result, derived with the aid of Eq. (105) is simply

$$K_g = \frac{K}{1 + 3Ka^3/(4\mu r^3)} \quad (108)$$

where  $a^3/r^3$  is the porosity. MacKenzie's relation is (neglecting cubic terms in porosity)

$$K_g = \frac{K(1 - a^3/r^3)}{1 + 3Ka^3/(4\mu r^3)} \quad (109)$$

Hashin's expression also reduces to Eq. (109). Evidently the result of our spherical calculation is fairly similar to that from these more complete elastic analyses. Equations (108) and (109) are compared in Figure 72.

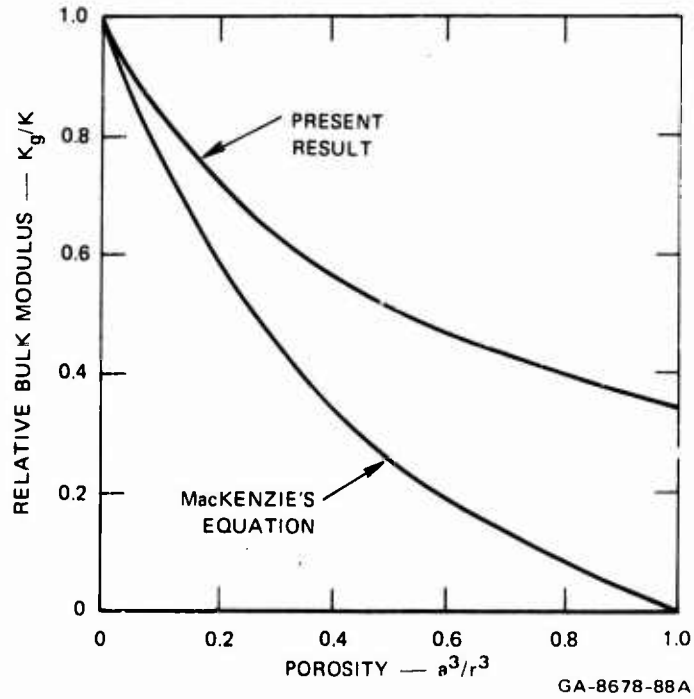


FIGURE 72 VARIATION OF ELASTIC BULK MODULUS FROM MACKENZIE'S EQUATION AND THE PRESENT RESULTS

## 2. EXTERNAL COMPRESSION PROBLEM

The compression of a void under an external compressive stress field is obtained from the tensile solution. The only change required is a change in the sign of  $Y$ , and hence of  $\epsilon$ . Then, Eqs. (79), (82), (83), and (84) give the stress field, Eq. (93) the displacement field, and Eqs. (100) and (101) the expressions for void diminution. For the compression problem there is no upper limit of stress as in the tensile problem.

Trajectories of the void boundary, elastic-plastic boundary and selected radii are shown in Figure 73.

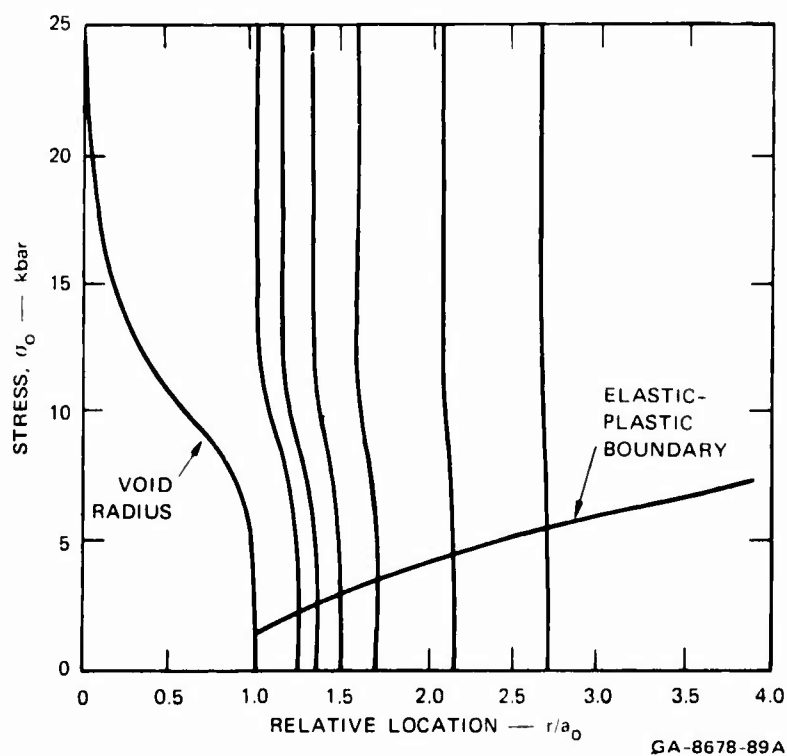


FIGURE 73 TRAJECTORIES OF THE VOID RADIUS, ELASTIC-PLASTIC BOUNDARY, AND SELECTED RADII FOR A POROUS MATERIAL UNDER COMPRESSION WHERE YIELD = 2 kbar

As expected, there is little motion of the points until the material at the point becomes plastic. The curves for  $c$ , the elastic-plastic boundary, appear to reach an asymptote as stress increases. This indicates that when the stress has reached a level such that the void has essentially disappeared, a small sphere of yielded material remains.

The compression of a void is of interest in analyzing the behavior of a porous material. Therefore, the computed results are depicted as specific volume versus stress in Figure 74. It may be noted that significant decreases in volume do not occur until the stress reaches several times the yield of the material. Then the volume decrease is gradual, as in the tensile case. These stress-volume curves are similar to those observed in the dynamic and static compression of porous materials (Ref. 5). The variation of bulk modulus for this same problem is

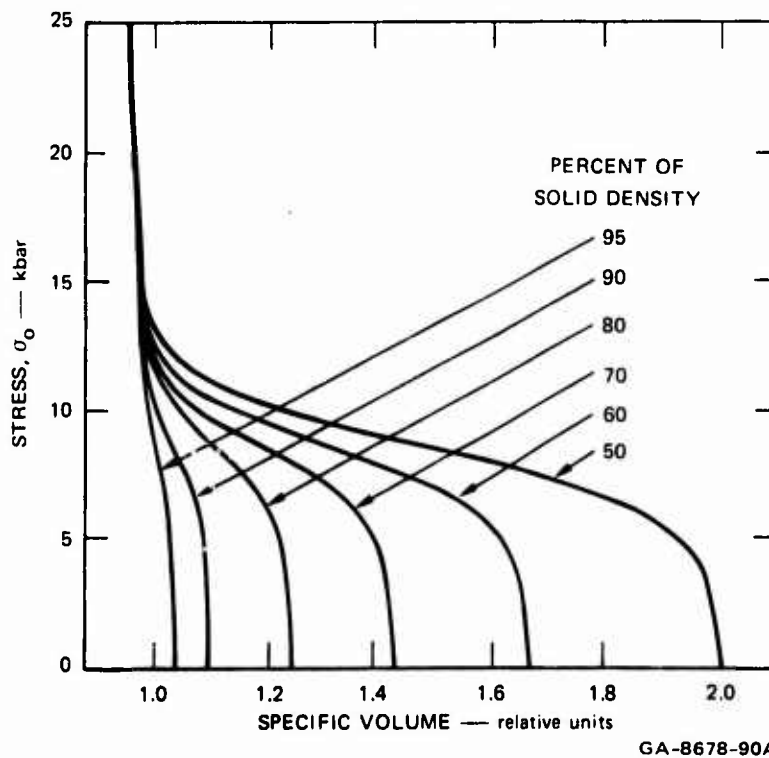


FIGURE 74 STRESS VERSUS SPECIFIC VOLUME FOR POROUS MATERIALS UNDERGOING COMPRESSION WHERE YIELD = 2 kbar

shown in Figure 75. The curves start at elastic values given by Eq. (108), drop rapidly as yielding begins, then increase again to the bulk modulus of the solid. From zero up to two or three times the yield strength, these compressive moduli follow paths very similar to those obtained in tension (Figure 71).

### 3. COMPARISON OF INTERNAL PRESSURE AND EXTERNAL TENSION SOLUTIONS

The solution to the problem of internal pressure in a void is very similar to that for uniform tension outside the void. The internal pressure case is presented here for comparison. The solution procedure follows that for external tension up to the definition of  $v$ :

$$du = v dc \quad (110)$$

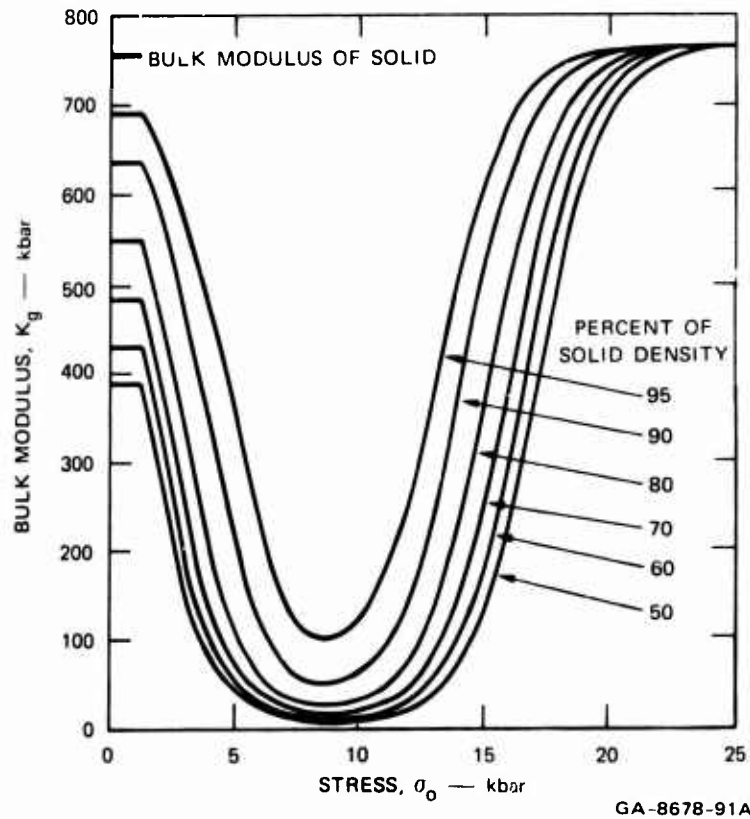


FIGURE 75 VARIATION OF BULK MODULUS DURING COMPRESSIVE LOADING ON MATERIALS WITH VARIOUS POROSITIES WHERE YIELD = 2 kbar

Here,  $v$  is the proportionality factor between  $du$  and  $dc$  instead of between  $du$  and  $da$ , as before. The expressions corresponding to Eqs. (91) and (92) are evaluated as before, replacing  $a$  by  $c$ . The constant of integration for Eq. (92) is determined at  $r = c$  using the fact from Hill (Ref. 46) that

$$v = \frac{\partial u / \partial c}{1 - \partial u / \partial r} \quad (111)$$

and that

$$u = \frac{Y}{6\mu} \frac{c^3}{r^2} \quad (112)$$

in the elastic material [as in Eq. (85), with  $\sigma_0 = 0$ ]. Then at  $r = c$  the value of  $v$  is

$$v_c = \frac{\delta(\Gamma - 1)}{1 + \frac{2}{3} \delta(\Gamma - 1)} \quad (113)$$

and the integral of the equation corresponding to Eq. (85) is

$$v = \frac{\delta}{1 - \delta} \left[ -\frac{r}{c} + \Gamma_i \left(\frac{c}{r}\right)^{2-3\delta} \right] \quad (114)$$

where

$$\Gamma_i = \frac{\Gamma - \frac{1}{3} \delta(\Gamma - 1)}{1 + \frac{2}{3} \delta(\Gamma - 1)}$$



and is approximately equal to  $\Gamma$ , because  $\delta$  is very small. Let  $v = du/dc$  be evaluated at  $r = a$  and eliminate  $dc$  and  $c$  with the aid of Eqs. (84') and (94'). The result is

$$\frac{da}{a} = \frac{\frac{\delta}{3} \left[ -1 + \Gamma_i e^{\alpha(1-\delta)} \right]}{1 - \delta \Gamma_i e^{\alpha(1-\delta)}} d\alpha \quad (115)$$

The integral of Eq. (115) is

$$\frac{a_2}{a_1} = \left\{ e^{\delta(\alpha_2 - \alpha_1)} \frac{\left[ 1 - \delta \Gamma_i e^{\alpha_2(1-\delta)} \right]}{1 - \delta \Gamma_i e^{\alpha_1(1-\delta)}} \right\}^{-1/3} \quad (116)$$

This result is very similar to Eq. (100) derived for external tension. The differences are in small terms of the order of  $\delta$ . As for the tensile case, a limiting stress is reached for which the numerator in Eq. (116) becomes zero. This limit is

$$\begin{aligned} \alpha_m &= -\frac{1}{1-\delta} \ln(\delta \Gamma_i) \\ &= -\frac{1}{1-\delta} \ln \left\{ \frac{\delta \Gamma \left[ 1 - \frac{\delta}{3} \left( 1 - \frac{1}{\Gamma} \right) \right]}{1 + \frac{2}{3} \delta (\Gamma - 1)} \right\}, \quad (117) \end{aligned}$$

which is evidently very nearly the same limit obtained in Eq. (103).

#### 4. SUMMARY

Expressions relating the static void size to the applied stresses were obtained for external tensile and compressive stresses and for internal pressure. The external tension case, corresponding to the problem of fracture of ductile materials by void growth, showed small radial growth until a critical stress of four or five times the yield strength was reached. Then the expansion was infinite. Thus a threshold stress for void growth was obtained.

For external compression, corresponding to the compaction of a porous ductile material, the volume change was slight until the stress was several times the yield stress. Then the volume decreased gradually with increasing stress. The collapse of the void left behind a sphere of yielded material.

The void growth under an internal pressure gave results that were similar, but not identical with the results for an external tension.

The stress-volume paths and bulk moduli obtained are expected to indicate qualitatively the correct constitutive relations to use for real porous materials.

NOMENCLATURE FOR APPENDIX IV

B	$1 - \frac{\delta}{3} (\alpha + 3 - 2\Gamma)$
C	$\delta \left[ \Gamma - \frac{\delta}{3} (\alpha + \Gamma) \right]$
F	$-[3 - \delta(1 + \alpha/\Gamma)]^{-1}$
K	bulk modulus, dyn/cm <sup>2</sup>
Y	yield strength, dyn/cm <sup>2</sup>
a	void radius, cm
a <sub>y</sub>	void radius at first yielding, cm
a <sub>0</sub>	initial void radius, cm
a <sub>1</sub>	void radius at beginning of integration step, cm
a <sub>2</sub>	void radius at current applied stress, cm
c	radius of elastic-plastic boundary, cm
r	radius
r <sub>i</sub>	internal radius, cm
u	radial particle velocity, cm/sec
v	proportionality factor between velocity of any point and the velocity of the void surface
Γ	$1 + 3K/4\mu$
Γ <sub>i</sub>	$\left[ \Gamma - \frac{\delta}{3} (\Gamma - 1) \right] / \left[ 1 + \frac{2\delta}{3} (\Gamma - 1) \right]$
α	$(3\sigma_0/2Y) - 1$ , dimensionless applied stress
α <sub>m</sub>	dimensionless stress to cause infinite void radius

$\delta$	$2Y/3K$ , dimensionless yield strength
$\mu$	shear modulus, $\text{dyn/cm}^2$
$\sigma_c$	radial stress at elastic-plastic boundary, $\text{dyn/cm}^2$
$\sigma_i$	internal radial stress, $\text{dyn/cm}^2$
$\sigma_m$	stress to cause infinite void radius, $\text{dyn/cm}^2$
$\sigma_0$	external radial tension, $\text{dyn/cm}^2$
$\sigma_r$	radial stress, $\text{dyn/cm}^2$
$\sigma_\theta$	circumferential stress, $\text{dyn/cm}^2$

## Appendix V

### TWO-DIMENSIONAL VOID GROWTH CALCULATIONS: VOID

#### 1. INTRODUCTION

The following calculations were made to guide in constructing constitutive relations for material containing voids. The material was idealized as an elastic-viscous-plastic material initially containing a uniform spacing of spherical voids. The "typical" element used in the computations was a cylinder with height equal to diameter and containing a spherical void. The cylindrical boundaries are fixed in radial position, whereas the planar boundaries move along the cylindrical axis to provide the forcing.

The computations were conducted with a computer program termed VOID, a special-purpose, finite-element, wave propagation code based on work of Wilkins (Ref. 48). The program is listed in this Appendix together with flow charts, sample input decks and sample printout. Special features that were added to Wilkin's development are documented below. The cell layout, which is described first, was constructed to fit the current problem - an external cylindrical boundary and an internal spherical boundary - with high fidelity and to permit large cell distortions.

The momentum conservation relations were modified to be better suited to the axisymmetric problem dealt with here. Calculations using the traditional form of Wilkins (Ref. 48) led to an excessive void growth along the axis of symmetry. Therefore, the momentum conservation relations are rederived here to be exact within the constraints of the finite element approximation. To provide accurately for the viscous void growth,

a fairly complete stress relaxation and strain hardening constitutive relation for multidimensional problems was incorporated into the program. This relation augments the Mie-Gruneisen equation of state already in the program. To ensure stability in the calculations, a general stability criterion was developed for multidimensional problems with arbitrarily complex equations of state. In addition, the strain computation was rederived to ascertain that its accuracy was consistent with that of the momentum calculations.

The purpose of the calculations was to provide stress-strain relations for material with voids and to determine the growth pattern of the void. Particular results expected were:

- Relation of growth velocity to average applied stress and material viscosity.
- Effect of a threshold stress on void growth.
- Relation of average pressure on the cell boundaries to the average specific volume of the solid material.
- Relation of average deviator stress to average axial strain and viscosity.
- Eccentricity of the void as it grows.

The average stresses mentioned above were found by averaging over the cylindrical or planar faces; the average axial strain was computed from the motion of the planar faces. In addition to the above results, we expected some insight into the problem from the listing of microscopic stresses near the void.

The computer runs made are described briefly, their output summarized, and constitutive relations are constructed from the results.

## 2. CELL LAYOUT AND BOUNDARY CONDITIONS

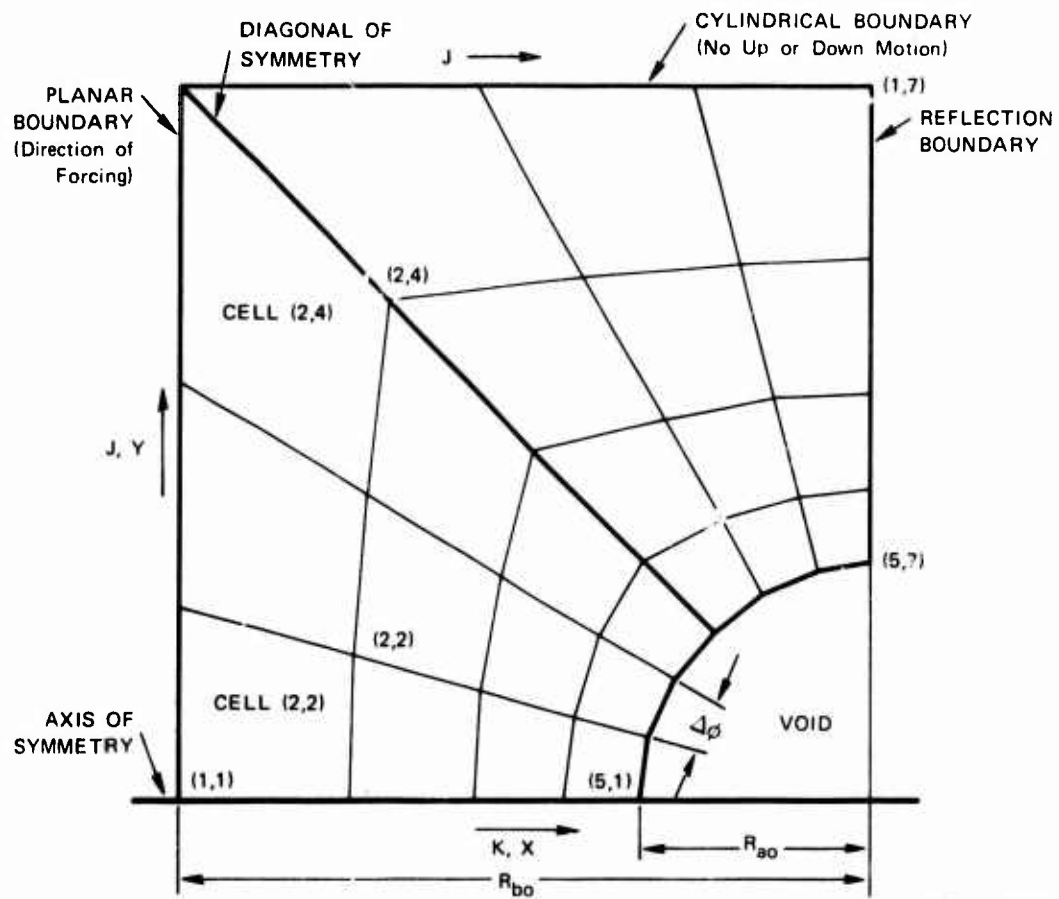
The cell layout is designed for maximum fidelity to both the external and the internal boundary conditions. The external boundaries are the cylindrical lateral boundary and the planar boundary in the direction of wave propagation. The internal boundary is initially spherical. Therefore, the cell layout is one that is appropriate for a spherically symmetric problem near the void and is simply a square layout near the external boundaries. Intermediate cells are laid out on the basis of a gradual transition between the two coordinate systems. All cells are designed with similar size cells adjacent to each other, and all cells are approximately square.

The planned cell layout is shown in Figure 76 along with the numbering system  $(k,j)$  for the coordinates and the cells. First, the radius increments are laid out along the axis of symmetry to provide an approximately square set of cells along this axis. The cells will be approximately square if the length in the radial direction  $(\Delta R)$  is equal to the average length in the angular direction  $(R\Delta\varphi)$ .

$$\Delta R = R\Delta\varphi \quad (118)$$

This criterion can be met if the cells are laid out according to the following formula for the radius

$$\begin{aligned} R_{k,1} &= (R_b)^{1-k/N_R} (R_a)^{k/N_R} = R_b \left( \frac{R_a}{R_b} \right)^{k/N_R} \\ &= R_{k-1,1} \left( \frac{R_a}{R_b} \right)^{1/N_R} \end{aligned} \quad (119)$$



GA-8678-102

FIGURE 76 CELL LAYOUT FOR AXISYMMETRIC VOID PROBLEM



where

$R$  = the radius with subscripts  $k$  and  $j$  ( $k$  varies from 1 at the outer boundary to the maximum at the void surface,  $j$  increases from the axis of symmetry)

$R_a$  = the initial radius of the void

$R_b$  = the radius to the external boundary along the axis of symmetry

$N_R$  = the number of cells in the radial direction

A slight modification of Eq. (119) is used to lay out the radii along other  $j$  rows,

$$R_{k,j} = R_b \sec(j-1)\Delta\varphi \left( \frac{R_a}{R_b \sec(j-1)\Delta\varphi} \right)^{k/N_R} \quad (120)$$

$$= R_{k-1,j} \left( \frac{R_a}{R_b \sec(j-1)\Delta\varphi} \right)^{1/N_R}$$

where  $\Delta\varphi$  is the uniform angular spacing between  $j$  rows. For the computations an orthogonal Eulerian grid is used to locate all the coordinates. The origin of coordinates is on the axis of symmetry as shown in Figure 76. The  $x$  axis lies on the axis of symmetry and is positive towards the right. The  $y$  axis is positive upward in the figure. The  $x$  and  $y$  values of the radial coordinate points given by Eq. (120) are:

$$X_{k,j} = R_{k,j} \cos(j-1)\Delta\varphi = X_{k-1,j} \left( \frac{R_a}{R_b \sec(j-1)\Delta\varphi} \right)^{1/N_R} \quad (121)$$

$$Y_{k,j} = R_{k,i} \sin(j-1)\Delta\varphi = Y_{k-1,j} \left( \frac{R_a}{R_b \sec(j-1)\Delta\varphi} \right)^{1/N_R} \quad (122)$$

Equations (120), (121), and (122) are used to determine the coordinate locations up to the diagonal of symmetry shown in Figure 76. From the diagonal of symmetry to the reflection boundary, the cells are laid out by reflecting the coordinate locations around the diagonal of symmetry.

The preceding layout of radii makes it possible to meet the requirement of Eq. (118) for essentially square cells. It is also necessary to choose correctly the value of  $\Delta\varphi$ . A set of radii computed from Eq. (120) can be inserted into Eq. (118) to compute the appropriate  $\Delta\varphi$

$$\Delta\varphi = \frac{1 - \left( \frac{R_a}{R_b \sec(j-1)\Delta\varphi} \right)^{1/N_R}}{\left( \frac{R_a}{R_b \sec(j-1)\Delta\varphi} \right)^{1/2N_R}} \quad (123)$$

The appropriate number  $N_\varphi$  of cells in the  $\varphi$  direction can now be determined.

$$N_\varphi = \frac{\pi}{2\Delta\varphi} \quad (124)$$

Equation (123) need not be solved exactly because it is used only as a guide in the choice of  $N_\varphi$ .

Since the grid may undergo large distortions during the calculation, it is well to consider possible cell shapes at later stages. If the problem is one in which the void enlarges, the cells will tend to shorten

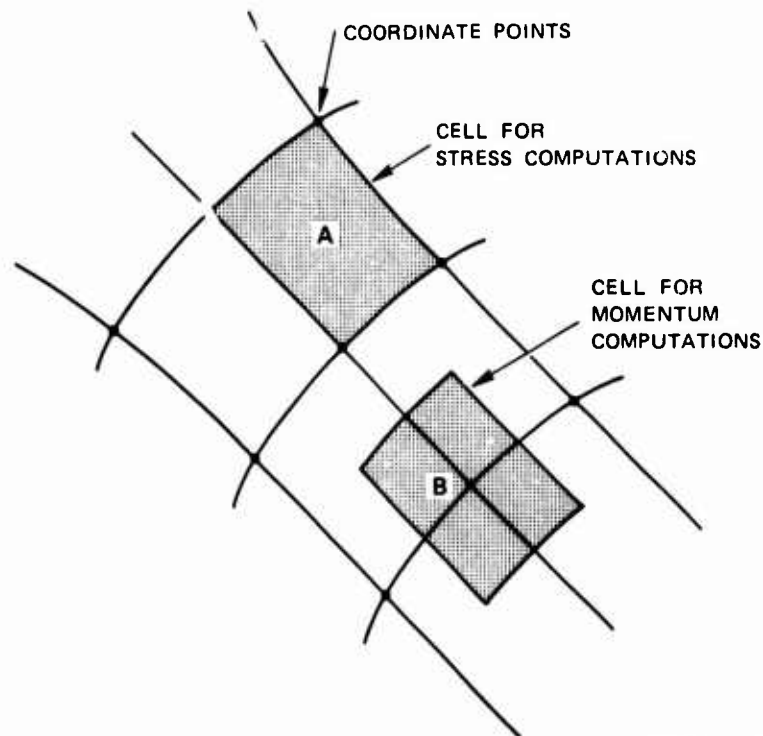
in the radial direction and elongate in the angular direction; therefore, it would be appropriate to choose  $N_{\varphi}$  somewhat larger than indicated by Eq. (124).

The loading is provided by moving the left planar boundary at a constant velocity, thus applying an approximately constant axial strain rate to the cylinder.

### 3. MOMENTUM CONSERVATION

In deriving momentum conservation relations it is possible to use either a discretization of the differential equations of momentum conservation or to consider force balances around a finite element. In the following derivation the second point of view, using the finite element, is followed. Therefore the steps in the calculation are to isolate a volume element for which the acceleration and velocity are computed, to compute the forces acting on that element, and to compute the mass of the element.

Two types of cells are defined for the wave propagation calculation. Both are shown in Figure 77, which contains a grid of coordinate points.



GA-8678-38

FIGURE 77 TYPES OF CELLS FOR STRESS AND MOMENTUM COMPUTATIONS

Cell A is the natural cell surrounded by four coordinate points. This is the cell for which the strains and stresses, which are homogeneous throughout each cell, are computed. The momentum computation determines the velocity of the coordinate points. For these calculations cell B, containing the mass around a coordinate point, is used. The calculations are broken into four portions corresponding to the parts lying in each of the surrounding stress cells. One typical portion is shown in Figure 78 with the nomenclature and sign convention that are used in the derivation.

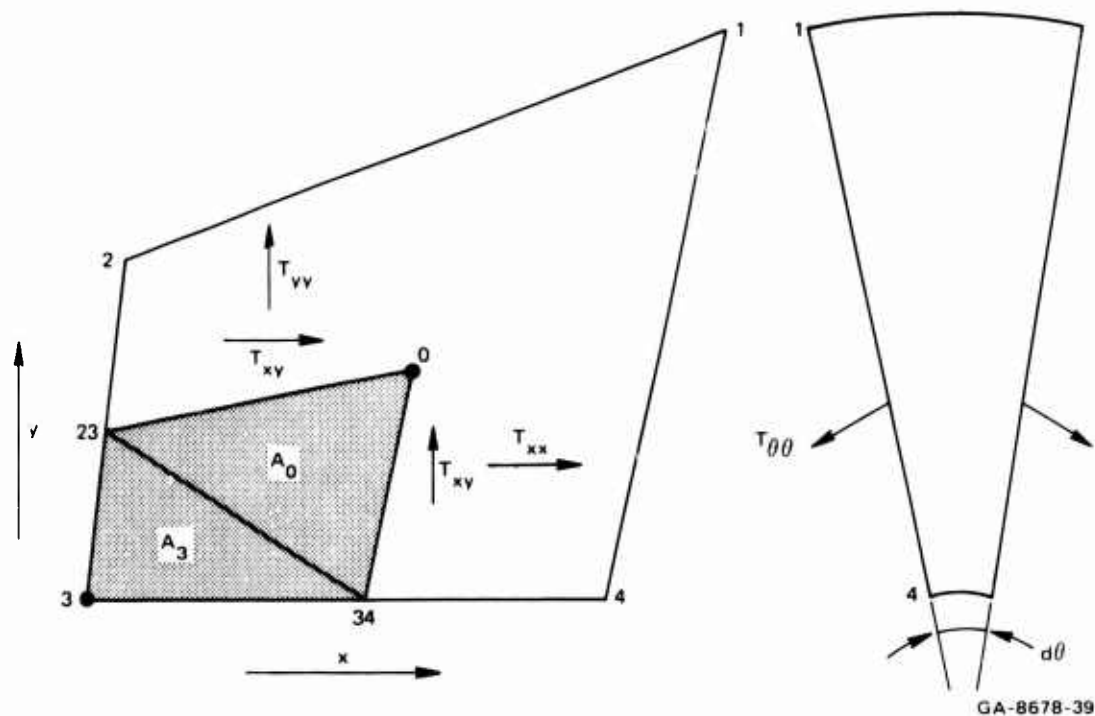


FIGURE 78 STRESS AND COORDINATE NOMENCLATURE FOR A CELL

The configuration of the shaded element is defined in such a way that the  $x$  and  $y$  coordinates of the point 0 are averages of the coordinates at the four corners of the stress cell. An end view is also shown in Figure 78 as a reminder of the three-dimensional character of

the element. The areas of the shaded element on which stresses act in the x and y directions are as follows:

$$A_{xx} = \frac{d\theta}{4} (y_2 - y_4) \left( \frac{y_2 + y_4}{2} + y_3 \right) \quad (125)$$

$$A_{yy} = \frac{d\theta}{2} \left[ \left( \frac{y_2 + y_3}{2} + y_0 \right) \left( x_0 - \frac{x_2 + x_3}{2} \right) - \left( \frac{y_3 + y_4}{2} + y_0 \right) \left( x_0 - \frac{x_3 + x_4}{2} \right) \right] \quad (126)$$

The area in the x-y plane on which the circumferential stress acts is broken into two portions  $A_0$  and  $A_3$  as shown in Figure 78. These portions and the total are:

$$A_0 = \frac{1}{8} [(2x_0 - x_3)(y_2 - y_4) + x_2(y_3 + y_4 - 2y_0) + x_4(2y_0 - y_2 - y_3)] \quad (127)$$

$$A_3 = \frac{1}{8} [x_4(y_2 - y_3) + x_3(y_4 - y_2) + x_2(y_3 - y_4)] \quad (128)$$

$$A_{xy} = A_0 + A_3 \quad (129)$$

Equations (127) and (128) are derived by simplifying the usual general relations for the area of a triangle.

The forces in the x and y directions applied to the small mass represented by the shaded area in Figure 78 are determined by multiplying the stresses shown in Figure 78 times the areas in Eqs. (125), (126), and (129). The expressions for the forces are:

$$F_x = T_{xy} \frac{A}{yy} + T_{xx} \frac{A}{xx} \quad (130)$$

and

$$F_y = T_{yy} \frac{A}{yy} + T_{xy} \frac{A}{xx} - T_{\theta\theta} \frac{A}{xy} \frac{d\theta}{d\theta} \quad (131)$$

The preceding relations for areas and forces are valid for any configuration with the mass element centered at point 3; therefore, these equations can be used for all four mass elements surrounding any coordinate point.

The mass of the small element is determined by multiplying the average density of the cell shown in Figure 78 times the volume of the element. The mass is as follows:

$$M = \rho \frac{d\theta}{3} \left[ A_0 \left( y_0 + y_3 + \frac{y_2 + y_4}{2} \right) + A_3 \left( \frac{y_2 + y_4}{2} + 2y_3 \right) \right] \quad (132)$$

Newton's law is applied to obtain the change in velocity at the coordinate point 3, considering force and mass contributions from four elements around the point.

$$\Delta u = \frac{\left( \sum_{i=1}^4 F_{xi} \right) \Delta t}{4 \sum_{i=1}^4 M_i} \quad (133)$$

where  $\Delta u$  is the change in velocity in the x direction over the time increment  $\Delta t$ . The foregoing procedure is in the VOID computer program.

#### 4. STRAIN COMPUTATION

The strain computations in the two-dimensional wave propagation program are based on the assumption that the strains are uniform throughout each cell of type A shown in Figure 77. The computations are constructed to meet the following consistency requirements.

$$\epsilon_x + \epsilon_y = \frac{\Delta A}{A} \quad (134)$$

$$\epsilon_x + \epsilon_y + \epsilon_\theta = \frac{\Delta V}{V} \quad (135)$$

where

$\epsilon_x, \epsilon_y, \epsilon_\theta$  = changes in the strain that occur during a time increment

$\Delta A$  = change in the cell areas in the x-y plane

$\Delta V$  = change in the volume of the cell

To ensure that compatibility of strains is enforced, we assume a velocity field, rather than a strain field. Strains that are uniform throughout a cell are produced by the following linearly varying velocity field.

$$u = u_0 + u_x x + u_y y \quad (136)$$

$$v = v_0 + v_x x + v_y y \quad (137)$$



The strain rates corresponding to these velocities are:

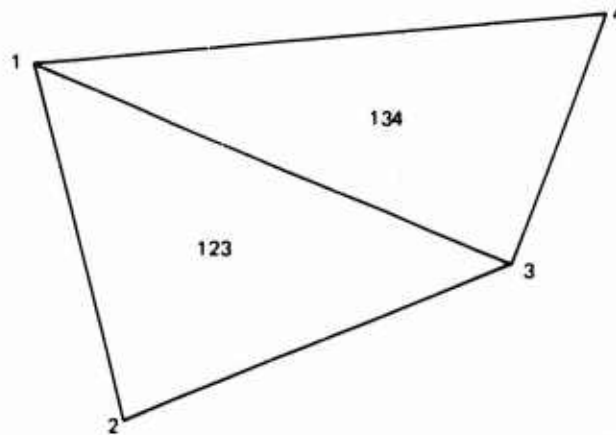
$$\dot{\epsilon}_x = \frac{\partial u}{\partial x} = u_x \quad (138)$$

$$\dot{\epsilon}_y = \frac{\partial v}{\partial y} = v_y \quad (139)$$

$$\dot{\gamma}_{xy} = \frac{\partial v}{\partial x} + \frac{\partial u}{\partial y} = v_x + u_y \quad (140)$$

$$\dot{\omega}_{xy} = \frac{1}{2} \left( \frac{\partial v}{\partial x} - \frac{\partial u}{\partial y} \right) = \frac{1}{2} (v_x - u_y) \quad (141)$$

The velocity fields of Eqs. (136) and (137) can be determined for any triangle if the velocities at the coordinate points are known. Consider for example the triangle in Figure 79 with coordinates 1, 2, and 3 and



GA-8678-40

FIGURE 79 QUADRILATERAL ELEMENT PRODUCED FROM TWO TRIANGLES

velocities in the  $x$  direction of  $u_1$ ,  $u_2$ , and  $u_3$ . The velocity field parameters  $u_0$ ,  $u_x$ , and  $u_y$  can then be determined from the following three equations:

$$\begin{aligned} u_1 &= u_0 + u_x x_1 + u_y y_1 \\ u_2 &= u_0 + u_x x_2 + u_y y_2 \\ u_3 &= u_0 + u_x x_3 + u_y y_3 \end{aligned} \tag{142}$$

where the  $x_i, y_i$  are coordinates of the  $i^{\text{th}}$  point at some (as yet undetermined) time. Solution of Eqs. (142) gives the following results for  $u_x$  and  $u_y$ :

$$u_x = \frac{(u_1 - u_2)(y_1 - y_3) - (u_1 - u_3)(y_1 - y_2)}{2A} \tag{143}$$

$$u_y = - \frac{(u_1 - u_2)(x_1 - x_3) - (u_1 - u_3)(x_1 - x_2)}{2A} \tag{144}$$

where  $A$ , the area of the triangle 123 shown in Figure 79, is

$$2A = (x_1 - x_2)(y_1 - y_3) - (x_1 - x_3)(y_1 - y_2) \tag{145}$$

Similarly the strain in the y direction can be determined.

$$v_x = \frac{(v_1 - v_2)(y_1 - y_3) - (v_1 - v_3)(y_1 - y_2)}{2A} \quad (146)$$

$$v_y = - \frac{(v_1 - v_2)(x_1 - x_3) - (v_1 - v_3)(x_1 - x_2)}{2A} \quad (147)$$

The next step is to specify  $x_i$ ,  $y_i$  in Eqs. (143) through (147) in such a way that Eq. (134) is satisfied. This calculation is performed in two steps; first the requirements are satisfied for each of the two triangles shown in Figure 78 and then the computation is made for the whole quadrilateral. To meet the requirement for triangle 123, the area  $A$  of Eq. (145) is taken as the average of the areas at the beginning and end of the time increment, that is,

$$A = \frac{1}{2}(A^0 + A^1) \quad (148)$$

A compatible form for the strain rate in the x direction is given by

$$\dot{\epsilon}_x = \frac{A^0 u_x^0 + A^1 u_x^1}{A^0 + A^1} \quad (149)$$

where values with a superscript 0 are computed with initial values of  $x$  and  $y$ , and values with a superscript 1 are evaluated with final values of  $x$  and  $y$ . These final values of coordinates are

$$x_i^1 = x_i^0 + u_i \Delta t \quad (150)$$

$$y_i^1 = y_i^0 + v_i \Delta t$$

When we substitute A from Eq. (148), the strains from Eq. (149), and  $\Delta A$  equal  $A^1 - A^0$ ; Eq. (134) now becomes an identity.

The extension of the result above to the full quadrilateral is accomplished, using the following definition of a strain rate

$$\dot{\epsilon}_x = \frac{A_{11}^{00} u_{1x} + A_{11}^{11} u_{1x} + A_{22}^{00} u_{2x} + A_{22}^{11} u_{2x}}{A_1^0 + A_1^1 + A_2^0 + A_2^1} \quad (151)$$

where subscript 1 refers to the triangle 123 and subscript 2 to the other triangle in Figure 79. For satisfying Eq. (134) the area A is now taken as one-half the denominator in Eq. (151), that is, the average of the areas at the beginning and end of the time increment.

For use in the computer program, it is advantageous to simplify Eq. (151) as much as possible. After considerable algebra and the aid of Eqs. (143), (144), (145), (146), and (147), the following results are obtained

$$\dot{\epsilon}_x = \frac{u_{13}^m y_{24}^m - u_{24}^m y_{13}^m}{A^0 + A^1} \quad (152)$$

$$\dot{\epsilon}_y = \frac{v_{24}^m x_{13}^m - v_{13}^m x_{24}^m}{A^0 + A^1} \quad (153)$$

$$\dot{\gamma}_{xy} = \frac{u_{24}^m x_{13}^m - u_{13}^m x_{24}^m + v_{13}^m y_{24}^m - v_{24}^m y_{13}^m}{A^0 + A^1} \quad (154)$$

$$\dot{\omega}_{xy} = \frac{u_{13}^m x_{24}^m - u_{24}^m x_{13}^m + v_{13}^m y_{24}^m - v_{24}^m y_{13}^m}{2(A^0 + A^1)} \quad (155)$$

where the doubly subscripted velocities and coordinates have the following meaning

$$u_{ij} = u_i - u_j \quad (156)$$

$$x_{ij}^m = x_i + \frac{1}{2}u_i \Delta t - x_j - \frac{1}{2}u_j \Delta t \quad (157)$$

The requirement given by Eq. (135) is met somewhat more readily in the computer program. The values of  $\epsilon_x$  and  $\epsilon_y$  are first determined from Eqs. (152) and (153), and the volume change is determined by calculations of the volume before and after a time step according to Eq. (132). Then only  $\epsilon_\theta$  is unknown in Eq. (135), and that equation is used to determine the strain in the circumferential direction; hence the requirement of Eq. (135) is satisfied exactly.

## 5. STRESS RELAXATION MODEL

A general two-dimensional model for stress relaxation has been developed including the effects of work hardening, incremental plasticity, loading and unloading. The model was devised to correspond to the normal concepts of viscosity that are used in simpler situations. In the development below, first the correspondence between the stress relaxation model and a simple viscous model is established in a very simple geometry. Then in preparation for the two-dimensional geometry, relations are derived for equivalent values of shear stress and plastic shear strain which represent the stress and strain tensors. A strain-hardening model developed by Wilkins (Ref. 49) is introduced. Then the full calculational procedure for two-dimensional problems is described.

### a. Comparison of Stress-Relaxation and Viscosity Models

The normal relation between shear stress  $\tau$  and shear strain  $\gamma$  for a viscosity model of an elastic-plastic solid is:

$$\left. \begin{aligned} \tau &= \mu\gamma & \tau < \frac{Y}{2} \\ &= \frac{Y}{2} + \eta\gamma & \tau \geq \frac{Y}{2} \end{aligned} \right\} \quad (158)$$

where

$\mu$  = the shear modulus

$\eta$  = the coefficient of viscosity

$Y$  = the yield strength

For stresses less than the yield strength the behavior is elastic. Above the yield strain the stress has both a plastic and a viscous component.

The stress relaxation model corresponding to the preceding viscous model is:

$$\left. \begin{aligned} \dot{\tau} &= \mu \dot{\gamma} \\ &= \mu \dot{\gamma} - \frac{\tau - \frac{Y}{2}}{T} \end{aligned} \right\} \begin{array}{l} \tau < \frac{Y}{2} \\ \tau \geq \frac{Y}{2} \end{array} \quad (159)$$

For stresses less than yielding, this model is also elastic. For stresses above yielding, a time constant  $T$  provides for a gradual return of the shear stress to the yield value. To examine further the correspondence between the two models, we integrate the equation for stress relaxation above yielding for the case in which the shear strain rate is a constant. The result is

$$\tau = \frac{Y}{2} + T\mu\dot{\gamma} (1 - e^{-(t-\Delta t)/T}) \quad (160)$$

where

$T$  = the time from the beginning of loading

$\Delta t$  = the time at which the shear stress reaches the yield point

The second part of Eq. (158) is equal to Eq. (160) for large times if

$$\eta = T\mu$$

The response of the viscous and stress relaxation models to a constant shear strain rate is shown in Figure 80. Evidently the viscous model has a somewhat unrealistic response in the vicinity of the yield point. For large times the stress relaxation model and the viscous model have the same behavior. From these observations we may conclude that if transient behavior and rapidly varying strain rates are to be dealt with, a stress relaxation model is required. If the times of interest are large with respect to the relaxation time and transient phenomena are not of importance, the viscous model is adequate.

To determine the type of model required for the two-dimensional calculations, it was necessary to consider the relaxation times anticipated for copper and for aluminum and to estimate the computational time increments for the void growth problem. For both copper and aluminum the relaxation times were about 1 nanosecond. The computational time increments anticipated for a void of 1 micron radius is about one-tenth of a nanosecond or less. Hence, the transient behavior will be of great importance, and it is necessary then to use the stress relaxation model.

b. Strain Hardening

A strain-hardening model should permit the yield strength to increase whenever the stress exceeds yielding. The yield strength should increase as a function of the total plastic strain; it should not increase indefinitely but should approach an asymptotic value for large plastic strains. Such an asymptotic strain-hardening function has been determined experimentally by Grace (Ref. 29) for OFHC copper. These requirements are met by the strain-hardening model of Wilkins (Ref. 49).



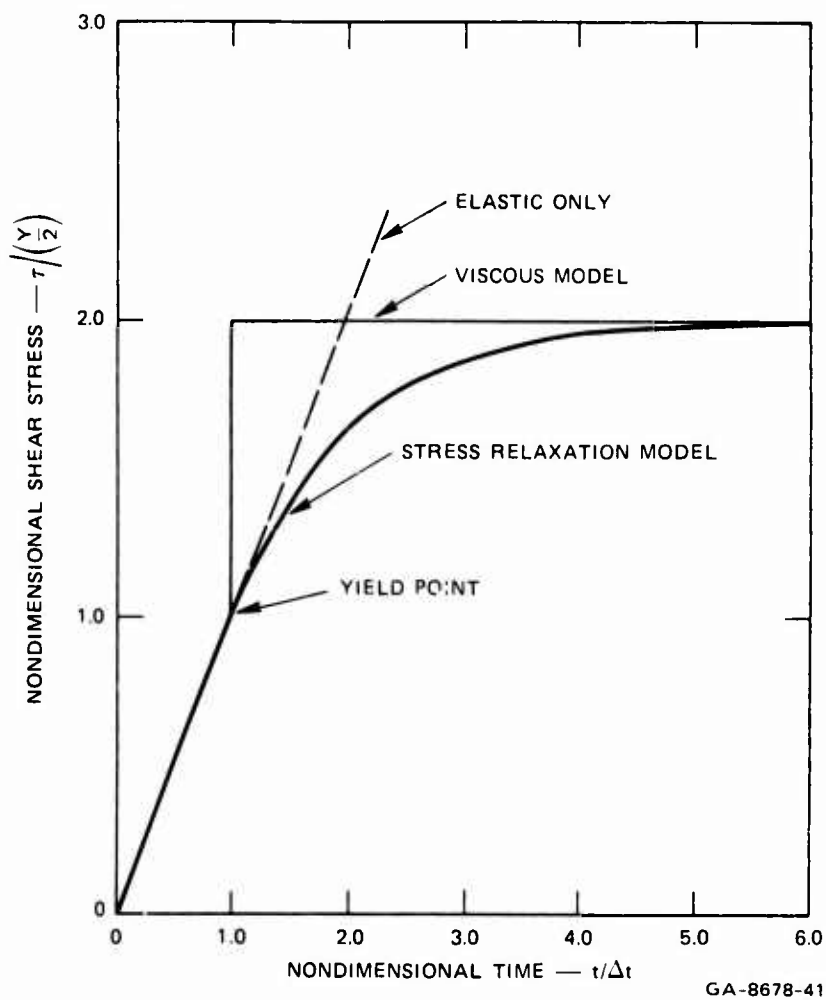


FIGURE 80 RESPONSE OF VISCOUS AND STRESS RELAXATION MODELS TO A CONSTANT SHEAR STRAIN RATE FOR THE CASE  $\tau = \Delta t$

The form of Wilkins' strain-hardening relation is

$$Y = Y_0 + \frac{Y^P M}{1 + bY^P} \quad (162)$$

where

$Y_0$  = the initial yield strength

$Y^P$  = the plastic strain

$M$  = the strain hardening modulus for small plastic strains

For large plastic strains the yield strength approaches  $Y_0 + M/b$ . In this equation the absolute value of the plastic strain is used so that strain hardening occurs under compressive or tensile loads.

c. Effective Values of Stress and Strain

The preceding sections dealt with a single stress quantity and a single strain quantity. For extension of these relations to the two-dimensional problem it is necessary to introduce new variables for stress and strain that in some way represent the shearing stress and shearing strain in the material. The choice for stress is the von Mises stress, which is closely related to the yield criterion of von Mises (see Hill, Ref. 46).

$$\bar{\sigma} = \sqrt{\frac{1}{2} \left[ (\sigma_1 - \sigma_2)^2 + (\sigma_2 - \sigma_3)^2 + (\sigma_3 - \sigma_1)^2 \right]} \quad (163)$$

where

$\sigma_1, \sigma_2, \sigma_3$  = the three principal stresses

$\bar{\sigma}$  = the effective stress

By this definition, in a uniaxial tension experiment in which  $\sigma_2$  and  $\sigma_3$  are zero,  $\bar{\sigma}$  is the applied tensile stress. According to the von Mises criterion, which will be used here, yielding occurs when  $\bar{\sigma}$  is equal to the yield strength. An alternate form for Eq. (163) which does not require that the principal stresses be known, is

$$\bar{\sigma} = \sqrt{\frac{3}{2}} \sqrt{\sigma_x'^2 + \sigma_y'^2 + \sigma_z'^2 + 2(\tau_{yz}^2 + \tau_{zx}^2 + \tau_{xy}^2)} \quad (164)$$

where

$\sigma'$  = a deviator stress

For any problem in which  $\sigma_2 = \sigma_3$ , it can be shown that

$$\bar{\sigma} = \sigma_1 - \sigma_2 = 3\sigma_1'/2 \quad \text{and} \quad \tau = (\sigma_1' - \sigma_2')/2 = 3\sigma_1'/4$$

Therefore

$$\bar{\sigma} = 2\tau \quad (165)$$

$$\sigma_1' = \frac{4}{3} \tau \quad (166)$$

Equation (166) is useful in transforming from the one-dimensional models of the preceding sections to the multidimensional case.

Common definitions for the effective shear strain follow the same form as Eq. (163).

$$\gamma_a = a \sqrt{(\epsilon_1 - \epsilon_2)^2 + (\epsilon_2 - \epsilon_3)^2 + (\epsilon_3 - \epsilon_1)^2} \quad (167)$$

where

$\gamma_a$  = the effective shear strain

$a$  = a constant

$\epsilon_1, \epsilon_2, \epsilon_3$  = principal strains

The value of  $a$  is determined in such a way that  $\gamma_a$  is the actual maximum shear strain in any situation in which  $\epsilon_2 = \epsilon_3$ . In such a case the derivation of Timoshenko (Ref. 50, p. 223) shows that the maximum shear strain is

$$\gamma = \epsilon_1 - \epsilon_2 \quad (168)$$

Therefore,  $a$  should be  $1/\sqrt{2}$ . We will use this relation for increments of plastic strain. Hence,

$$d\gamma^P = \sqrt{\frac{1}{2}} \sqrt{(d\epsilon_1^P - d\epsilon_2^P)^2 + (d\epsilon_2^P - d\epsilon_3^P)^2 + (d\epsilon_3^P - d\epsilon_1^P)^2} \quad (169)$$

where

$$d\gamma^P = \text{the effective plastic strain}$$

Because the sum of the plastic strains is zero, Eq. (169) has the alternate form

$$d\gamma^P = \sqrt{\frac{3}{2}} \sqrt{(d\epsilon_1^P)^2 + (d\epsilon_2^P)^2 + (d\epsilon_3^P)^2} \quad (170)$$

Somewhat different definitions of effective plastic strain have been used by other investigators. Hill (Ref. 46) used  $a = \sqrt{2/3}$ ; in this way Hill's effective strain  $d\bar{\epsilon}^P$  is equal to the axial strain in simple tension. Wilkins (Ref. 49) used  $a = 2/3$ . Evidently the value of  $a$  is arbitrary and can be selected to fit the particular computations in mind.

For any case in which  $d\epsilon_2^P = d\epsilon_3^P$ , then  $d\epsilon_2^P = -\frac{1}{2} d\epsilon_1^P$  and

$$d\gamma^P = \frac{3}{2} d\epsilon_1^P \quad (171)$$

This equation is needed in the transformation from the one-dimensional to the multidimensional case.

Because the principal strains are generally unknown, it is expedient to put Eq. (170) into a form using any orthogonal strains. For the axisymmetric condition

$$d\gamma^P = \sqrt{\frac{3}{2}} \sqrt{(d\epsilon_x^P)^2 + (d\epsilon_y^P)^2 + (d\epsilon_3^P)^2 + \frac{1}{2}(d\gamma_{xy}^P)^2} \quad (172)$$

where the third (circumferential) direction is always a direction of principal strain.

d. Two-Dimensional Model for Stress Relaxation

The multidimensional stress relaxation model has the form of Eq. (159) but also incorporates the general plasticity formulation of Hill (Ref. 46). In Hill's analysis the plastic strain increment is given as

$$d\epsilon_{ij}^P = \frac{3\sigma'_{ij} d\bar{\sigma}}{2\bar{\sigma} H} \quad (173)$$

where H, a plastic modulus, is

$$H = \frac{d\bar{\sigma}}{d\epsilon^P} = \frac{3d\bar{\sigma}}{2d\gamma^P} \quad (174)$$

since  $d\gamma^P = 3/2 \cdot d\epsilon^P$  (Eq. (171)).

Elimination of H from Eqs. (173) and (174) gives

$$\sigma'_{ij} = \bar{\sigma} \frac{d\epsilon_{ij}^P}{d\gamma^P} \quad (175)$$

In an equilibrium situation  $\bar{\sigma}$  is equal to the yield strength. Then, during stress relaxation, the amount by which the deviator stress exceeds its equilibrium value is

$$\text{excess deviator} = \sigma'_{ij} - \bar{\sigma} \frac{d\epsilon_{ij}^P}{d\gamma^P} \quad (176)$$

where  $\bar{\sigma}_P$  is the yield strength. The elastic relation between strain and stresses from reference 46 is

$$d\epsilon_{ij} - \frac{\delta_{ij}}{3} \sum_{i=1}^3 d\epsilon_{ii} = \frac{d\sigma'_{ij}}{2\mu} \quad (177)$$

where the terms on the lefthand side equal the strain deviator

$\delta_{ij}$  = the Kronecker delta

$\mu$  = the shear modulus

Equations (176) and (177) are assembled into an equation of the form of Eq. (159) as follows:

$$\frac{d\sigma'_{ij}}{dt} = 2\mu \left( \frac{d\epsilon_{ij}}{dt} - \frac{\delta_{ij}}{3} \sum \frac{d\epsilon_{ii}}{dt} \right) - \frac{\sigma'_{ij} - \bar{\sigma}_P \frac{d\epsilon_{ij}^P}{dY^P}}{T} \quad (178)$$

To verify that this equation has the correct form, we may simplify it to the one-dimensional problem:

$$\frac{d\sigma'_1}{dt} = \frac{4}{3}\mu \frac{d\epsilon_1}{dt} - \frac{\sigma'_1 - \frac{2}{3}Y}{T} \quad (179)$$

The viscous equation corresponding to Eq. (178) is

$$\sigma'_{ij} = \bar{\sigma}_P \frac{d\epsilon_{ij}^P}{d\gamma^P} + 2\eta \left( \frac{d\epsilon_{ij}}{dt} - \frac{\delta_{ij}}{3} \sum \frac{d\epsilon_{ii}}{dt} \right) \quad (180)$$

which is in agreement with the forms of Rouse (Ref. 251, p. 203) and Prager (Ref. 52).

Equation (178) has been constructed to provide for differential changes in the deviator stress. However, under some circumstances it may be necessary to account for large time increments. Therefore, Eq. (178) is integrated to produce the following equation:

$$\sigma'_{ij} = \sigma'_{ij0} + \left[ -\sigma'_{ij0} + \bar{\sigma}_P \frac{d\epsilon_{ij}^P}{d\gamma^P} + 2\eta \left( \frac{d\epsilon_{ij}}{dt} - \frac{\delta_{ij}}{3} \sum \frac{d\epsilon_{ii}}{dt} \right) \right] (1 - e^{-(t-t_0)/T}) \quad (181)$$

where

$\sigma'_{ij}$  = the deviator stress at the end of the time increment

$\sigma'_{ij0}$  = the deviator stress at the beginning of the increment

$t_0$  = the time at the beginning of the increment

For the integration, the strain rate is taken as constant through the time increment. This form of the equation is usable if the ratio

$d\epsilon_{ij}^P / d\gamma^P$  can be estimated. This estimate is made with the aid of

Eq. (175) using elastic estimates for  $\bar{\sigma}$  and  $\sigma'_{ij}$ .



The calculational procedure used in the program has the following steps: first, compute the increments in the deviator stresses from an elastic calculation, then compute  $\bar{\sigma}$  from the elastic deviators. Using Eq. (175) to estimate the ratio of plastic strains, compute a second estimate of the deviator stress from Eq. (181). From these second estimates of deviator stress, recompute  $\bar{\sigma}$  and also compute  $d\gamma^P$  and  $d\epsilon_{ij}^P$ . Compute the new value of yield strength  $\bar{\sigma}_p$ . Then repeat the calculation of Eq. (181) for the third estimate of the deviator stress. We assumed that this double iteration would provide sufficient accuracy in the deviator stresses.

## 6. STABILITY CRITERION FOR TWO-DIMENSIONAL CALCULATIONS

For one-dimensional hydrodynamic calculations a fairly full investigation of stability of the computations has been undertaken by Richtmyer and Morton (Ref. 53) and by Herrmann, et al. (Ref. 54). Wilkins (Ref. 44) has outlined a procedure for establishing the stability of calculations in two dimensions. However, a further development is required for a situation in which real material viscosity is included in one- or two-dimensional calculations.

This new concept for stability is based on the hypothesis that all forms of stability depend simply on an effective sound speed. The addition of artificial viscosity or other types of viscosity tend to require shorter time steps in the calculations because they increase the effective sound speed. This effective sound speed is related to an effective modulus for the material as follows:

$$M_e = \frac{\Delta P + Q}{-\frac{\Delta V}{V}} + \frac{\frac{2}{3} \Delta \sigma'_i}{\epsilon_i - \frac{\Delta V}{3V}} \quad (182)$$

where

$\Delta P$  = the change in pressure at a given cell during the current time increment

$\Delta \sigma'_i$  = the change in deviator stress

$Q$  = the artificial viscous stress

$\frac{\Delta V}{V}$  = the relative change in volume

the strain in the  $i^{\text{th}}$  direction

First a calculation is made for the one-dimensional problem to compare the results from the hypothesis above with that of the more usual approach followed by Herrmann, et al. (Ref. 54). The linear and quadratic forms for the artificial viscosity are

$$Q = C_L \Delta X C \frac{\partial \rho}{\partial t} + \rho C_Q^2 \left( \frac{1}{\rho} \frac{\partial \rho}{\partial t} \right)^2 \quad (183)$$

where

$C_L, C_Q$  = coefficients of the linear and quadratic terms for artificial viscosity

$\Delta X$  = cell thickness

$C$  = sound speed for elastic waves

$\rho$  = density

$t$  = time.

This expression is used only if  $Q$  is positive, that is, for compression;  $Q$  is set to 0 for rarefaction waves. Equation (183) is transformed by using the identities relating density and specific volume, and the following equation describing mass conservation

$$\frac{1}{\rho} \frac{\partial \rho}{\partial t} = - \frac{\partial u}{\partial x} \quad (184)$$

Equation (183) then takes the following form in which the absolute value sign is used with the change in particle velocity so that  $Q$  will be positive in compression.

$$Q = - \frac{\Delta V}{V} \rho \frac{\Delta X}{\Delta t} [C_Q^2 |\Delta u| + C_L C] \quad (185)$$

where

$\Delta t$  = the time increment used in the computations

$V$  = the specific volume.

From Eq. (185), a modulus can be defined as in Eq. (182), that is,

$$M_Q = \frac{Q}{-\frac{\Delta V}{V}} = \rho \frac{\Delta X}{\Delta t} [C_Q^2 |\Delta u| + C_1 C] \quad (186)$$

Then the effective sound speed, which will govern stability of the calculations, is from Eqs. (182) and (186)

$$\bar{c}^2 = \frac{M_e}{\rho} = \frac{\Delta P}{-\rho \frac{\Delta V}{V}} + \frac{Q}{-\rho \frac{\Delta V}{V}} + \frac{\frac{2}{3} \Delta \sigma'_i}{\rho \left( \epsilon_i - \frac{\Delta V}{3V} \right)} \quad (187a)$$

$$= \frac{K}{\rho} + \frac{M_Q}{\rho} + \frac{\frac{4}{3} \mu}{\rho} \quad (187b)$$

$$= c^2 + (C_Q^2 |\Delta u| + C_1 C) \frac{\Delta X}{\Delta t} \quad (187c)$$

where

$K$  = bulk modulus

$\mu$  = shear modulus

$C$  = the usual sound speed based on these moduli

For stable calculations, the Courant-Friedrichs-Lewy condition as follows is used to determine the time increment permitted

$$\Delta t \leq \frac{\Delta X}{C^*} \quad (188)$$

where  $C^*$  is usually interpreted to be the local sound speed, but here it will be taken as the effective sound speed  $\bar{C}$  given by Eq. (187). Insertion of Eq. (187) into Eq. (188) gives

$$\Delta t^2 = \frac{\Delta X^2}{\bar{C}^2} = \frac{\Delta X^2}{c^2 + (c_Q^2 |\Delta u| + c_1 c) \frac{\Delta X}{\Delta t}} \quad (189)$$

When this quadratic is solved for the time increment, the criterion is found to be

$$\Delta t = \frac{\Delta X}{C} \left[ - \left( c_Q^2 \frac{|\Delta u|}{C} + c_1 \right) + \sqrt{\left( c_Q^2 \frac{|\Delta u|}{C} + c_1 \right)^2 + 1} \right] \quad (190)$$

This expression is identical with that found on page 73 of reference 54. Hence the new concept does appear to give the correct stability criterion for one-dimensional flow.

For multidimensional problems, the last term in Eq. (187a) is taken as the maximum of the values in the three principal directions. An alternate, and simpler, course is to use the last term from Eq. (187b) with  $\mu$  equal to the largest shear modulus. Then the effective sound speed is

$$\bar{C}^2 = \frac{\Delta P + Q}{-\rho \frac{\Delta V}{V}} + \frac{4\mu_{\max}}{3\rho} \quad (191)$$

This criterion is sufficiently general for the stress relaxation problem.

## 7. RESULTS OF VOID GROWTH COMPUTATIONS

Three computations were made and analyzed to assist in defining constitutive relations for materials with voids and to indicate the shape of the void. Variables in the three calculations are given in Table XVIII. The only difference between calculations 4 and 5 was that work hardening was permitted in 4, varying the yield strength from 1 to 4 kbar. In all three problems the boundary velocity was constant, leading to a constant engineering strain rate on the cylinder. During loading the stress initially rises rapidly in response to the strain. Then, as the void growth begins to account for larger proportions of the applied strain, the stress reaches a peak (as shown in Figure 81) and then declines. The peak stress listed in Table XVIII is the force acting on the planar face of the cylinder divided by the area of that face.

A comparison of calculations 4 and 5 shows the effect of strong work hardening. Comparison of runs 5 and 8 gives some indication of the effect of relative void volume.

TABLE XVIII  
VOID GROWTH COMPUTATIONS

No.	$R_0$ ( $\mu$ )	$R_{final}$ ( $\mu$ )	$R_{cyl}$ ( $\mu$ )	$\dot{\epsilon}$ ( $10^6/sec$ )	$(\sigma_1)_{max}$ (kbar)	Yield (kbar)	Duration ( $\mu sec$ )	$V_v/V_0$ (pct)
4	1.0	1.75	3	2.67	22.5	1 to 4	0.047	2.6%
5	1.0	1.68	3	2.67	20.3	1	0.052	2.6
8	1.0	2.68	10	0.80	33.6	1	0.045	0.067

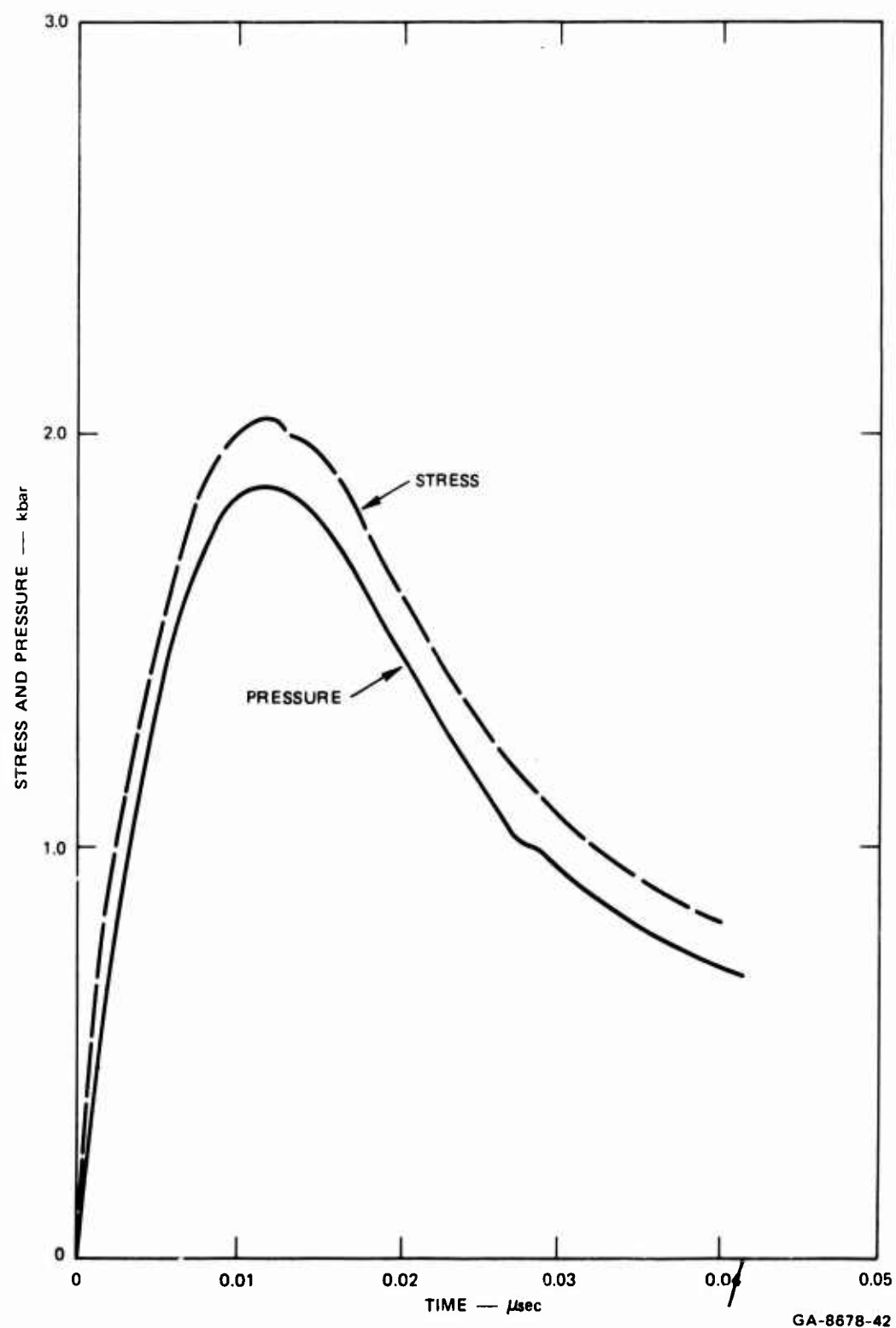


FIGURE 81 VARIATIONS OF AXIAL STRESS AND PRESSURE WITH TIME FOR COMPUTATION 5

a. Void Shape Changes

The voids appear to grow in a stable manner under the tensile loading and to maintain an approximately spherical shape. An indication of the growth pattern is shown in Figure 82; the void surface is a smooth curve at all times, and the trajectories of the coordinate points are nearly radial from the center of the void. The eccentricity that does appear in the three calculations is shown in Figure 83, along with the eccentricity of the loading. The eccentricity of both loading

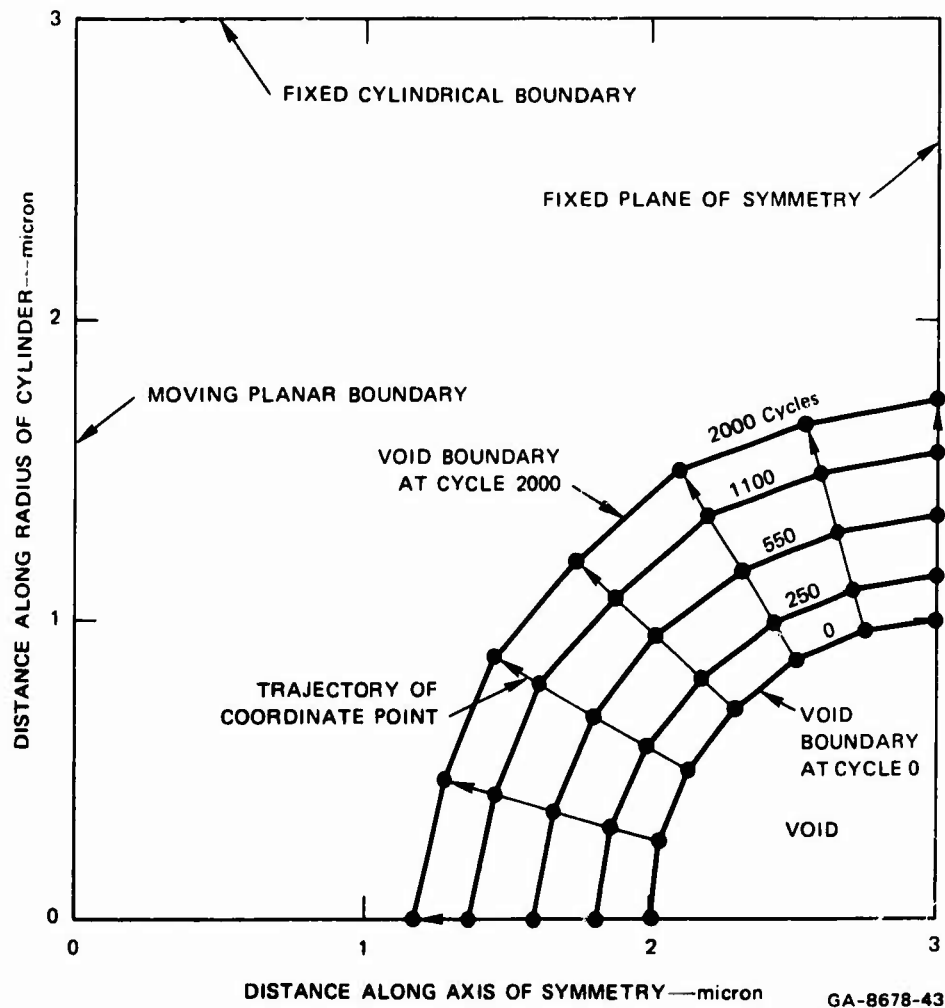


FIGURE 82 SUCCESSIVE VOID SURFACES DURING CALCULATION 4



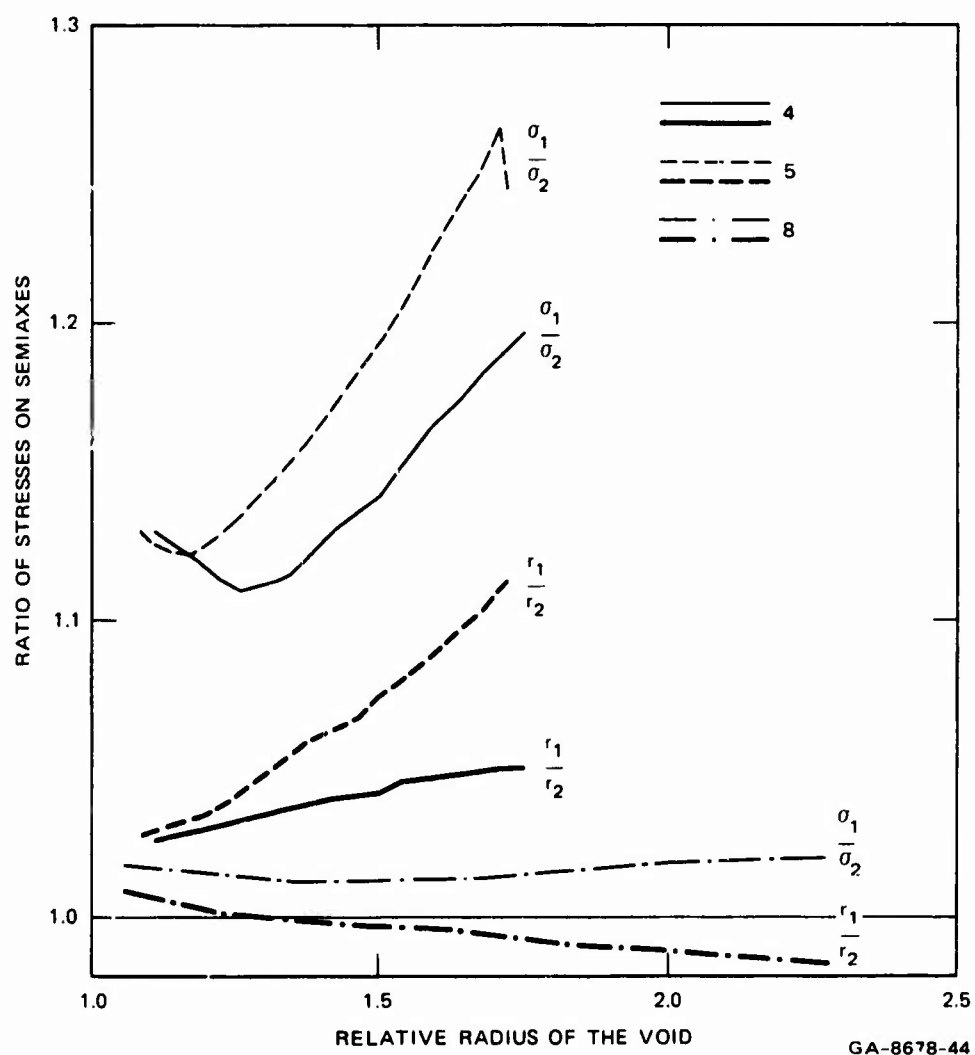


FIGURE 83 ECCENTRICITY OF THE VOID AND OF THE LOADING

and void increases with growth for the two large void volume cases (4 and 5). For the third case, the change in loading and void eccentricity is almost negligible. For the two with marked eccentricity, the stress eccentricity is double or triple the void eccentricity. This result contrasts with Berg's analysis (Ref. 2) of growth of a circular void in a plate under plane stress; the two eccentricities were equal in his case. We also note that there is less eccentricity for case 4, with the larger yield strength.

b. Pressure-Volume Curves

The VOID calculations were intended to supply an equation of state for use in a one-dimensional code such as SRI PUFF. Such an equation of state is a relation between the average stresses on a gross section and the specific volume of the solid material (or gross specific volume, or other macroscopic strain quantity). As usual, these stresses were separated into a pressure term and a deviator stress term, each being an average over the gross section.

For estimation purposes, we assumed that the pressure-volume relation for the material with voids had the form

$$\frac{\bar{P}_1}{1 - \alpha V_{v1}} - \frac{\bar{P}_0}{1 - \alpha V_{v0}} = K \frac{V_{s1} - V_{s0}}{\frac{1}{2} (V_{s1} + V_{s0})} \quad (192)$$

where

$\bar{P}_1$  and  $\bar{P}_0$  = average pressures acting on gross sections at the end and beginning of a time increment

$V_{v1}$  and  $V_{v0}$  = relative void volumes at the end and beginning of the time increment

$V_{s1}$  and  $V_{s0}$  = specific volumes of the solid material at either end of the time increment

$K$  = the bulk modulus of the solid material

$\alpha$  = a constant

To evaluate the appropriateness of Eq. (192), we plotted the average pressures as a function of the specific volume of the solid for the three runs, as shown in Figures 84, 85, and 86. In each case the computed

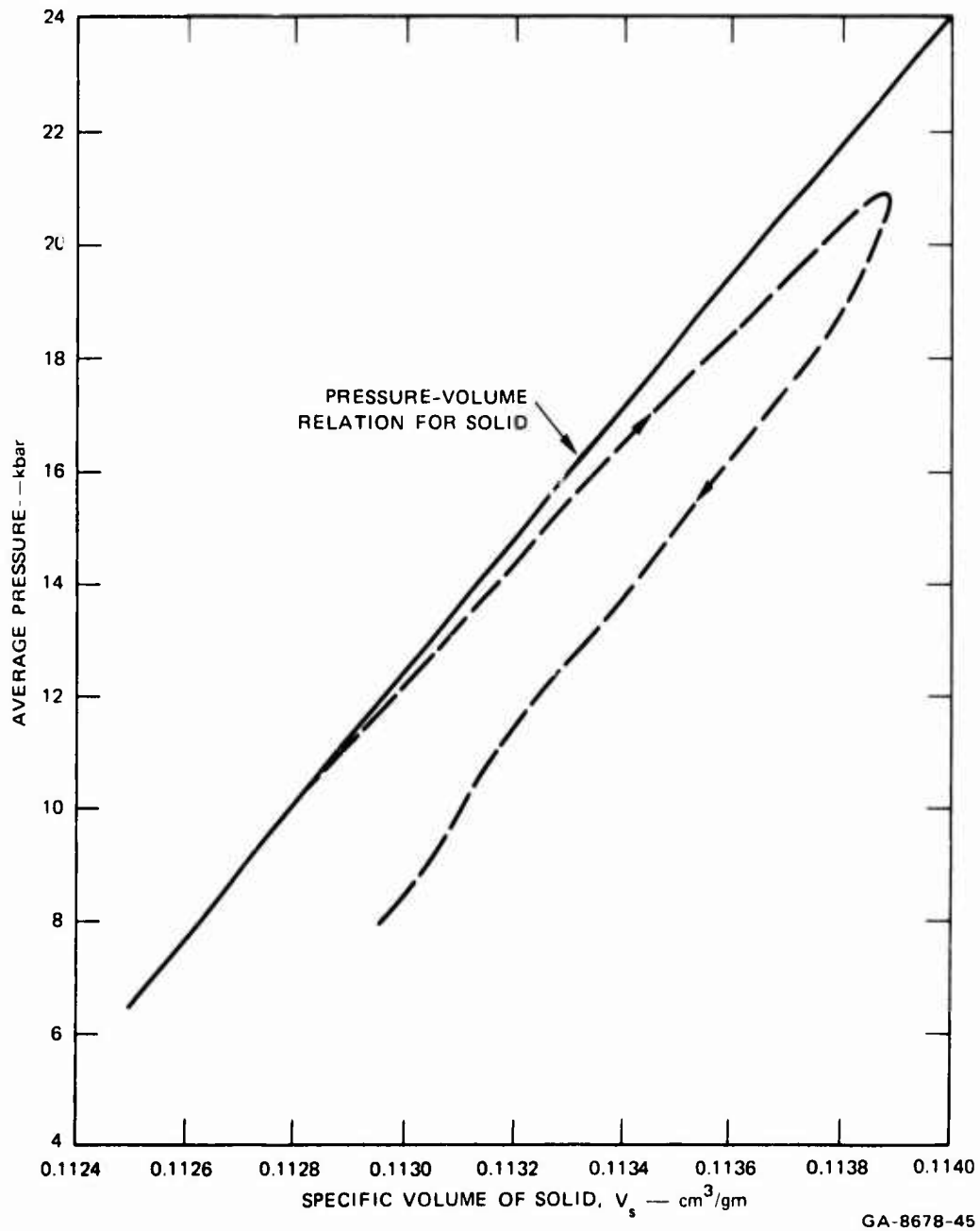


FIGURE 84 PRESSURE-VOLUME RELATION FROM CALCULATION 4

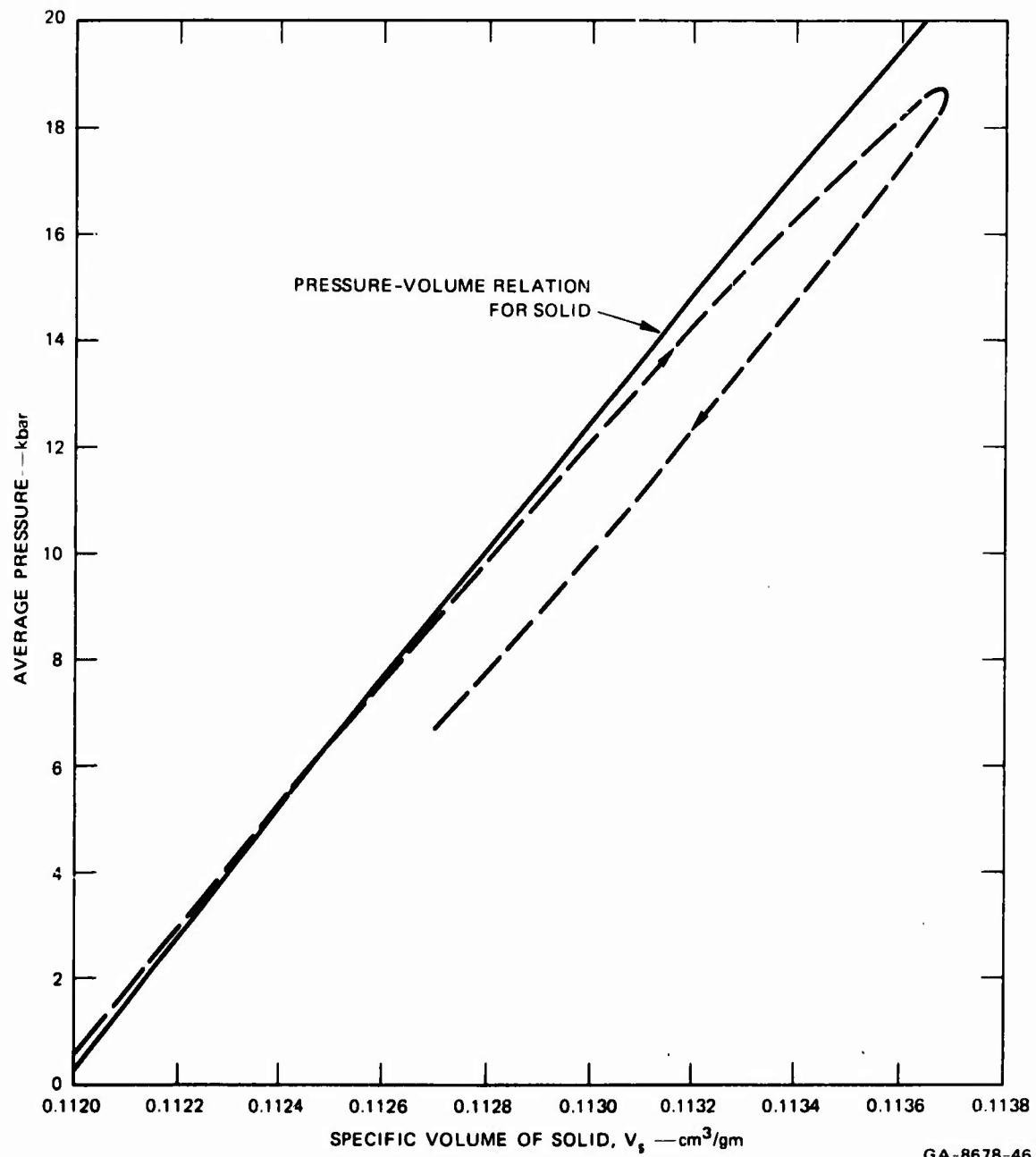


FIGURE 85 PRESSURE-VOLUME RELATION FROM CALCULATION 5

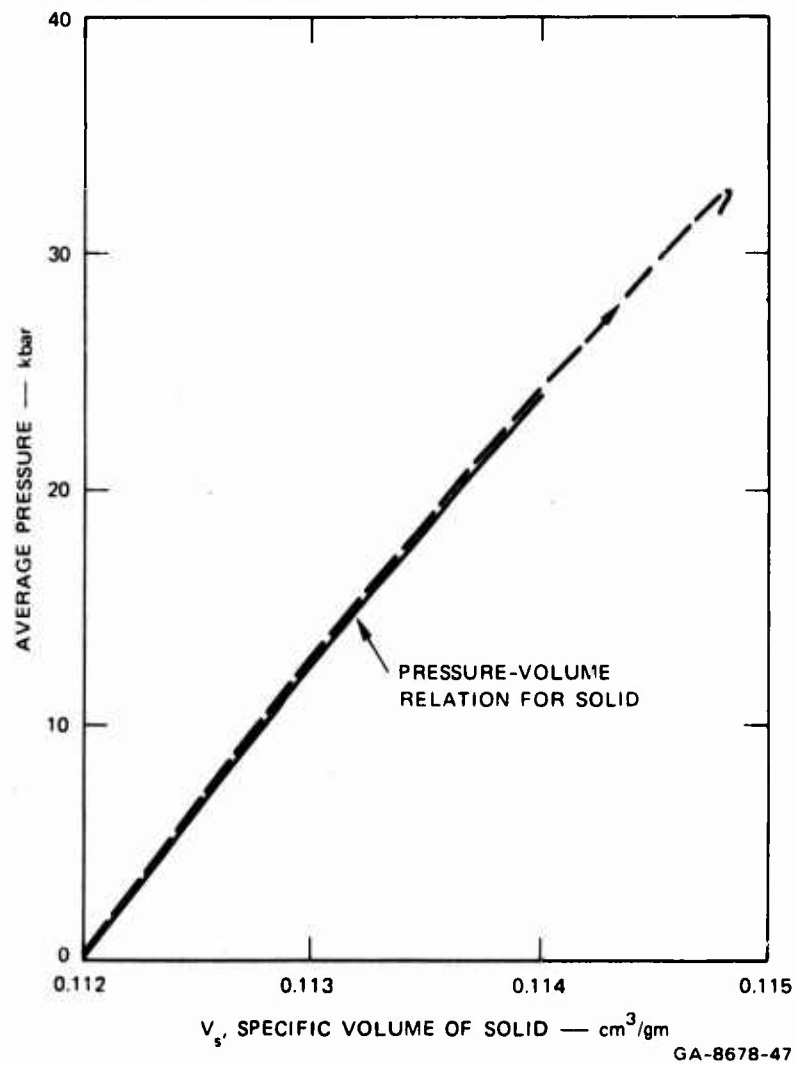


FIGURE 86 PRESSURE-VOLUME RELATION FROM CALCULATION 8

curves approximate the pressure-volume relation for the solid at small void volumes. As the void volume increases, there is greater deviation. The data in Figures 84 and 85 were used in Eq. (192) to find values of  $\alpha$ . The results, shown in Figure 87, indicate that  $\alpha = \sim 2$  during most of the growth process. Therefore, in the SRI PUFF calculations we use Eq. (192) and  $\alpha = 2$  for the pressure portion of the equation of state.

### c. Deviator Stress

The deviator stress was also obtained from the three calculations. These stresses are given as a function of relative void volume in Figures 88, 89, and 90. To organize this information, we presumed that the deviator stress has form

$$\sigma' = \frac{4}{3} \mu (1 - \beta V_v) \frac{\Delta V}{V} \frac{\sigma' - \frac{2}{3} Y}{T} \quad (193)$$

where

$\mu$  = the shear modulus

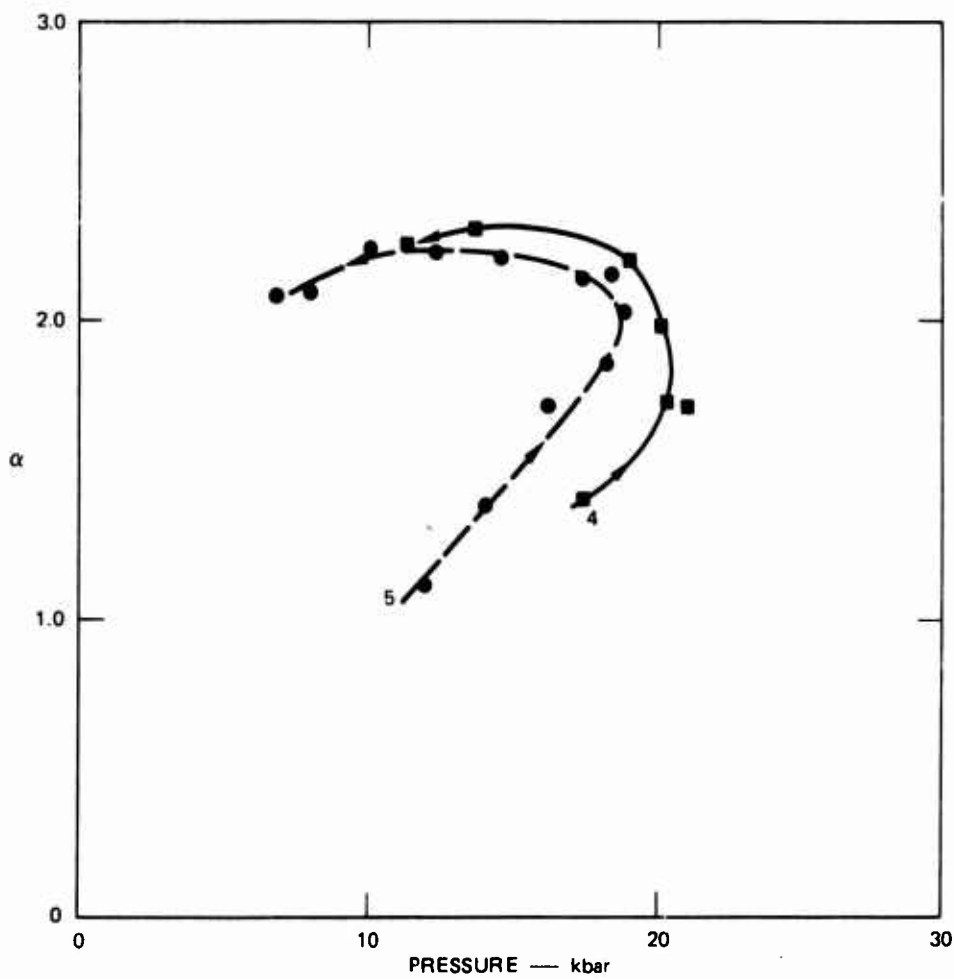
$\beta$  = a constant ( $\sim 4$ )

$V_v$  = the relative void volume

$T = \mu/\eta$ , a relaxation time

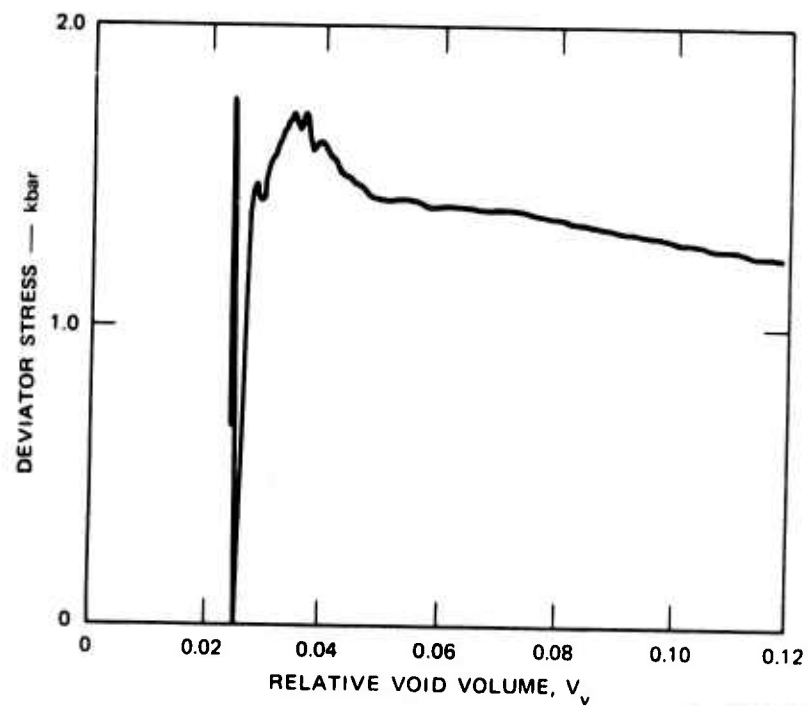
$\eta$  = the coefficient of viscosity

Thus, the elastic modulus is reduced as a function of void volume while the second term on the right allows for stress relaxation. This equation describes the results in Figures 88 and 89 fairly well with a coefficient of viscosity of 250 poise, i.e., the one used in the microscopic calculations. The differences between Figures 88 and 89 are readily explained



GA-8678-48

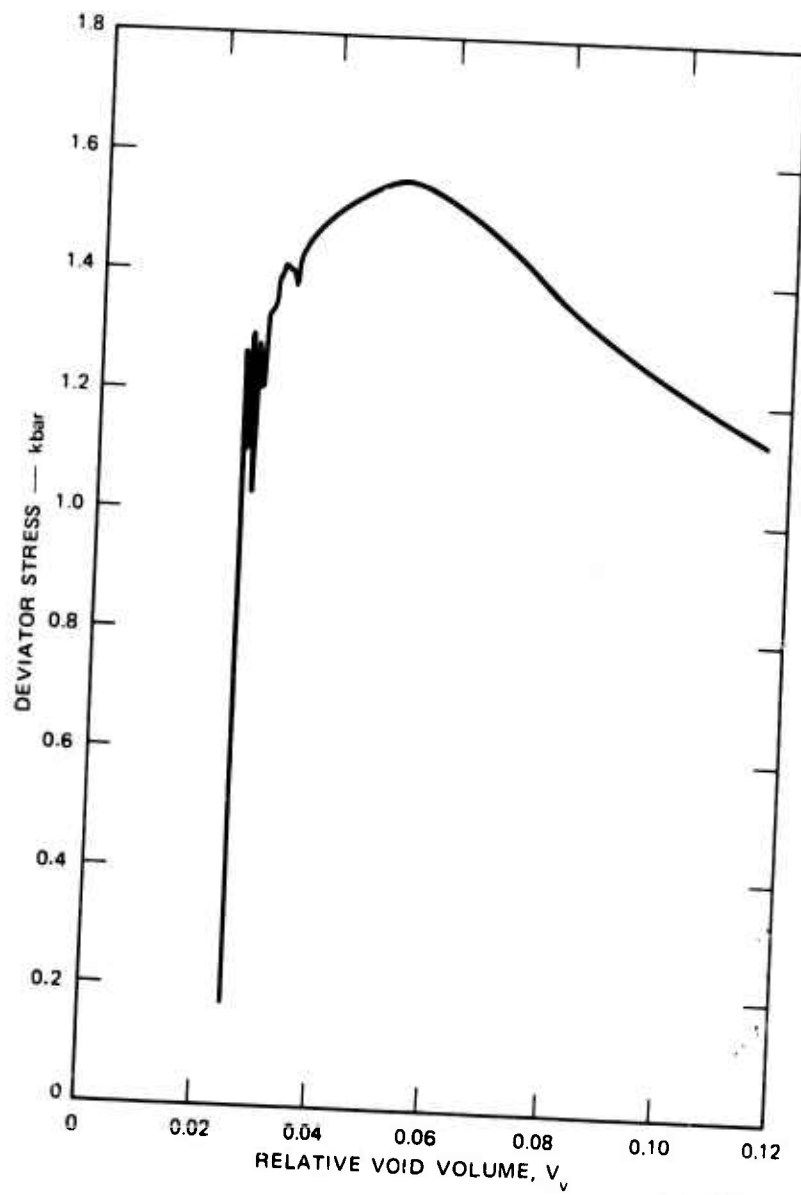
FIGURE 87 VARIATION OF  $\alpha$  FROM COMPUTATIONS 4 AND 5



GA-8678-49

FIGURE 88 DEVIATOR STRESS VARIATIONS FROM CALCULATION 4





GA-8678-50

FIGURE 89 DEVIATOR STRESS VARIATIONS FROM CALCULATION 5

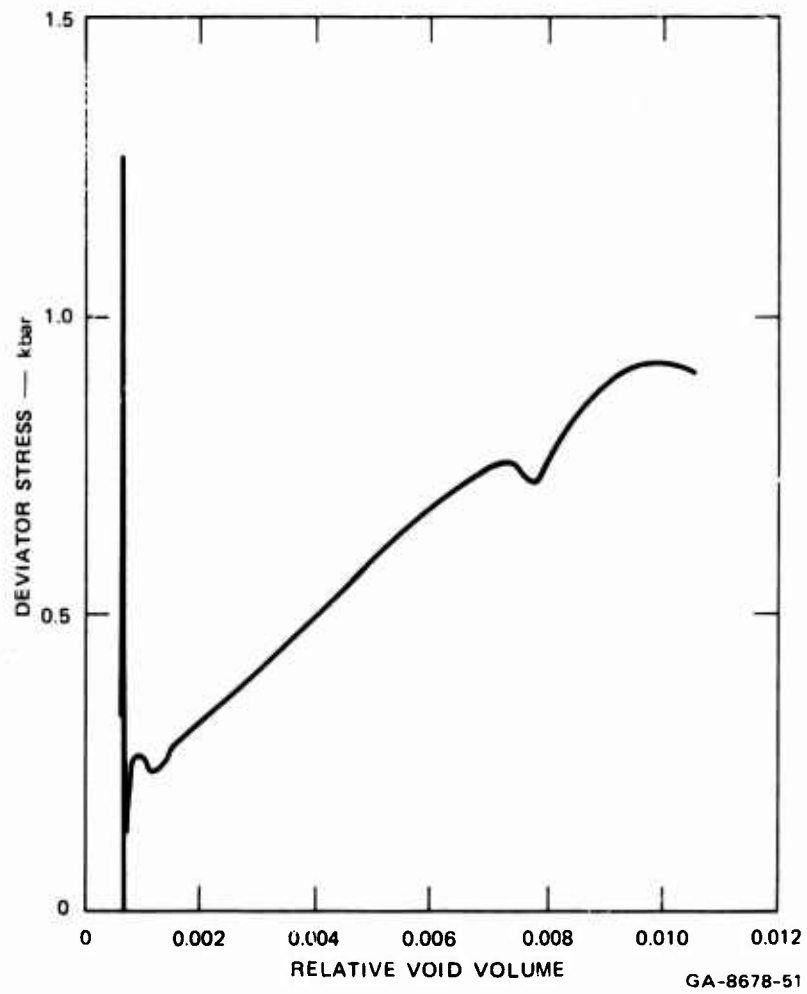


FIGURE 90 DEVIATOR STRESS VARIATIONS FROM CALCULATION 8

by the work hardening permitted in calculation 4. The results of Figure 90 do not fit the form of Eq. (193). This difference has not been explained but indicates that the functional form of the deviator stress is more complex than Eq. (193). Currently an integrated form of Eq. (193) is used in the ductile fracture routine for the deviator stress calculations.

d. Void Growth Rate

According to the spherically symmetric solution and to Berg's plane strain solution (Ref. 2), the growth rate of a void in a viscous material is given by

$$\dot{R} = \frac{\bar{p} - p_0}{4\eta} R \quad (194)$$

where

$\bar{p}$  = the pressure in the spherical case and the average of the two applied stresses in the planar case

$\eta$  = the viscosity

$p_0$  = a threshold pressure

The growth rate results from the VOID calculations, shown in Figures 91-93, generally follow the form of Eq. (194). The slight scatter in the points is probably caused by oscillations. For case 4, where work hardening was permitted, the initial value of  $p_0$  is about zero, whereas it is 3 kbar on the unloading branch of the curve in Figure 91. For calculation 5, the threshold pressure is between 0 and 0.3 kbar. For case 8, the threshold appears to be about 1 kbar. The velocity relationships tend to curve upward, exhibiting a somewhat smaller

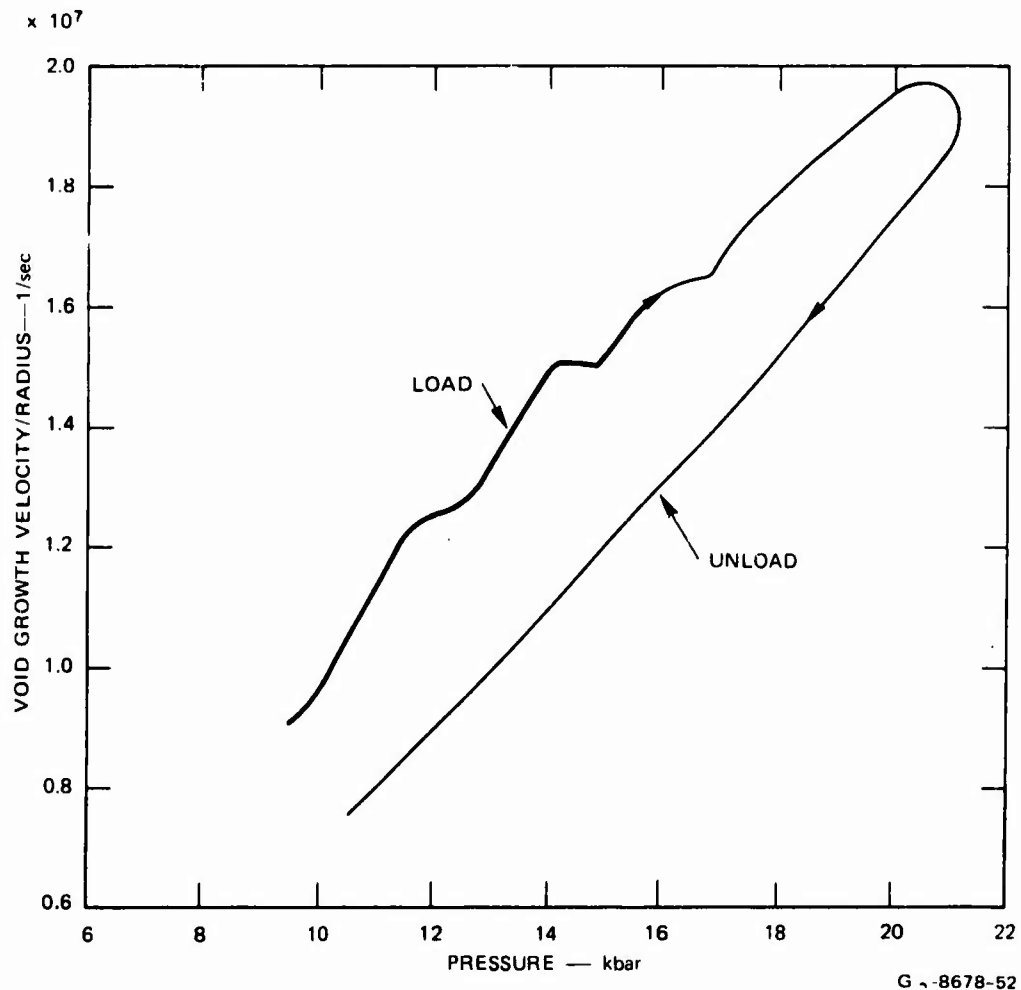


FIGURE 91 VOID GROWTH AS A FUNCTION OF PRESSURE FROM CALCULATION 4

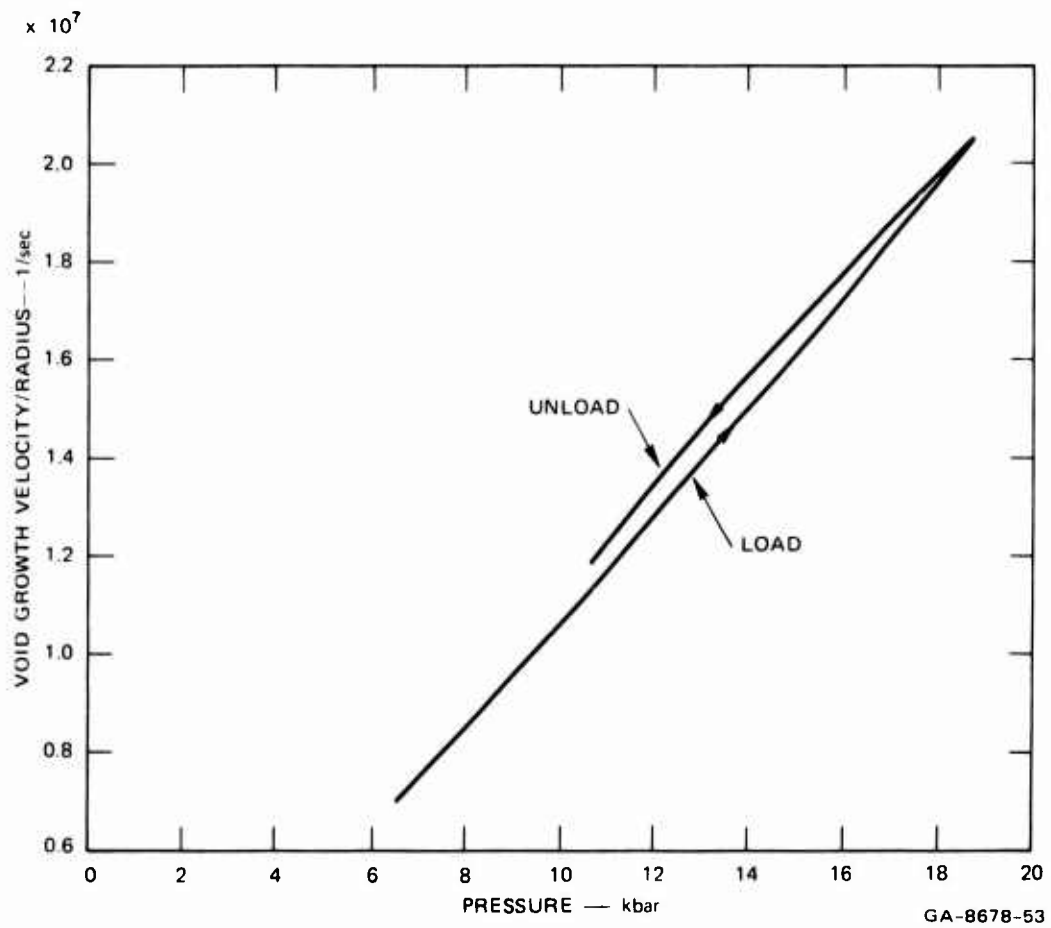


FIGURE 92 VOID GROWTH VELOCITY AS A FUNCTION OF PRESSURE FROM CALCULATION 5

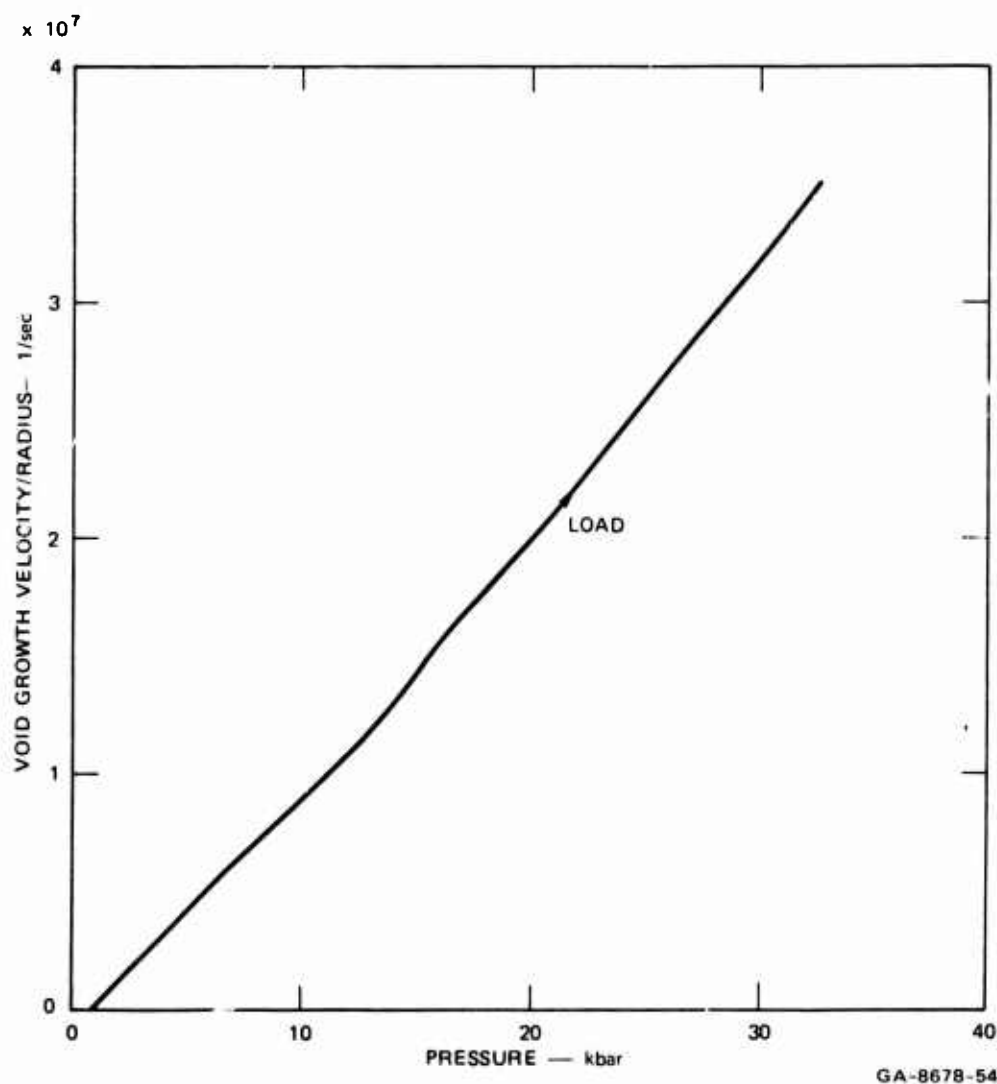


FIGURE 93 VOID GROWTH VELOCITY AS A FUNCTION OF PRESSURE FROM CALCULATION 8

viscosity than the 250 poise used. For calculation 5,  $\eta$  from Eq. (194) is 225 poise;  $\eta$  is 200 poise for calculation 8. This upward curvature and the variation of  $\eta$  from the value used in VOID may have been caused by the excessive cell distortion that occurred during all calculations, but especially during 8.

A comparison of the foregoing VOID results with the earlier results of Berg (Ref. 2) and the spherically symmetric void calculations of Appendix III suggests that Eq. (194) should be used with  $\eta$  as the

value of the material viscosity and  $p_0$  as  $2Y/3$ . These values are used in the ductile fracture calculations.

e. Summary

In the VOID calculations, the voids tend to retain a shape that is more spherically symmetric than the applied stress field. The computed form of the void is very smooth, showing no evidence of local instabilities or other problems, although the adjacent cells undergo very large deformations.

Stress-volume relations for the damaged material can be constructed by considering the pressure and deviatoric stress response of the solid phase only.

The viscous growth relation derived for simpler geometries appears to hold for this microscopically one-dimensional flow also. The threshold stress for growth is small, of the order of the yield strength.

## 8. LISTING OF THE VOID PROGRAM

In the following pages the VOID program and its two subroutines, SWEEPV and SCRIBE, are listed with their flow charts. Next is a set of input decks and some sample printout. The program was written for the CDC 6400 at SRI in Fortran IV. The memory required is about 100,000 octal words.

The VOID program, as presented, is a special purpose program and therefore will not have wide application. However, it may serve as the basis of a more general two-dimensional code or of other special purpose codes.

The input cards and variables are as follows:

- Card 1: Free field format, heading only.
- Card 2: Control variables. Format is A10, I10, A10, I10.  
IMAX is the maximum number of cycles permitted.  
NMTRLS is the number of materials.
- Card 3: Characteristics of the calculations. Format is 4(A10, E10.3).  
DELTAT is the maximum time step, sec.  
SMAX is the uniform one-dimensional stress used in the initialization, dyn/cm<sup>2</sup> (positive in tension).  
XD(2) is the velocity of the plane of forcing, cm/sec.  
TS is the stop time of the calculation, sec.
- Card 4: Print controls. Format 3(A10, I10).  
IPRINT is the modular number of cycles at which a complete listing is given of positions and stresses.  
NJED is the number of historical listings requested.  
KPRINT is not used.



Card 5: Historical print controls. Format A10, 7(I6, I2, I2).

JEDT is a number associated with a variable for which a historical listing is desired. The correspondence between JEDT and the variable is spelled out in SWEEPV following location 660. The location number is 670 + JEDT.

JEDK is the K coordinate of the desired variable.

JEDJ is the J coordinate of the desired variable.

Up to 60 values of the JEDs may be used so that several cards may be required.

Card 6: First material card. Format 3A10, E10.3, A10, A8, I2.

AMAT is the material name.

RHO is the density, gm/cm<sup>3</sup>.

NYAM is an indicator for yield behavior:

- 0 no yield strength
- 1 perfect plasticity
- 2 viscous, work hardening.

Cards 7

and 8: Equation of state parameters. Format 4(A10, E10.3).

CA, CB, CC are parameters of the hydrostat (dyn/cm<sup>2</sup>):  $P = CA \cdot \mu + CB \cdot \mu^2 + CC \cdot \mu^3$ .

EQSTE is not implemented.

EQSTG is the Gruneisen ratio.

EQSTH is not implemented.

PMIN is the minimum pressure permitted, dyn/cm<sup>2</sup>.

YCC is the yield strength, dyn/cm<sup>2</sup>.

Card 8a: Yield card, required only for NYAM  $\neq$  0. FORMAT 4(A10.3).

For NYAM = 1, YCC, YCT, and MU are used.

For NYAM = 2, FB, FM, MU, and ETA are used.

YCC is yield in compression (and tension for 2nd model).

YCT is yield in tension, dyn/cm<sup>2</sup>.

MU is the shear modulus, dyn/cm<sup>2</sup>.

FB is  $b$ , a work-hardening parameter in Eq. (162), dimensionless.

FM is  $M$ , a work-hardening modulus in Eq. (162),  $\text{dyn/cm}^2$ .

ETA is the material viscosity, poise.

Card 9: Geometrical Layout. Format 4(A10, E10.3).

RIN is the radius of the void, cm.

ROUT is the radius of the cylinder, cm.

NRAD is the number of cell rings in a radial direction.

NTHETA is the number of cells in a circumferential direction in any cell ring.

```

PROGRAM VOID(INPUT,OUTPUT,TAPE5=INPUT,TAPE6=OUTPUT,TAPE8=
1  OUTPUT,TAPE4,TAPE3,PUNCH)
REAL MU,MCON
COMMON CA(4),CB(4),CC(4),EQSTE(4),EQSTG(4),EQSTH(4),AMAT(4),MU(4),
1  RHO(4),YCC(4),YCT(4),MCON(4),SCON(4),PMIN(4),SP(4)
2  ,FM(4),FB(4),ETA(4)
COMMON IMAX,IPRINT,ICYCLE,KINT,KMID,KMN,KMX,JMX,IRMAX,IRT,KT,JT,
1  KWF,I STATE,IFLAG,J1,MIRR,IJBUNO,IFCUT,DRED,URMIN,KCUT,L ALPHA,
2  NDIM
COMMON NKED,KPRINT,KEDR(20),KED(20),NJED,JEDR(60),JEDT(60),
1  JEDK(60),JEDJ(60),NSCRIBE,NJKED,KEDIT(120)
COMMON R(120),SK(20),SJ(60),XDK(20),VK(20)
COMMON JM(2),KM(2),AKEA(2),DELX(2),DELY,XD(2),VCON,CQSQ,STRESS
COMMON TYME,XDINT,DELTA,DELTH,DELTHW,DELTMIN,DISCPT(10)
COMMON CALTIM
COMMON AX(45,15),AXH(45,15),AXDH(45,15),IMA(45,15),
1  AY(45,15),AYH(45,15),AYDH(45,15),AE(45,15),
2  AA(45,15),AV(45,15),AP(45,15),
3  ASXX(45,15),ASY(45,15),ASXY(45,15),ASTT(45,15),
4  ATXX(45,15),ATY(45,15),ATXY(45,15),ATTT(45,15),
5  ASBARP(45,15),ASBAR(45,15),AVZ(45,15)
C
C ***** READ AND PRINT INPUT DATA
C
JA=45 $ KA=15 $ JB=KB=0
III=770+22*JA*KA
100 DO 101 I=1,III
101 CA(I)=0.
PRINT 1000
CALL SDATE(DISCPT(2))
DISCPT(1)=10H DATE =
READ 1100,(DISCPT(I),I=3,10)
IF (EOF,5) 102,103
102 STOP 70001
103 PRINT 1100,(DISCPT(I),I=1,2)
PRINT 1100,(DISCPT(I),I=3,10)
CALL SECOND(TIMEO)
READ 1102,A1,IMAX,A2,NMTRLS
PRINT 1102,A1,IMAX,A2,NMTRLS
CQSQ=4.
READ 1104,A1,DELTA,A2,SMAX,A3,XD(2),A4,TS
PRINT 1104,A1,DELTA,A2,SMAX,A3,XD(2),A4,TS
READ 1103,A1,IPRINT,A2,NJED,A3,KPRINT
PRINT 1103,A1,IPRINT,A2,NJED,A3,KPRINT
NJKED=NJED
120 IF (NJED .EQ. 0) GO TO 130
N1=1
125 N2=MINO(N1+6,NJED)
READ 1125,A1,(JEDT(I),JEDK(I),JEDJ(I),I=N1,N2)
PRINT 1125,A1,(JEDT(I),JEDK(I),JEDJ(I),I=N1,N2)
IF (N2 .EQ. NJED) GO TO 130
N1=N2+1
GO TO 125
130 CONTINUE
VCON=.666667*3.1416
DU 150 M=1,NMTRLS
READ 1130,AMAT(M),A1,A2,RHO(M),A3,A4,NYAM
PRINT 1130,AMAT(M),A1,A2,RHO(M),A3,A4,NYAM
READ 1104,A1,CA(M),A2,CB(M),A3,EQSTE(M),A4,EQSTG(M),A5,EQSTH(M),
1  A6,CC(M),A7,PMIN(M),A8,YCC(M)
PRINT 1104,A1,CA(M),A2,CB(M),A3,EQSTE(M),A4,EQSTG(M),A5,EQSTH(M),
1  A6,CC(M),A7,PMIN(M),A8,YCC(M)
IF (NYAM-1) 140,135,137
135 READ 1104,A1,YCCM,A2,YCTM,A3,MU(M)
PRINT 1104,A1,YCCM,A2,YCTM,A3,MU(M)
YCC(M)=0.666667*YCCM*YCCM
YCT(M)=0.666667*YCTM*YCTM
GO TO 140
VOID0010
VOID0020
VOID0030
VOID0040
VOID0050
VOID0060
VOID0070
VOID0080
VOID0090
VOID0100
VOID0110
VOID0120
VOID0130
VOID0140
VOID0150
VOID0160
VOID0170
VOID0180
VOID0190
VOID0200
VOID0210
VOID0220
VOID0230
VOID0240
VOID0250
VOID0260
VOID0270
VOID0280
VOID0290
VOID0300
VOID0310
VOID0320
VOID0330
VOID0340
VOID0350
VOID0360
VOID0370
VOID0380
VOID0390
VOID0400
VOID0410
VOID0420
VOID0430
VOID0440
VOID0450
VOID0460
VOID0470
VOID0480
VOID0490
VOID0500
VOID0510
VOID0520
VOID0530
VOID0540
VOID0550
VOID0560
VOID0570
VOID0580
VOID0590
VOID0600
VOID0610
VOID0620
VOID0630
VOID0640
VOID0650
VOID0660
VOID0670
VOID0680

```

PROGRAM VOID

```

137 READ 1104,A1,FB(M),A2,FM(M),A3,MU(M),A4,ETA(M)          VOID0690
    PRINT 1104,A1,FB(M),A2,FM(M),A3,MU(M),A4,ETA(M)        VOID0700
    JAKA=JA*KA                                              VOID0710
    DO 139 I=1,JAKA                                         VOID0720
139 ASBARP(I)=YCC(M)                                       VOID0730
140 SP(M)=SQRT((CA(M)+1.333333*MU(M))/RHU(M))             VOID0740
150 SCON(M)=2.*MU(M)                                       VOID0750
C                                                         VOID0760
C ***** LAYOUT FOR SPHERICAL VOIDS                      VOID0770
C                                                         VOID0780
600 READ 1160,A1,RIN,A2,ROUT,A3,NRAD,A4,NTHETA             VOID0790
    NTHETA=((NTHETA-1)/2)*2+2                               VOID0800
    PRINT 1160,A1,RIN,A2,ROUT,A3,NRAD,A4,NTHETA           VOID0810
    XDINT=0.                                                VOID0820
C     SIGN CONVENTION IS NOW POSITIVE IN TENSION          VOID0830
    EME=-YCC(1)/(2.*MU(1))                                  VOID0840
    SE=0.6667*YCC(1)-((CC(1)*EME+CB(1))*EME+CA(1))*EME    VOID0850
    IF (SMAX .GT. SE) GO TO 605                             VOID0860
C     ELASTIC ROUTE                                       VOID0870
    EMU=-SMAX/(CA(1)+1.333*MU(1))                          VOID0880
    EMM=-SMAX/(CA(1)+1.333*MU(1))*(CB(1)+EMO*CC(1))*EMU   VOID0890
    PMAX=-((CC(1)*EMM+CB(1))*EMM+CA(1))*EMM               VOID0900
    EMAX=0.5*SMAX*(1./(1.+EMM)-1.)/RHU(1)                 VOID0910
    VMAX=1./((1.+EMM)*RHU(1))                             VOID0920
    ASBAR(1,1)=1.5*(SMAX-PMAX)                             VOID0930
    GO TO 607                                               VOID0940
C     PLASTIC ROUTE                                       VOID0950
605 EMO=- (SMAX-0.6667*YCC(1))/CA(1)                       VOID0960
    EMM=- (SMAX-0.6667*YCC(1))/(CA(1)+EMO*(CB(1)+EMO*CC(1))) VOID0970
    PMAX=-((CC(1)*EMM+CB(1))*EMM+CA(1))*EMM               VOID0980
    ASBAR(1,1)=YCC(1)                                       VOID0990
    VE=1./((1.+EME)*RHU(1))                                VOID1000
    VMAX=1./((1.+EMM)*RHU(1))                              VOID1010
    EMAX=0.5*SE*(VE-1./RHU(1))+ (SMAX+SE)*(VMAX-VE)      VOID1020
607 V=VMAX*RHO(1)                                         VOID1030
    SD=SMAX-PMAX                                           VOID1040
    SU2=-.5*SD                                             VOID1050
    PRINT 1607,SE,PMAX,EME,EMO,EMM,VE,VMAX,EMAX          VOID1060
    RINCR=(RIN/ROUT)**(1./FLOAT(NRAD))                    VOID1070
C     LAY OUT ALONG AXIS OF SYMMETRY AND REFLECTION BOUNDARY VOID1080
    N=NTHETA+1                                             VOID1090
    KINT=NRAD+1                                           VOID1100
C     SET COORDINATES OF CORNER POINTS                    VOID1110
    AY(1,N)=AYH(1,N)=ROUT                                  VOID1120
    AX(1,N)=AXH(1,N)=ROUT                                  VOID1130
    AX(KINT,1)=AXH(KINT,1)=ROUT-RIN                      VOID1140
    AY(KINT,N)=AYH(KINT,N)=RIN                            VOID1150
    AX(KINT,N)=AXH(KINT,N)=ROUT                           VOID1160
C     LAYOUT X AND Y ALONG RIGHT BOUNDARY AND X ON AXIS OF ROTATION VOID1170
    RF=ROUT                                                VOID1180
    DO 610 I=2,NRAD                                        VOID1190
    RF=RF*RINCR                                           VOID1200
    AX(I,N)=AXH(I,N)=ROUT                                  VOID1210
    AY(I,N)=AYH(I,N)=RF                                    VOID1220
610 AX(I,1)=AXH(I,1)=ROUT-RF                              VOID1230
    IF (IJBUND .EQ. 4) GO TO 650                          VOID1240
    THETA=3.14159265/(2.*FLOAT(NTHETA))                  VOID1250
    NTH=NTHETA/2+1                                        VOID1260
    DO 630 J=2,NTH                                         VOID1270
    N1=N+1-J                                              VOID1280
    N2=N+2-J                                              VOID1290
    AY(1,J)=AYH(1,J)=ROUT*TAN((J-1)*THETA)               VOID1300
    AX(1,N1)=AXH(1,N1)=ROUT-AY(1,J)                      VOID1310
    AX(1,J)=AXH(1,J)=0.                                    VOID1320
    AY(1,N1)=AYH(1,N1)=ROUT                               VOID1330
    RINCR=(RIN/ROUT*COS((J-1)*THETA))** (1./NRAD)        VOID1340
    DO 625 K=2,KINT                                        VOID1350
    AY(K,N1)=AYH(K,N1)=AY(K-1,N1)*RINCR                  VOID1360

```

PROGRAM VOID (Continued)

```

AX(K,J)=AXH(K,J)=ROUT-AY(K,N1)
AY(K,J)=AYH(K,J)=AY(K-1,J)*RINCR
AX(K,N1)=AXH(K,N1)=ROUT-AY(K,J)
AV(K,N2)=AV(K,J)=V
A124=0.5*(AX(K,J-1)*(AY(K,J)-AY(K-1,J))-AX(K,J)*(AY(K,J-1)
1 -AY(K-1,J))+AX(K-1,J)*(AY(K,J-1)-AY(K,J)))
A234=0.5*(AX(K,J-1)*(AY(K-1,J)-AY(K-1,J-1))+AX(K-1,J)*(AY(K-1,J-1)
1 -AY(K,J-1))+AX(K-1,J-1)*(AY(K,J-1)-AY(K-1,J)))
AA(K,N2)=AA(K,J)=A124+A234
AVZ(K,J)=VCUN*(A124*(AY(K,J-1)+AY(K,J)+AY(K-1,J))
1 +A234*(AY(K-1,J-1)+AY(K,J-1)+AY(K-1,J)))
AVZ(K,J)=AVZ(K,J)/V
AVZ(K,N2)=VCUN*(A124*(AY(K,N1)+AY(K,N2)+AY(K-1,N1))+A234*(AY(K-1,
1 N1)+AY(K,N2)+AY(K-1,N2)))
AVZ(K,N2)=AVZ(K,N2)/V
IMA(K,J)=IMA(K,N2)=1
ASBAR(K,J)=ASBAR(K,N2)=ASBAR(1,1)
ASXX(K,J)=ASXX(K,N2)=SD
ATXX(K,J)=ATXX(K,N2)=SMAX
ASYY(K,J)=ASYY(K,N2)=ASTT(K,J)=ASTT(K,N2)=SD
ATYY(K,J)=ATYY(K,N2)=ATTT(K,J)=ATTT(K,N2)=+PMAX+SD2
AP(K,J)=AP(K,N2)=PMAX
AE(K,J)=AE(K,N2)=EMAX
625 CONTINUE
630 CONTINUE
650 JM(1)=NTHETA+1
KM(1)=KINT
IF (NDIM .EQ. 1) JM(1)=1
KMID=KINT+1
TYME=0.
ICYCLE=0
DELTH=1.E-12
DELTN=.5*DELTH
KMAX=KINT
KMN=1
C
C PRINT INITIAL LAYOUT FOR SPHERICAL PROBLEMS.
C
PRINT 1000
PRINT 1100, (DISCPT(I), I=1, 10)
JM1=JM(1)
PRINT 1603
DO 661 J=1, JM1
661 PRINT 1600, (AX(K,J), K=1, KINT)
PRINT 1602
DO 663 J=1, JM1
663 PRINT 1600, (AY(K,J), K=1, KINT)
PRINT 1602
DO 665 J=1, JM1
665 PRINT 1600, (AV(K,J), K=1, KINT)
PRINT 1602
DO 667 J=1, JM1
667 PRINT 1600, (AA(K,J), K=1, KINT)
PRINT 1602
DO 669 J=1, JM1
669 PRINT 1600, (AVZ(K,J), K=1, KINT)
PRINT 1601, THETA, NTHETA
JMX=JM(1)
IRT=JT=1
KT=KMN-1
CALL SECOND(TIMNOW)
CALTIM=TIMNOW-TIMED
PRINT 9999, CALTIM
XU2=XU(2)
C
C ***** CALL SWEEP FOR A CALCULATIONAL CYCLE
C

```

```

VOID1370
VOID1380
VOID1390
VOID1400
VOID1410
VOID1420
VOID1430
VOID1440
VOID1450
VOID1460
VOID1470
VOID1480
VOID1490
VOID1500
VOID1510
VOID1520
VOID1530
VOID1540
VOID1550
VOID1560
VOID1570
VOID1580
VOID1590
VOID1600
VOID1610
VOID1620
VOID1630
VOID1640
VOID1650
VOID1660
VOID1670
VOID1680
VOID1690
VOID1700
VOID1710
VOID1720
VOID1730
VOID1740
VOID1750
VOID1760
VOID1770
VOID1780
VOID1790
VOID1800
VOID1810
VOID1820
VOID1830
VOID1840
VOID1850
VOID1860
VOID1870
VOID1880
VOID1890
VOID1900
VOID1910
VOID1920
VOID1930
VOID1940
VOID1950
VOID1960
VOID1970
VOID1980
VOID1990
VOID2000
VOID2010
VOID2020
VOID2030

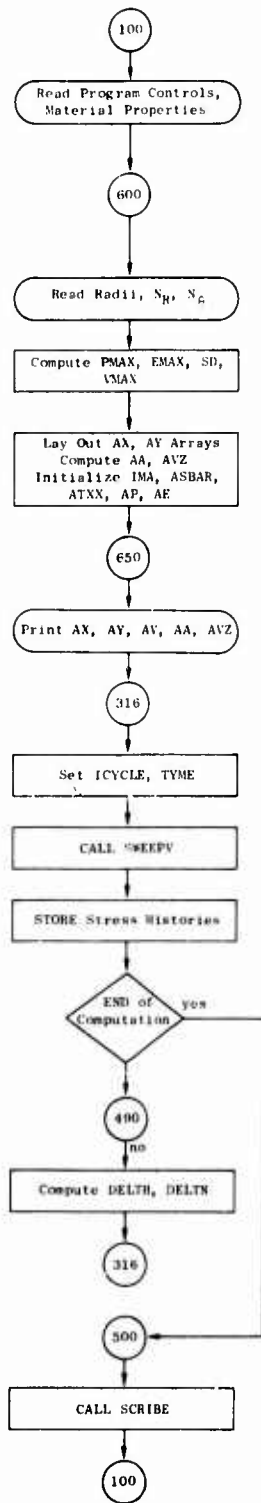
```

PROGRAM VOID (Continued)

316	ICYCLE=ICYCLE+1	VOID2040
	IF (MOD(ICYCLE,(PRINT)*MOD(ICYCLE,KPRINT)) .NE. 0) GO TO 320	VOID2050
	CALL SECOND(TIMNOW)	VOID2060
	CALTIM=TIMNOW-TIME0	VOID2070
320	TYME=TYME+DELTH	VOID2080
	IF (ICYCLE .EQ. 2000) XD(2)=0.	VOID2090
	IF (ICYCLE .EQ. 2200) XD(2)=-XD2	VOID2100
	KMN=MAX0(KMN-1,1)	VOID2110
	IF (KMAX .LT. KM(1)) KMAX=KMAX+1	VOID2120
	CALL SWEEPV(KMN,KMAX,JMX,KA,JA)	VOID2130
410	TG=TYME*1.E6	VOID2140
420	IF (NJED .LE. 0) GO TO 430	VOID2150
	DO 425 I=1,NJED	VOID2160
	R(I)=SJ(I)	VOID2170
425	SJ(I)=0.	VOID2180
430	CONTINUE	VOID2190
C	STORE STRESS HISTORIES	VOID2200
	IF (NJKED .GT. 0) WRITE (4) ICYCLE,TG,(R(I),I=1,NJKED)	VOID2210
C	ERROR FINISH	VOID2220
	IF (NSCRIBE .GT. 0) GO TO 500	VOID2230
C	***** CHECK FOR END OF CALCULATION AND SET NEXT TIME STEP	VOID2240
C		VOID2250
	IF (TYME .GE. TS) GO TO 500	VOID2260
	IF (ICYCLE .GE. IMAX) GO TO 500	VOID2270
490	DELTHW=AMINI(DELTHW,DELTAI)	VOID2280
	DELTN=DELTH	VOID2290
	DELTH=AMINI(0.9*DELTHW,AMAXI(1.2*DELTH,0.035*DELTHW))	VOID2300
	DELTN=.5*(DELTN+DELTH)	VOID2310
	IF (DELTH .GT. 1.E-12) GO TO 310	VOID2320
500	CALL SECOND(TIMNOW) \$ CALTIM=TIMNOW-TIME0	VOID2330
	PRINT 1500,TYME,TS,ICYCLE,IMAX,DELTH,NSCRIBE,CALTIM	VOID2340
	PRINT 1501,NJED,NJKED	VOID2350
	NJED=MINO(NJED,60)	VOID2360
540	IF (NJED .LE. 0) GO TO 560	VOID2370
	DO 550 I=1,NJED	VOID2380
550	KEDIT(I)=JEDJ(I)+100*JEDK(I)+10000*JEDT(I)	VOID2390
560	CONTINUE	VOID2400
	PRINT 1560,NJKED,ICYCLE,(KEDIT(I),I=1,NJKED)	VOID2410
	CALL SCRIBE (TIME0)	VOID2420
	GO TO 100	VOID2430
1000	FORMAT (1H1)	VOID2440
1100	FORMAT (10A10)	VOID2450
1102	FORMAT (A10,I10,A10,I10)	VOID2460
1103	FORMAT (4(A10,I10))	VOID2470
1104	FORMAT (4(A10,E10.3))	VOID2480
1125	FORMAT (A10,7(I6,I2,I2))	VOID2490
1130	FORMAT (3A10,E10.3,A10,A8,I2)	VOID2500
1160	FORMAT(2(A10,E10.3),2(A10,I10))	VOID2510
1430	FORMAT (I3,F8.6,I3F9.3/(I1X,I3F9.3))	VOID2520
1500	FORMAT (/ * STOP, TYME =*E10.3, * TS=*E10.3, * ICYCLE=*15, * IMAX= *	VOID2530
	1 15, * DELTH= *E10.3, * NSCRIBE= *13, * CALTIM=*E10.3)	VOID2540
1501	FORMAT ( * VALUES OF NJED=*15, * NJKED=*15)	VOID2550
1560	FORMAT ( * VOID - NJKED=*13, * ICYCLE=*13, * KED=*10110/(33X,10110))	VOID2560
1600	FORMAT (1X,1SE9.2)	VOID2570
1601	FORMAT(/ * INITIAL ANGLES, THETA =*,E10.3, * NTHETA =*,14)	VOID2580
1602	FORMAT ( )	VOID2590
1603	FORMAT ( * LISTING OF X, Y, V, A, AND VZ*/)	VOID2600
1607	FORMAT(* SE=*E10.3, * PMAX=*E10.3, * MU=*3E10.3, * V=*2E10.3,	VOID2610
	1 * E=*,E10.3)	VOID2620
9999	FORMAT (10H CALTIM = ,E10.3)	VOID2630
	END	VOID2640

PROGRAM VOID (Concluded)

Program VOID



The main program reads input data, lays out the finite difference grid, calls SWEEPV at each time step, and calls SCRIBE at the end of a computation.

Input data controlling the length of the computation, printout required, nature of the computation and number of materials are read. For each material, 3 cards are read describing the equation of state. For materials with strength and viscosity, an additional card is read.

One additional card gives the number of cells in the radial and circumferential directions.

Compute stresses, energies, and specific volumes associated with an initial uniform one-dimensional stress state.

The X, Y coordinates of all cells, the areas of the cells and their volumes are computed. The yield strength, stresses and energies of the cells are initialized to the one-dimensional state computed in the previous step.

Call Subroutine SWEEPV for calculations of coordinates and stresses at the next time increment.

Write on tape the quantities to be listed in historical printouts at the conclusion of the calculation.

Test the ending criteria based on number cycles, duration of computation, or presence of an error (NSCRIBE)

Compute the time increment for the next computational cycle.

Call subroutine SCRIBE to list the stored values in a historical printout.

Return to 100 to read the next data deck.

FLOW CHART OF PROGRAM VOID

```

SUBROUTINE SWEEPV(KMIN,KMAX,JMAX,KD,JD)
REAL MU,MCON
COMMON CA(4),CB(4),CC(4),EQSTE(4),EQSTG(4),EQSTH(4),AMAT(4),MU(4),
1 RHO(4),YCC(4),YCT(4),MCON(4),SCUN(4),PMIN(4),SP(4)
2 ,FM(4),FB(4),ETA(4)
COMMON IMAX,IPRINT,ICYCLE,KINT,KMID,KMN,KMX,JMX,IRMAX,IRT,KT,JT,
1 KWF,ISTATE,IFLAG,J1,MIRK,IJBUND,IFCUT,URED,URMIN,KCUT,LALPHA,
2 NDIM
COMMON NKED,KPRINT,KEOR(20),KED(20),NJED,JEDK(60),JEDT(60),
1 JEDK(60),JEDJ(60),NSCRIBE,NJKED,KEDIT(120)
COMMON R(120),SK(20),SJ(60),XOK(20),VK(20)
COMMON JM(2),KM(2),AREA(2),DELX(2),DELY,XD(2),VCON,CQSQ,STRESS
COMMON TYME,XOINT,DELTN,DELTH,DELTHW,DELTMIN,DISCPT(10)
COMMON CALTIM
COMMON AX(45,15),AXH(45,15),AXDH(45,15),IMA(45,15),
1 AY(45,15),AYH(45,15),AYDH(45,15),AE(45,15),
2 AA(45,15),AV(45,15),AP(45,15),
3 ASXX(45,15),ASYY(45,15),ASXY(45,15),ASTT(45,15),
4 ATXX(45,15),ATYY(45,15),ATXY(45,15),ATTT(45,15),
5 ASBARP(45,15),SBARP(45,15),AVZ(45,15)
DIMENSION X(45,15),XH(45,15),XDH(45,15),M(45,15),
1 Y(45,15),YH(45,15),YDH(45,15),E(45,15),
2 A(45,15),V(45,15),P(45,15),
3 SXX(45,15),SYY(45,15),SXY(45,15),STT(45,15),
4 TXX(45,15),TTY(45,15),TXY(45,15),TTT(45,15),
5 SBARP(45,15),SBAR(45,15),VZ(45,15)
DIMENSION SX(75),SY(75)
DIMENSION CAPA(15),BI(15),SIGLON(15),GAM(15,15)
EQUIVALENCE (AX,X),(AXH,XH),(AXDH,XDH),(IMA,M),(AY,Y),(AYH,YH),
1 (AYDH,YDH),(AE,E),(AA,A),(AV,V),(AP,P),(ASXX,SXX),(ASYY,SYY),
2 (ASXY,SXY),(ASTT,STT),(ATXX,TXX),(ATYY,TTY),(ATXY,TXY),
3 (ATTT,TTT),(ASBARP,SBARP),(SBAR,SBAR),(AVZ,VZ)
C
DVMIN=0.
C DELTH,XDNH,EXXH,QQNH,DELZ ARE DEFINED AT HALF STEP
C X,Y,STRESS, E, P, SQRTA, AREAXD ARE DEFINED AT FULL STEP
CLIN=0.5
KE=KPR=JE=0
IHEAD=KHEAD=1
IR=1
JM2=(JMAX+1)/2
AISUM=AICAPAS=AIBIS=0.
IF (ICYCLE .GT. 1) GO TO 15
TMASS=RHO(1)*(X(1,JMX)*Y(1,JMX)**2-2./3.*Y(KINT,JMX)**3)/V(2,2)
RAVG=Y(KINT,JMX)
DO 10 I=1,225
10 GAM(I)=0.
TXXW=TYYW=TXYW=TTTW=EW=VW=PW=QQNH=SPSQ=XDNH=YDNH=0.
15 CONTINUE
IF (MOD(ICYCLE,IPRINT) .EQ. 0) IHEAD=2
IF (MOD(ICYCLE,KPRINT) .EQ. 0) KHEAD=2
30 IF (NJED .EQ. 0) GO TO 40
32 IF (JEDK(JE+1) .GE. KMIN .OR. JE .GE. 60) GO TO 35
JE=JE+1 $ GO TO 32
35 JE=JE+1
40 CONTINUE
DTSUM=1.
SPMIN=1.E25
DO 900 K=KMIN,KMAX
KM1=K-1
KPI=K+1
DO 800 J=1,JMAX
JP1=J+1
JM1=J-1
IM=M(K,J)
IF (IR .NE. 1 .OR. K .NE. KMIN) GO TO 200
SX(J)=XH(KM1,J)=X(KM1,J)
SY(J)=YH(KM1,J)=Y(KM1,J)
SWEEP010
SWEEP020
SWEEP030
SWEEP040
SWEEP050
SWEEP060
SWEEP070
SWEEP080
SWEEP090
SWEP0100
SWEP0110
SWEP0120
SWEP0130
SWEP0140
SWEP0150
SWEP0160
SWEP0170
SWEP0180
SWEP0190
SWEP0200
SWEP0210
SWEP0220
SWEP0230
SWEP0240
SWEP0250
SWEP0260
SWEP0270
SWEP0280
SWEP0290
SWEP0300
SWEP0310
SWEP0320
SWEP0330
SWEP0340
SWEP0350
SWEP0360
SWEP0370
SWEP0380
SWEP0390
SWEP0400
SWEP0410
SWEP0420
SWEP0430
SWEP0440
SWEP0450
SWEP0460
SWEP0470
SWEP0480
SWEP0490
SWEP0500
SWEP0510
SWEP0520
SWEP0530
SWEP0540
SWEP0550
SWEP0560
SWEP0570
SWEP0580
SWEP0590
SWEP0600
SWEP0610
SWEP0620
SWEP0630
SWEP0640
SWEP0650
SWEP0660
SWEP0670
SWEP0680

```

SUBROUTINE SWEEPV



```

C
C ***** FIN) STRESSES AND MASSES AROUND POINT -K,J-
C
200 FX = FY = AMASS = 0.
    DO 280 I=1,4
    GO TO (210,220,230,240) I
C** I=1, UPPER RIGHT QUADRANT
210 IF (J .EQ. JMAX .OR. K .EQ. KMAX) GO TO 280
    X1 = X(KP1,JP1) $ Y1 = Y(KP1,JP1)
    X2 = X(K,JP1) $ Y2S = Y2 = Y(K,JP1)
    X3 = X(K,J) $ Y3 = Y(K,J)
    X4 = X(KP1,J) $ Y4 = Y(KP1,J)
    JJ = JP1 $ KK = KP1
    GO TO 250
C** I=2, UPPER LEFT QUADRANT
220 IF (J .EQ. JMAX .OR. (K .EQ. 1 .AND. J .GE. JM2)) GO TO 280
    IF (K .NE. 1) GO TO 225
C SPECIAL EXTERNAL PRESSURE BOUNDARY
    FX = -STRESS * (Y(K,JP1)**2 - Y(K,J)**2) / 4. + FX
    GO TO 280
C NORMAL PATH
225 X1 = X(KM1,JP1) $ Y1 = Y(KM1,JP1)
    X2 = X(KM1,J) $ Y2 = Y(KM1,J)
    X3 = X(K,J) $ Y3 = Y(K,J)
    X4 = X(K,JP1) $ Y2S = Y4 = Y(K,JP1)
    JJ = JP1 $ KK = K
    GO TO 250
C** I=3, LOWER LEFT QUADRANT
230 IF (J .EQ. 1 .OR. (K .EQ. 1 .AND. J .GT. JM2)) GO TO 280
    IF (K .NE. 1) GO TO 235
C SPECIAL EXTERNAL PRESSURE BOUNDARY
    FX = -STRESS * (Y(K,J)**2 - Y(K,JM1)**2) / 4. + FX
    GO TO 280
235 X1 = X(KM1,JM1) $ Y1 = Y(KM1,JM1)
    X2 = X(K,JM1) $ Y4S = Y2 = Y(K,JM1)
    X3 = X(K,J) $ Y3 = Y(K,J)
    X4 = X(KM1,J) $ Y4 = Y(KM1,J)
    JJ = J $ KK = K
    GO TO 250
C** I=4, LOWER RIGHT QUADRANT
240 IF (J .EQ. 1 .OR. K .EQ. KMAX) GO TO 280
    X1 = X(KP1,JM1) $ Y1 = Y(KP1,JM1)
    X2 = X(KP1,J) $ Y2 = Y(KP1,J)
    X3 = X(K,J) $ Y3 = Y(K,J)
    X4 = X(K,JM1) $ Y4S = Y4 = Y(K,JM1)
    JJ = J $ KK = KP1
C COMPUTE AREAS, FORCES AND MASSES
250 Y0 = 0.25 * (Y1+Y2+Y3+Y4) $ XU = 0.25 * (X1+X2+X3+X4)
    Y23 = 0.5 * (Y2 + Y3)
    Y24 = 0.5 * (Y2 + Y4)
    Y34 = 0.5 * (Y3 + Y4)
    DY24 = Y2 - Y4
    AXX = DY24 * (Y24 + Y3) / 4.
    AYY = ((Y23+Y0)*(X0-0.5*(X2+X3)) - (Y34+Y0)*(X0-0.5*(X3+X4)))/2.
    AT = (X0-X3)*DY24 + 2.*X2*(Y34-Y0) + 2.*X4*(Y0-Y23)
    A3 = (Y2-Y3) - X3*DY24 + X2*(Y3-Y4)
    A0 = 25*(A0+A3)
    A1 = X(K, JJ)
    AMASS = RHO(IMA)/V(KK, JJ)*(A0*(Y24+Y3+Y0) +
    A3*(Y24+2.*Y3))/24.
    FX = FX + TXY(KK, JJ)*AYY + TXX(KK, JJ)*AXX
    FY = FY + TYY(KK, JJ)*AYY + TXY(KK, JJ)*AXX - TTT(KK, JJ)*AXY
280 CONTINUE
C
C ***** COMPUTE NEW POSITIONS AND VELOCITIES AT POINT -K,J-
C
300 XN = X(K,J)
    YN = Y(K,J)

```

SUBROUTINE SWEEPV (Continued)

C	COMPUTE NEW AREAS FOR VELOCITY	SWEP1370
	IF (J .EQ. JM(IR)) Y2S = YN	SWEP1380
	IF (J .EQ. 1) Y4S = 0.	SWEP1390
	AREAXD = (Y2S+Y4S+2.*YN) * (Y2S-Y4S)	SWEP1400
	IF (J .GT. 1) GO TO 305	SWEP1410
C	ZERO THE -Y- VALUES ALONG THE LINES OF SYMMETRY.	SWEP1420
	YNW=YNH=YDNH=ALFA=YDEF=0.	SWEP1430
	GO TO 314	SWEP1440
305	CONTINUE	SWEP1450
	YDNH = 0.	SWEP1460
	IF (J .GE. JM2 .AND. K .EQ. 1) GO TO 312	SWEP1470
	YDNH = YDH(K,J) + DELTN*FY/AMASS	SWEP1480
312	YNW = YN + YDNH*DELTH	SWEP1490
	YNH = (YN+YNW)/2.0	SWEP1500
314	IF (J .EQ. JMAX) GO TO 320	SWEP1510
	XDNH = XDH(K,J) + DELTN*FX/AMASS	SWEP1520
	GO TO 325	SWEP1530
320	XDNH=XDINT	SWEP1540
325	XNW = XN+XDNH*DELTH	SWEP1550
	XNH = (XN +XNW)/2.0	SWEP1560
C	ROUTINE FOR CONSTANT STRAIN ON OUTER BOUNDARY	SWEP1570
	IF (J.GT. 1 .AND. K .GT. 1) GO TO 340	SWEP1580
	IF (K .GT. 1) GO TO 330	SWEP1590
	IF (J .NE. JM2) GO TO 600	SWEP1600
	XDA=XD(2)	SWEP1610
	XA=XN+XDA*DELTH	SWEP1620
	XAH=.5*(XA+XN)	SWEP1630
	DO 337 I=1,JM2	SWEP1640
	SX(I)=XA	SWEP1650
	XH(1,I)=XAH	SWEP1660
	XDH(1,I)=XDA	SWEP1670
337	CONTINUE	SWEP1680
	XNW=XA	SWEP1690
	XNH=XAH	SWEP1700
	XDNH=XDA	SWEP1710
330	IF (J .EQ. 1 .OR. K .EQ. 1) GO TO 600	SWEP1720
C		SWEP1730
C	***** COMPUTE NEW AREA AND VOLUME FOR CELL -K,J-	SWEP1740
C		SWEP1750
340	X1=XNW	SWEP1760
	X2=SX(J)	SWEP1770
	X3=X(KM1,JM1)	SWEP1780
	X4=SX(JM1)	SWEP1790
	Y1=YNW	SWEP1800
	Y2=SY(J)	SWEP1810
	Y3=Y(KM1,JM1)	SWEP1820
	Y4=SY(JM1)	SWEP1830
	AN=A(K,J)	SWEP1840
	VN=V(K,J)	SWEP1850
	X42 = X4-X2	SWEP1860
	Y42 = Y4-Y2	SWEP1870
	A124=0.5*(X4*(Y1-Y2)-X1*Y42+X2*(Y4-Y1))	SWEP1880
	A234=0.5*(X4*(Y2-Y3)+X2*(Y3-Y4)+X3*Y42)	SWEP1890
	AW= A124 + A234	SWEP1900
	AH= 0.5*(AW+AN)	SWEP1910
	SQRTA=ABS(X1-X2+X42+Y1-Y3-Y42)/4.	SWEP1920
	VW=VCUN*(A124*(Y4+Y1+Y2)+A234*(Y3+Y4+Y2))/VZ(K,J)	SWEP1930
355	VH= 0.5 *(VW+VN)	SWEP1940
	DELVH = VW - VN	SWEP1950
	IF (ABS(DELVH) .LT. 1.E-8) DELVH=0.	SWEP1960
	DELVV = DELVH / VH	SWEP1970
	DELTV = DELVV / DELTH	SWEP1980
C		SWEP1990
C	***** COMPUTE STRAINS AT HALF-TIME STEP BACK	SWEP2000
C		SWEP2010
	9 ECGN = 0.5*DELTH/AH	SWEP2020
	XH13 = XNH -XH(KM1,JM1)	SWEP2030
	XH42 = XH(K,JM1)-XH(KM1,J)	SWEP2040

SUBROUTINE SWEEPV (Continued)

	YH13 = YNH -YH(KM1, JM1)	SWEP2050
	YH42 = YH(K, JM1)-YH(KM1, J)	SWEP2060
	XDH13= XDNH - XDH(KM1, JM1)	SWEP2070
	XDH42= XDH(K, JM1) - XDH (KM1, J)	SWEP2080
	YDH13= YDNH - YDH(KM1, JM1)	SWEP2090
	YDH42= YDH(K, JM1) -YDH(KM1, J)	SWEP2100
	EXXH = ECON*(XDH42*YH13-YH42*XDH13)	SWEP2110
	EYYH =-ECON*(YDH42*XH13-XH42*YDH13)	SWEP2120
	EXYH = ECON*(YDH42*YH13-YH42*YDH13-XH42*XH13 +XH42*XDH13)	SWEP2130
	ETTH = DELVV -EXXH-EYYH	SWEP2140
C		SWEP2150
C	***** COMPUTE DEVIATOR STRESSES AT PRESENT TIME	SWEP2160
C		SWEP2170
	SCUNC = DELVV/3.0	SWEP2180
	SXXN = SXX(K, J)	SWEP2190
	SYYN = SYY(K, J)	SWEP2200
	SXYN = SXY(K, J)	SWEP2210
	EN = E(K, J)	SWEP2220
	ALFA = 0.5*ECON*(YDH42*YH13-YH42*YDH13+XDH42*XH13-XH42*XDH13)	SWEP2230
	ALFA = - ALFA	SWEP2240
	BETA = 2*SXYN*ALFA	SWEP2250
	SXXW = SXXN +SCON(IM)*(EXXH-SCUNC)+BETA	SWEP2260
	SYYW = SYYN +SCON(IM)*(EYYH-SCUNC)-BETA	SWEP2270
	SXYW = SXYN +MU(IM)*EXYH+(SYYN-SXXN)*ALFA	SWEP2280
	STTW = STT(K, J)+SCON(IM)*(ETTH-SCUNC)	SWEP2290
	IF (ETA(IM)+FM(IM) .GT. 0.) GO TO 450	SWEP2300
C		SWEP2310
C	ROUTE FOR PERFECT PLASTICITY	SWEP2320
	IF (YCT(IM) .EQ. 0.) GO TO 490	SWEP2330
	CY = 1.	SWEP2340
	IF (YCT(IM) .EQ. YCC(IM)) GO TO 24	SWEP2350
	IF (ABS(SXXW) .LT. ABS(SYYW)) GO TO 421	SWEP2360
	SCUNC = SXXW	SWEP2370
	GO TO 22	SWEP2380
421	SCUNC = SYYW	SWEP2390
22	IF (ABS(STTW) .GT. ABS(SCUNC)) SCUNC = STTW	SWEP2400
	IF (SCUNC .LT. 0.) 23,24	SWEP2410
23	YC = YCC(IM)	SWEP2420
	GO TO 425	SWEP2430
24	YC = YCT(IM)	SWEP2440
425	SJNW=SXXW*SXXW+SYYW*SYYW+STTW*STTW+2.*SXYW*SXYW	SWEP2450
	IF (SJNW - YC .LE. 0.) GO TO 490	SWEP2460
	CY = SQRT(YC / SJNW)	SWEP2470
	SXXW = CY * SXXW	SWEP2480
	SYYW = CY * SYYW	SWEP2490
	STTW = CY * STTW	SWEP2500
	SXYW = CY * SXYW	SWEP2510
	GO TO 490	SWEP2520
C		SWEP2530
C	ROUTE FOR VISCOUS WORK-HARDENING	SWEP2540
450	SBPW=SBARP(K, J)	SWEP2550
	SJNW=1.5*(SXXW*SXXW+SYYW*SYYW+STTW*STTW+2.*SXYW*SXYW)	SWEP2560
	SBW=SQRT(SJNW)	SWEP2570
C	COMPARE DEVIATOR (SBW) WITH YIELD(SBARP)	SWEP2580
	IF (SBW .LE. SBPW .AND. SBAR(K, J) .LE. SBPW) GO TO 490	SWEP2590
	IF (SBW .EQ. SBAR(K, J)) GO TO 490	SWEP2600
	IF (SBAR(K, J) .GT. SBPW) GO TO 460	SWEP2610
C	SET SXXN, ETC. TO VALUES AT YIELD	SWEP2620
	SSR=(SBPW-SBAR(K, J))/(SBW-SBAR(K, J))	SWEP2630
	SXXN=SXXN+(SXXW-SXXN)*SSR	SWEP2640
	SYYN=SYYN+(SYYW-SYYN)*SSR	SWEP2650
	SXYN=SXYN+(SXYW-SXYN)*SSR	SWEP2660
	STTN=STT(K, J)+(STTW-STT(K, J))*SSR	SWEP2670
460	CONTINUE	SWEP2680
C	FIRST CYCLE TO COMPUTE DEVIATOR	SWEP2690
	DTP=DELTH*(AMAX1(SBPW, SBW)-AMAX1(SBPW, SBAR(K, J)))/(SBW-SBAR(K, J))	SWEP2700
	ALF=DTP*MU(IM)/ETA(IM)	SWEP2710

SUBROUTINE SWEEPV (Continued)

```

BET=ALF/(1.+0.5*ALF) SWEP2720
SXXA=SXXN+(-SXXN+SBPW*SXXW/SBW+2.*ETA(IM)*(EXXH-SCUNC)/DELTH)*BET SWEP2730
SYYA=SYYN+(-SYYN+SBPW*SYYW/SBW+2.*ETA(IM)*(EYYH-SCUNC)/DELTH)*BET SWEP2740
SXYA=SXYN+(-SXYN+SBPW*SXYW/SBW+ETA(IM)*EXYH/DELTH)*BET SWEP2750
STTA=STTN+(-STTN+SBPW*STTW/SBW+2.*ETA(IM)*(ETTH-SCUNC)/DELTH)*BET SWEP2760
SBA=SQRT(1.5*(SXXA*SXXA+SYYA*SYYA+STTA*STTA+2.*SXYA*SXYA)) SWEP2770
C COMPUTE FACTOR RELATING PLASTIC TO TOTAL STRAIN - CYM SWEP2780
CYM=(SBW-SBA)/(SBW-SBAR(K,J)) SWEP2790
DGA=SQRT(1.5*(EXXH*EXXH+EYYH*EYYH+ETTH*ETTH+.5*EXYH*EXYH))*CYM SWEP2800
I +1.E-10 SWEP2810
C ADJUST YIELD STRESS FOR WORK HARDENING SWEP2820
GAMW=GAM(K,J)+ABS(DGA) SWEP2830
SBPW=GAMW*FM(IM)/(1.+FB(IM)*GAMW)+YCC(IM) SWEP2840
C SECOND CYCLE TO COMPUTE DEVIATOR SWEP2850
DTP=DELTH*(AMAX1(SBPW,SBW)-AMAX1(SBPW,SBAR(K,J)))/(SBW-SBAR(K,J)) SWEP2860
ALF=DTP*MU(IM)/ETA(IM) SWEP2870
BET=ALF/(1.+0.5*ALF) SWEP2880
SXXW=SXXN+(-SXXN+SBPW*CYM*EXXH/DGA+2.*ETA(IM)*(EXXH-SCUNC)/DELTH) SWEP2890
I *BET SWEP2900
SYYW=SYYN+(-SYYN+SBPW*CYM*EYYH/DGA+2.*ETA(IM)*(EYYH-SCUNC)/DELTH) SWEP2910
I *BET SWEP2920
STTW=STTN+(-STTN+SBPW*CYM*ETTH/DGA+2.*ETA(IM)*(ETTH-SCUNC)/DELTH) SWEP2930
I *BET SWEP2940
SXYW=SXYN+(-SXYN+.5*SBPW*CYM*EXYH/DGA+ETA(IM)*EXYH/DELTH)*BET SWEP2950
SBB=SQRT(1.5*(SXXW*SXXW+SYYW*SYYW+STTW*STTW+2.*SXYW*SXYW)) SWEP2960
CYMB=(SBW-SBB)/(SBW-SBAR(K,J)) SWEP2970
DGA=DGA*CYM/CYMB SWEP2980
GAM(K,J)=GAM(K,J)+ABS(DGA) SWEP2990
SBAR(K,J)=GAM(K,J)*FM(IM)/(1.+FB(IM)*GAM(K,J))+YCC(IM) SWEP3000
SBAR(K,J)=SBB SWEP3010
490 CONTINUE SWEP3020
C ***** COMPUTE Q, P, E AND TOTAL STRESSES AT PRESENT TIME SWEP3030
C SWEP3040
C ARTIFICIAL VISCOSITY COMPUTATION SWEP3050
QQNH = -RHU(IM)/VH*VDOV*(CQSQ*ABS(AH)*VDOV-CLIN*SQRTA*SP(IM)) SWEP3060
3082 CONTINUE SWEP3070
C DISTORTIONAL STRAIN ENERGY SWEP3080
DELZ=.5*VH*((SXXW+SXXN)*EXXH+(SYYW+SYYN)*EYYH+(STTW+STT(K,J))* SWEP3090
I ETTH+(SXYW+SXYN)*EXYH)/RHU(IM) SWEP3100
C PRESSURE CALCULATION AND ENERGY CALCULATION SWEP3110
ECUN=(1.-VW)/VW SWEP3120
PHUG = -ECUN*(CA(IM)+ECUN*(CB(IM)+ECUN*CC(IM))) SWEP3130
PW = (PHUG*(1.-EQSTG(IM)*ECUN/2.)-EQSTG(IM)/VW*((EN+DELZ)*RHU(IM) SWEP3140
I -QQNH*DELVH))/(1.+EQSTG(IM)/VW*DELVH) SWEP3150
IF (PW .GT. PMIN(IM)) WRITE (8,1004) PW,IK,ICYCLE,TIME,J,K SWEP3160
PW = AMIN1(PW,PMIN(IM)) SWEP3170
EW = EN+DELZ+(PW+QQNH)*DELVH/RHU(IM) SWEP3180
C FIND TOTAL STRESSES AT PRESENT TIME. SWEP3190
TXXW = SXXW + PW + QQNH SWEP3200
TYYW = SYYW + PW + QQNH SWEP3210
TXYW=SXYW SWEP3220
TTTW = STTW + PW + QQNH SWEP3230
C COMPUTE SOUND SPEED SWEP3240
EMODUL=0. SWEP3250
IF (DELVH .EQ. 0.) GO TO 560 SWEP3260
EMODUL = -PW/ECUN + QQNH/DELVH + SCUN(IM) SWEP3270
560 SPSQ=AMAX1(CA(IM)+SCUN(IM),EMODUL)*VH/RHU(IM) SWEP3280
C CHECK FOR MINIMUM DELTH AT HALF TIME STEP AHEAD(CHECK FOR STABILITY) SWEP3290
DTSQ=AMIN1(((Y1-Y3)**2+(X1-X3)**2)/2.,(Y42*Y42+X42*X42)/2., SWEP3300
I .25*((Y1-Y2-Y3+Y4)**2+(X1-X2-X3+X4)**2), SWEP3310
I .25*((Y1+Y2-Y3-Y4)**2+(X1+X2-X3-X4)**2))/SPSQ SWEP3320
IF (DTSQ .GE. DTSQM) GO TO 600 SWEP3330
KT=K $ JT=J $ IRT=IK SWEP3340
DTSQM=DTSQ SWEP3350
IF (DTSQM .LE. 0) GO TO 950 SWEP3360

```

SUBROUTINE SWEEPV (Continued)





```

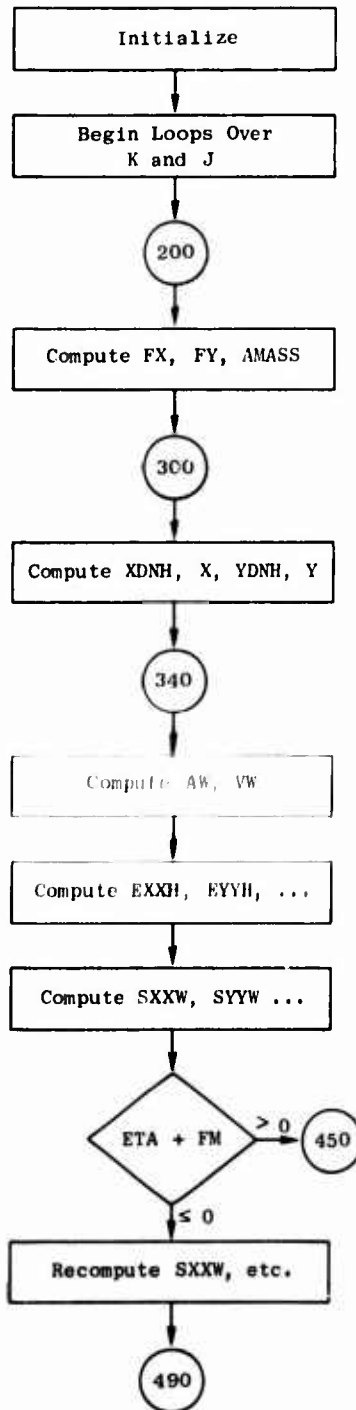
950  NSCRIBE=1                                SWEP4710
     PRINT 1950,KT, JT, IRT, VW, DELZ, EW, PW, TXXW, TYYW, TXYW, TTTW, SXXW, SYYW, SWEP4720
1    SXYW, STTW, VXXW, VYYW, VXYW, VTTW, DTSQ, SPSQ, DELVV SWEP4730
2    ,Y1,Y2,Y3,Y4,X1,X2,X3,X4,Y42,X42 SWEP4740
     RETURN SWEP4750
C SWEP4760
C SWEP4770
1000 FORMAT (13H0*** ICYCLE=14,* TYME=*E10.3,* DELTH=*E10.3,* IRT,KT, SWEP4780
1AND JT=*314,* CALTIM=*E10.3,* KMIN,KMAX,KRED,KCUT=*414) SWEP4790
1001 FORMAT (15H0INTERFACE=COL.,14) SWEP4800
1002 FORMAT (* REGION *12,* K-COL.*14,10X,**X(J=1)*E10.3,* Y(J=1)*E SWEP4810
110.3,10X,**X,Y IN CM, STRESS IN DYN/CM2*, SWEP4820
1 /* J X Y TXXW TYYW TXYW*, * SWEP4830
2 TTTW EW VW PW QQNH SPSQ X SWEP4840
3DNH YDNH*) SWEP4850
1003 FORMAT (15,13E10.3) SWEP4860
1004 FORMAT (* PRESSURE =*E10.3,* IR=*12,* ICYCLE=*13,* TYME=*E10.3 SWEP4870
1,* J=*13,* K=*12, 20X,*-----*) SWEP4880
1950 FORMAT (* ERROR FINISH AT K=*13,* J=*13,* IR=*13,* V=*E10.3, SWEP4890
1 * DELZ=*E10.3,* E=*E10.3,* P=*E10.3,* T=*4E10.3,* S=*4E10.3, SWEP4900
2 * V=*4E10.3,* DTSQ=*E10.3,* SPSQ=*E10.3,* DELVV=*E10.3/ SWEP4910
2 * Y=*4E10.3,* X=*4E10.3,* Y42=*E10.3,* X42=*E10.3) SWEP4920
END SWEP4930

```

SUBROUTINE SWEEPV (Concluded)

Subroutine SWEEPV

The routine computes positions and stresses of all cells at each call. It is called by VOID at each time step.



Initialize print variables for each cycle and initialize TMASS and GAM on first cycle.

Begin loops to compute new positions and stresses for each (K, J) value.

For each coordinate point compute the stresses and masses of adjacent cells.

Compute the new coordinate velocities and positions from conservation of momentum.

Compute new area and volume of the cell (K, J).

Compute strains during time increment.

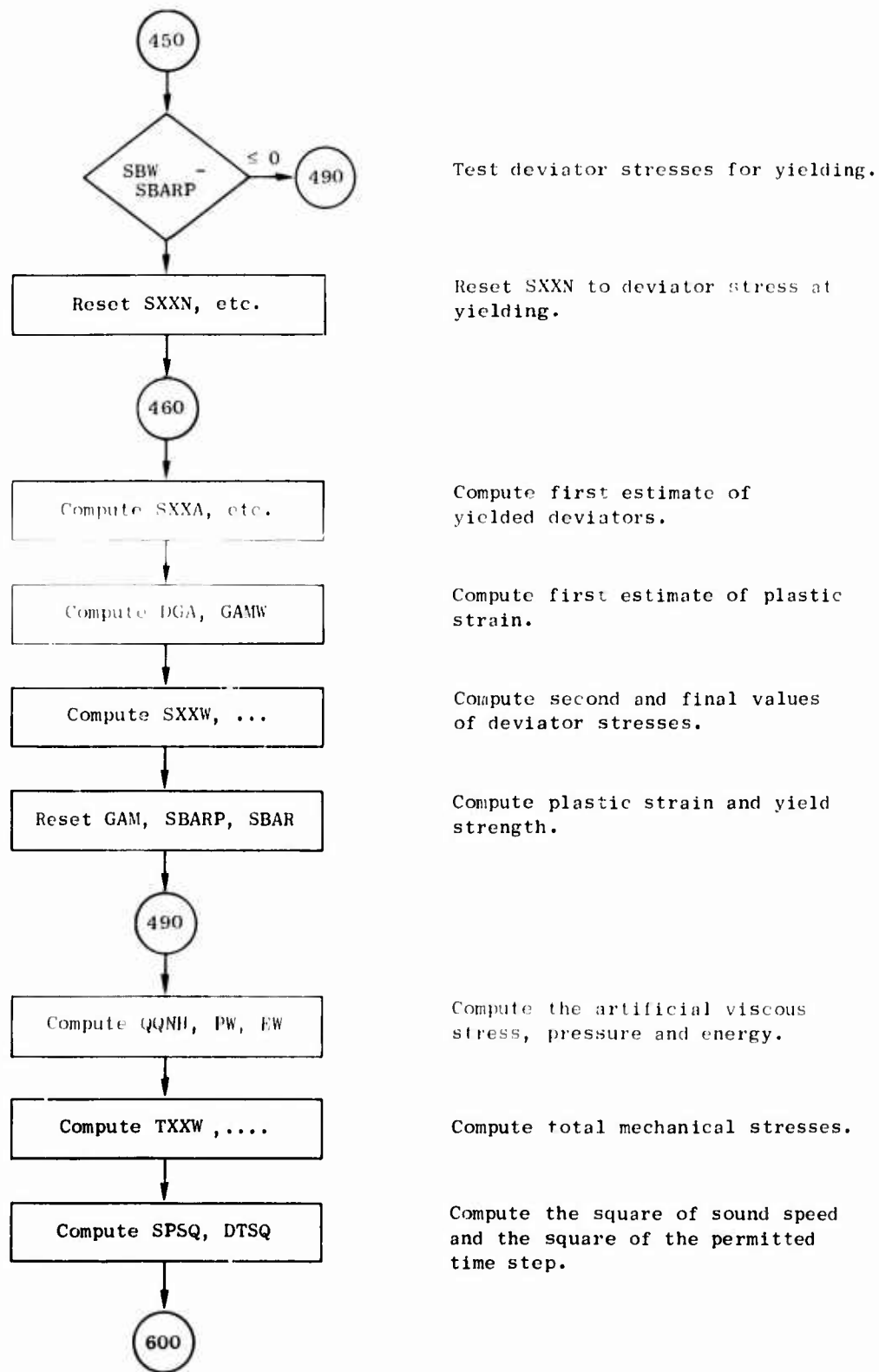
Compute elastic deviator stresses.

Test for type of yielding model to use. If viscous, work-hardening is used, then go to 450.

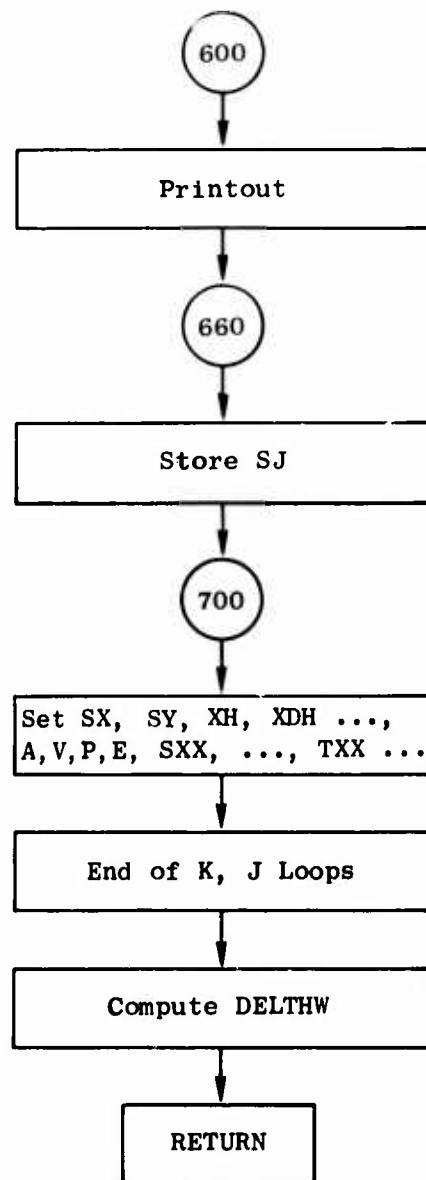
Perfect plasticity route for computation of yielded deviator stresses.

FLOW CHART OF SUBROUTINE SWEEPV





FLOW CHART OF SUBROUTINE SWEEPV (Continued)



Print coordinate positions and stresses if required by the print controls.

Store computed quantities in the SJ array as required by the JED input cards. The SJ array is stored on tape after each computation cycle.

Reset the array variables with the local variables.

The permitted time step for the next cycle is computed from the smallest value of DTSQ.

FLOW CHART OF SUBROUTINE SWEEPV (Concluded)

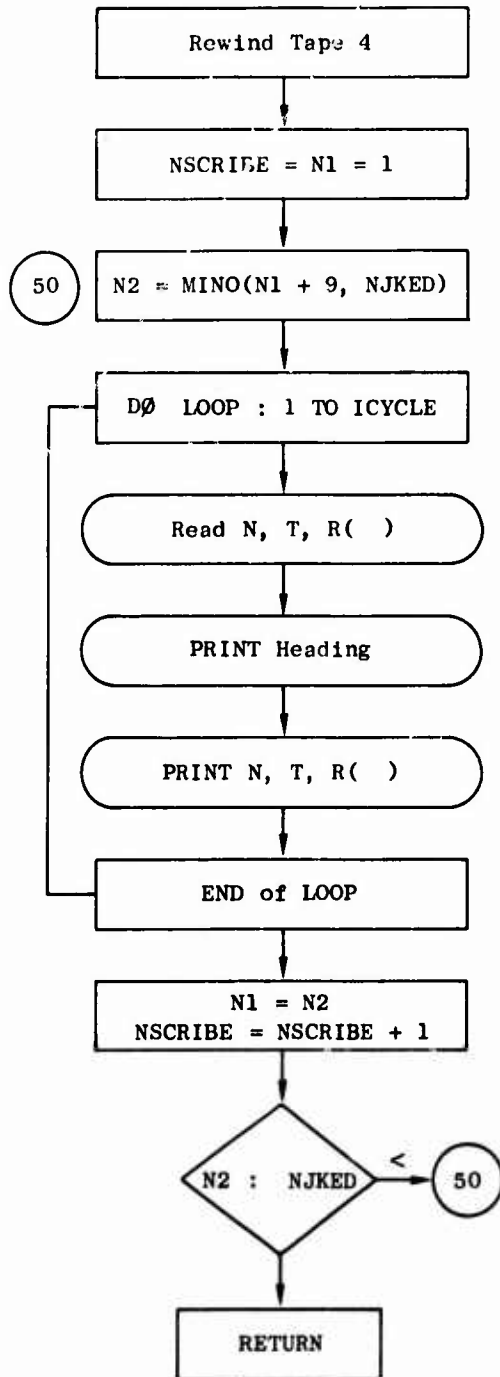
```

SUBROUTINE SCRIBE(TIMEU)
REAL MU,MCUN
COMMON CA(4),CB(4),CC(4),EQSTE(4),EQSTG(4),EQSTH(4),AMAT(4),MU(4),
1 RHO(4),YCC(4),YCT(4),MCON(4),SCON(4),PMIN(4),SP(4)
2 ,FM(4),FB(4),ETA(4)
COMMON IMAX,IPRINT,ICYCLE,KINT,KMID,KMN,KMX,JMX,IRMAX,IKT,KT,JT,
1 KWF,ISTATE,IFLAG,J1,MIRK,IJBUND,IFCUT,CRCD,URMIN,KCUT,LALPHA,
2 NDIM
COMMON NKED,KPRINT,KEDR(20),KED(20),NJED,JEDR(60),JEDF(60),
1 JEDK(60),JEDJ(60),NSCRIBE,NJKED,KEDIT(120)
COMMON R(120),SK(20),SJ(60),XOK(20),VK(20)
COMMON JM(2),KM(2),AREA(2),DELX(2),DELY,XD(2),VCUN,CQSW,STRESS
COMMON TYME,XUINT,DELTA,DELTH,DELTHW,DELTMIN,DISCPT(10)
COMMON CALTIM
COMMON AX(45,15),AXH(45,15),AXDH(45,15),IMA(45,15),
1 AY(45,15),AYH(45,15),AYDH(45,15),AL(45,15),
2 AA(45,15),AV(45,15),AP(45,15),
3 ASXX(45,15),ASYY(45,15),ASXY(45,15),ASTT(45,15),
4 ATXX(45,15),ATYY(45,15),ATXY(45,15),ATTT(45,15),
5 ASBARP(45,15),ASBAR(45,15),AVZ(45,15)
COMMON DISC(16),S(10,580),TIM(580),IND(7)
DIMENSION IA(24)
EQUIVALENCE (IA,DISCPT(3))
DIMENSION SMX(120),SMN(120),SMXJ(10),SMNJ(10),SMXK(3),SMNK(3)
REWIND 4
NSCRIBE=N1=1
50 N2=MING(N1+9,NJKED)
DO 100 NP=1,ICYCLE
READ (4) N,T,(K(I),I=1,NJKED)
IF (MOD(N,50) .EQ. 1) WRITE (8,1000) DISCPT,NSCRIBE,(KEDIT(I),I=N1
1 ,N2)
100 WRITE (8,1100) N,T,(K(I),I=N1,N2)
REWIND 4
135 N1=N2+1
NSCRIBE=NSCRIBE+1
IF (N2 .LT. NJKED) GO TO 50
137 CALL SECOND(TIMNDW)
CALTIM=TIMNOW-TIMEU
PRINT 9999, CALTIM
RETURN
1000 FORMAT (1H1,10A10/* NSCRIBE=*13,* STRESS HISTORIES, - TIME IN MICROSECS, STRESS IN KBAR, VELOCITY IN MM/MICROSEC, VOLUME IN CC/GRAM*
2/* INTEGER CODE RUNOKJ WHERE K=REGION, N=TYPE - 1=TX, 2=TY, 3=
3=TX, 4=TY, 5=SXX, 6=SYY, 7=STT, 8=PW, 9=QW, 10=TXC*/
4OR NOROK WHERE N=TYPE - 0=AVERAGE STRESS, 1=AVERAGE SPECIFIC VOLUME,
5E, 2=AVERAGE PARTICLE VELOCITY, K=REGION, K=K-KW*/
6ME*10I12/)
1100 FORMAT (15,F11.6,10F12.5)
9999 FORMAT (10H CALTIM = ,E10.3)
END

```

SUBROUTINE SCRIBE

Subroutine SCRIBE



The routine provides a historical listing of all variables requested in the JED input cards. The routine is called by VOID at the end of the computation.

Rewind the tape containing the stored historical arrays, SJ.

The work of this routine is performed in two loops. The outer loop provides for printing N, time and 10 variables at a time. The inner loop runs over ICYCLE, the number of cycles, and makes the historical listing of the variables.

FLOW CHART OF SUBROUTINE SCRIBE

```

IDENT = 5V, START WITH 1-D STRESS STATE, THEN APPLY CONSTANT STRAIN
IMAX = 3000 NMIRLS = 1
DELTAT = 1.0 SMAX = 1.000E+09 XD(2) = -800. TS = 1.000E-06
IPRINT = 50 NJED = 30 KPRINT = 10000
JED = 1 2 2 5 2 2 20 2 2 3 2 2 1 2 3 1 2 4 1 2 7
      3 2 7 20 2 7 22 5 1 1 5 2 3 5 2 20 5 2 5 5 4
      20 5 4 3 5 4 1 5 7 3 5 7 20 5 7 2 5 7 11 5 7
      12 5 7 13 5 7 14 5 7 15 5 7 16 5 7 23 5 7 17 5 7
      18 5 7 19 5 7
COPPER OFHC RHU = 8.93 NYAM = 2
CA = 1.407E+12 CB = 2.871E+12 EQSTE = 5.250E+10 EQSTG = 2.04
EQSTH = .25 CC = 2.335E+12 PMIN = 1.000E+11 YCC = 1.000E+09
FB = 7.0 FM = 0. MU = 5.180E+11 ETA = 250.
RIN = 1.000E-04 RCUT = 3.000E-04 NRAD = 4 NTHETA = 6

```

```

IDENT = 8V, LONG RUN WITH CONSTANT VELOCITY, 1 MU VOID AND 10 MU CYL.
IMAX = 2500 NMIRLS = 1
DELTAT = 1.0 SMAX = 1.000E+09 XD(2) = -800. TS = 1.000E-06
IPRINT = 50 NJED = 10 KPRINT = 10000
JED = 22 7 1 11 7 5 13 7 5 14 7 5 15 7 5 16 7 5 23 7 5
      17 7 5 18 7 5 19 7 5
COPPER OFHC RHU = 8.93 NYAM = 2
CA = 1.407E+12 CB = 2.871E+12 EQSTE = 5.250E+10 EQSTG = 2.04
EQSTH = .25 CC = 2.335E+12 PMIN = 1.000E+11 YCC = 1.000E+09
FB = 7.0 FM = 0. MU = 5.180E+11 ETA = 250.
RIN = 1.000E-04 RCUT = 1.000E-03 NRAD = 6 NTHETA = 4

```

LISTING OF TWO INPUT DECKS FOR THE VOID PROGRAM

IDENT = 8V, LONG RUN WITH CONSTANT VELOCITY, 1 MU VOID AND 10 MU CYL.  
 LISTING OF X, Y, V, A, AND WZ

0.	3.19E-04	5.36E-04	6.84E-04	7.85E-04	8.53E-04	9.00E-04
0.	3.28E-04	5.48E-04	6.96E-04	7.96E-04	8.63E-04	9.08E-04
0.	3.57E-04	5.86E-04	7.34E-04	8.29E-04	8.90E-04	9.29E-04
5.86E-04	7.21E-04	8.13E-04	8.74E-04	9.15E-04	9.43E-04	9.62E-04
1.00E-03	1.00E-03	1.00E-03	1.00E-03	1.00E-03	1.00E-03	1.00E-03

0.	0.	0.	0.	0.	0.	0.
4.14E-04	2.79E-04	1.87E-04	1.26E-04	8.47E-05	5.69E-05	3.83E-05
1.00E-03	6.43E-04	4.14E-04	2.66E-04	1.71E-04	1.10E-04	7.07E-05
1.00E-03	6.72E-04	4.52E-04	3.04E-04	2.04E-04	1.37E-04	9.24E-05
1.00E-03	6.81E-04	4.64E-04	3.16E-04	2.15E-04	1.47E-04	1.00E-04

0.	0.	0.	0.	0.	0.	0.
0.	1.00E+00	1.00E+00	1.00E+00	1.00E+00	1.00E+00	1.00E+00
0.	1.00E+00	1.00E+00	1.00E+00	1.00E+00	1.00E+00	1.00E+00
0.	1.00E+00	1.00E+00	1.00E+00	1.00E+00	1.00E+00	1.00E+00
0.	1.00E+00	1.00E+00	1.00E+00	1.00E+00	1.00E+00	1.00E+00

0.	0.	0.	0.	0.	0.	0.
0.	1.12E-07	5.14E-08	2.36E-08	1.08E-08	4.94E-09	2.26E-09
0.	1.66E-07	7.19E-08	3.11E-08	1.34E-08	5.81E-09	2.51E-09
0.	1.66E-07	7.19E-08	3.11E-08	1.34E-08	5.81E-09	2.51E-09
0.	1.12E-07	5.14E-08	2.36E-08	1.08E-08	4.94E-09	2.26E-09

0.	0.	0.	0.	0.	0.	0.
0.	1.24E-10	3.83E-11	1.18E-11	3.63E-12	1.12E-12	3.44E-13
0.	6.23E-10	1.75E-10	4.94E-11	1.39E-11	3.93E-12	1.11E-12
0.	8.78E-10	2.50E-10	7.10E-11	2.02E-11	5.75E-12	1.64E-12
0.	5.99E-10	1.85E-10	5.75E-11	1.78E-11	5.53E-12	1.71E-12

INITIAL ANGLES, THETA = 3.927E-01 NTHETA = 4  
 CALTIM = 1.010E-01  
 VVA = 3.465E-01 VVC = 8.040E-01

INITIAL LAYOUT FROM CALCULATION 8V



DATE = 0\*/21/71 IJENT = AV. LONG. RUN WITH CONSTANT VELOCITY, 1 MU-VOID AND 10 MU CYL.  
 VSCRIBE = 1 STRESS HISTORIES, - TIME IN MICROSECS, STRESS IN KBAR, VELOCITY IN MM/MICROSEC, VOLUME IN CC/GRAM  
 INTEGER CODE MONOKUJ #MEKE #REGION #TYPE - 1=TK, 2=TY, 3=TX, 4=TT, 5=SK, 6=SY, 7=ST, 8=PW, 9=QQ, 10=TYC  
 ON #UMUK #MEKE #TYPE - 0=AVERAGE STRESS, 1=AVERAGE SPECIFIC VOLUME, 2=AVERAGE PARTICLE VELOCITY, P=REGION, K=K-RG

N	TIME	1220701	1110705	1130705	1140705	1150705	1140705	1220705	1170705	1180705	1190705
101	.0052*1	A.37632	7.11787	6.66930	.46877	.00513	1.01619	1.01606	.11250	.11254	.00070
102	.005303	A.97598	7.19479	6.74812	.45067	.00483	1.01649	1.01640	.11251	.11259	.00070
103	.005366	A.57565	7.27766	6.82949	.44777	.00461	1.01678	1.01640	.11251	.11259	.00070
104	.005424	A.97531	7.35440	6.91379	.44061	.00447	1.01705	1.01702	.11252	.11260	.00070
105	.005490	A.97496	7.42902	6.99934	.42968	.00441	1.01733	1.01730	.11252	.11260	.00070
106	.005552	A.97461	7.50194	7.08609	.41545	.00443	1.01761	1.01758	.11253	.11261	.00070
107	.005615	A.97426	7.57204	7.17363	.39841	.00452	1.01789	1.01785	.11254	.11261	.00070
108	.005677	A.97392	7.64072	7.26125	.37948	.00462	1.01817	1.01813	.11254	.11262	.00070
109	.005734	A.97357	7.70772	7.34841	.35912	.00470	1.01847	1.01840	.11255	.11263	.00070
110	.005801	A.97321	7.77320	7.43546	.33774	.00476	1.01876	1.01868	.11255	.11263	.00070
111	.005864	A.97284	7.83736	7.52154	.31576	.00482	1.01906	1.01895	.11256	.11264	.00070
112	.005926	A.97247	7.90019	7.60662	.29357	.00489	1.01937	1.01922	.11256	.11264	.00070
113	.005988	A.97211	7.96204	7.69048	.27155	.00497	1.01968	1.01950	.11257	.11265	.00070
114	.006050	A.97175	8.02298	7.77293	.25005	.00505	1.01999	1.01979	.11257	.11265	.00070
115	.006112	A.97140	8.08318	7.85379	.22939	.00512	1.02031	1.02008	.11258	.11266	.00070
116	.006174	A.97107	8.14277	7.93249	.20988	.00520	1.02063	1.02038	.11258	.11266	.00070
117	.006236	A.97074	8.20187	8.01009	.19178	.00535	1.02096	1.02070	.11259	.11267	.00071
118	.006299	A.97039	8.26074	8.08463	.17616	.00551	1.02130	1.02102	.11260	.11268	.00071
119	.006361	A.97003	8.31958	8.15656	.16301	.00565	1.02165	1.02135	.11260	.11268	.00071
120	.006423	A.96966	8.37829	8.22591	.15038	.00577	1.02201	1.02169	.11261	.11269	.00071
121	.006485	A.96927	8.43697	8.29270	.14427	.00589	1.02238	1.02202	.11261	.11269	.00071
122	.006547	A.96887	8.49564	8.35701	.13862	.00602	1.02275	1.02236	.11262	.11270	.00071
123	.006609	A.96847	8.55431	8.41897	.13534	.00614	1.02313	1.02271	.11262	.11270	.00071
124	.006671	A.96807	8.61301	8.47875	.13426	.00627	1.02352	1.02306	.11263	.11271	.00071
125	.006733	A.96766	8.67172	8.53654	.13519	.00640	1.02392	1.02343	.11263	.11271	.00071
126	.006794	A.96722	8.73047	8.59258	.13789	.00655	1.02432	1.02380	.11264	.11272	.00071
127	.006856	A.96682	8.78925	8.64713	.14212	.00670	1.02474	1.02418	.11264	.11273	.00071
128	.006916	A.96639	8.84806	8.70048	.14758	.00685	1.02516	1.02458	.11265	.11273	.00071
129	.006974	A.96594	8.90691	8.75290	.15400	.00700	1.02559	1.02498	.11266	.11274	.00072
130	.007032	A.96549	8.96574	8.80468	.16111	.00715	1.02603	1.02539	.11266	.11274	.00072
131	.007104	A.96503	9.02472	8.85609	.16863	.00729	1.02649	1.02581	.11267	.11275	.00072
132	.007165	A.96455	9.08371	8.90738	.17633	.00743	1.02694	1.02624	.11267	.11275	.00072
133	.007227	A.96417	9.14276	8.95880	.18396	.00756	1.02741	1.02668	.11268	.11276	.00072
134	.007289	A.96378	9.20189	9.01054	.19135	.00769	1.02788	1.02712	.11268	.11276	.00072
135	.007350	A.96339	9.26110	9.06279	.19832	.00781	1.02837	1.02759	.11269	.11277	.00072
136	.007412	A.96290	9.32043	9.11570	.20473	.00792	1.02885	1.02803	.11269	.11278	.00072
137	.007474	A.96250	9.37988	9.16940	.21048	.00802	1.02935	1.02850	.11270	.11278	.00072
138	.007535	A.96210	9.43947	9.22397	.21550	.00812	1.02985	1.02897	.11270	.11279	.00072
139	.007597	A.96169	9.49922	9.27948	.21974	.00821	1.03035	1.02945	.11271	.11279	.00072
140	.007658	A.96129	9.55915	9.33598	.22317	.00830	1.03086	1.02993	.11272	.11280	.00073
141	.007720	A.96089	9.61927	9.39348	.22580	.00840	1.03138	1.03042	.11272	.11280	.00073
142	.007781	A.96048	9.67961	9.45197	.22764	.00850	1.03190	1.03091	.11273	.11281	.00073
143	.007842	A.95996	9.74017	9.51143	.22874	.00860	1.03243	1.03140	.11273	.11281	.00073
144	.007904	A.95955	9.80097	9.57182	.22915	.00869	1.03294	1.03191	.11274	.11282	.00073
145	.007965	A.95913	9.86211	9.63310	.22891	.00879	1.03350	1.03242	.11274	.11282	.00073
146	.008026	A.95870	9.92332	9.69520	.22811	.00887	1.03405	1.03293	.11275	.11283	.00073
147	.008088	A.95828	9.98468	9.75807	.22682	.00895	1.03459	1.03344	.11275	.11284	.00073
148	.008149	A.95784	10.04672	9.82162	.22509	.00902	1.03515	1.03397	.11276	.11284	.00073
149	.008210	A.95740	10.10981	9.88580	.22301	.00908	1.03570	1.03449	.11276	.11285	.00074
150	.008271	A.95694	10.17318	9.95053	.22064	.00913	1.03626	1.03502	.11277	.11285	.00074

A PORTION OF THE SCRIBE LISTING FROM CALCULATION 8V



NOMENCLATURE FOR APPENDIX V

$A^0, A^1$	areas at beginning and ending of a time increment, $\text{cm}^2$
$A_0, A_3$	areas of triangles 0-23-34 and 3-23-34 in the x-y plane, $\text{cm}^2$
$A, A_{xy}$	area of an element in the x-y plane, $\text{cm}^2$
$A_{xx}, A_{yy}$	projected areas of an element in the x and y directions, respectively, $\text{cm}^2$
$C$	sound speed, $\text{cm}/\text{sec}$
$\bar{C}, C^*$	effective sound speed governing stability, $\text{cm}/\text{sec}$
$C_L, C_Q$	coefficients of linear and quadratic terms for artificial viscosity
$F_x, F_y$	forces in the x and y directions, dyn
$H$	a plastic modulus, $\text{dyn}/\text{cm}^2$
$J, j$	Lagrangian cell and coordinate index in direction normal to the radius of the void
$K$	bulk modulus, $\text{dyn}/\text{cm}^2$
$K, k$	Lagrangian cell and coordinate index in radial direction of the void
$M$	strain hardening modulus, $\text{dyn}/\text{cm}^2$ or mass of a cell, gm
$M_e$	effective modulus for sound speed calculations, $\text{dyn}/\text{cm}^2$
$N_R, N_\varphi$	numbers of cells in the radial and polar angle directions
$\bar{P}$	average pressure, $\text{dyn}/\text{cm}^2$
$P, p$	pressure, $\text{dyn}/\text{cm}^2$

$Q$	artificial viscous stress, $\text{dyn/cm}^2$
$R_a$	radius of void, cm
$R_b$	radius of cylinder, cm
$R_{k,j}$	radial position of coordinate point $(k,j)$ , cm
$T$	relaxation time, sec
$T_{xx}, T_{yy}, T_{\theta\theta}$	total mechanical stresses in the $x$ , $y$ , and $\theta$ directions, respectively, $\text{dyn/cm}^2$
$T_{xy}$	shear stress on the $x$ - $y$ plane, $\text{dyn/cm}^2$
$V$	volume of a cell, $\text{cm}^3$
$V_s$	specific volume of solid material, $\text{cm}^3/\text{g}$
$V_v$	relative void volume
$X, x$	position in direction of loading, cm
$Y$	yield strength, $\text{dyn/cm}^2$
$Y, y$	radial position normal to loading direction, cm
$Y_0$	initial value of yield strength
$a$	a constant
$b$	a constant in the work hardening function
$p_0$	threshold pressure for void growth, $\text{dyn/cm}^2$
$t$	time, sec
$u, v$	velocities in the $x$ and $y$ directions, $\text{cm/sec}$
$\Delta\varphi$	angular spacing between $j$ rows
$\alpha$	a constant
$\beta$	a constant

$\gamma$	shear strain
$\gamma_a$	effective shear strain
$\gamma^p$	plastic shear strain
$\gamma_{xy}$	shear strain in the x-y plane
$\delta_{ij}$	Kronecker delta
$\epsilon_1, \epsilon_2, \epsilon_3$	principal strains
$\epsilon_i^p$	plastic strain in the $i^{\text{th}}$ principal direction
$\epsilon_x, \epsilon_y, \epsilon_\theta$	strains in x, y and $\theta$ directions
$\eta$	material viscosity, dyn-sec/cm <sup>2</sup>
$\theta$	coordinate in the circumferential direction
$\mu$	shear modulus, dyn/cm <sup>2</sup>
$\rho$	density, g/cm <sup>3</sup>
$\bar{\sigma}$	effective stress, dyn/cm <sup>2</sup>
$\sigma'$	deviator stress, dyn/cm <sup>2</sup>
$\sigma_1, \sigma_2, \sigma_3$	principal stresses, dyn/cm <sup>2</sup>
$\sigma_{ij}, \epsilon_{ij}^p$	components of the stress and plastic strain tensors
$\sigma_x, \sigma_y, \sigma_z$	stresses in the x, y and z directions, dyn/cm <sup>2</sup>
$\tau$	shear stress, dyn/cm <sup>2</sup>
$\tau_{xy}, \tau_{yz}, \tau_{xz}$	shear stresses in x-y, y-z and x-z planes, dyn/cm <sup>2</sup>
$\omega_{xy}$	rotation in the x-y plane

## Appendix VI

### MATERIAL VISCOSITY DERIVED FROM THE STEADY-STATE SHOCK FRONT

The viscosity of a material is a basic macroscopic material property that governs phenomena such as the rate of void growth, the shape of shock front profiles, the rates of attenuation of precursor waves, and hysteresis. All these manifestations of viscosity do not lead to the same values of viscosity because of the effects of different loading rates and stress amplitudes. In connection with a study of the fracture of metals by void growth, it was found that the growth rate was related to the material viscosity. Thus, if viscosity is known, some aspects of fracture can be immediately predicted. The required viscosity is that appropriate to strains and stresses in excess of the elastic stress, and to loading durations of the order of tens or hundreds of nanoseconds.

Plastic shock front profiles are known to be governed by the amount of viscosity; the stresses are in the plastic range and the rise times are usually a few nanoseconds. Therefore, the shape of the shock front profile should lead to appropriate values of the viscosity.

In the following discussion the governing equations are introduced and solved to provide the shape of the shock front and the rise time as functions of the linear viscosity. These theoretical rise times are then compared with available experimental values of rise times to determine the value of viscosity for several materials.

The Eulerian equations for conservation of mass and momentum control the stress rise through the shock front:

$$\frac{\partial \rho}{\partial t} + u \frac{\partial \rho}{\partial X} + \rho \frac{\partial u}{\partial X} = 0 \quad (\text{mass}) \quad (195)$$

$$\rho \left( \frac{\partial u}{\partial t} + u \frac{\partial u}{\partial X} \right) + \frac{\partial P}{\partial X} - \frac{4}{3} \eta \frac{\partial^2 u}{\partial X^2} = 0 \quad (\text{momentum}) \quad (196)$$

where

$\rho$  = density

$t$  = time

$u$  = particle velocity

$X$  = fixed coordinate position

$P$  = thermodynamic stress in direction of propagation

$\eta$  = coefficient of linear viscosity

Under the assumption of a steady-state profile, these equations can be integrated to provide the slope of the stress-time or stress-distance profiles and also the complete profile. The procedure used here is to perform one integration to obtain the maximum value of the slope of the particle velocity profile  $(\partial u / \partial x)_{\max}$ . Then the shock front thickness can be approximated as  $u_f / (\partial u / \partial x)_{\max}$  where  $u_f$  is the final, steady-state value. As a first step, the conservation equations are transformed to a coordinate system moving with the shock velocity  $U$  in the  $X$  direction. Then  $\partial / \partial t$  is replaced by  $-U \partial / \partial x$ , where  $x = X - Ut$ , and  $\partial / \partial X$  by  $\partial / \partial x$ .

Then

$$(u - U) \frac{\partial \rho}{\partial x} + \rho \frac{\partial u}{\partial x} = 0 \quad \text{or} \quad \frac{\partial}{\partial x} [(u - U)\rho] = 0 \quad (\text{mass}) \quad (197)$$

$$\rho(u - U) \frac{\partial u}{\partial x} + \frac{\partial P}{\partial x} - \frac{4}{3} \eta \frac{\partial^2 u}{\partial x^2} = 0 \quad (\text{momentum}) \quad (198)$$

Let  $w = U - u$ . Then from Eq. (197)

$$\rho w = \text{constant} = \rho_0 U \quad (199)$$

Equation (198) becomes

$$\rho_0 U \frac{\partial w}{\partial x} + \frac{\partial P}{\partial x} + \frac{4}{3} \eta \frac{\partial^2 w}{\partial x^2} = 0 \quad (200)$$

Because it is assumed that the shock front is steady state, we can replace  $\partial P/\partial x$  by expressions in  $w$  and  $\rho$ .

$$\frac{\partial P}{\partial x} = \left( \frac{\partial P}{\partial \rho} \right) \left( \frac{\partial \rho}{\partial x} \right) = - \rho_0 U \left( \frac{c^2}{w^2} \right) \left( \frac{\partial w}{\partial x} \right) \quad (201)$$

Equation (201) was obtained by setting  $c^2 = \partial P/\partial \rho$  and using Eq. (199) to evaluate  $\rho$ . With the aid of Eq. (201), the momentum equation, (200), is written

$$\frac{4}{3} \eta \frac{\partial^2 w}{\partial x^2} + \rho_0 U \left( 1 - \frac{c^2}{w^2} \right) \frac{\partial w}{\partial x} = 0 \quad (202)$$

Because of the special form of Eq. (202), a first integration can be performed by replacing  $\partial w/\partial x$  by  $z$  and  $\partial^2 w/\partial x^2$  by  $z \partial z/\partial w$ . Then the slope  $z$  is given by

$$\frac{\partial z}{\partial w} = - \frac{3\rho_o U}{4\eta} \left( 1 - \frac{c^2}{w^2} \right) \quad (203)$$

or

$$z = - \frac{3\rho_o U}{4\eta} \int \left( 1 - \frac{c^2}{w^2} \right) dw \quad (204)$$

It is known that the shock is supersonic with respect to the material ahead ( $w > c$ ) and subsonic with respect to the material behind the front ( $w < c$ ). Therefore  $w = c$  at some point along the shock front. According to Eq. (203),  $\partial z/\partial w$  is zero at the point, so  $z$  reaches an extremum (a maximum) there. The value of  $w$  at that point will be designated  $w_m$ .

The value of  $z_{\max}$  is obtainable from either of the integrals:

$$z_{\max} = - \frac{3\rho_o U}{4\eta} \int_U^{w_m} \left( 1 - \frac{c^2}{w^2} \right) dw \quad (205)$$

$$z_{\max} = \frac{3\rho_o U}{4\eta} \int_{w_m}^{U-u_f} \left( 1 - \frac{c^2}{w^2} \right) dw \quad (206)$$

which are obtained from Eq. (204) by noting that  $z = 0$  at  $w = U$  and at  $w = U - u_f$ , where  $u_f$  is the steady-state particle velocity following the shock.

At this point an equation of state is required to evaluate  $c$  through the shock. The Murnaghan form was chosen:

$$P = A[(\rho/\rho_0)^\gamma - 1] \quad (207)$$

To evaluate  $c$ , it is assumed that the thermodynamic stress  $P$  follows the Hugoniot path during the shock.

Actually the path traverses states with somewhat higher energies, and the derivative should be along an isentrope instead of on the Hugoniot; however, this approximation is reasonable except for very strong shocks. Differentiating Eq. (207) by  $\rho$  and replacing  $\rho$  by  $w$  leads to

$$c^2 = \frac{\partial P}{\partial \rho} = \frac{\gamma A}{\rho_0} \left(\frac{U}{w}\right)^{\gamma-1} \quad (208)$$

where  $w_0 = U$

Using the condition that  $w_m^2 = c^2$ , we obtain

$$w_m = \left(\frac{\gamma A}{\rho_0}\right)^{1/(\gamma+1)} U^{(\gamma-1)/(\gamma+1)} \quad (209)$$

The shock velocity is obtained by combining the Murnaghan equation with Eq. (199) and  $P_f = \rho_0 U u_f$ , where the subscript  $f$  refers to the final state. Then

$$U^2 = \frac{P_f}{\rho_0 \left[1 - \left(\frac{P_f}{A} + 1\right)^{-1/\gamma}\right]} \quad (210)$$



The value of  $c$  from Eq. (208) can be placed in Eqs. (203) and (204) to obtain

$$z_{\max} = \frac{3\rho_o U}{4\eta} \left[ U - w_m + \frac{AU^{\gamma-1}}{\rho_o} \left( \frac{1}{U^\gamma} - \frac{1}{w_m^\gamma} \right) \right] \quad (211)$$

$$= \frac{3\rho_o U}{4\eta} \left[ U - u_f - w_m + \frac{AU^{\gamma-1}}{\rho_o} \left( \frac{1}{(U - u_f)^\gamma} - \frac{1}{w_m^\gamma} \right) \right]$$

The two expressions for  $z_{\max}$  are equal. The shock front thickness is then defined to be

$$\Delta x = \frac{u_f}{z_{\max}} \quad (212)$$

and the rise time is

$$\Delta t = \frac{u_f}{U z_{\max}} \quad (213)$$

By expanding the expressions for  $z_{\max}$ ,  $u_f$ , and  $U$  in powers of  $P_f/A$ , we obtain an indication of the functional relationships.

$$z_{\max} = \frac{3A}{32\eta} \left( \frac{P_f}{A} \right)^2 \frac{(\gamma + 1)}{\gamma} \left( 1 - \frac{P_f}{2A} \right) \quad (214)$$

$$\Delta x = \frac{32\eta}{3P_f(\gamma + 1)} \left( \frac{A\gamma}{\rho_o} \right)^{\frac{1}{2}} \left[ 1 + \frac{1}{4} \left( 1 - \frac{1}{\gamma} \right) \frac{P_f}{A} \right] \quad (215)$$

$$\Delta t = \frac{32\eta}{3P_f(\gamma + 1)} \left( 1 - \frac{P_f}{2\gamma A} \right) \quad (216)$$

These expressions are accurate within a few percent for  $P_f/A$  less than 1. Evidently the shock front thickness and rise time are linearly related to the coefficient of viscosity.

Sample curves obtained from plotting Eq. (213) with the Murnaghan parameters for several materials are shown in Figures 94 and 95. The curves of Figure 95 have been plotted using a nondimensional shock front thickness parameter  $\Delta t_n$ , which is indicated in Eq. (216), i.e.,

$$\Delta t_n = \frac{3\Delta t}{32\eta} P_f (1 + \gamma) \quad (217)$$

This second figure provides a sensitive measure of the viscosity when compared with experimental values of shock front thickness.

As a further guide in comparing the experimental shock front thickness with these expressions for  $\Delta x$  and  $\Delta t$ , the shock front profile was obtained by evaluating particle velocity as a function of distance:

$$z = - \frac{du}{\partial x} = - \frac{3\rho_o U^2}{4\eta} \left\{ - \frac{u}{U} + \frac{A}{\rho_o U^2} \left[ 1 - \left( \frac{U}{U-u} \right)^\gamma \right] \right\} \quad (218)$$

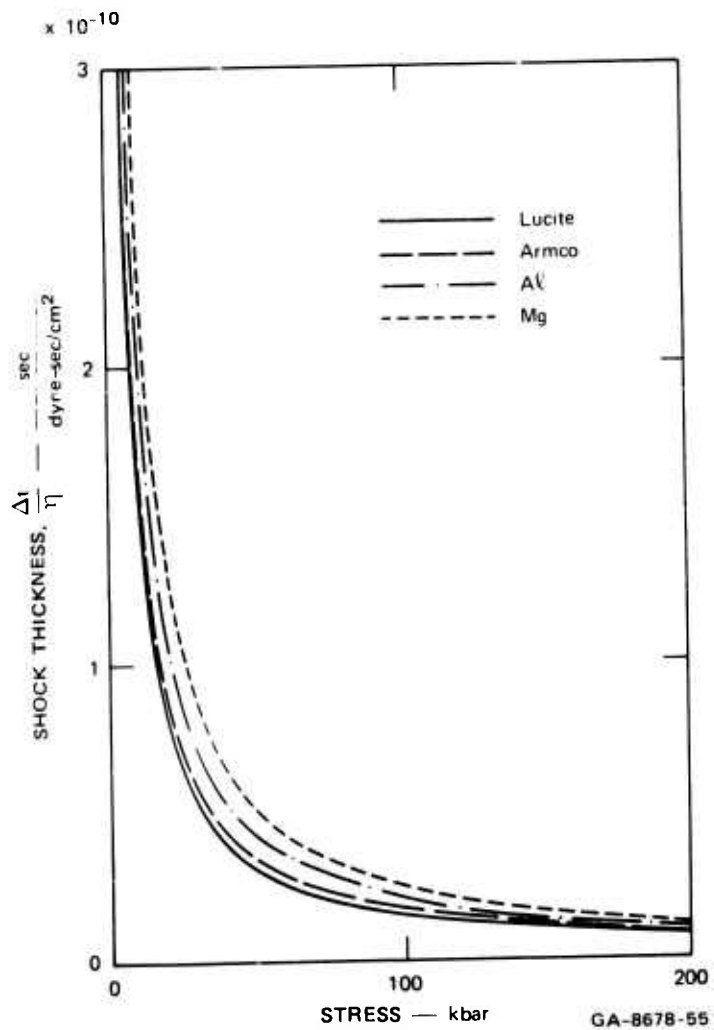
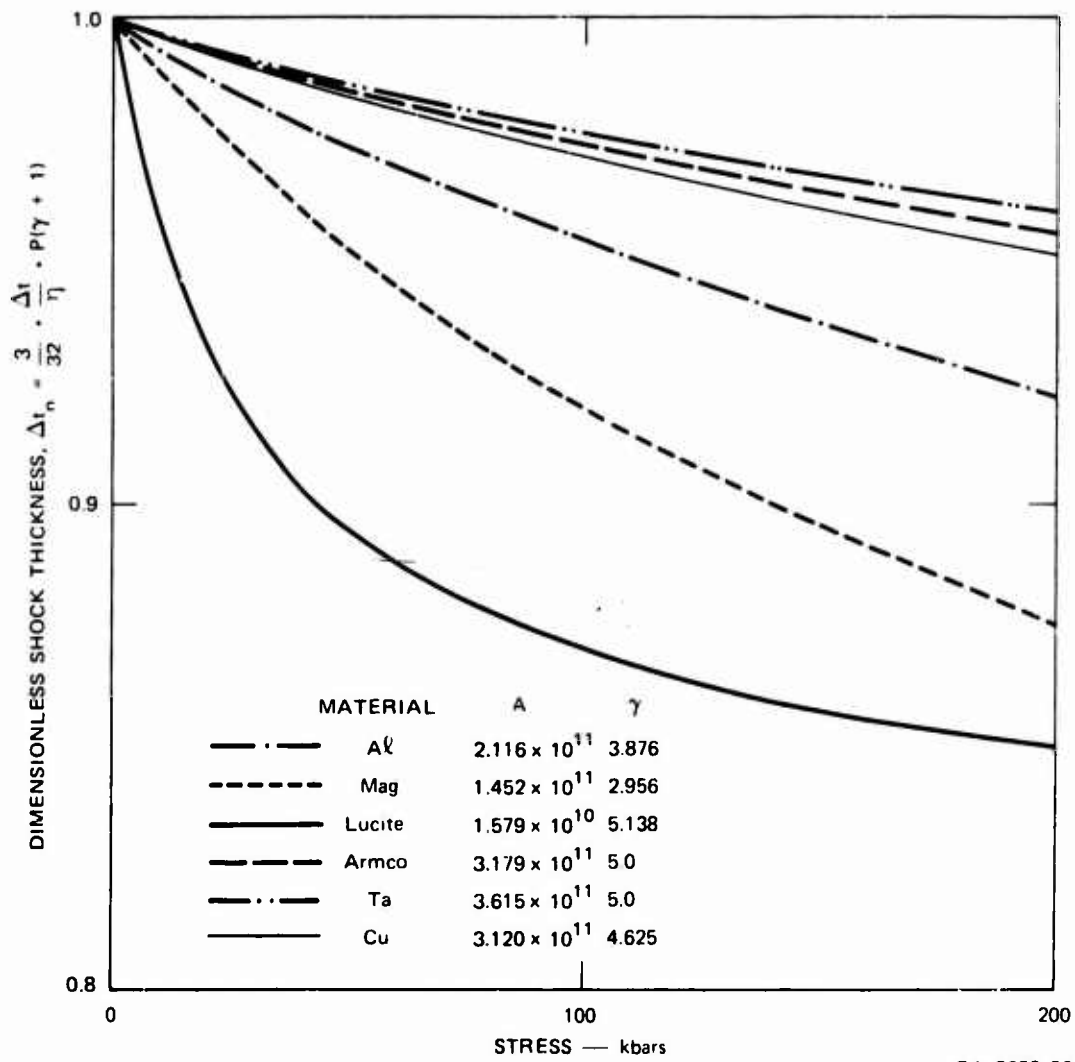


FIGURE 94 SHOCK FRONT THICKNESS AS A FUNCTION OF STRESS LEVEL



GA-8678-56

FIGURE 95 NONDIMENSIONAL SHOCK FRONT THICKNESS AS A FUNCTION OF STRESS LEVEL

Equation (218) was integrated numerically by the trapezoidal rule starting at  $u_m = U - w_m$  and proceeding either up or down along the profile.

A sample of these wave front results is shown in Figure 96. On this nondimensional plot it is clear that higher stress waves tend to rise faster with the same material viscosity.

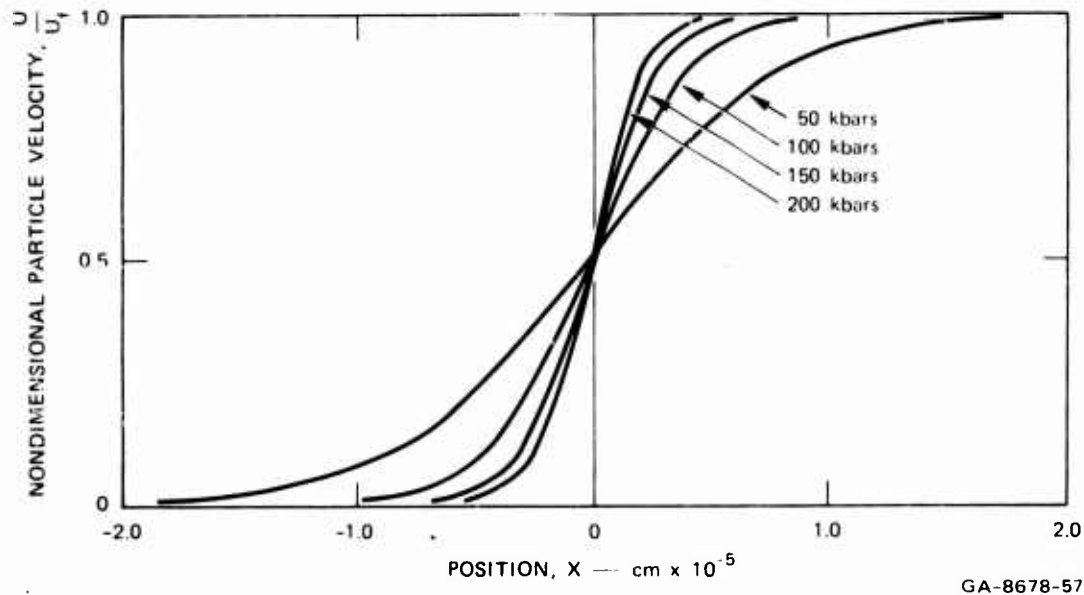


FIGURE 96 SHOCK FRONT PROFILES AT SEVERAL STRESS LEVELS

NOMENCLATURE FOR APPENDIX VI

A	coefficient in the Murnaghan equation, $\text{dyn/cm}^2$
P	thermodynamic stress in the direction of propagation, $\text{dyn/cm}^2$
U	shock velocity
X	position, cm
c	sound speed
t	time
u	particle velocity, cm/sec
$u_f$	final or steady-state particle velocity, cm/sec
w	$U - u$
z	$\partial w / \partial x$
$\Delta t$	shock front rise time, sec
$\Delta t_n$	nondimensional rise time
$\Delta X$	shock front thickness, cm
$\gamma$	exponent in Murnaghan equation of state
$\eta$	material viscosity, $\text{dyn-sec/cm}^2$
$\rho$	density, $\text{gm/cm}^3$
$\rho_0$	initial density, $\text{gm/cm}^3$

## APPENDIX VII

### DUCTILE FRACTURE SUBROUTINE: DFRACT

The ductile fracture subroutine, DFRACT, and the equations contained in it are described in this appendix. The present routine replaces the two previous routines, HFRACT and JFRACT. This consolidation into one routine was dictated by a desire to make the routine readily usable in one-dimensional artificial viscosity wave propagation codes other than SRI PUFF. This present routine can be employed in codes with either one- or two-step integration schemes.

All the formal parameters of DFRACT must be input from the calling routine. The output quantities are H3, S, P, NM, NT, and Y. If a two-step integration scheme is employed, then NM, NT, and Y should be reset in DFRACT only for half step or full step calls, not for both.

In SRI PUFF 5, common variables are used in the call statement at the half step, and local variables at the full step. In this way, the corresponding actual parameters H(J,3), SHL, PHL, NEM, NET, and YHL--are reset only at the half step. Note that H3 and JS are integers; all others are floating-point.

#### 1. DERIVATION OF EQUATIONS FOR DUCTILE FRACTURE

The critical damage parameters calculated in ductile fracture are the volume of voids and the number of voids. At each time step both of the quantities are incremented as functions of the applied pressure. The incremental changes are described physically as nucleation of new voids and growth of existing voids.

Consider first the nucleation of a group of voids with different sizes. Let  $\rho(R)$  be the concentration or number at each radius  $R$ . Then the total number nucleated (per unit volume) is  $\Delta N$

$$\Delta N = \int_0^{\infty} \rho(R) dR \quad (219)$$

The nucleated volume of voids is found by multiplying the volume of each void by the number at that radius:

$$\Delta V_n = \frac{4\pi}{3} \int_0^{\infty} R^3 \rho(R) dR = c R_n^3 \Delta N \quad (220)$$

where

$\alpha$  = a constant depending on the distribution  $\rho(R)$

$R_n$  = a radius parameter of the distribution ( $R_n = T_3$  in the code).

For example, if the nucleated distribution has a form similar to the final (observed) distribution, the  $\rho(R)$  can be represented by

$$\rho(R) = \frac{\Delta N}{R_n} \exp(-R/R_n) \quad (221)$$

Then  $\alpha = 8\pi$ . Alternatively, if the voids are all nucleated with the same radius  $R_n$ , then  $\alpha = 4\pi/3$ . In the subsequent analysis it is found convenient to assume that Eq. (221) describes the distribution at all times.



The nucleation rate governing  $\Delta N$  is assumed to have the following form

$$\frac{\Delta N}{\Delta t} = T_4 \exp\left(\frac{p - p_{n0}}{T_6}\right) \quad (222)$$

where

$T_4, T_6$  = nucleation parameters

$p_{n0}$  =  $T_5$  in the code, a threshold pressure

At each time increment, the void volume is incremented by an amount DVVG, a quantity with the dimensions of specific volume. Since DVVG and the void volume VVO are dimensional, they do not automatically expand or contract with the gross specific volume; their expansion follows the growth and nucleation laws. The increment in void volume is found by combining Eqs. (220) and (222).

$$DVVG_n = \frac{\alpha R_n^3 T_4}{D} \exp\left(\frac{p - p_{n0}}{T_6}\right) \Delta t \quad (223)$$

where we have divided by  $D$ , the gross density, so that  $DVVG_n$  is the volume change for a particular mass of material. In the code,  $p$  is taken as the average of the pressures at either end of the time increment.

The growth contribution to DVVG is derived from the basic viscous law

$$\dot{R} = AR = \frac{p - p_{g0}}{4\eta} R = \frac{T_1}{3} (p - p_{g0}) R \quad (224)$$

where

- $\dot{R}$  = the time derivative of radius, a growth velocity
- $p_{g0}$  = the threshold pressure ( $p_{g0} = T_2$  in the code)
- $\eta$  = the material viscosity
- $T_1 = 0.75/\eta$  is the viscosity parameter used in the code

For a time increment in which the pressure varies linearly with time, Eq. (219) can be integrated to provide the final radius.

$$R_1 = R_0 \exp \left[ \frac{T_1}{3} \left( \frac{p_1 + p_0}{2} - p_{g0} \right) \Delta t \right] \quad (225)$$

where

- $p_1, p_0$  = pressures at the end and beginning of the time increment
- $R_1, R_0$  = radii at either end of the time increment

The volume of a void at the end of the increment is

$$\begin{aligned} v_1 &= \frac{4}{3} \pi R_1^3 = \frac{4}{3} \pi R_0^3 \exp \left[ T_1 \left( \frac{p_1 + p_0}{2} - p_{g0} \right) \Delta t \right] \\ &= v_0 \exp \left[ T_1 \left( \frac{p_1 + p_0}{2} - p_{g0} \right) \Delta t \right] \end{aligned} \quad (226)$$

where

- $v_1, v_0$  = volumes at the end and beginning of the time increment

The change in volume for all voids is found by multiplying the volume of each void times the concentration  $\rho(R)$ .

$$\begin{aligned}
DVVG_g &= V_{v1} - V_{v0} = \frac{4\pi}{3D} \int_0^{\infty} R^3 \rho(R) dR - V_{v0} \\
&= \frac{4\pi}{3D} \int_0^{\infty} R_0^3 \exp\left[T_1 \left(\frac{p_1 + p_0}{2} - p_{g0}\right) \Delta t\right] \rho(R_0) dR_0 - V_{v0} \quad (227)
\end{aligned}$$

which is obtained with the aid of Eq. (226). The concentration  $\rho(R)dR$  has been replaced by  $\rho(R_0)dR_0$  because the number of voids has not changed. When the invariant terms are taken outside the integral and we recognize that

$$V_{v0} = \frac{4\pi}{3D} \int_0^{\infty} R_0^3 \rho(R_0) dR_0 \quad (228)$$

then

$$DVVG_g = V_{v0} \left\{ \exp\left[T_1 \left(\frac{p_1 + p_0}{2} - p_{g0}\right) \Delta t\right] - 1 \right\} \quad (229)$$

The combination of Eqs. (223) and (229) gives the total growth in the volume of voids.

In the fracturing routine an iteration procedure is used to determine the applied pressure. First, two estimates of pressure (PJ and PK) are made, and the change in void volume DVVG associated with each is calculated. Then, from the equation of state, pressures PA and PB are computed based on the two values of DVVG. The four values of pressure

are used to make a new estimate of PJ. The convergence criterion is a sufficiently small difference between PJ and PA.

The first estimate of PJ is simply the pressure PO of the previous cycle. The estimate of PK is the minimum of three pressures:

- The pressure based on no void volume change so that all volume change is taken in strain.
- PG, the pressure that would cause void growth to absorb the entire volume change.
- PN, the pressure that would cause nucleation to absorb the entire volume change.

The strain-based pressure is the usual one:

$$PK = PO - K \frac{\Delta V}{V_s} \quad (230)$$

where

K = the bulk modulus

$\Delta V$  = the change in gross specific volume

$V_s$  = the specific volume of the solid material

For the growth-based pressure, replace DVVG<sub>g</sub> in Eq. (229) by  $\Delta V$  and solve for  $p_1 = PG$ . Then

$$PG = \frac{2}{T_1 \Delta t} \ln \left( \frac{\Delta V}{V_{v0}} + 1 \right) + 2p_{g0} - p_0 \quad (231)$$

Similarly the nucleation-based pressure is derived from Eq. (223) by replacing DVVG<sub>n</sub> by  $\Delta V$  and solving for  $p_1 = PN$ . Then

$$PN = 2T_6 \ln \left( \frac{D \cdot \Delta V}{\Delta T \cdot Z_3} \right) + 2p_{n0} - p_0 \quad (232)$$

where

$$Z_3 = \alpha R_n^3 T_4$$

The pressures PA and PB are average pressures on the gross area of any cross section through the material. Therefore they are derived from the specific volume of the solid and the ratio of the solid area to the gross area of the section. This ratio is  $(1 - \alpha \frac{V}{c} D)$ , where  $\alpha_c$  is a constant. Let  $p'_a$  be the pressure in the solid material. Then

$$\begin{aligned} p'_a &= \frac{PA}{1 - \alpha \frac{V}{c} D} = p'_0 - K \frac{V_s - V_{s0}}{V_s} \\ &= \frac{p_0}{1 - \alpha \frac{V}{c} D} - K \frac{V_s - V_{s0}}{V_s} \end{aligned} \quad (233)$$

This form for the equation-of-state relation is verified by the two-dimensional code calculations of Appendix V. In those results it was found that  $\alpha_c$  should be about 2.

The deviator stress is computed from the following elastic-plastic-viscous relations

$$\begin{aligned} \Delta SD &= \frac{4}{3} \mu \frac{\Delta V}{V_0} & |SD| &< \frac{2}{3} Y \frac{V_s}{V_0} \\ &= \frac{2}{3} Y F_1 + \frac{4\eta}{3 V \Delta t} \frac{\Delta V}{V_0} F_2 & |SD| &\geq \frac{2}{3} Y \frac{V_s}{V_0} \end{aligned} \quad (234)$$

where

$Y$  = the yield strength

$V_0$  = the gross specific volume

$\eta$  = the viscosity

$F_1$  = a thermal strength reduction factor, which is set to 1.0 in these calculations

$F_2$  =  $1 - 4V_v/V_0$ , a reduction factor derived from the results of Appendix V

In the code  $4\eta/3$  is replaced by  $1/T_1$ , and the change in density rather than change in specific volume is used in the viscous portion of the relations.

In some cases the direct use of Eq. (233) leads to unstable iterations in the routine. For small values of DVVG (the usual condition), PA becomes less negative (smaller tensile value) with increasing DVVG. But after some critical value of DVVG, further increases can lead to a more tensile value of PA. This reversed relationship between PA and DVVG occurs for large values of  $V_v$  as the denominators in Eq. (233) become important. The critical value of DVVG is obtained by differentiating the coded form of Eq. (233) with respect to DVVG. Setting this derivative equal to zero, we find that the extremum of PA occurs approximately at

$$DVVG_{\max} = \frac{1 - \alpha_c (NM)}{2 D \alpha_c} \quad (235)$$

where  $NM = V_{v0} D_0$ , the relative void volume at the beginning of the time increment. To maintain stability in the iterations, it is then required that DVVG never exceed  $DVVG_{\max}$ .

## 2. CODE CHANGES TO ACCOMMODATE FRACTURING

The changes required in a wave propagation code to include the DFRACT routine are similar to those for BFRACT, the brittle fracture subroutine. The changes for both are described in Subsection 2 of the following appendix.

## 3. LISTING AND FLOW CHARTS FOR DFRACT

The DFRACT subroutine and a flow chart are given on the following pages. Next is a sample input deck for an SRI PUFF calculation of ductile fracturing and some sample printout.

The additional input data required for fracturing are included as the first six variables of the  $TSR(M,)$  array. These six are used as T1, T2, . . . T6 in the subroutine. They are described in the nomenclature list with the subroutine and in the preceding derivation of equations.



```

SUBROUTINE DFRACT(H3,S,P,NM,NT,DH,DOLD,T1,T2,T3,T4,T5,T6,DT,EQSTCM,DFR 0010
1 ,MUM,Y,YD,F) DFR 0020
C PJ, PK TWO ESTIMATES OF PRESSURE DFR 0030
C PL STORAGE FOR PREVIOUS ESTIMATE OF PRESSURE DFR 0040
C PA, PB COMPUTED PRESSURES, BASED ON PJ AND PK DFR 0050
C PN, PG PRESSURES ASSOCIATED WITH NUCLEATION AND GROWTH DFR 0060
C DVVG CHANGE IN VOID VOLUME, CM3/GM DFR 0070
C NM RELATIVE VOID VOLUME DFR 0080
C NT VOID DENSITY, NUMBER/CM3 DFR 0090
C T1 GROWTH CONSTANT = 3/(4*ETA) DFR 0100
C T2 GROWTH THRESHOLD DFR 0110
C T3 NUCLEATION RADIUS DFR 0120
C T5 NUCLEATION THRESHOLD DFR 0130
C T4,T6 PARAMETER FOR THE GROWTH AND NUCLEATION DFR 0140
C DENSITY EXPONENTS (T3, T6) DFR 0150
C DFR 0160
C DFR 0170
REAL NM,NT,MUM DFR 0180
INTEGER H3 DFR 0190
DATA ALF,SMF/2.,1.88/ DFR 0200
IF (H3 .EQ. 6) RETURN DFR 0210
H3=3 $ YT=Y $ PJ=PO=P $ NC=0 $ RED=1. DFR 0220
VVO=NM/DOLD $ VSU=1./JULD-VVO $ DELV=1./DH-1./DOLD DFR 0230
DVVGMAX=(1.-ALF*NM)/(2.*ALF*DH) DFR 0240
Z3=8.*3.1416*T3**3*T4 DFR 0250
C ESTIMATE PK BASED ON STRAIN, GROWTH, AND NUCLEATION DFR 0260
PK=PO-EQSTCM*DELV/VVO DFR 0270
IF (DELV .LE. 0.) GO TO 30 DFR 0280
PG=PL=PK DFR 0290
IF (VVO .EQ. 0.) GO TO 25 DFR 0300
PG=2./(T1*DT)*ALOG(1.+DELV/VVO)+2.*T2-PG DFR 0310
25 PN=2.*T6*ALOG(DELV*DH/Z3/DT)+2.*T5-PG DFR 0320
PK=AMAX1(PK,PG,PN) DFR 0330
30 PN=AMINI(0.5*(PK+PG)-T5,0.) DFR 0340
IF (PN .LT. 0.) PN=EXP(PN/T6) DFR 0350
PG=AMINI(0.5*(PK+PG)-T2,0.) DFR 0360
DVVG=AMINI(DVVGMAX,VVO*(EXP(T1*PG*DT)-1.))+Z3*PN*DT/DH DFR 0370
C COMPUTE STRESS CORRESPONDING TO DVVG AND PK DFR 0380
RVV=NM+DVVG*DH DFR 0390
RED=AMAX1(0.,1.-4.*RVV) DFR 0400
PB=(P/(1.-ALF*NM)-2.*EQSTCM*(DELV-DVVG)/(2.*VSU+DELV-DVVG))* DFR 0410
1 (1.-ALF*RVV) DFR 0420
50 CONTINUE DFR 0430
C DFR 0440
C BEGINNING OF ITERATION LOOP DFR 0450
C COMPUTE STRESS CORRESPONDING TO DVVG AND PJ DFR 0460
55 PN=AMINI(0.5*(PJ+PG)-T5,0.) DFR 0470
IF (PN .LT. 0.) PN=EXP(PN/T6) DFR 0480
PG=AMINI(0.5*(PJ+PG)-T2,0.) DFR 0490
DVVG=AMINI(DVVGMAX,VVO*(EXP(T1*PG*DT)-1.))+Z3*PN*DT/DH DFR 0500
RVV=NM+DVVG*DH DFR 0510
RED=AMAX1(0.,1.-4.*RVV) DFR 0520
PA=(P/(1.-ALF*NM)-2.*EQSTCM*(DELV-DVVG)/(2.*VSU+DELV-DVVG))* DFR 0530
1 (1.-ALF*RVV) DFR 0540
SDH=S-P-AMAX1(MUM*(1.-SMF*RVV),0.)*DELV*DH DFR 0550
IF (ABS(SDH) .LT. Y*F*RED) GO TO 70 DFR 0560
YT=AMINI(ABS(SDH),(Y+YD*ABS(DH-DOLD))*RED) DFR 0570
SDH=SIGN(YT*F,SDH)-1.0/T1*(DH-DOLD)/DH/DT*RED DFR 0580
70 SA=PA+SDH DFR 0590
PL=PJ DFR 0600
PJ=(PK*PA-PB*PJ)/(PA-PB+PK-PJ) DFR 0610
NC=NC+1 DFR 0620
C TEST FOR COMPLETION OF ITERATIONS DFR 0630
IF (NC .GE. 10) GO TO 300 DFR 0640
IF (ABS(PL-PA) .LT. 1.E8) GO TO 300 DFR 0650
IF (ABS(PA-PJ) .GT. ABS(PO-PJ)) GO TO 55 DFR 0660
PB=PA $ PK=PL $ GO TO 55 DFR 0670

```

SUBROUTINE DFRACT

```

C
C      ENDING ROUTINE
300  NM=UH*(VVD+DVVG)
      NT=NT*DH/DOLU+T4*PN*DT
      IF (NM .GT. 0.6/ALF) GO TO 400
      P=PA $ S=SA
      Y=YT/RED
      RETURN
C
C      END WITH SEPARATION
400  S=P*0. $ Y=YT/RED $ H3=6
      RETURN
      END

```

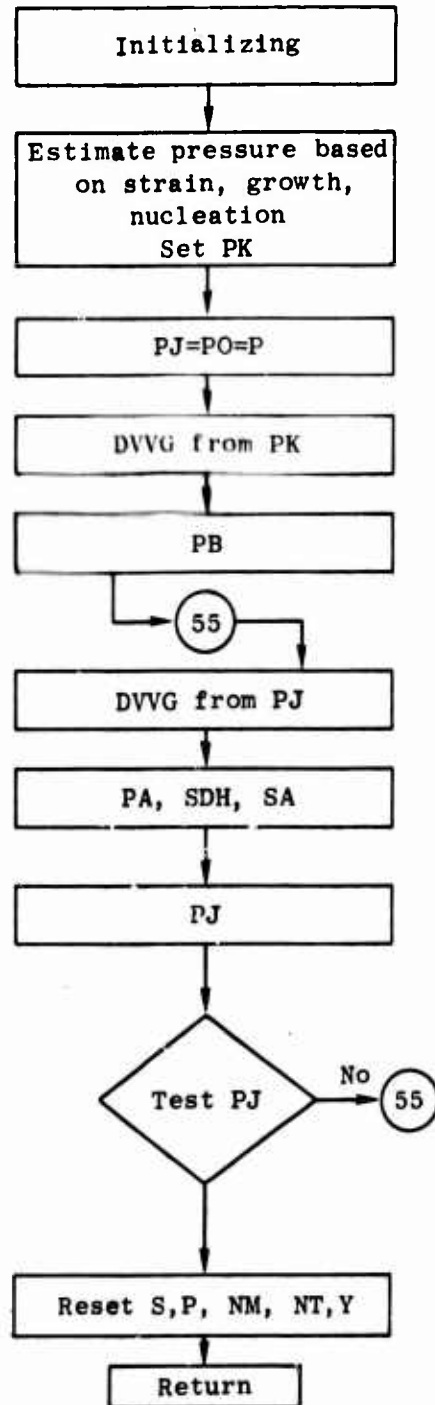
```

DFR 0680
DFR 0690
DFR 0700
DFR 0710
DFR 0720
DFR 0730
DFR 0740
DFR 0750
DFR 0760
DFR 0770
DFR 0780
DFR 0790
DFR 0800

```

SUBROUTINE DFRACT (Concluded)

DFRACT



This routine provides the equation of state for a ductile material undergoing fracture. It also provides the void volume and number of voids.

Set indicators; compute  $\bar{\epsilon}_3$ , the nucleation void volume.

Make estimates of new pressure, assuming that all volume change is taken in strain, or void growth, or nucleation. The smallest tensile value of these is PK.

Set PJ to pressure of previous cycle.

Compute void volume change based on the pressure estimate.

Compute pressure associated with DVVG and PK.

Compute void volume change associated with PJ

Compute pressure associated with DVVG

Compute a new estimate of PJ based on linear interpolations of PA and PB with PJ and PK.

Test for convergence of PJ by comparing it with PA. If unsatisfactory, take closest of the two previous estimates as PK; then return to location 55 for another iteration.

Compute average stress and pressure, update the void volume and number, and reset current yield strength.

FLOW CHART FOR SUBROUTINE DFRACT

```

IDENT 939L (4A) FRACTURE, 1145 AL, 609FPS, JULY, 1971
1 NYEDT = 0 NJEDIT = 18 -0 -0
JEDITS = 27 28 29 30 31 32 15 16 17 18 19 20 21 22
          23 24 25 26
6 NEDTM = 11111 NEDIT = 20 NPERN = 1 -0
7 STOPS = -0 JCYCS = 150 CKS = 3.000E+00 TS = 1.400E-06
8 NMTRLS = 2 MATFL = 1 UZERO = 1.856E+04 -0*****

ALUMINUM FLYER RHOS = 2.700E+00 NSRM = 0 NYAM = 31 NPOR = 0 NCON = 0
EQSYC = 7.600E+11 EQSTD = 1.500E+12 EQSTE = 1.220E+11 EQSTG = 2.040E+00
EQSTM = 2.500E-01 EQSTS = 0. EQSTN = -0.
TENS = -1.000E+11 -0. -1.000E+00
COSQ = 4.000E+00 C1 = 5.000E-02 -0.
Y0 = 2.000E+09 MU = 3.000E+11 -0. -0.

ALUMINUM TARGET RHOS = 2.700E+00 NSRM = 6 NYAM = 31 NPOR = 0 NCON = 0
EQSYC = 7.600E+11 EQSTD = 1.500E+12 EQSTE = 1.220E+11 EQSTG = 2.040E+00
EQSTM = 2.500E-01 EQSTS = 0. EQSTN = -0.
TSR(1) = -1.000E-02 TSR(2) = -4.000E+09 TSR(3) = 1.000E-04 TSR(4) = 3.000E+09
TSR(5) = -3.000E+09 TSR(6) = -4.000E+08 -0. -0.
TENS = -1.200E+10 -0. -1.000E+00
COSQ = 4.000E+00 C1 = 5.000E-02 -0.
Y0 = 2.000E+09 MU = 3.000E+11 -0. -0.

NLAYER = 2 JMAT = 1 2 -0 -0 -0 -0 -0 -0 -0 -0
NZONES = 1 10 CELLS IN 1.140E-01 CM -0. -0.
NZONES = 1 25 CELLS IN 3.180E-01 CM -0. -0.

```

```

IDENT 847K FRACTURE IN 1145 AL, 423 FPS, JULY 1971
1 NYEDT = 0 NJEDIT = 18 -0 -0
JEDITS = 27 28 29 30 31 32 15 16 17 18 19 20 21 22
          23 24 25 26
6 NEDTM = 11111 NEDIT = 20 NPERN = 1 -0
7 STOPS = -0 JCYCS = 150 CKS = 3.000E+00 TS = 3.000E-06
8 NMTRLS = 2 MATFL = 1 UZERO = 1.289E+04 -0*****

ALUMINUM FLYER RHOS = 2.700E+00 NSRM = 0 NYAM = 31 NPOR = 0 NCON = 0
EQSYC = 7.600E+11 EQSTD = 1.500E+12 EQSTE = 1.220E+11 EQSTG = 2.040E+00
EQSTM = 2.500E-01 EQSTS = 0. EQSTN = -0.
TENS = -1.000E+11 -0. -1.000E+00
COSQ = 4.000E+00 C1 = 5.000E-02 -0.
Y0 = 2.000E+09 MU = 3.000E+11 -0. -0.

ALUMINUM TARGET RHOS = 2.700E+00 NSRM = 6 NYAM = 31 NPOR = 0 NCON = 0
EQSYC = 7.600E+11 EQSTD = 1.500E+12 EQSTE = 1.220E+11 EQSTG = 2.040E+00
EQSTM = 2.500E-01 EQSTS = 0. EQSTN = -0.
TSR(1) = -1.000E-02 TSR(2) = -4.000E+09 TSR(3) = 1.000E-04 TSR(4) = 3.000E+09
TSR(5) = -3.000E+09 TSR(6) = -4.000E+08 -0. -0.
TENS = -1.200E+10 -0. -1.000E+00
COSQ = 4.000E+00 C1 = 5.000E-02 -0.
Y0 = 2.000E+09 MU = 3.000E+11 -0. -0.

NLAYER = 2 JMAT = 1 2 -0 -0 -0 -0 -0 -0 -0 -0
NZONES = 1 10 CELLS IN 2.360E-01 CM -0. -0.
NZONES = 1 25 CELLS IN 6.380E-01 CM -0. -0.

```

TWO INPUT DECKS FOR CURRENT VERSION OF SRI PUFF FOR DUCTILE FRACTURE PROBLEMS

DATE = 07/09/71 IDENT 939L (46) FRACTURE.1145 AL. 609FPS. JULY, 1971

TIME EDIT NO. 7 AT N = 140. TIME = 1.12177E+06 SECS. JSTAR = 37. CALC TIME IS 9.732 SECS

J	CELL	X	CM/SEC	U	RHL	PHL	SHL	EHL	DHL	CHL	J	COND	MOM	P1	P2	
		CM	DYN/CM2	DYN/CM2	DYN/CM2	DYN/CM2	DYN/CM2	ERGS	GM/CM3	CM/SEC	CELL		TAPS			
1	.06124	507	0.823E+07	3.051E+07	4.991E+07	2.280E+05	2.7001	6.5549E+05	1	S	S	B	ALUMINUM	1.333E+09	-8.043E+07	
2	.01523	400	0.038E+07	1.329E+09	5.740E+09	7.023E+06	2.7066	6.5673E+05	2	S	N	B	ALUMINUM	1.333E+09	-1.271E+09	
3	.02690	445	1.435E+07	1.206E+09	1.436E+07	1.167E+07	2.7040	6.5659E+05	3	S	N	B	ALUMINUM	1.333E+09	-1.220E+09	
4	.03020	443	3.525E+07	1.236E+09	2.989E+07	1.325E+07	2.7041	6.5663E+05	4	S	N	B	ALUMINUM	1.333E+09	-1.266E+09	
5	.04966	446	6.073E+07	1.209E+09	6.073E+07	1.350E+07	2.7040	6.5659E+05	5	S	N	B	ALUMINUM	1.333E+09	-1.249E+09	
6	.06102	399	2.203E+07	1.218E+09	2.373E+07	1.392E+07	2.7041	6.5661E+05	6	S	N	B	ALUMINUM	1.333E+09	-1.242E+09	
7	.07243	426	9.132E+07	1.123E+09	9.132E+07	1.417E+07	2.7037	6.5651E+05	7	S	N	B	ALUMINUM	1.333E+09	-1.215E+09	
8	.08381	425	9.261E+07	1.108E+09	9.728E+07	1.431E+07	2.7037	6.5650E+05	8	S	N	B	ALUMINUM	1.333E+09	-1.205E+09	
9	.09520	372	9.113E+07	1.137E+09	9.113E+07	1.449E+07	2.7038	6.5652E+05	9	S	N	B	ALUMINUM	1.333E+09	-1.228E+09	
10	.10658	385	5.737E+07	1.258E+09	4.771E+07	1.471E+07	2.7042	6.5665E+05	10	S	N	B	ALUMINUM	1.333E+09	-1.210E+09	
11	.11797	391	0.	0.	0.	0.	2.7040	6.5546E+05	11	S	L	B	ALUMINUM	1.333E+09	0.	
12	.11847	6956	8.040E+08	5.077E+08	8.040E+08	1.602E+07	2.7015	6.5591E+05	12	S	S	B	ALUMINUM	1.290E+02	-0.	
13	.13118	7143	2.753E+09	1.420E+09	2.753E+09	1.743E+07	2.6946	6.5489E+05	13	S	N	B	ALUMINUM	3.711E+02	-0.	
14	.14396	7513	4.950E+09	3.622E+09	4.950E+09	2.105E+07	2.6868	6.5469E+05	14	S	N	C	ALUMINUM	6.227E+02	0.964E+09	
15	.15671	7524	6.267E+09	5.139E+09	6.306E+09	2.482E+07	2.6815	6.5466E+05	15	S	N	C	ALUMINUM	8.809E+02	8.798E+07	
16	.16951	6172	5.130E+09	4.805E+09	5.255E+09	2.387E+07	2.6826	6.5467E+05	16	S	N	C	ALUMINUM	1.116E+03	1.474E+05	
17	.18231	5408	5.402E+09	5.044E+09	5.408E+09	2.443E+07	2.6816	6.5467E+05	17	S	N	C	ALUMINUM	1.315E+03	6.417E+05	
18	.19512	5264	5.542E+09	5.170E+09	5.566E+09	2.488E+07	2.6809	6.5472E+05	18	S	N	C	ALUMINUM	1.499E+03	1.714E+04	
19	.20792	4938	5.463E+09	5.124E+09	5.465E+09	2.510E+07	2.6794	6.5462E+05	19	S	N	C	ALUMINUM	1.674E+03	3.679E+04	
20	.22072	4973	5.584E+09	5.119E+09	5.584E+09	2.596E+07	2.6794	6.5462E+05	20	S	N	C	ALUMINUM	1.844E+03	7.924E+04	
21	.23359	4944	5.584E+09	5.119E+09	5.584E+09	2.649E+07	2.6794	6.5462E+05	21	S	N	C	ALUMINUM	2.015E+03	1.197E+03	
22	.24638	5012	5.582E+09	4.782E+09	5.592E+09	2.902E+07	2.6737	6.5460E+05	22	S	N	C	ALUMINUM	2.186E+03	2.585E+03	
23	.25921	5228	5.670E+09	4.400E+09	5.670E+09	3.281E+07	2.6716	6.5467E+05	23	S	N	C	ALUMINUM	2.361E+03	2.585E+03	
24	.27204	5312	5.652E+09	4.170E+09	5.652E+09	3.427E+07	2.6701	6.5452E+05	24	S	N	C	ALUMINUM	2.542E+03	5.450E+03	
25	.28493	5399	5.607E+09	4.120E+09	5.607E+09	3.806E+07	2.6664	6.5423E+05	25	S	N	C	ALUMINUM	2.726E+03	6.867E+03	
26	.29781	5440	5.452E+09	4.261E+09	5.452E+09	4.217E+07	2.6605	6.5422E+05	26	S	N	C	ALUMINUM	2.912E+03	2.901E+02	
27	.31090	6464	5.130E+09	4.074E+09	5.130E+09	4.584E+07	2.6459	6.5427E+05	27	S	N	C	ALUMINUM	3.117E+03	5.992E+07	
28	.32450	6903	4.236E+09	3.387E+09	4.237E+09	4.903E+07	2.6404	6.5418E+05	28	S	N	C	ALUMINUM	3.346E+03	5.278E+02	
29	.33784	7214	2.810E+09	2.833E+09	2.810E+09	5.902E+07	2.6384	6.5418E+05	29	S	N	C	ALUMINUM	3.589E+03	2.997E+02	
30	.35058	7463	1.963E+09	2.393E+09	1.995E+09	6.862E+07	2.6384	6.5427E+05	30	S	N	C	ALUMINUM	3.841E+03	4.400E+03	
31	.36331	7021	6.213E+08	2.170E+09	8.376E+08	2.102E+07	2.6300	6.5463E+05	31	S	N	C	ALUMINUM	4.090E+03	3.802E+03	
32	.37601	6707	6.699E+08	6.694E+08	6.699E+08	1.699E+07	2.6273	6.5471E+05	32	S	N	C	ALUMINUM	4.325E+03	7.350E+04	
33	.38881	7072	1.093E+09	7.520E+07	1.092E+09	1.258E+07	2.6295	6.5429E+05	33	S	N	C	ALUMINUM	4.562E+03	3.026E+05	
34	.40154	7971	2.174E+08	3.824E+08	2.163E+08	9.343E+06	2.6294	6.5433E+05	34	S	N	C	ALUMINUM	4.802E+03	7.308E+07	
35	.41427	8710	2.184E+08	2.063E+08	2.184E+08	5.292E+06	2.6291	6.5460E+05	35	S	N	C	ALUMINUM	5.107E+03	4.333E+08	
36	.42702	8666	1.677E+08	1.096E+08	1.677E+08	1.148E+05	2.6296	6.5541E+05	36	S	N	B	ALUMINUM	5.408E+03	0.	
37	.43974	8836	0.	0.	0.	0.	2.7000	6.5546E+05	37	S	L	B	ALUMINUM	5.713E+03	-0.	
N#	150	JSTAR	37	TIME	1.254E+06	CALC TIME	10.923	SECS	JTS	2	CTNH	1.319E+08	SHMAX	1.674E+09	JSMAX	15

FINAL TIME EDIT FOR SRI PUFF CALCULATION — 939L FOR DUCTILE FRACTURE IN ALUMINUM (for J = 12 to 37, P1 = Relative Void Volume and Ps = number of voids/cm<sup>3</sup>)

DATE = 07/69/71 IDENT 939L (46) FRACTURE:1145 AL. 609PPS. JULY, 1971  
 FIRST SCRIBE, INTERFACE AND JEDIT STRESS HISTORIES

N	TIME MUSEC	S12 KBAR	S23 KBAR	S34 KBAR	S (27) KBAR	S (28) KBAR	S (29) KBAR	S (30) KBAR	S (31) KBAR	S (32) KBAR	JTS	DTNH NANOSEC	DELTIM SEC
101	.712	-200	0.000	0.000	3.0208	2.9138	3.1208	3.0678	2.3518	1.1538	9	1.147	.410
102	.714	-205	0.000	0.000	2.9668	2.8338	2.9718	2.9208	2.3518	1.0228	9	1.147	.050
103	.715	-206	0.000	0.000	2.9028	2.7308	2.9718	2.7908	1.6528	.8678	9	1.682	.051
104	.717	-200	0.000	0.700	2.8288	2.6258	2.5758	2.6228	1.6528	.6818	9	1.983	.051
105	.720	-184	0.000	0.000	2.7428	2.4928	2.3168	2.1678	1.3198	.4808	4	2.379	.052
106	.723	-152	0.000	0.000	2.6428	2.3328	2.0088	1.8058	.9198	.1968	10	2.855	.051
107	.726	-100	0.000	0.000	2.5268	2.1418	1.6378	1.3638	.4448	-.1178	10	3.426	.050
108	.730	.067	0.000	0.000	2.3938	1.9088	1.2018	.8108	-.1158	-.4878	10	4.111	.050
109	.735	.067	0.000	0.000	2.2388	1.6238	.6908	.1518	-.7658	-.9218	10	4.933	.050
110	.741	.150	0.000	0.000	2.0518	1.2648	.0988	-.6448	-1.5668	-1.4508	10	5.920	.052
111	.748	.174	0.000	0.000	1.8118	.5148	-.5828	-1.6408	-2.5298	-1.9738	10	7.104	.051
112	.757	.079	0.000	0.000	1.4648	.2348	-1.3608	-2.7708	-3.6213	-2.5458	5	8.525	.051
113	.767	-120	0.000	0.000	.8998	-.5998	-2.2648	-3.9848	-4.1408	-3.0698	5	10.229	.053
114	.779	-201	0.000	0.000	-.0998	-1.6658	-3.3358	-5.1548	-5.9268	-4.9898	9	12.275	.056
115	.792	.063	0.000	0.000	-1.7238	-2.4748	-4.5378	-5.9268	-5.9268	-3.8628	10	13.183	.060
116	.805	.173	0.000	0.000	-3.8318	-4.1948	-5.6518	-6.2048	-5.7928	-4.4388	10	13.159	.062
117	.819	-.069	0.000	0.000	-6.1378	-6.8748	-7.4728	-6.2018	-5.6798	-5.2848	9	13.180	.067
118	.832	-.160	0.000	0.000	-8.2798	-8.8718	-7.0928	-6.0758	-5.6328	-6.1018	8	13.170	.073
119	.845	.025	0.000	0.000	-9.9828	-9.7618	-7.0968	-6.2138	-5.9298	-6.8858	10	13.178	.076
120	.858	.083	0.000	0.000	-10.1298	-10.0858	-6.4878	-6.6798	-6.4258	-6.3278	7	13.165	.079
121	.871	-.011	0.000	0.000	-9.3708	-9.4388	-9.1308	-7.5918	-6.9598	-5.9848	9	13.173	.441
122	.885	-.038	0.000	0.000	-8.6588	-8.5798	-8.2858	-8.7798	-7.3808	-6.2208	8	13.180	.085
123	.898	-.010	0.000	0.000	-7.5948	-7.7468	-8.9718	-9.5548	-7.8688	-6.8408	10	13.169	.082
124	.911	-.015	0.000	0.000	-6.8798	-7.1578	-9.3778	-9.3938	-8.5438	-7.3668	7	13.185	.083
125	.924	-.000	0.000	0.000	-6.5618	-6.8018	-7.5778	-8.4388	-8.0658	-7.6558	2	13.175	.084
126	.937	-.003	0.000	0.000	-6.4028	-6.5638	-6.8668	-7.3788	-8.0808	-7.7248	8	13.181	.090
127	.950	-.035	0.000	0.000	-6.2658	-6.3518	-6.2788	-6.7878	-7.4698	-7.4498	5	13.175	.084
128	.964	-.137	0.000	0.000	-6.1308	-6.1508	-6.0128	-6.2468	-5.8438	-6.2928	7	13.183	.086
129	.977	-.048	0.000	0.000	-6.0098	-6.0828	-5.9428	-5.4678	-5.8438	-4.3688	10	13.180	.084
130	.990	-.063	0.000	0.000	-5.9128	-5.9858	-5.7128	-5.1678	-4.7148	-4.3688	6	13.179	.088
131	1.003	-.246	0.000	0.000	-5.8318	-5.9108	-5.2508	-4.7358	-3.8018	-2.6088	9	13.182	.086
132	1.016	-.347	0.000	0.000	-5.7668	-5.8108	-4.6918	-4.1958	-2.7718	-1.1638	2	13.184	.086
133	1.029	-.353	0.000	0.000	-5.7028	-5.5398	-4.0848	-3.4678	-1.8898	-.8368	10	13.184	.086
134	1.043	-.383	0.000	0.000	-5.6398	-5.3768	-3.4668	-1.8768	-1.4208	-.8518	3	13.179	.087
135	1.056	-.440	0.000	0.000	-5.5768	-5.1968	-3.0128	-1.6138	-1.0258	-.6408	9	13.182	.087
136	1.069	-.423	0.000	0.000	-5.5208	-4.8218	-2.9388	-1.7158	-.9428	-.5148	2	13.184	.084
137	1.082	-.409	0.000	0.000	-5.4238	-3.7488	-3.0378	-2.0178	-1.0198	-.0538	10	13.181	.085
138	1.095	-.446	0.000	0.000	-5.2948	-3.3608	-2.9848	-2.3388	-1.0948	.3578	3	13.188	.085
139	1.109	-.416	0.000	0.000	-5.1958	-3.6638	-2.7798	-2.3388	-.10548	.6338	2	13.181	.085
140	1.122	-.378	0.000	0.000	-5.1308	-4.2378	-2.8108	-1.9958	-.0388	.6668	10	13.184	.084
141	1.135	-.466	0.000	0.000	-5.0578	-4.5828	-3.1068	-1.4708	-.5378	.2778	5	13.181	.442
142	1.148	-.628	0.000	0.000	-5.1308	-4.4998	-3.3108	-1.2908	-.3478	-.2778	9	13.187	.085
143	1.161	-.672	0.000	0.000	-5.0668	-4.1838	-3.1278	-1.6038	-.6428	-.1.6678	2	13.185	.087
144	1.175	-.673	0.000	0.000	-4.9978	-3.8088	-2.7328	-1.6038	-.6428	-.1.6678	2	13.185	.087
145	1.188	.031	0.000	0.000	-4.6998	-3.4948	-2.5848	-2.1678	-1.8498	-2.4838	10	13.188	.082
146	1.201	.555	0.000	0.000	-4.1568	-3.3098	-2.9408	-2.8288	-3.0828	-3.0228	5	13.188	.081
147	1.214	.649	0.000	0.000	-3.7558	-3.3318	-3.0118	-3.6708	-4.5868	-3.5108	2	13.186	.083
148	1.227	.265	0.000	0.000	-3.7788	-3.3318	-3.0118	-4.6048	-4.7488	-4.0548	6	13.185	.082
149	1.240	-.148	0.000	0.000	-4.1468	-3.7258	-4.8448	-5.1418	-4.5238	-4.3888	10	13.184	.083
150	1.254	-.116	0.000	0.000	-4.6678	-5.6288	-5.4438	-5.1678	-4.5368	-4.3818	7	13.184	.083
151			0.000	0.000				-5.0508	-4.7498	-4.2648	2	13.188	.083

ONE PAGE OF HISTORICAL LISTING FOR 939L FOR DUCTILE FRACTURE IN ALUMINUM

NOMENCLATURE FOR APPENDIX VII

A	$(p-p_{g0})/4\eta$ , growth parameter, 1/sec
D	gross density, gm/cm <sup>3</sup>
DH	current density, gm/cm <sup>3</sup>
DØLD	density of previous cycle, gm/cm <sup>3</sup>
DT	time increment, sec
DVVG	change in void volume, cm <sup>3</sup> /gm
EQSTCM	bulk modulus, dyn/cm <sup>2</sup>
F <sub>1</sub>	thermal strength reduction factor; varying from 0 for no strength to 1 for no reduction
F <sub>2</sub>	reduction factor based on void volume
H3	fracturing indicator = 2 in SRI PUFF for no damage = 3 for partial damage = 6 for full spall
K	bulk modulus, dyn/cm <sup>2</sup>
MUM	shear modulus, dyn/cm <sup>2</sup>
N	number of voids, number/cm <sup>3</sup>
NM	relative void volume
NT	number of voids/cm <sup>3</sup>
P	pressure, dyn/cm <sup>2</sup>
PA,PB	pressure computed from the equation of state

PJ,PK	estimates of pressure
R	void radius, cm
$R_n$	a parameter in the nucleated distribution function, cm
S	stress (negative for tension), $\text{dyn/cm}^2$
SDH	deviator stress
T1	coefficient of growth equation, $\text{cm}^2/\text{dyn}/\text{sec}$
T2	threshold stress for growth, $\text{dyn/cm}^2$
T3	radius at nucleation, cm
T4	nucleation rate coefficient, $\text{no./cm}^3/\text{sec}$
T5	threshold stress for nucleation, $\text{dyn/cm}^3$
T6	a nucleation factor, $\text{dyn/cm}^2$
VSO	solid volume, $\text{cm}^3/\text{gm}$
VVO	void volume, $\text{cm}^3/\text{gm}$
$V_o$	gross specific volume, $\text{cm}^3/\text{gm}$
$V_s$	solid specific volume, $\text{cm}^3/\text{gm}$
$V_v$	specific volume of voids, $\text{cm}^3/\text{gm}$
Y	yield strength, $\text{dyn/cm}^2$
YD	strain hardening modulus, defined so that the increase in yield is $YD \cdot  DH - D\theta LD $ , $\text{dyn-cm/gm}$
p	pressure, $\text{dyn/cm}^2$
$p_a$	pressure in the solid material, $\text{dyn/cm}^2$
$p_{go}$	threshold pressure for growth, $\text{dyn/cm}^2$
$p_{no}$	threshold pressure for nucleation, $\text{dyn/cm}^2$



$t$	time, sec
$v$	volume of a void, $\text{cm}^3$
$\alpha$	a constant
$\alpha_c$	a constant
$\eta$	material viscosity, $\text{dyn-sec/cm}^2$
$\mu$	shear modulus, $\text{dyn/cm}^2$
$\rho(R)$	concentration of voids at a radius $R$ , $\text{number/cm}^4$

## APPENDIX VIII

### BRITTLE FRACTURE SUBROUTINE: BFRACT

The brittle fracture subroutine, BFRACT, and the equations contained in it are described in this appendix. The routine provides a calculation of stress, as well as fracture damage, for a given internal energy and density; hence, the routine contains the equation-of-state relations for a material undergoing brittle fracture. The routine is intended for use in one-dimensional artificial viscosity wave propagation codes with either one- or two-step integration schemes. In one-step codes, the routine is called at each cycle for each cell in which fracturing has begun. In two-step codes, one of the steps (preferably the one that calculates stress as a midcell quantity) should use BFRACT as the equation of state during fracturing. The other step should merely take the average of stresses in adjacent cells and not call BFRACT for a stress calculation.

All the formal parameters of BFRACT must be input from the calling routine. The output quantities among these parameters are H3, S, P, NM, NT, and Y. (Note that LS, H3, and JS are integers; the other parameters are floating-point.) In addition to these parameters are two large arrays defined within the routine: CL for crack radii and CN for number of cracks. These two arrays are printed out on calls from EDIT following each TIME EDIT listing.

### DERIVATIONS OF EQUATIONS FOR BRITTLE FRACTURE

At each call, the subroutine is provided with a new density, and it computes stress and pressure and also the current extent of damage. Because the damage and stress level are related nonlinearly, the stress

is determined through an iteration process. First, a stress is estimated and the damage is computed. From this damage, a stress is determined from the equation-of-state relations. Then a new stress estimate is made. This process is repeated until the estimated and computed stresses are sufficiently close.

The damage is characterized by groups of penny-shaped cracks; each group has a concentration CN and a radius CL. At each time increment, a new group may be nucleated and all current cracks may be permitted to grow (if the tensile stress is large enough).

Nucleation is assumed to occur by the development of a number of new cracks of the same size. The nucleation function has the same form as for ductile fracture

$$\frac{\Delta N}{\Delta t} = T_4 \exp\left(\frac{\sigma - \sigma_{n0}}{T_6}\right) \quad \sigma < \sigma_{n0} \quad (236)$$

where

$\Delta N / \Delta t$  = the nucleation rate

$\sigma$  = the stress, negative in tension

$\sigma_{n0} = T_5$  = the nucleation threshold stress

$T_4, T_5, T_6$  = nucleation parameters used in BFRACF

The form of Eq. (236) is justified a posteriori by the observation that the crack distributions computed with it compare fairly well with the observed.

The growth of the brittle cracks is assumed to follow the relation of Dulaney and Brace (Ref. 35) for the propagation of a Griffith-type crack.

$$\frac{V_c}{V_t} = 1 - \frac{R^*}{R} \quad R > R^* \quad (237)$$

$$= 0 \quad R \leq R^*$$

where

$V_c$  = the current crack growth velocity

$V_t$  = the terminal velocity

$R$  = the crack radius

$R^*$  = the critical crack radius

According to Sneddon (Ref. 34) the critical crack radius for a penny-shaped crack is

$$R^* = \frac{\pi E \gamma}{4\sigma^2(1 - \nu^2)} = \frac{\pi K_{IC}^2}{4\sigma^2} \quad (238)$$

where

$E$  = the elastic modulus

$\gamma$  = the surface energy

$\sigma$  = the nominal applied stress

$\nu$  = Poisson's ratio

$K_{IC}$  = the fracture toughness in the opening mode

In BFRACT, for each damage calculation, the cracks in all groups are tested against the critical crack size. For those cracks exceeding the

critical size, crack velocities are computed. The new crack radii are obtained from a Simpson's rule integration of the crack velocity over the time increment.

$$CL_1 = CL_0 + \frac{\Delta t}{6}(V_{c0} + 4V_{cm} + V_{c1}) \quad (239)$$

where

$CL_1, CL_0$  = the radii at the beginning and end of the increment  $\Delta t$

$V_{c0}, V_{cm}, V_{c1}$  = velocities at the beginning, middle and end of the increment

With the aid of Eqs. (237) and (238),  $V_{c0}$  is computed from  $\sigma_0$ ,  $V_{c1}$  from  $\sigma_1$ , and  $V_{cm}$  from  $1/2(\sigma_0 + \sigma_1)$ , where  $\sigma_0$  and  $\sigma_1$  are stresses at the beginning and end of the time increment.

Only ten crack groups are provided in BFRACT for each cell. If more groups are nucleated, these added groups are averaged into the tenth group, as follows

$$CL(10) = \frac{\left[ CN(10) \cdot CL(10)^3 + CN_0 \cdot T_3^3 \right]^{\frac{1}{3}}}{CN(10) + CN_0} \quad (240)$$

$$CN(10) = CN(10) + CN_0 \quad (241)$$

where

$CN_0$  = the number in the newly nucleated group

$T_3$  = the nucleation radius

The averaging in Eq. (240) is performed in such a way that the crack volume is correct for the current cycle. The use of only ten groups has proved satisfactory in our experience. The largest cracks at the end of the calculation are those that were nucleated first. Since these first ones also contribute the most to the crack volume, it is important to represent them accurately. The approximation entailed in the averaging of Eq. (240) should normally have a small effect on the computed crack volume, and hence on the stresses and damage parameters.

The stress and pressure are computed, taking into account the presence of the cracks. When tensile stress is applied to a penny-shaped crack, the crack opens to the volume given by Irwin (Ref. 32)

$$v' = \frac{4\pi R^3 \sigma}{3E} \quad (242)$$

The total crack volume is the sum over all crack groups

$$v_{TOT} = \frac{4\pi\sigma}{3E} \sum_{i=1}^{NCG} CN_i (CL_i)^3 \quad (243)$$

The crack volume is used in the same way the void volume is used in DFRACT to determine the specific volume of the solid. The calculation of pressure, deviator stress, and stress follow the same relations as in DFRACT except that a rate-independent relation is used for deviator stress.

To begin the iteration for stress, two estimates are made of the new stress: one based on strain, the other on expansion of the cracks. The first of these, labelled SCA, is based on the usual equation-of-state relations for the solid, plus the assumption that the crack volume

does not change during the cycle. The second estimate, labelled SCG, is based on the assumption that the existing cracks merely open or close to reflect the volume change. From Eq. (242), this estimate is

$$\sigma_1 = \left( v_1 \frac{\sigma_0}{v_0} \right) \quad (244)$$

where

$\sigma_0$  = the stress at the beginning of the time step

$v_0, v_1$  = crack volume at each end of the time step

In the code nomenclature this equation is

$$SCG = SCO(1 + DELV/VVO) \quad (245)$$

As in DFRACT, the amount of crack volume increase that occurs in any one cycle is limited by DVVGMAX.

## 2. CODE CHANGES TO ACCOMMODATE FRACTURING

Several changes are required in initialization, printout, and calling in any artificial viscosity code to permit use of the routines BFRACT and DFRACT. The changes required for SRI PUFF 3 (Ref. 55) are described here as an example.

### a. Initialization

Ductile and brittle fracture are implemented as material models 6 and 7, respectively, that is, NSR = 6 or 7 (they are mutually exclusive).

The new material data required for fracturing are inserted into the TSR array through READ statements, which are already present. Crack or void volume is stored in NEM(J) and the number per cubic centimeter is stored in NET(J): both are existing arrays. An auxiliary array, EXMAT (M, 10), has been added. One element of this array is used as follows to store an elastic parameter  $4\pi/(3E)$ , used in BFRACT.

```
IF (NSR(M) .EQ. 7) EXMAT(M,2)=0.4654*(1./EQSTC(M)+3./MU(M))      GSR 1875
```

In BFRACT, EXMAT(M,2) is equivalent to the formal parameter FACT.

### b. Printout

For ductile fracturing, the only new variables are the void volume and number of voids. These are stored in the NEM and NET arrays and are listed in each EDIT under the headings P1 and P2, respectively. In addition, the second SCRIBE listing prints the history of NEM and NET at the first six JEDITS.



In brittle fracturing the same printout of NEM and NET occurs as for ductile, but also the CL and CN arrays are printed following each EDIT. This printing is accomplished with the following CALL to BFRACT in the EDIT routine:

```
IF (NSR(M) .EQ. 7 .AND. LSUB(12) .GT. 0) CALL BFRACT(2)           EDI 0495
```

The printing is controlled in BFRACT so that a listing is given only for cells in which fracturing is occurring.

c. Calling

The routines DFRACT and BFRACT have the function of equations of state and therefore replace the call to EQST after damage occurs. The CALLs are from HSTRESS and JSTRESS. The following changes permit both routines to be used simultaneously, if desired. In HSTRESS replace HST 0260 and 0270 with the following (this is the form that would be used in a one-step code):

```

C      IF (NSR(M) .EQ. 7) GO TO 51                                HST 0261
      DUCTILE FRACTURE PATH                                       HST 0262
      CALL DFRACT(H(J,3),SHL(J),PHL(J),NEM(J),NET(J),DH,DOLD,TSR(M,1),
1     TSR(M,2),TSR(M,3),TSR(M,4),TSR(M,5),TSR(M,6),.5*(DTNH+DTN),
2     EQSTC(M),MUM,YHL(J),YADDM,F)                                HST 0263
      L(5)=50                                                       HST 0264
      GO TO 70                                                       HST 0265
C      BRITTLE FRACTURE PATH                                       HST 0266
51     JS=J                                                           HST 0267
      CALL BFRACT(LSUB(12),H(J,3),SHL(J),PHL(J),NEM(J),NET(J),DH,DOLD,
1     TSR(M,1),TSR(M,2),TSR(M,3),TSR(M,4),TSR(M,5),TSR(M,6),
2     .5*(DTNH+DTN),EQSTC(M),MU(M),YHL(J),YADD(M),F,EXMAT(M,2),JS)
      L(5)=51                                                       HST 0268
      HST 0269
      HST 0270
      HST 0271
      HST 0272
      HST 0273

```

and replace HST 0760 by

```
IF (NSR(M) .LT. 6 .OR. H(J,3) .GT. 2) GO TO 100
```

HST 0761

Note that the LSUB array has been extended to 12 elements. It provides control of initialization in the BFRACT routine.

In JSTRESS the line JST 0280 is replaced by

```
C      BRITTLE OR DUCTILE FRACTURE                                JST 0281
      IF (NSR(MJ) .EQ. 7) GO TO 70                                JST 0282
      CALL DFRACT(HJ3,S(JJ),P(JJ),NEMH,NETH,D(JJ),DULD,TSR(MJ,1), JST 0283
1     TSR(MJ,2),TSR(MJ,3),TSR(MJ,4),TSR(MJ,5),TSR(MJ,6),DTNH,EQSTC(MJ) JST 0284
2     ,MUM,YJ,YADDM,F)                                          JST 0285
```

d. Rezoning

The REZONE subroutine has not been revised to especially accommodate rezoning in the regions undergoing fracture. For ductile fracture, the usual mass-weighted averaging will control computation of void volume and number. For brittle fracture, however, the CN and CL arrays are not rezoned; if rezoning occurs in cells undergoing brittle fracture, the results will be nonsense. However, normal rezoning can be permitted in any cells that have not begun to fracture. In radiation problems, where rezoning is most important, that rezoning should occur early, generally before either front surface or rear surface spall. Hence, if rezoning is controlled carefully, its advantages can be gained even with fracturing calculations.

### 3. LISTING AND FLOW CHARTS FOR BFRACT

In the following pages the BFRACT subroutine is given with a flow chart, sample input decks for SRI PUFF calculations for brittle fracture, and some sample printout.

The additional input data required for fracturing are included as the first six variables of the  $TSR(M, )$  array. These six are used as T1, T2, ... T6 in the subroutine and are given in the nomenclature list. Their functions are described in the derivation of equations in section 1. With these input decks it should be noted that the cell zoning information is provided at the end, rather than with each material. This reflects a recent change to separate material and layer numbering, a change that is not in SRI PUFF 3.

```

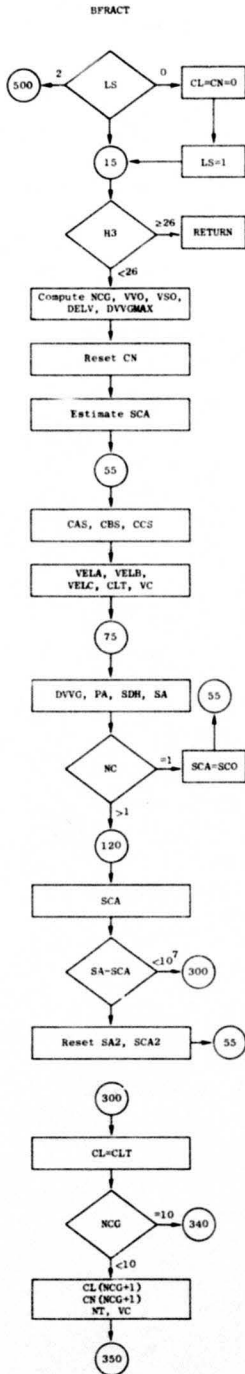
SUBROUTINE BFRACT(LS,H3,S,P,NM,NT,DH,DOLD,T1,T2,T3,T4,T5,T6,DT,
1 EQSTCM,MUM,Y,YU,F,FACT,JS)
C
C NEM -- RELATIVE VOLUME OF CRACKS
C NET -- NUMBER OF CRACKS/UNIT VOLUME
C T1 -- CRACK GROWTH VELOCITY, CM/SEC
C T2 -- FRACTURE TOUGHNESS, KIC, DYNE*SQRT(CM)/CM2
C T3 -- NUCLEATION CRACK RADIUS
C T4 -- NUCLEATION RATE COEFFICIENT
C T5 -- THRESHOLD STRESS FOR NUCLEATION
C T6 -- DENOMINATOR OF EXPONENTIAL STRESS FUNCTION
C CL AND CLT -- RADIUS OF CRACK, CM
C CN -- CRACK DENSITY, NUMBER/CM3
C
DIMENSION CL(100,10),CLT(10),CN(100,10),CNT(10)
REAL NM,NT,MUM
INTEGER H3
DATA A,F,SMF/2.0,1.88/
IF (LS .GT. 0) GO TO 15
DO 10 IZ=1,1000
10 CL(IZ)=CN(IZ)=0.
LS=1
15 IF (LS .EQ. 2) GO TO 500
IF (H3 .GE. 20) RETURN
NC=0 $ YT=Y $ NCG2=H3-3 $ NCG=(NCG2+1)/2 $ SCU=S
VVO=NM/DOLD $ VSO=1./DOLD-VVO $ DELV=1./DH-1./DOLD
DVVGMAX=(1.-ALF*NM)/(2.*ALF*DH)
C RESET NO. OF CRACKS/CM3
IF (NCG .LE. 0) GO TO 21
DO 20 N=1,NCG
20 CN(JS,N)=CN(JS,N)*DH/DOLD
21 CONTINUE
C ESTIMATE SCA BASED ON STRAIN AND CRACK EXPANSION
SCA=P-EQSTCM*DELV/VSO+AMAX1(S-P-AMAX1(MUM*(1.-SMF*NM),0.)*DELV
1 *DH,-Y*F*(1.-NM))
IF (DELV .LE. 0.) GO TO 30
SCG=SCU=SCA
IF (VVO .EQ. 0.) GO TO 25
IF (SCU .GT. 0.) GO TO 25
SCG=SCU*(1.+DELV/VVO)
25 SCA=AMAX1(SCA,SCG)
30 CONTINUE
C *** BEGIN ITERATION LOOP - COMPUTE NUCLEATION AND GROWTH OF CRACKS
55 VC=DC=DVVG=0.
NC=NC+1
IF (SCA .LT. T5) VC=-SCA*FACT*T3**3*T4*EXP(((SCA+SCU)/2.-T5)/T6)*DT
C COMPUTE CRITICAL CRACK SIZES FOR STRESSES DURING DT
IF (H3 .LE. 3 .OR. SCA .GE. 0.) GO TO 75
CAS=CBS=CCS=1.
IF (SCU .LT. 0.) CAS=0.7854*(T2/SCU)**2
IF (SCU+SCA .LT. 0.) CBS=0.7854*(T2/(0.5*(SCU+SCA)))**2
IF (SCA .LT. 0.) CCS=0.7854*(T2/SCA)**2
DO 73 N=1,NCG
VELA=VELB=VELC=0.
IF (CL(JS,N) .GT. CAS) VELA=T1*(1.-CAS/CL(JS,N))
IF (CL(JS,N) .GT. CBS) VELB=T1*(1.-CBS/CL(JS,N))
IF (CL(JS,N) .GT. CCS) VELC=T1*(1.-CCS/CL(JS,N))
CLT(N)=CL(JS,N)+(VELA+4.*VELB+VELC)*DT/6.
73 VC=VC-SCA*FACT*CN(JS,N)*CLT(N)**3
75 CONTINUE
VC=VC/DH
DVVG=AMINI(VC-VVO,DVVGMAX)
C COMPUTE STRESS CORRESPONDING TO DVVG AND SCA
80 RVV=NM+DVVG*DH
PA=(P/(1.-ALF*NM)-2.*EQSTCM*(DELV-DVVG)/(2.*VSO+DELV-DVVG))
1 *(1.-ALF*RVV)
SDH=S-P-AMAX1(MUM*(1.-SMF*RVV),0.)*DELV*DH
IF (ABS(SDH) .LT. Y*F*(1.-RVV)) GO TO 100
BFR 0010
BFR 0020
BFR 0030
BFR 0040
BFR 0050
BFR 0060
BFR 0070
BFR 0080
BFR 0090
BFR 0100
BFR 0110
BFR 0120
BFR 0130
BFR 0140
BFR 0150
BFR 0160
BFR 0170
BFR 0180
BFR 0190
BFR 0200
BFR 0210
BFR 0220
BFR 0230
BFR 0240
BFR 0250
BFR 0260
BFR 0270
BFR 0280
BFR 0290
BFR 0300
BFR 0310
BFR 0320
BFR 0330
BFR 0340
BFR 0350
BFR 0360
BFR 0370
BFR 0380
BFR 0390
BFR 0400
BFR 0410
BFR 0420
BFR 0430
BFR 0440
BFR 0450
BFR 0460
BFR 0470
BFR 0480
BFR 0490
BFR 0500
BFR 0510
BFR 0520
BFR 0530
BFR 0540
BFR 0550
BFR 0560
BFR 0570
BFR 0580
BFR 0590
BFR 0600
BFR 0610
BFR 0620
BFR 0630
BFR 0640
BFR 0650
BFR 0660
BFR 0670
BFR 0680
BFR 0690

```

SUBROUTINE BFRACT

	YT=AMINI(ABS(SDH),Y+YD*ABS(JH-DOLD))	BFR 0700
	SDH=SIGN(YT*F*(1.-RVV),SDH)	BFR 0710
100	SA=PA+SDH	BFR 0720
	IF (NC.EQ.1 .AND. VC.EQ.0. .AND. SCU.GE.0.) GO TO 300	BFR 0730
	IF (NC .GT. 1) GO TO 120	BFR 0740
C	PREPARE FOR 2ND ITERATION	BFR 0750
	SCA2=SCA \$ SA2=SA \$ SCA=SCU \$ GO TO 55	BFR 0760
120	CONTINUE	BFR 0770
	SCB=SCA	BFR 0780
C	INTERPOLATION FOR NEW ESTIMATE OF STRESS	BFR 0790
	SCA=(SCA2*SA-SA2*SCA)/(SA-SA2+SCA2-SCA)	BFR 0800
C	TEST FOR COMPLETION OF ITERATIONS	BFR 0810
	IF (NC .GE. 10) GO TO 300	BFR 0820
	IF (ABS(SCB-SA) .LT. 1.E7) GO TO 300	BFR 0830
	IF (ABS(SA-SCA) .GT. ABS(SA2-SCA)) GO TO 55	BFR 0840
	SA2=SA \$ SCA2=SCB \$ GO TO 55	BFR 0850
C		BFR 0860
C	ENDING ROUTINE	BFR 0870
300	NT=0.	BFR 0880
	IF (NCG .LE. 0) GO TO 325	BFR 0890
	DO 320 N=1,NCG	BFR 0900
	CL(JS,N)=CLT(N)	BFR 0910
	NT=NT+CN(JS,N)	BFR 0920
320	CONTINUE	BFR 0930
325	CONTINUE	BFR 0940
	IF (SCA .GT. T5) GO TO 350	BFR 0950
	IF (MOD(NCG2,2) .EQ. 1 .OR. NCG2 .EQ. 20) GO TO 340	BFR 0960
	H3=H3+1	BFR 0970
	CL(JS,NCG+1)=T3	BFR 0980
	CN(JS,NCG+1)=T4*EXP(((SCA+SCU)/2.-T5)/T6)*DT	BFR 0990
	NT=NT+CN(JS,NCG+1)	BFR 1000
	VC=VC-SCA*FACT*T3**3*CN(JS,NCG+1)	BFR 1010
	GO TO 350	BFR 1020
340	CNU=T4*EXP(((SCA+SCU)/2.-T5)/T6)*DT	BFR 1030
	CL(JS,NCG)=((CN(JS,NCG)*CL(JS,NCG)**3+CNU*T3**3)/(CN(JS,NCG)+CNU))	BFR 1040
	1 **((1./3.))	BFR 1050
	CN(JS,NCG)=CN(JS,NCG)+CNU	BFR 1060
	IF (NCG2 .LT. 20) H3=H3+1	BFR 1070
	NT=NT+CNU	BFR 1080
350	NM=VC	BFR 1090
	IF (NM .GT. 0.6/ALF) GO TO 400	BFR 1100
	P=PA	BFR 1110
	S=SA	BFR 1120
	Y=YT	BFR 1130
	RETURN	BFR 1140
C		BFR 1150
C	END WITH SEPARATION	BFR 1160
400	S=P=0.	BFR 1170
	Y=YT \$ H3=26	BFR 1180
	RETURN	BFR 1190
C		BFR 1200
C	FINAL PRINTOUT	BFR 1210
C		BFR 1220
500	IZERO=1	BFR 1230
	DO 520 I=1,100	BFR 1240
	IF (CL(I,1)+CN(I,1) .EQ. 0.) GO TO 520	BFR 1250
	IF (IZERO .EQ. 1) WRITE (6,1500)	BFR 1260
	IZERO=2	BFR 1270
	CNT(1)=CN(I,1)	BFR 1280
	DO 510 IN=2,10	BFR 1290
510	CNT(IN)=CNT(IN-1)+CN(I,IN)	BFR 1300
	WRITE (6,1510) I,(CL(I,K),K=1,10),(CN(I,K),K=1,	BFR 1310
	1 10)	BFR 1320
520	CONTINUE	BFR 1330
	RETURN	BFR 1340
1500	FORMAT(IHO,* LISTING OF CRACK LENGTH AND NUMBER FOR EVERY *,	BFR 1350
	1 *FRACTURING CELL*/)	BFR 1360
1510	FORMAT (* CELL NUMBER*15/ * CL=*10E11.3/* CN=*10E11.3/* CUM=	BFR 1370
	1*10E11.3/)	BFR 1380
	END	BFR 1390

SUBROUTINE BFRACT (Concluded)



This routine contains the equation-of-state relations for material undergoing brittle fracture. It computes stress and also number and size of cracks at each call.

For LS = 0, initialize the CL and CN arrays which will contain radii and numbers of cracks. For LS = 2 go to printout section.

If H3=26, separation has occurred and stresses are no longer computed.

Compute several quantities which are used throughout later calculations.

Recompute CN to pertain to the new specific volume of material.

Estimate stress for the first cycle based on either strain only or void expansion only.

Begin iteration loop for stress.

Based on the estimated stress, compute the critical crack radii.

For each crack group, compute the velocities of growth, new radius, and total volume.

Compute the change in crack volume, and the stress quantities.

Following the first iteration cycle (NC=1), set the stress estimate to SCO, the previous stress, and return for another iteration.

Reestimate SCA from results of 2 previous iterations.

Compare estimated stress with stress resulting from equation of state to determine convergence.

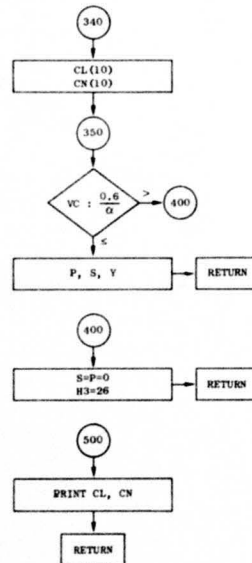
For next iteration and interpolation choose best results of previous iterations.

Ending routine.

Reset crack radii to most recent computed values.

For nucleation of new groups test NCG. If there are 10 groups go to 340.

Add parameters for a newly nucleated crack group.



Average the radius of the new group with that in tenth group to find a composite radius.

Test crack volume with the separation criterion.

Reset stress quantities and return.

For separation, zero the stress quantities and return.

Printing is done for all cells in which fracturing has been begun.

FLOW CHART FOR SUBROUTINE BFRACT

```

IDENT = 110J SHOT 886 IN ARMCO IRON - GROWTH GOVERNED BY FRACTURE TOUGHNESS
NTEST = 0 NJEDIT = 18 NREZON = 1 -0
JEDITS = 27 28 29 30 31 32 33 34 35 36 1A 20 22
          23 24 25 26
NEDTM = 10000 NEDIT = 10 NPERN = 1 -0
STOPS = 0 JCYCS = 102 CKS = 3.000E+00 TS = 1.000E+05
NMTRLS = 2 MATFL = 1 UZERO = 9.150E+03 NSCRB = 110000

ARMCO IRON RHOS = 7.850E+00 -0 NYAM = 11 -0
EQSTC = 1.589E+12 EQSTD = 5.170E+12 EQSTF = 7.360E+10 EQSTG = 1.690E+00
EQSTM = 2.500E-01 EQSTS = 5.170E+13 -0.
TENS(1) = -1.000E+11 TENS(2) = 0. TENS(3) = -1.000E+00
YO = 5.500E+09 MU = 8.190E+11 YADD = 0. -0.

ARMCO IRON RHOS = 7.850E+00 NSR = 7 NYAM = 1 -0
EQSTC = 1.589E+12 EQSTD = 5.170E+12 EQSTF = 7.360E+10 EQSTG = 1.690E+00
EQSTM = 2.500E-01 EQSTS = 5.170E+13 -0.
TSR(1) = 3.000E+04 TSR(2) = 3.400E+07 TSR(3) = 1.000E-04 TSR(4) = 1.000E+13
TSR(5) = -3.000E+09 TSR(6) = -9.500E+09 -0. -0.
YO = 5.500E+09 MU = 8.190E+11 YADD = 0. -0.

NLAYER = 2 JMAT = 1 2 -0 -0 -0 -0 -0 -0 -0 -0
NZONES = 1 10 CELLS IN 2.360E-01 CM -0. -0.
NZONES = 1 25 CELLS IN 6.350E-01 CM -0. -0.

```

```

IDENT = 111 F SHOT A678-1-S25 IN ARMCO IRON
NTEST = 0 NJEDIT = 18 NREZON = 1 -0
JEDITS = 27 28 29 30 31 32 33 34 38 39 1A 20 22
          23 24 25 26
NEDTM = 10000 NEDIT = 10 NPERN = 1 -0
STOPS = 0 JCYCS = 130 CKS = 3.000E+00 TS = 1.000E+05
NMTRLS = 3 MATFL = 1 UZERO = 1.960E+04 NSCRB = 110000

ARMCO IRON RHOS = 7.850E+00 -0 NYAM = 11 -0
EQSTC = 1.589E+12 EQSTD = 5.170E+12 EQSTF = 7.360E+10 EQSTG = 1.690E+00
EQSTM = 2.500E-01 EQSTS = 5.170E+13 -0.
TENS = -1.000E+11 TENS = 0. TENS = 0.
YO = 5.500E+09 MU = 8.190E+11 YADD = 0. -0.

ARMCO IRON RHOS = 7.850E+00 NSR = 7 NYAM = 1 -0
EQSTC = 1.589E+12 EQSTD = 5.170E+12 EQSTF = 7.360E+10 EQSTG = 1.690E+00
EQSTM = 2.500E-01 EQSTS = 5.170E+13 -0.
TSR(1) = 3.000E+04 TSR(2) = 3.400E+07 TSR(3) = 1.000E-04 TSR(4) = 1.000E+13
TSR(5) = -3.000E+09 TSR(6) = -9.500E+09 -0. -0.
YO = 5.500E+09 MU = 8.190E+11 YADD = 0. -0.

PMMA-RKB (BARKER) RHOS = 1.184E+00 -0 1 -0
EQSTC = 7.000E+10 EQSTD = 4.050E+11 EQSTF = 1.000E+10 EQSTG = 1.000E+00
EQSTM = 2.500E-01 EQSTS = 3.640E+11 -0.
YO = 1.000E+06 MU = 1.950E+10 YADD = 2.850E+09 -0.

NLAYER = 3 JMAT = 1 2 3 -0 -0 -0 -0 -0 -0 -0
NZONES = 1 10 CELLS IN 1.138E-01 CM -0. -0.
NZONES = 1 25 CELLS IN 3.156E-01 CM -0. -0.
NZONES = 1 22 CELLS IN 4.800E-01 CM: DX = 1.250E-02 RATIO = 1.050E+00

```

INPUT DECKS FOR CALCULATION OF BRITTLE FRACTURE IN ARMCO IRON

DATE = 07/09/71 IDENT = 111 E SHOT 867A-1-S25 IN ARMCO IRON

TIME EDIT NO. 13 AT N = 130. TIME = 1.52287E-06 SECS, JSTAR = 60. CALC TIME IS 20.128 SECS

CELL	J	X	U	RHL	DYN/CM2	PHL	SML	EHL	DHL	CHL	J	COND	MOM	P1	P2	
		CM	CM/SEC	DYN/CM2	DYN/CM2	DYN/CM2	DYN/CM2	ERGS	GM/CM3	CM/SEC	CELL	J	TAPS			
005236	1		575	-8.629E+05	1.707E+05	-8.629E+05	1.263E+05	7.8500	5.8440E+05	1	S	B	ARMCO IRO 0.	3.667E+09	-1.034E+06	
.016616	2		575	-2.640E+06	3.631E+09	-2.640E+06	7.492E+06	7.8673	5.8672E+05	2	S	B	ARMCO IRO 5.136E+01	3.667E+09	-3.633E+09	
.027971	3		577	-4.540E+06	3.636E+09	-4.540E+06	1.342E+07	7.8670	5.8669E+05	3	S	B	ARMCO IRO 1.028E+02	3.667E+09	-3.664E+09	
.039326	4		580	-5.082E+06	3.632E+09	-5.082E+06	1.681E+07	7.8648	5.8667E+05	4	S	N	ARMCO IRO 1.545E+02	3.667E+09	-3.638E+09	
.050682	5		584	-1.684E+06	3.627E+09	-1.684E+06	1.793E+07	7.8647	5.8666E+05	5	S	N	ARMCO IRO 2.064E+02	3.667E+09	-3.629E+09	
.062038	6		588	-5.023E+06	3.632E+09	-5.023E+06	1.832E+07	7.8647	5.8666E+05	6	S	N	ARMCO IRO 2.589E+02	3.667E+09	-3.627E+09	
.073394	7		592	9.750E+06	3.634E+09	9.750E+06	1.891E+07	7.8666	5.8665E+05	7	S	N	ARMCO IRO 3.114E+02	3.667E+09	-3.627E+09	
.084750	8		596	8.849E+06	3.634E+09	8.849E+06	1.946E+07	7.8666	5.8665E+05	8	S	N	ARMCO IRO 3.644E+02	3.667E+09	-3.625E+09	
.096106	9		599	5.008E+06	3.645E+09	5.008E+06	2.001E+07	7.8666	5.8665E+05	9	S	N	ARMCO IRO 4.178E+02	3.667E+09	-3.640E+09	
.107462	10		600	1.267E+06	3.653E+09	1.267E+06	2.099E+07	7.8666	5.8665E+05	10	S	N	ARMCO IRO 4.713E+02	3.667E+09	-3.652E+09	
.118818	11		601	0.	0.	0.	0.	7.8500	5.8440E+05	11	S	L	B	ARMCO IRO 5.250E+02	0.	
	J	X	U	RHL	DYN/CM2	PHL	SML	EHL	DHL	CHL	J	COND	MOM	P1	P2	
.119640	12		2127	-4.471E+07	3.080E+09	-4.471E+07	2.213E+07	7.8637	5.8626E+05	12	S	B	ARMCO IRO 5.250E+02	-0.	-0.	
.132242	13		2131	-1.439E+08	2.633E+09	-1.439E+08	2.102E+07	7.8543	5.8461E+05	13	S	N	ARMCO IRO 7.359E+02	1.162E+05	7.086E+05	
.144859	14		2169	-2.317E+08	2.649E+09	-2.317E+08	2.058E+07	7.8452	5.8461E+05	14	S	N	ARMCO IRO 9.490E+02	2.753E+05	1.427E+06	
.157492	15		2271	-3.035E+08	2.663E+09	-3.035E+08	2.020E+07	7.8394	5.8449E+05	15	S	N	ARMCO IRO 1.1169E+03	3.956E+05	1.712E+06	
.170135	16		2409	-3.010E+08	3.192E+09	-3.010E+08	2.000E+07	7.8334	5.8446E+05	16	S	N	ARMCO IRO 1.401E+03	4.360E+05	2.098E+06	
.182788	17		2554	-2.392E+08	3.427E+09	-2.392E+08	2.002E+07	7.8282	5.8444E+05	17	S	N	ARMCO IRO 1.647E+03	3.582E+05	2.315E+06	
.195433	18		2813	-3.384E+08	3.327E+09	-3.384E+08	2.080E+07	7.8070	5.8469E+05	18	S	N	ARMCO IRO 1.913E+03	4.480E+05	2.864E+06	
.208148	19		3084	-3.245E+08	3.341E+09	-3.245E+08	2.195E+07	7.7725	5.8468E+05	19	S	N	ARMCO IRO 2.205E+03	4.616E+05	2.899E+06	
.220900	20		3354	-2.377E+08	3.428E+09	-2.377E+08	2.280E+07	7.7478	5.8444E+05	20	S	N	ARMCO IRO 2.524E+03	3.373E+05	3.057E+06	
.233692	21		3594	-2.012E+08	3.465E+09	-2.012E+08	2.650E+07	7.6660	5.8437E+05	21	S	N	ARMCO IRO 2.868E+03	2.907E+05	3.383E+06	
.246620	22		3820	-2.481E+08	3.471E+09	-2.481E+08	3.663E+07	7.4593	5.8469E+05	22	S	N	ARMCO IRO 3.235E+03	1.431E+04	3.999E+06	
.259912	23		4723	-2.905E+08	3.371E+09	-2.905E+08	4.227E+07	7.4258	5.8448E+05	23	S	N	ARMCO IRO 3.658E+03	1.830E+04	4.476E+06	
.273265	24		5843	-2.981E+08	3.365E+09	-2.981E+08	4.294E+07	7.5106	5.8451E+05	24	S	N	ARMCO IRO 4.184E+03	1.377E+04	5.269E+06	
.286465	25		6773	-3.069E+08	3.355E+09	-3.069E+08	4.350E+07	7.4054	5.8448E+05	25	S	N	ARMCO IRO 4.611E+03	7.464E+05	6.628E+06	
.299499	26		7243	-2.852E+08	3.380E+09	-2.852E+08	4.211E+07	7.5577	5.8436E+05	26	S	N	ARMCO IRO 5.508E+03	4.921E+05	7.810E+06	
.312441	27		7552	-2.445E+08	3.421E+09	-2.445E+08	4.245E+07	7.6791	5.8430E+05	27	S	N	ARMCO IRO 6.239E+03	3.896E+05	8.465E+06	
.325348	28		7789	-1.273E+08	3.453E+09	-1.273E+08	3.911E+07	7.7173	5.8421E+05	28	S	N	ARMCO IRO 6.999E+03	1.619E+05	7.480E+06	
.338149	29		7824	4.931E+08	3.792E+09	4.931E+08	4.066E+07	7.7218	5.8428E+05	29	S	N	ARMCO IRO 7.779E+03	0.	5.830E+06	
.351023	30		7866	8.417E+08	4.118E+09	8.240E+08	4.893E+07	7.6948	5.8418E+05	30	S	N	ARMCO IRO 8.549E+03	0.	4.792E+06	
.363954	31		7750	1.263E+09	4.350E+09	1.237E+09	1.801E+07	7.7804	5.8432E+05	31	S	N	ARMCO IRO 9.322E+03	0.	3.921E+06	
.376831	32		7733	1.521E+09	4.350E+09	1.521E+09	1.801E+07	7.8491	5.8432E+05	32	S	N	ARMCO IRO 1.009E+04	0.	3.043E+06	
.389568	33		7729	1.711E+09	4.257E+09	1.705E+09	1.517E+07	7.8491	5.8432E+05	33	S	N	ARMCO IRO 1.084E+04	0.	1.968E+06	
.402193	34		7703	2.035E+09	3.993E+09	2.035E+09	5.276E+06	7.8610	5.8439E+05	34	S	N	ARMCO IRO 1.165E+04	0.	1.099E+06	
.414799	35		7703	2.035E+09	3.993E+09	2.035E+09	5.276E+06	7.8610	5.8439E+05	35	S	N	ARMCO IRO 1.239E+04	-0.	-0.	
.427392	36		7674	2.331E+09	1.633E+09	2.331E+09	4.208E+05	7.8540	5.8454E+05	36	S	N	ARMCO IRO 1.315E+04	-0.	-0.	
.440003	37		7685	0.	0.	0.	0.	7.8500	5.8440E+05	37	S	L	B	ARMCO IRO 1.391E+04	-0.	-0.
.453003	38		7685	2.356E+09	2.499E+09	2.356E+09	4.637E+07	1.2196	3.1884E+05	38	S	R	B	PMMA-BKB ( 1.391E+04	5.502E+08	-1.422E+08
.466006	39		7831	2.409E+09	2.540E+09	2.409E+09	4.745E+07	1.2201	3.1933E+05	39	S	R	B	PMMA-BKB ( 1.401E+04	5.501E+08	-1.312E+08
.479008	40		7854	2.493E+09	2.607E+09	2.493E+09	4.933E+07	1.2209	3.2008E+05	40	S	R	B	PMMA-BKB ( 1.415E+04	5.498E+08	-1.134E+08
.492128	41		8201	2.539E+09	2.643E+09	2.539E+09	5.099E+07	1.2213	3.2094E+05	41	S	N	B	PMMA-BKB ( 1.428E+04	5.494E+08	-1.033E+08
.505247	42		8251	2.682E+09	2.756E+09	2.682E+09	5.399E+07	1.2227	3.2177E+05	42	S	N	B	PMMA-BKB ( 1.442E+04	5.489E+08	-7.349E+07
.518366	43		8667	2.707E+09	2.769E+09	2.707E+09	5.592E+07	1.2229	3.2202E+05	43	S	N	B	PMMA-BKB ( 1.457E+04	5.479E+08	-6.880E+07
.531485	44		8714	2.713E+09	2.778E+09	2.713E+09	5.598E+07	1.2230	3.2200E+05	44	S	N	B	PMMA-BKB ( 1.473E+04	5.466E+08	-6.447E+07
.544604	45		8764	2.949E+09	2.963E+09	2.949E+09	6.091E+07	1.2252	3.2260E+05	45	S	N	B	PMMA-BKB ( 1.491E+04	5.445E+08	-1.414E+07
.557723	46		9587	3.185E+09	3.145E+09	3.180E+09	6.596E+07	1.2273	3.2260E+05	46	S	N	B	PMMA-BKB ( 1.510E+04	5.421E+08	-3.503E+07
.570842	47		9692	3.128E+09	3.099E+09	3.125E+09	6.596E+07	1.2273	3.2255E+05	47	S	N	B	PMMA-BKB ( 1.531E+04	5.389E+08	2.865E+07
.583961	48		10023	3.613E+09	3.484E+09	3.613E+09	7.578E+07	1.2312	3.2296E+05	48	S	N	B	PMMA-BKB ( 1.553E+04	5.352E+08	1.288E+08

SAMPLE TIME EDIT FROM CALCULATION OF BRITTLE FRACTURE IN ARMCO IRON



LISTING OF CRACK LENGTH AND NUMBER FOR EVERY FRACTURING CELL

CELL NUMBER	24	9.825E-03	8.163E-03	6.772E-03	5.502E-03	4.298E-03	3.098E-03	1.773E-03	1.406E-04	0.
CL#	1.165E-02	6.453E-05	7.053E-05	2.028E-06	2.932E-05	9.458E-05	7.296E-05	4.224E-05	1.552E-05	0.
CN#	3.251E-05	7.704E-05	1.318E-06	2.028E-06	2.932E-05	9.458E-05	7.296E-05	4.224E-05	1.552E-05	0.
CUM#	3.251E-05	7.704E-05	1.318E-06	2.028E-06	2.932E-05	9.458E-05	7.296E-05	4.224E-05	1.552E-05	5.269E-06
CELL NUMBER	25	7.166E-03	5.879E-03	4.771E-03	3.768E-03	2.777E-03	1.702E-03	2.810E-04	0.	0.
CL#	6.707E-03	6.392E-05	9.484E-05	1.224E-06	1.362E-06	1.699E-06	6.073E-05	1.810E-05	0.	0.
CN#	3.671E-05	1.006E-06	1.955E-06	3.179E-06	4.541E-06	5.640E-06	6.247E-06	6.428E-06	6.428E-06	6.428E-06
CUM#	3.671E-05	1.006E-06	1.955E-06	3.179E-06	4.541E-06	5.640E-06	6.247E-06	6.428E-06	6.428E-06	6.428E-06
CELL NUMBER	26	5.628E-03	4.757E-03	3.881E-03	2.955E-03	1.999E-03	7.182E-04	0.	0.	0.
CL#	6.488E-03	9.851E-05	1.655E-06	1.947E-06	1.527E-06	8.280E-05	3.983E-05	0.	0.	0.
CN#	4.688E-05	1.454E-06	3.109E-06	5.054E-06	6.583E-06	7.411E-06	7.810E-06	7.810E-06	7.810E-06	7.810E-06
CUM#	4.688E-05	1.454E-06	3.109E-06	5.054E-06	6.583E-06	7.411E-06	7.810E-06	7.810E-06	7.810E-06	7.810E-06
CELL NUMBER	27	5.449E-03	4.591E-03	3.751E-03	2.877E-03	1.926E-03	6.271E-04	0.	0.	0.
CL#	6.279E-03	9.657E-05	1.436E-06	2.341E-06	1.708E-06	8.006E-05	3.794E-05	0.	0.	0.
CN#	4.304E-05	1.396E-06	3.236E-06	5.577E-06	7.285E-06	8.006E-05	3.794E-05	0.	0.	0.
CUM#	4.304E-05	1.396E-06	3.236E-06	5.577E-06	7.285E-06	8.006E-05	3.794E-05	0.	0.	8.465E-06
CELL NUMBER	28	5.347E-03	4.506E-03	3.660E-03	2.790E-03	1.813E-03	5.859E-04	0.	0.	0.
CL#	6.166E-03	8.105E-05	1.217E-06	1.950E-06	1.635E-06	8.320E-05	3.899E-05	0.	0.	0.
CN#	3.635E-05	8.982E-05	1.672E-06	2.722E-06	3.971E-06	5.053E-06	5.658E-06	5.830E-06	5.830E-06	5.830E-06
CUM#	3.635E-05	8.982E-05	1.672E-06	2.722E-06	3.971E-06	5.053E-06	5.658E-06	5.830E-06	5.830E-06	5.830E-06
CELL NUMBER	29	5.347E-03	4.506E-03	3.660E-03	2.790E-03	1.813E-03	5.859E-04	2.810E-04	1.406E-04	0.
CL#	6.166E-03	8.105E-05	1.217E-06	1.950E-06	1.635E-06	8.320E-05	3.899E-05	1.719E-05	3.341E-05	0.
CN#	3.635E-05	8.982E-05	1.672E-06	2.722E-06	3.971E-06	5.053E-06	5.658E-06	4.458E-06	4.792E-06	0.
CUM#	3.635E-05	8.982E-05	1.672E-06	2.722E-06	3.971E-06	5.053E-06	5.658E-06	4.458E-06	4.792E-06	4.792E-06
CELL NUMBER	30	5.347E-03	4.506E-03	3.660E-03	2.790E-03	1.813E-03	5.859E-04	2.810E-04	1.406E-04	0.
CL#	6.166E-03	8.105E-05	1.217E-06	1.950E-06	1.635E-06	8.320E-05	3.899E-05	1.719E-05	3.341E-05	0.
CN#	3.635E-05	8.982E-05	1.672E-06	2.722E-06	3.971E-06	5.053E-06	5.658E-06	4.458E-06	4.792E-06	0.
CUM#	3.635E-05	8.982E-05	1.672E-06	2.722E-06	3.971E-06	5.053E-06	5.658E-06	4.458E-06	4.792E-06	4.792E-06
CELL NUMBER	31	5.347E-03	4.506E-03	3.660E-03	2.790E-03	1.813E-03	5.859E-04	2.810E-04	1.406E-04	0.
CL#	6.166E-03	8.105E-05	1.217E-06	1.950E-06	1.635E-06	8.320E-05	3.899E-05	1.719E-05	3.341E-05	0.
CN#	3.748E-05	8.247E-05	1.265E-06	1.712E-06	2.203E-06	2.872E-06	3.215E-06	3.615E-06	3.921E-06	0.
CUM#	3.748E-05	8.247E-05	1.265E-06	1.712E-06	2.203E-06	2.872E-06	3.215E-06	3.615E-06	3.921E-06	3.921E-06
CELL NUMBER	32	5.347E-03	4.506E-03	3.660E-03	2.790E-03	1.813E-03	5.859E-04	2.810E-04	1.406E-04	0.
CL#	6.166E-03	8.105E-05	1.217E-06	1.950E-06	1.635E-06	8.320E-05	3.899E-05	1.719E-05	3.341E-05	0.
CN#	3.245E-05	7.077E-05	1.130E-06	1.574E-06	2.008E-06	2.798E-06	3.043E-06	3.043E-06	3.043E-06	0.
CUM#	3.245E-05	7.077E-05	1.130E-06	1.574E-06	2.008E-06	2.798E-06	3.043E-06	3.043E-06	3.043E-06	3.043E-06
CELL NUMBER	33	5.347E-03	4.506E-03	3.660E-03	2.790E-03	1.813E-03	5.859E-04	2.810E-04	1.406E-04	0.
CL#	6.166E-03	8.105E-05	1.217E-06	1.950E-06	1.635E-06	8.320E-05	3.899E-05	1.719E-05	3.341E-05	0.
CN#	3.128E-05	7.047E-05	1.124E-06	1.503E-06	1.827E-06	1.968E-06	1.968E-06	1.968E-06	1.968E-06	0.
CUM#	3.128E-05	7.047E-05	1.124E-06	1.503E-06	1.827E-06	1.968E-06	1.968E-06	1.968E-06	1.968E-06	1.968E-06
CELL NUMBER	34	5.347E-03	4.506E-03	3.660E-03	2.790E-03	1.813E-03	5.859E-04	2.810E-04	1.406E-04	0.
CL#	6.166E-03	8.105E-05	1.217E-06	1.950E-06	1.635E-06	8.320E-05	3.899E-05	1.719E-05	3.341E-05	0.
CN#	3.016E-05	6.364E-05	9.574E-05	1.099E-06	1.099E-06	1.099E-06	1.099E-06	1.099E-06	1.099E-06	0.
CUM#	3.016E-05	6.364E-05	9.574E-05	1.099E-06	1.099E-06	1.099E-06	1.099E-06	1.099E-06	1.099E-06	1.099E-06

LISTING OF RADII (CL) AND NUMBER 1 cm<sup>3</sup> (CN) FOR EACH CRACK GROUP FOR A CALCULATION OF BRITTLE FRACTURE IN ARMCO IRON

DATE = 07/09/71 IDENT = 111 E SHOT 867A-1-S25 IN ARNCO IRON  
 FIRST SCRIBE, INTERFACE AND JEDII STRESS HISTORIES

N	TIME	MUSFC	512	523	S34	S ( 27 )	S ( 28 )	S ( 29 )	S ( 30 )	S ( 31 )	S ( 32 )	JTS	DTNH	DELTIM
			KBAR	KBAR	KBAR	KBAR	KBAR	KBAR	KBAR	KBAR	KBAR		MANOSEC	SEC
51	.471	15.296	.564	.564	34.2878	28.3858	26.8728	14.5398	17.4128	10.9328	9.3538	10	12.976	.473
52	.484	13.015	.863	.863	35.9918	31.5468	24.5608	17.4128	20.8028	12.3948	9.9228	10	13.041	.062
53	.497	10.250	1.192	1.192	37.0668	34.0358	24.1538	20.8028	24.4508	17.4498	10.9268	10	13.121	.061
54	.510	7.325	1.484	1.484	37.6828	35.8038	31.3208	24.4508	28.0138	14.6648	12.4908	8	13.204	.064
55	.523	4.671	1.671	1.671	38.0108	36.9398	31.8408	28.0138	31.4208	10.8038	14.6648	8	13.271	.063
56	.536	2.700	1.717	1.717	38.1788	37.6048	35.6488	31.1618	24.3928	17.4238	9	13.303	.065	
57	.550	1.713	1.669	1.669	38.2668	37.9648	36.8218	33.6658	27.8578	20.6688	10	13.277	.063	
58	.563	1.447	1.624	1.624	38.3158	38.1528	37.5168	35.4458	30.8748	23.9358	10	13.295	.064	
59	.576	1.202	1.717	1.717	38.3408	38.2468	37.8938	36.6158	33.2248	27.0378	10	13.278	.064	
60	.590	1.157	2.075	2.075	38.3478	38.2938	38.0708	37.2528	34.8198	29.5768	8	13.309	.067	
61	.603	.874	2.658	2.658	38.3188	38.3018	38.1188	37.5068	35.6778	31.3428	8	13.325	.504	
62	.616	.418	3.342	3.342	38.2168	38.2478	38.0348	37.4458	35.8968	32.3078	3	13.329	.067	
63	.630	.262	3.869	3.869	37.9828	38.0878	37.7878	37.0048	35.4538	32.6238	10	13.329	.066	
64	.643	.166	4.382	4.382	37.5208	37.9528	37.3328	36.2338	35.4148	32.4498	2	13.321	.067	
65	.656	.132	5.076	5.076	36.6828	37.1368	36.5648	35.1978	32.4298	31.0668	9	13.329	.067	
66	.670	.150	5.859	5.859	35.2938	36.0878	35.4788	34.0028	32.7708	31.5268	4	13.330	.069	
67	.683	.110	6.336	6.336	33.2018	34.4398	34.0028	32.7708	31.5268	30.2098	4	13.330	.069	
68	.696	.059	6.723	6.723	30.3458	32.0838	32.1928	31.5388	30.5988	29.2698	10	13.331	.066	
69	.710	.018	6.992	6.992	26.8128	29.9518	30.0678	30.1858	29.4988	28.0068	2	13.330	.070	
70	.723	.022	6.938	6.938	22.8668	25.5304	27.5758	28.4578	28.4578	26.0718	2	13.331	.069	
71	.736	.029	6.543	6.543	18.9068	21.7838	24.6298	26.2508	26.2508	24.0998	2	13.332	.537	
72	.750	.018	6.051	6.051	16.8338	18.2348	21.1988	23.2708	23.2708	21.3268	2	13.331	.072	
73	.763	.003	5.777	5.777	15.0588	16.3768	17.8438	19.4908	19.4908	17.8018	2	13.332	.072	
74	.776	.002	5.819	5.819	13.6018	14.5248	15.6008	16.2268	16.2268	15.7238	3	13.333	.070	
75	.790	.003	5.997	5.997	12.4938	12.7318	13.2748	13.3318	13.3318	12.5998	2	13.333	.073	
76	.803	.003	6.021	6.021	11.6608	11.0308	10.8618	10.2898	10.2898	9.2338	2	13.334	.080	
77	.816	.015	5.925	5.925	10.9278	9.4578	4.3848	7.1848	7.1848	5.8528	2	13.332	.073	
78	.830	.016	5.856	5.856	10.0718	7.9948	5.9128	4.1028	4.1028	2.3868	2	13.331	.071	
79	.843	.000	5.832	5.832	8.8978	6.5428	3.5378	1.1578	1.1578	-2.068	2	13.332	.071	
80	.856	.003	5.764	5.764	7.2888	4.9498	1.3388	-1.5108	-1.5108	-2.7038	2	13.333	.074	
81	.870	.026	5.574	5.574	5.2028	3.0738	-0.6618	-3.7688	-3.7688	-4.8128	2	13.333	.566	
82	.883	.025	5.313	5.313	2.6448	0.8478	-2.4978	-5.5988	-5.5988	-6.5058	2	13.333	.099	
83	.896	.010	5.067	5.067	-0.3598	-1.7038	-4.2518	-6.8698	-6.8698	-7.6778	2	13.333	.094	
84	.910	.021	4.836	4.836	-3.7538	-4.4908	-6.0248	-7.7698	-7.7698	-8.4118	2	13.333	.101	
85	.923	.007	4.536	4.536	-7.4828	-7.4558	-7.8428	-8.3778	-8.3778	-8.3078	2	13.332	.123	
86	.936	.030	4.227	4.227	-11.3998	-10.5078	-9.6878	-8.8258	-8.8258	-7.4578	2	13.332	.129	
87	.950	.019	3.955	3.955	-15.2628	-13.5638	-11.5058	-9.1848	-9.1848	-7.6748	2	13.332	.140	
88	.963	.005	3.705	3.705	-18.7748	-16.5058	-13.2208	-9.6318	-9.6318	-8.0378	2	13.333	.147	
89	.976	.005	3.440	3.440	-23.6128	-19.1368	-14.7728	-10.3748	-10.3748	-8.4488	2	13.333	.158	
90	.990	.015	3.166	3.166	-28.4701	-21.1641	-16.1321	-11.4011	-11.4011	-8.9531	2	13.332	.166	
91	1.003	.027	2.946	2.946	-34.0741	-22.2471	-17.2411	-12.5061	-12.5061	-9.4001	2	13.332	.181	
92	1.016	.037	2.916	2.916	-40.9281	-22.0901	-17.9131	-13.3531	-13.3531	-9.6131	2	13.332	.193	
93	1.030	.044	3.092	3.092	-48.9281	-20.5511	-17.8151	-13.6001	-13.6001	-9.4781	2	13.332	.200	
94	1.043	.054	3.280	3.280	-57.3174	-17.5964	-16.6084	-13.0374	-13.0374	-8.9594	2	13.332	.209	
95	1.056	.079	3.343	3.343	-67.2834	-13.6494	-14.1544	-11.6534	-11.6534	-8.0904	2	13.332	.214	
96	1.070	.129	3.304	3.304	-78.4020	-9.6980	-10.7499	-9.6419	-9.6419	-6.9579	2	13.332	.225	
97	1.083	.204	3.241	3.241	-90.1109	-6.1109	-6.3579	-6.9569	-6.9569	-5.6535	2	13.332	.214	
98	1.096	.290	3.177	3.177	-103.6690	-3.7360	-3.9519	-5.0539	-5.0539	-4.3149	2	13.332	.230	
99	1.110	.374	3.116	3.116	-122.0610	-1.9320	-2.1049	-3.1610	-3.1610	-3.1250	2	13.332	.236	
100	1.123	.452	3.027	3.027	-151.1070	-0.9220	-1.1329	-1.8440	-1.8440	-2.1120	2	13.332	.238	

PORTION OF SCRIBE HISTORICAL LISTING OF STRESSES

NOMENCLATURE FOR APPENDIX VIII

CAS,CBS,CCS	critical crack size at beginning, middle, and end of time increment, cm/sec
CL	array containing crack radii of each crack group
CLT	temporary array for crack radii
CN	array containing no./cm <sup>3</sup> for each crack group
CNT	cumulative no./cm <sup>3</sup> , summing from the large crack to the small
DH	current density, gm/cm <sup>3</sup>
DOLD	density at previous cycle, gm/cm <sup>3</sup>
DT	time increment, sec
DVVG	change in total crack volume, cm <sup>3</sup> /gm
DVVGMAX	maximum permitted change in crack volume
E	Young's modulus, dyn/cm <sup>2</sup>
EQSTCM	bulk modulus, dyn/cm <sup>2</sup>
F	thermal strength reduction factor
FACT	$\frac{4\pi}{27} \left( \frac{1}{K} + \frac{3}{\mu} \right) = \frac{4\pi}{3E}$ , cm <sup>2</sup> /dyn
H3	H(J,3), a fracturing indication in SRI PUFF H3 = 2 for no damage H3 = 26 for full separation H3-3 = NCG, the number of crack groups

K	bulk modulus, EQSTC, dyn/cm <sup>3</sup>
K <sub>IC</sub>	fracture toughness in the opening mode, dyn/cm <sup>3/2</sup>
MUM	shear modulus, dyn/cm <sup>2</sup>
N	number of cracks, number/cm <sup>3</sup>
NCG	H3-3, the number of crack groups
NM	relative crack volume
NT	number of cracks/cm <sup>3</sup>
P	pressure, dyn/cm <sup>3</sup>
PA	pressure computed from equation of state, dyn/cm <sup>2</sup>
R	crack radius in plan, cm
R*	critical crack radius, cm
S	stress (negative for tension), dyn/cm <sup>2</sup>
SA	stress computed from equation of state, dyn/cm <sup>2</sup>
SCA	estimate of stress for an iteration, dyn/cm <sup>2</sup>
SCG	stress estimate based on growth of crack volume, dyn/cm <sup>2</sup>
SCO	S, stress at previous cycle, dyn/cm <sup>2</sup>
SDH	deviator stress
T1	limiting crack growth velocity, cm/sec
T2	fracture toughness, K <sub>IC</sub> , dyn/cm <sup>3/2</sup>
T3	nucleation crack radius, cm
T4	nucleation rate coefficient, no./cm <sup>3</sup> /sec
T5	nucleation threshold stress, dyn/cm <sup>2</sup>

T6	nucleation parameter, $\text{dyn/cm}^2$
VC	total crack volume, $\text{cm}^3/\text{gm}$
VELA, VELB, VELC	crack growth velocity at beginning, middle, and end of time increment, $\text{cm/sec}$
VSO	solid specific volume, $\text{cm}^3/\text{gm}$
VVO	specific volume of cracks, $\text{cm}^3/\text{gm}$
$V_c$	velocity of a crack, $\text{cm/sec}$
$V_t$	limiting crack velocity, $\text{cm/sec}$
Y	yield strength
YD	strain hardening modulus, defined so that the increase in yield is $YD \cdot  DH - D\theta LD $ , $\text{dyn-cm/gm}$
t	time
v	crack volume per unit volume of material, dimensionless
$v'$	volume of a crack, $\text{cm}^3$
$\gamma$	surface energy, $\text{erg/cm}^2$
$\mu$	shear modulus, MU, $\text{dyn/cm}^2$
$\nu$	Poisson's ratio
$\sigma$	stress in the direction of propagation, $\text{dyn/cm}^2$
$\sigma_{n0}$	threshold stress for nucleation, $\text{dyn/cm}^2$

## APPENDIX IX

### STATISTICAL ANALYSIS OF CRACKS

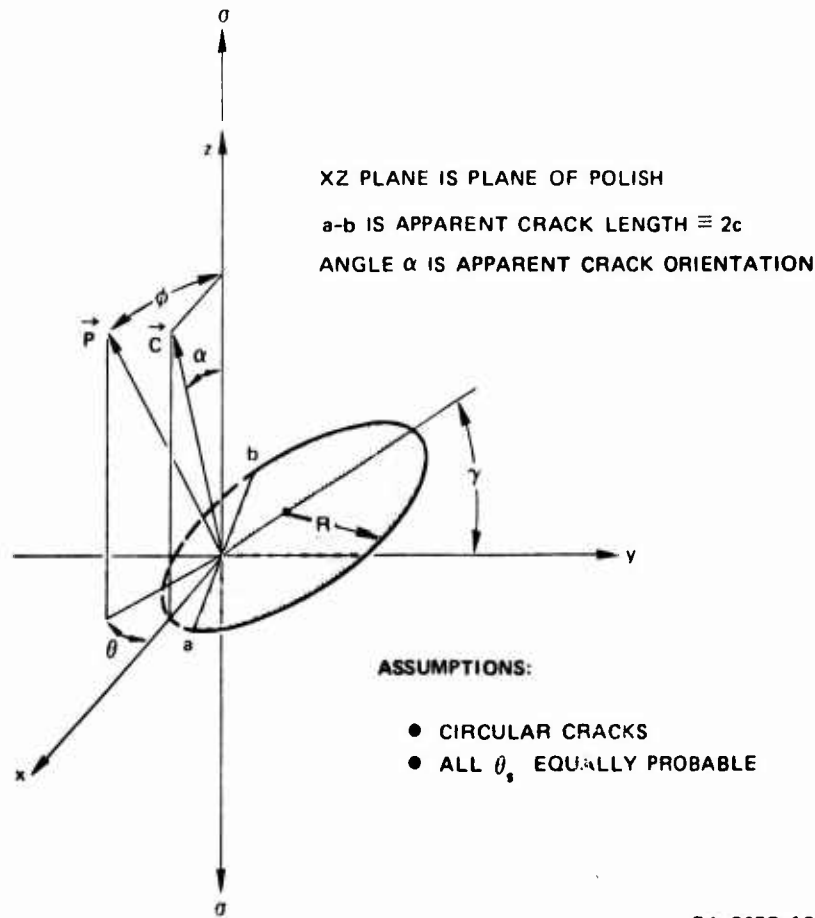
It is necessary for the present study to determine the volume density of cracks as a function of applied conditions. Our experimental knowledge of the crack distribution is derived from microphotographs of polished sections of the shocked specimens. A crack is characterized by the trace length,  $2c$ , of its intersection with the polished surface (the surface was always parallel to the shock propagation direction "z"), the trace width,  $w$ , and the angle of inclination,  $\alpha$ , to the intersection of the shock front with the surface. Thus an areal crack density function  $n(c, w, \alpha, z)$  of cracks of  $c, w, \alpha$ , and position  $z$  could be experimentally determined from the microphotograph. The implicit assumption here of one-dimensional symmetry is justifiable if only the central portions of the specimen are used to determine the density function (in our case it was roughly the central third), if only the first few reverberations of the shock wave have a significant effect upon the crack distribution, and if these reverberations are planar. To satisfy these requirements, only the central third of the specimen was used for analysis.

The problem discussed here is that of determining the volume density of cracks from the observed areal density  $n(c, w, \alpha)$ .<sup>\*</sup> If we assume that an individual crack is penny-shaped, it can be described by its size, shape, and orientation. A convenient way to describe the orientation of

---

\* For the calculations in this appendix, the variables  $z$ ,  $x$ ,  $\sigma$  and  $t$  which are related to shock history and discussed in the test, are dropped because they do not enter into the transformation problem.

the crack plane is by the angle of inclination  $\omega$  of the crack normal to the tensile axis (or shock direction) and the angle of rotation  $\theta$  of the normal about the tensile axis. The angular relationships of  $\theta, \omega,$  and  $\alpha$  are shown in Figure 97 where the angle  $\gamma$  is also defined. In the special case of spherical voids only the radius  $c$  is important. The present statistical analysis for brittle cracks will contain the spherical void mode of fracture as a special case.



GA-8678-16

FIGURE 97 CIRCULAR CRACK INTERSECTING PLANE OF POLISH

In our work, observations have been made on only one polish plane in the specimens so that we have only the experimental variables  $c, w$ , and  $\alpha$ . Until we have more extensive data (such as from sections on planes of a number of orientations) it is desirable to make assumptions on crack shape and orientation to reduce to two the number of parameters needed to describe the volume distribution. A number of ways to do this are possible. For example, an elliptical crack shape could be assumed in which the aspect ratio is a function of the angle  $\phi$ . In addition the orientation distribution could be assumed to have a direct relationship to the metallurgical structure and a measured distribution of cleavage planes. Although, within our experimental limitations, these assumptions might be the most physically reasonable, they also lead to a relatively complex analysis. Therefore, as elsewhere in this study, we have used the simplest assumptions consistent with experimental observation and physical intuition. If these prove inadequate for the central problem of prediction of shock-induced damage, we can go back and refine the analysis further.

The assumptions of the analysis described below are: (1) cracks are circular and specified by crack radius  $R$ , (2) the crack distribution is axisymmetric with respect to  $\phi$ , and (3) the finite crack width  $w$  can be ignored in the statistical analysis. Assumption (1) is not as unrealistic as it might first appear because of the qualitative observations that most cracks have small inclination angles  $\alpha$ , and the stresses are high enough that the crack growth velocities are probably near the limiting value in most directions. Assumption (2) is plausible for polycrystalline materials without texture. Assumption (3) will be satisfied if the crack width is a function of the crack radius for given stress conditions, as is the case for ideal penny-shaped cracks (Ref.32). Thus the problem of this appendix is to compute the volume density of cracks  $\rho(R, \phi)$  of



radius  $R$  and inclination  $\varphi$  from a knowledge of the areal density  $n(c, \alpha)$  of cracks with intersection trace lengths,  $2c$ , and apparent inclination  $\alpha$ .

#### 1. DERIVATION OF THE TRANSFORMATION EQUATION

We first relate  $n(R, \varphi, \theta)$ , the number of cracks with specified  $R, \varphi$ , and  $\theta$ , which intersect the plane of polish, to the volume density  $\rho(R, \varphi)$ . Then the observed areal density  $n(c, \alpha)$ , which is a function of apparent length  $c$  and apparent inclination  $\alpha$ , is related to  $n(R, \varphi, \theta)$ . These relations lead to an equation between areal density  $n(c, \alpha)$  and volume density  $\rho(R, \varphi)$ . This equation provides the required transformation.

The surface density of cracks  $n(R, \varphi, \theta)$  is related to the volume density  $\rho(R, \varphi)$  in two steps. If the crack is to be cut by the plane of polish, that plane must fall within the length  $2R \cos \gamma$ , the length of the crack normal to the plane of polish as shown in Figure 97. The number of cracks with centers in that volume is  $2R\rho(R, \varphi, \theta) \cos \gamma$  per unit area, where  $\rho(R, \varphi, \theta)$  is the volume density, which is not necessarily axisymmetric (independent of  $\theta$ ). Therefore

$$n(R, \varphi, \theta) = 2R\rho(R, \varphi, \theta) \cos \gamma \quad (246)$$

If all angles  $\theta$  are taken as equally probable, then

$$\rho(R, \varphi, \theta) = \rho(R, \varphi)P(\theta) = \frac{1}{2\pi} \rho(R, \varphi) \quad (247)$$

where  $P(\theta)$  is the probability of finding a crack of angle  $\theta$ . Therefore

$$n(R, \varphi, \theta) = \frac{R}{\pi} \rho(R, \varphi) \cos \gamma \quad (248)$$

From Figure 97 the following relations can be derived:

$$\begin{aligned} \tan \alpha &= \cos \theta \tan \varphi \\ \tan \gamma &= \sin \theta \tan \varphi \end{aligned} \quad (249)$$

Since  $\varphi$  and  $\alpha$  are sufficient to specify the crack orientation as long as the orientation of the polish plane is fixed,  $n(r, \varphi, \theta)$  can be transformed to  $n(R, \varphi, \alpha)$  through the use of the following equations:

$$n(R, \varphi, \alpha) = n(R, \varphi, \theta) \left[ \left( \frac{\partial \theta}{\partial \alpha} \right)_{\varphi} \right] \quad (250)$$

$$\cos \gamma = \left[ 1 + \frac{\cos^2 \alpha - \cos^2 \varphi}{\cos^2 \alpha \cos^2 \varphi} \right]^{-1/2} \quad (251)$$

The expression for  $\cos \gamma$  can be derived from Eq. (249). Combining these results with Eq. (248) leads to

$$n(R, \varphi, \alpha) = \frac{R \rho(R, \varphi)}{\pi \left\{ 1 + \frac{\cos^2 \alpha - \cos^2 \varphi}{\cos^2 \alpha \cos^2 \varphi} \right\}^{1/2}} \left| \left( \frac{\partial \theta}{\partial \alpha} \right)_{\varphi} \right| \quad (252)$$

From the first of Eqs. (249) we can also compute the Jacobian of the transformation.

$$\left(\frac{\partial \theta}{\partial \alpha}\right)_{\varphi} = \frac{-\cos \varphi}{\cos \alpha \left\{ \cos^2 \alpha - \cos^2 \varphi \right\}^{\frac{1}{2}}} \quad (253)$$

and  $n(c, \alpha)$  can be related to  $n(R, \varphi, \alpha)$

$$n(c, \alpha) = \int_c^{\infty} \int_{\alpha}^{\pi/2} P(c | R, \varphi, \alpha) n(R, \varphi, \alpha) dR d\varphi \quad (254)$$

where  $P(c | R, \varphi, \alpha)$  is the probability that if a crack of  $R, \varphi$ , and  $\alpha$  is intersected, the trace will be of length  $2c$ . Now the probability is derived.

Suppose  $r$  is the radial distance of the crack trace from the crack center. Since the probability of intersection at  $r \pm \frac{\delta r}{2}$  is proportional only to  $\delta r$ , it is easy to derive

$$P(c | R, \varphi, \alpha) = \frac{c}{R \sqrt{R^2 - c^2}} \quad (255)$$

Thus from Eqs. (252), (253), (254), and (255) we have the desired transformation equation:

$$n(c, \alpha) = \frac{c}{\pi \cos \alpha} \int_c^{\infty} \int_{\alpha}^{\pi/2} \frac{\cos \varphi \rho(R, \varphi) dR d\varphi}{\left\{ \left( 1 + \frac{\cos^2 \alpha - \cos^2 \varphi}{\cos^2 \alpha \cos^2 \varphi} \right) (\cos^2 \alpha - \cos^2 \varphi) (R^2 - c^2) \right\}^{\frac{1}{2}}} \quad (256)$$

Equation (256) is an integral equation for  $\rho(R, \varphi)$ , and a method for its solution is described in the next section.

An equation similar to Eq. (256) was derived by Kaechele and Tetelman (Ref. 30) who considered the same problem but adopted the simplifying assumption that the probability that a crack will intersect a polished surface parallel to the tensile axis is independent of the crack orientation. This assumption is equivalent to assuming that a tilted crack is elongated in such a way that its shape projected on the plane of the shock front remains a circle. In terms of this analysis, their result is then obtained by dropping the  $\cos \gamma$  term from Eq. (248). The consequences of their convenient, but unrealistic assumption have not yet been examined in detail, but can be expected to lead to appreciable error in materials where many cracks of large inclination  $\varphi$  are observed.

## 2. SOLUTION OF THE INTEGRAL EQUATION

The objective is to determine the volume distribution  $\rho(R, \varphi)$  from the surface distribution  $n(c, \alpha)$  by solution of the integral equation, Eq. (256). The procedure used is a generalization to two dimensions of the matrix inversion method reported by Scheil (Refs. 56, 57) and Saltykov (Ref. 58) for computing the volume density of spherical particles.

To simplify notation in Eq. (256), define for  $R \geq c$  and  $\varphi \geq \alpha$

$$G(\alpha, c, R, \varphi) \equiv \frac{\frac{c \cos \varphi}{\pi \cos \alpha}}{\left\{ \left( 1 + \frac{\cos^2 \alpha - \cos^2 \varphi}{\cos^2 \alpha \cos^2 \varphi} \right) (\cos^2 \alpha - \cos^2 \varphi) (R^2 - c^2) \right\}^{\frac{1}{2}}}$$

$$= \frac{c \sec^2 \alpha}{\pi \left\{ (1 + \tan^2 \varphi - \tan^2 \alpha) (\tan^2 \varphi - \tan^2 \alpha) (R^2 - c^2) \right\}^{\frac{1}{2}}} \quad (257)$$

Define  $G(R, \varphi, c, \alpha) \equiv 0$  for  $R < \alpha$ . Then the integral equation to be solved is

$$n(c, \alpha) = \int_c^\infty \int_\alpha^{\pi/2} G(R, \varphi, c, \alpha) \rho(R, \varphi) dR d\varphi \quad (258)$$

The solution is carried out by discretizing the functions  $n$  and  $\rho$  into matrices. These matrices are  $N_{ij}$  and  $\rho_{rs}$ , defined as follows

$$N_{ij} \equiv \int_{\alpha_i}^{\alpha_{i+1}} d\alpha \int_{c_j}^{c_{j+1}} dc n(c, \alpha) \quad (259)$$

$$\rho_{rs} \equiv \int_{\alpha_r}^{\alpha_{r+1}} d\varphi \int_{c_s}^{c_{s+1}} dR \rho(R, \varphi) \quad (260)$$

that is,  $\rho_{rs}$  is the number of cracks per unit volume with orientation  $\varphi$  between  $\alpha_r$  and  $\alpha_{r+1}$  and radius  $R$  between  $c_s$  and  $c_{s+1}$ . The limits are expressed in terms of  $\alpha_r$  and  $c_s$  to emphasize that the same intervals are chosen for  $\varphi$  and  $\alpha$ , and for  $c$  and  $R$ . These matrices  $N_{ij}$  and  $\rho_{rs}$  are related through a tensor equation analogous to Eq. (258).

$$N_{ij} = \sum_{rs} a_{ijrs} \rho_{rs} \quad (261)$$

The elements of the tensor  $a_{ijrs}$  are found as follows. Replace  $n(c, \alpha)$  in Eq. (259) by its value in Eq. (258) to obtain

$$N_{ij} = \int_{\alpha_i}^{\alpha_{i+1}} d\alpha \int_{c_j}^{c_{j+1}} dc \int_c^{\infty} dR \int_{\alpha}^{\pi/2} d\varphi G(R, \varphi, c, \alpha) \rho(R, \varphi) \quad (262)$$

Now change the order of integration, discard terms that go to zero, and obtain

$$\begin{aligned}
N_{ij} &= \int_{\alpha_i}^{\alpha_{i+1}} d\varphi \int_{c_j}^{c_{j+1}} dR \int_{\alpha_i}^{\alpha_{i+1}} d\alpha \int_{c_j}^{c_{j+1}} dc G(R, \varphi, c, \alpha) \rho(R, \varphi) \\
&+ \int_{\alpha_{i+1}}^{\pi/2} d\varphi \int_{c_j}^{c_{j+1}} dR \int_{\alpha_i}^{\alpha_{i+1}} d\alpha \int_{c_j}^{c_{j+1}} dc G(R, \varphi, c, \alpha) \rho(R, \varphi) \\
&+ \int_{\alpha_i}^{\alpha_{i+1}} d\varphi \int_{c_{j+1}}^{\infty} dR \int_{\alpha_i}^{\alpha_{i+1}} d\alpha \int_{c_j}^{c_{j+1}} dc G(R, \varphi, c, \alpha) \rho(R, \varphi) \\
&+ \int_{\alpha_{i+1}}^{\pi/2} d\varphi \int_{c_{j+1}}^{\infty} dR \int_{\alpha_i}^{\alpha_{i+1}} d\alpha \int_{c_j}^{c_{j+1}} dc G(R, \varphi, c, \alpha) \rho(R, \varphi) \tag{263}
\end{aligned}$$

The next step is to perform the two outer integrals over the same discrete intervals used to define  $\rho_{rs}$ . Then, by comparing Eqs. (260), (261), and (263), we find the elements of  $a_{ijrs}$  are ratios of this type

$$a_{ijrs} = \frac{\int_{\alpha_r}^{\alpha_{r+1}} d\varphi \int_{c_s}^{c_{s+1}} dR \int_{\alpha_i}^{\alpha_{i+1}} d\alpha \int_{c_j}^{c_{j+1}} dc G(R, \varphi, c, \alpha) \rho(R, \varphi)}{\int_{\alpha_r}^{\alpha_{r+1}} d\varphi \int_{c_s}^{c_{s+1}} dR \rho(R, \varphi)} \tag{264}$$

where  $r > i$  and  $s > j$ .

For terms in which  $i = r$ , the upper limit for the integral over  $\alpha$  must be replaced by  $\varphi$ . Similarly, for terms in which  $j = s$ , the upper limit in the integral over  $c$  must be replaced by  $R$ . Formally, the problem is solved by evaluating Eq. (263) for the matrix elements, computing the inverse matrix  $a_{ijrs}^{-1}$ , and writing the solution as

$$\rho_{ij} = \sum_{rs} a_{ijrs}^{-1} N_{rs} \quad (265)$$

### 3. EVALUATION OF THE MATRIX ELEMENTS

The  $a_{ijrs}$  can be easily evaluated if the intervals  $\delta\alpha$  and  $\delta c$  are chosen small enough that over each interval  $\rho(R, \varphi)$  can be considered to be constant. In this case  $\rho(R, \varphi)$  can be cancelled out of the terms in Eq. (264), and we are left with integrals such as

$$a_{ijrs} = \frac{1}{\delta\alpha_r \delta c_s} \int_{\alpha_r}^{\alpha_{r+1}} d\varphi \int_{c_s}^{c_{s+1}} dR \int_{\alpha_i}^{\alpha_{i+1}} d\alpha \int_{c_j}^{c_{j+1}} \frac{c \sec^2 \alpha dc}{\pi \left\{ (1 + \tan^2 \varphi - \tan^2 \alpha) (\tan^2 \varphi - \tan^2 \alpha) (R^2 - c^2) \right\}^{\frac{1}{2}}} \quad (266)$$

which are independent of the form of the distribution. This integral can be separated into two independent parts, one containing length variables and one with angle variables, as follows:

$$a_{ijrs} = \frac{F_{js} G_{ir}}{2\pi \delta\alpha_r \delta c_s} \quad (267)$$



where

$$F_{js} = \int_{c_s}^{c_{s+1}} dr \int_{c_j}^{c_{j+1}} \frac{2dc}{\sqrt{R^2 - c^2}} \quad (268)$$

and

$$G_{ir} = \int_{\alpha_r}^{\alpha_{r+1}} d\varphi \int_{\alpha_i}^{\alpha_{i+1}} \frac{\sec^2 \alpha d\alpha}{[(1 + \tan^2 \varphi - \tan^2 \alpha)(\tan^2 \varphi - \tan^2 \alpha)]^{1/2}} \quad (269)$$

Equations (268) and (269) are written for the cases  $s > j$  and  $r > i$ . For  $s = j$  and  $r = i$ , the upper limit of the inner integrals are  $R$  and  $\varphi$ , respectively.  $F$  and  $G$  are zero for  $s < j$  and  $r < i$ . The value of  $F$  can be obtained analytically. For  $s > j$

$$\begin{aligned} F_{js} &= c_{s+1} \sqrt{c_{s+1}^2 - c_j^2} - c_s \sqrt{c_s^2 - c_j^2} \\ &\quad - c_{s+1} \sqrt{c_{s+1}^2 - c_{j+1}^2} + c_s \sqrt{c_s^2 - c_{j+1}^2} \\ &\quad - c_j^2 \log \left| \frac{c_{s+1} + \sqrt{c_{s+1}^2 - c_j^2}}{c_s + \sqrt{c_s^2 - c_j^2}} \right| + c_{j+1}^2 \log \left| \frac{c_{s+1} + \sqrt{c_{s+1}^2 - c_{j+1}^2}}{c_s + \sqrt{c_s^2 - c_{j+1}^2}} \right| \end{aligned} \quad (270)$$

For  $s = j$

$$F_{jj} = c_{j+1} \sqrt{c_{j+1}^2 - c_j^2} - c_j^2 \log \left| \frac{c_{j+1} + \sqrt{c_{j+1}^2 - c_j^2}}{c_j} \right| \quad (271)$$

To integrate Eq. (269) it is convenient to replace  $\alpha$  by the variable

$$u = \sin^{-1} \left( \frac{\tan \alpha}{\tan \varphi} \right) \quad (272)$$

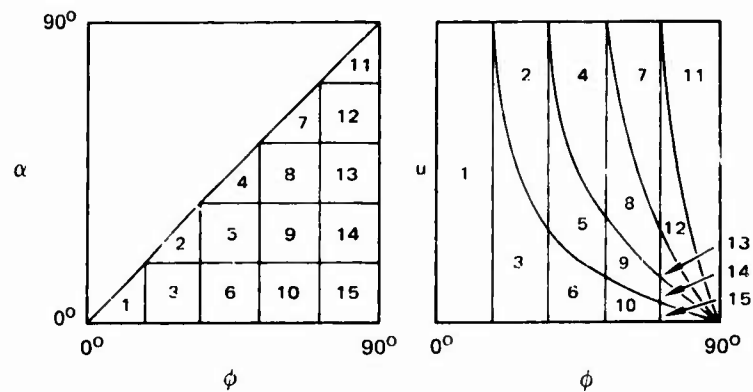
With this transformation Eq. (269) becomes

$$G_{ir} = \int_{\alpha_r}^{\alpha_{r+1}} d\varphi \int_{\alpha_i}^{\alpha_{i+1}} \frac{du}{[1 + \cos^2 u \tan^2 \varphi]^{1/2}} \quad (273)$$

When the order of integration is reversed, the inner integral can be evaluated analytically.

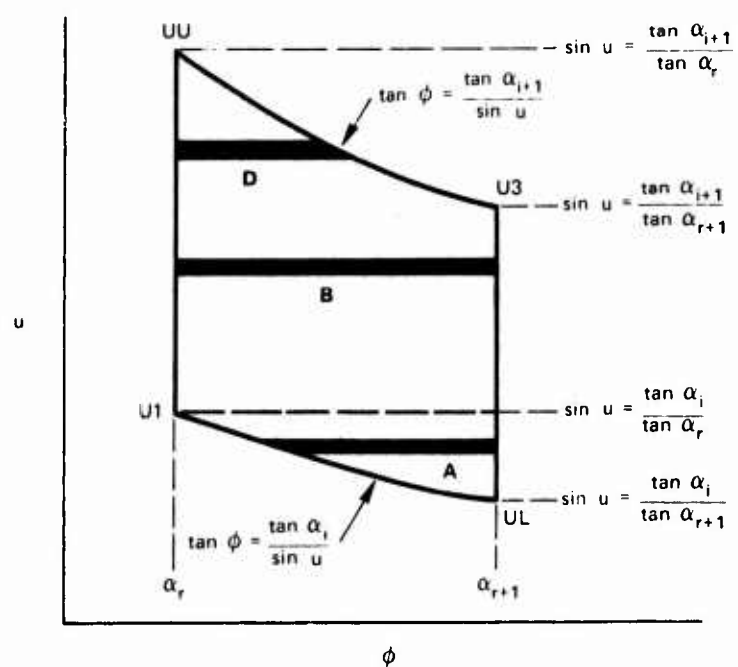
$$G_{ir} = \int_{\arcsin(\tan \alpha_i / \tan \alpha_{r+1})}^{\arcsin(\tan \alpha_{i+1} / \tan \alpha_{r+1})} \frac{du}{\sin u} \int_{\varphi=\alpha_r}^{\varphi=\alpha_{r+1}} d[\arcsin(\sin u \sin \varphi)] \quad (274)$$

The limits of integration and the meaning of the reversal of order of integration may be visualized with the aid of Figure 98. In Figure 98a the region of integration in the  $\alpha$ - $\varphi$  plane is shown. Each numbered triangle or square represents a region of integration for one element of the  $G_{ir}$  matrix. The transformed areas are shown in Figure 98b in the



a. REGION OF INTEGRATION IN  $\alpha - \phi$  PLANE

b. INTEGRATION REGION IN  $u - \phi$  PLANE



c. A TYPICAL SEGMENT OF THE REGION OF INTEGRATION IN THE  $u - \phi$  PLANE

GA-8678-77

FIGURE 98 REGION OF INTEGRATION FOR COMPUTING ELEMENTS OF THE ANGLE FUNCTION,  $G_{ij}$

u-φ plane. A typical numbered element is shown in Figure 98c with its u-φ coordinates labeled. The inner integral in Eq. (274) is evaluated over a strip such as B; then the outer integral is evaluated by adding together values from all strips. It is apparent from Figures 98b and 98c that the simple limits given in Eq. (274) for the inner integral must be modified for strips such as A and D. The combination of numerical and analytical integration required to obtain  $G_{ir}$  was written into a small computer program called ANGLINT; it is described in the next appendix.

Following computation of  $F_{js}$  and  $G_{ir}$ ,  $a_{ijrs}$  was obtained from Eq. (267), and Eq. (265) was used to obtain  $\rho(R, \varphi)$ . The results of some sample calculations are given in the following subsection.

#### 4. EXAMPLE VOLUME DISTRIBUTION CALCULATED FROM SURFACE DISTRIBUTION

The computer programs called BABS 2 and ANGLINT, which were written to compute the volume distribution of cracks  $\rho_{ij}$ , are described in Appendix X. Here we give an illustrative example of results from such computations.

The example is an artificial case selected to test the computer routines. In Eq. (256) we see that the integral is appreciably simplified if  $\rho(R, \varphi)$  is assumed to be

$$\rho(R, \varphi) = \frac{4R \tan \varphi \sec^2 \varphi}{R_m^2} \quad (275)$$

for  $0 \leq \varphi \leq 45^\circ$  and

$$\rho(R, \varphi) = 0 \quad (276)$$

for  $\varphi > 45^\circ$ , where  $R_m$  is the maximum crack radius. In this case Eq. (262) can be easily integrated to yield

$$N_{ij} = \frac{2}{3\pi R_m^2} \left[ \left( R_m^2 - C_j^2 \right)^{3/2} - \left( R_m^2 - C_{j+1}^2 \right)^{3/2} \right] \\ \times \int_{\tan \alpha_i}^{\tan \alpha_{i+1}} \ln | 3 - 2y^2 + 2(2 - 3y^2 + y^4)^{1/2} | dy \quad (277)$$

Furthermore, Eq. (261) can be integrated to yield the volume distribution of cracks

$$\rho_{ij} = \int_{\varphi_i}^{C_{i+1}} d\varphi \int_{R_j}^{R_{j+1}} dR \rho(R, \varphi) \\ = (R_{j+1}^2 - R_j^2) (\tan^2 \varphi_{i+1} - \tan^2 \varphi_i) R_m^2 \quad (278)$$

for  $R \leq R_m$  and  $\varphi \leq 45^\circ$ .

Thus, we get a good test of the computer routine if we assume that we observed a surface distribution given by Eq. (277), and then compute the values of the volume distribution  $\rho_{ij}$  from Eq. (265) with the computer

routines. These results may then be compared with the "true" values obtained from Eq. (278). This has been done; the results are shown in Figure 99. In this figure we plot the crack angle distributions summed over all lengths, namely,

$$\rho_i = \sum_j \rho_{ij} \quad (279)$$

and

$$N_i = \sum_j N_{ij} \quad (280)$$

and the crack length distributions summed over all angles, namely,

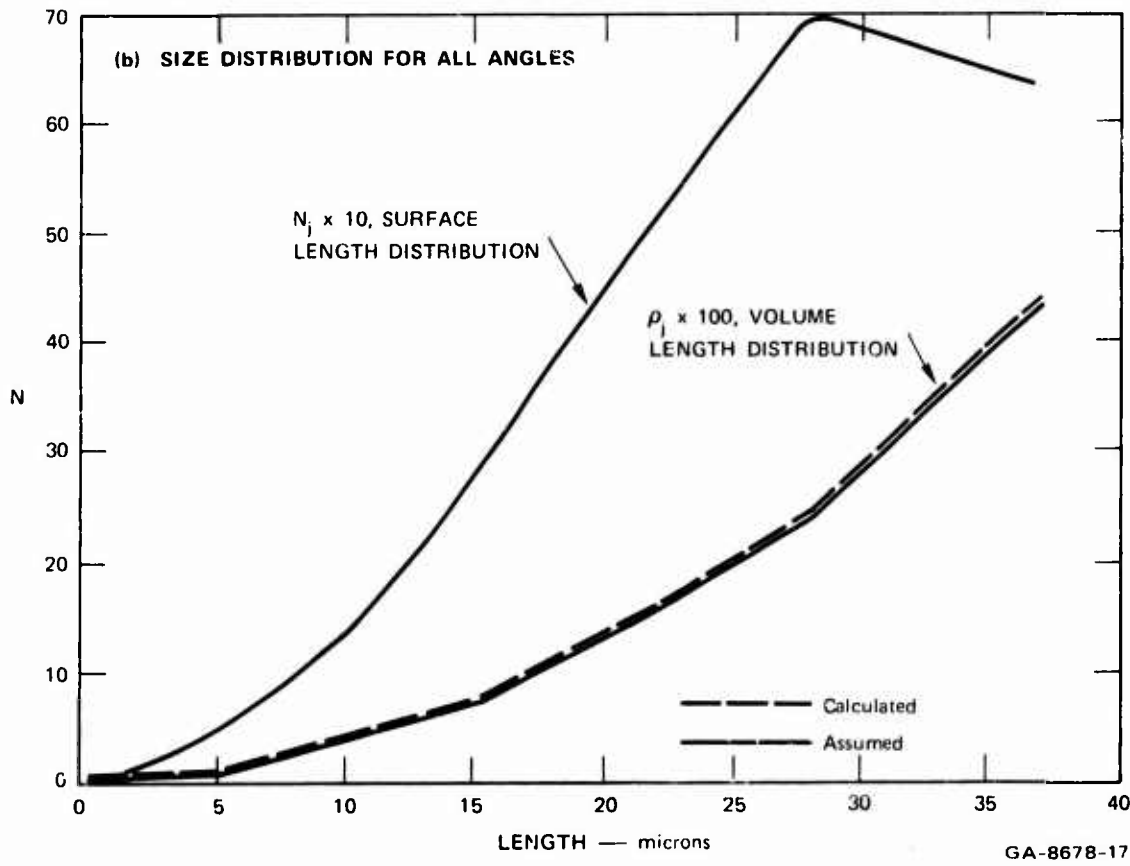
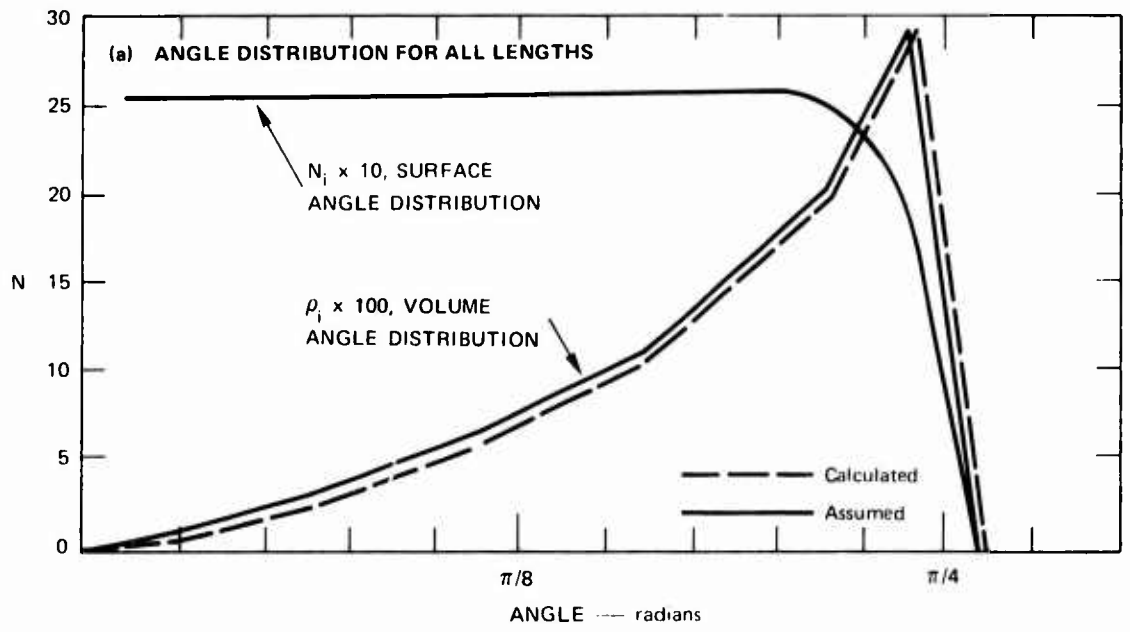
$$\rho_j = \sum_i \rho_{ij} \quad (281)$$

and

$$N_j = \sum_i N_{ij} \quad (282)$$

Good agreement is attained between the computed and the "true" curves, indicating that the computer code functions properly.

This example is particularly interesting because the angle distribution happens to be very similar to those discussed by Kaechele and Tetelman (Ref. 30) as being of the type expected in Armco iron because of the distribution of cleavage planes in that material. However, Kaechele and Tetelman measured angle distributions that differed from the expected ones; the normals to the crack planes were grouped at smaller angles to the major principal stress direction than expected. Our measurements in Armco iron also show this effect, and examples of



GA-8678-17

FIGURE 99 TEST CASE: COMPUTED VOLUME DISTRIBUTIONS COMPARED WITH TRUE VOLUME DISTRIBUTIONS. The discrepancy is too small to be resolved in these graphs.

volume distributions calculated from observed surface distributions with the computer program BABS 2 are given in the text.

Another test of the BABS 2 program is that it should yield results identical to the BABS 1 program, which was developed earlier (Ref. 12) for ductile spherical voids, if the cracks are assumed to be independent of angle and to have only a size distribution. This case was computed, and the results were found to indeed agree with the results of the BABS 1 computation.

In summary, the BABS 2 program for converting observed surface distributions of cracks to volume distributions has been tested and has been found to function satisfactorily.



NOMENCLATURE FOR APPENDIX IX

$F_{js}$	transformation factor dependent only on R and c, cm
$G_{ir}$	transformation factor dependent only on $\varphi$ and $\alpha$
$G(\alpha, c, R, \varphi)$	transformation factor
$N_{ij}$	areal density of cracks within the $i^{\text{th}}$ interval in $\varphi$ and $j^{\text{th}}$ interval in c, number/cm <sup>2</sup>
R	radius of crack, cm
$a_{ijrs}$	fourth rank tensor relating areal and volume crack densities
c	half length of crack trace on a surface, cm
n	observed areal density of cracks, number/cm <sup>2</sup>
w	observed crack opening, cm
x	direction on plane of polish perpendicular to direction of propagation
y	direction perpendicular to plane of polish
z	direction of shock propagation
$\alpha$	observed angle of inclination of normal to crack with respect to z axis
$\nu$	inclination to x-y plane of line in crack plane perpendicular to crack trace on plane of polish
$\delta\alpha_i$	$\alpha_{i+1} - \alpha_i$
$\delta c_i$	$c_{j+1} - c_j$

$\theta$  angle of rotation about z axis

$\rho$  volume density of cracks, number/cm<sup>3</sup>

$\rho_{rs}$  volume density of cracks within the r<sup>th</sup> interval  
in  $\alpha$  and s<sup>th</sup> interval in c, number/cm<sup>3</sup>

$\phi$  actual inclination of normal to crack with respect  
to z axis

## Appendix X

### Statistical Analysis Program: BABS 2

#### 1. LISTING AND FLOW CHARTS FOR BABS 2

BABS 2 is a computer program that carries out the procedure outlined in Appendix IX. It analyzes surface count data from partially fractured specimens and converts these numbers to volume count data. The storage required is about 31,500 (octal) words, and the running time per problem on SRI's CDC 6400 is about 7 seconds. BABS 2 is an extension of the spherical void count program BABS 1 reported earlier (Ref. 12).

Another small program, ANGLINT, evaluates certain integrals over the crack orientation angle intervals that are chosen in the original surface count. The angle integrals are those appearing in Eq. (269) of Appendix IX. The results from ANGLINT are punched on data cards and are used as input to BABS 2. If the chosen crack orientation angle intervals are the same for several different experimental specimens, the same ANGLINT results may be used as BABS 2 input for all these specimens. In the cases reported in this report, we have chosen either 10 or 20 angle intervals between  $0^\circ$  and  $90^\circ$ . The storage required for ANGLINT is about 13,000 (octal) words, and the running time is about 20 seconds, or about three times that for BABS 2. It is therefore efficient to maintain the same angle intervals from specimen to specimen and thus to minimize the number of times that ANGLINT must be run.

The output of ANGLINT consists of a table of values for  $G_{ik}$  of Eq. (269) in Appendix IX, where  $G_{ir}$  is called  $GS(I,K)$  in the program listing. To save memory location, the matrix  $GS(I,K)$  is relisted as the quantity  $GT(L)$ , a vector containing all the nonzero terms in  $GS(I,K)$ .

In this vector  $L = (I-1) \cdot (K_{\max} - I/2) + K$ , and where  $L$  runs from 1 to  $(I_{\max} - 1) \cdot (K_{\max} - I_{\max}/2) + K_{\max}$ .

In this appendix we give program listings, flow charts, and glossaries for BABS 2 and for the auxiliary program ANGLINT.

## 2. SAMPLE COMPUTATION WITH ANGLINT AND BABS

In the following pages are the printout from an ANGLINT run and the printout from a BABS 2 run for Armco iron shot S25.

There is no input to ANGLINT. The output is simply the GT array, which is printed (as shown) and punched on cards.

The BABS 2 printout includes a list of all input data, in a form similar to the input for convenience. The input includes a line of identification, the GT array from ANGLINT, the crack radius information, the number of zones and number of photos. Then for each zone, the area of the zone on each photo and the crack counts are listed as shown. The table of crack counts contains elements for each angle interval ( $J$ ) and radius interval ( $I$ ). These count data are normalized according to the areas and smoothed to produce the NAC table shown for the same intervals of angle and radius. The transformation produces the NPR table, the volume distribution. For convenience the NPR values are summed over all angles to produce the NPR (LEN) vector at the end of the listing. Only the printout for the first zone is shown.

```

PROGRAM BABS2 (OUTPUT,INPUT,TAPE5=INPUT,TAPE6=OUTPUT,TAPE4)      BAB 0010
DIMENSION FS(10,10),GS(10,10),AS( 55,55 ),NPR(10,10),NAC(10,10),  BAB 0020
IGT( 55),A(10),C(11),AREA(10),NAC1(10,10,10),NACN(10,10,10)    BAB 0030
2   ,AVG(10,10)                                                  BAB 0040
C                                                                    BAB 0050
C   NA IS NUMBER OF ANGLE INTERVALS BETWEEN 0 AND PI/2          BAB 0060
C                                                                    BAB 0070
C   NUMBER OF RADIUS INTERVALS IS 10                             BAB 0080
C                                                                    BAB 0090
C   GS,AS,NPR,NAC,GT, ABOVE SHOULD BE GS(NA,NA),AS(NF,55),NPR(NA,10),  BAB 0100
C   NAC(NA,10), AND GT(NF)                                       BAB 0110
C   REAL NAC,NPR,NACN                                           BAB 0120
C   NA=10                                                         BAB 0130
C   NF=NA*(NA+1)/2                                              BAB 0140
C   A(1)=10H DATE =                                             BAB 0150
C   CALL SDATE(DAT)                                             BAB 0160
C   A(2)=DAT                                                    BAB 0170
C   READ GENERAL HEADING CARD                                    BAB 0180
100  READ (5,1604)(A(I),I=3,10)                                  BAB 0190
C   IF (EOF,5) 102,103                                          BAB 0200
102  STOP 20102                                                 BAB 0210
103  WRITE (6,1611)                                             BAB 0220
C   WRITE (6,1604) (A(I),I=1,2)                                  BAB 0230
C   WRITE (6,1604) (A(I),I=3,10)                                  BAB 0240
C   READ ANGLE FUNCTION GS(I,K) IN A LINEAR ARRAY (FROM ANGLINT)  BAB 0250
C   READ(5,1600)(GT(L),L=1,NF)                                   BAB 0260
C   IF (NF .LE. 10) 105,107                                     BAB 0270
105  WRITE (6,1602) (GT(L),L=1,NF)                               BAB 0280
C   GO TO 109                                                    BAB 0290
107  WRITE (6,1602) (GT(L),L=1,10)                               BAB 0300
C   WRITE (6,1606) (GT(L),L=11,NF)                              BAB 0310
109  CONTINUE                                                  BAB 0320
C   READ C(2) - FIRST LENGTH INTERVAL, RATIO - THE RATIO OF SUCCE-  BAB 0330
C   SIVE INTERVALS, NZONES - NO. OF ZONES ON EACH PHOTO, NPHOTOS.  BAB 0340
C   READ (5,1601)A1,C(2),A2,RATIO,A3,NZONES,A4,NPHOTOS          BAB 0350
C   WRITE(6,1601)A1,C(2),A2,RATIO,A3,NZONES,A4,NPHOTOS         BAB 0360
C   DA=3.1416/(2*NA)                                           BAB 0370
C   L=0.                                                         BAB 0380
C   DO 110 I=1,NA                                               BAB 0390
C   DO 110 K=I,NA                                               BAB 0400
C   L=L+1                                                        BAB 0410
110  GS(I,K)=GT(L)                                             BAB 0420
C   C(1)=0.                                                      BAB 0430
C   DC=C(2)                                                       BAB 0440
C   DO 111 J=3,11                                              BAB 0450
C   DC=DC*RATIO                                                 BAB 0460
111  C(J)=C(J-1)+DC                                           BAB 0470
C   PRINT 1609,(C(J),J=1,11)                                    BAB 0480
C   SET FACTORS FOR SMOOTHING THE RAW DATA                     BAB 0490
C   FA=0.7 $ FB=0.075                                          BAB 0500
C   WRITE (6,1704) FA,FB                                       BAB 0510
C   COMPUTE SIZE FUNCTION FS(J,M)                               BAB 0520
C   SR1=SR2=SR3=SR4=SR5=0.                                     BAB 0530
C   DO 200 J=1,10                                              BAB 0540
C   DO 160 M=J,10                                              BAB 0550
C   CJ=C(J)                                                      BAB 0560
C   CJP=C(J+1)                                                  BAB 0570
C   CM=C(M)                                                      BAB 0580
C   CMP=C(M+1)                                                  BAB 0590
C   IF (M.NE.J) GO TO 120                                       BAB 0600
C   IF (CJ.NE.0.) GO TO 115                                     BAB 0610
C   FS(J,M)=CJP/DA                                             BAB 0620
C   GO TO 150                                                  BAB 0630
115  SR1=SQRT(CJP*CJP-CJ*CJ)                                    BAB 0640
C   FS(J,M)=(CJP*SR1-CJ*CJ*ALUG((CMP*SK1)/CJ))/(DA*(CJP-CJ))  BAB 0650
C   GO TO 150                                                  BAB 0660

```

LISTING OF PROGRAM BABS2

120	SR2=SQRT(CMP*CMP-CJ*CJ)	BAB 0670
	SR3=SQRT(CM*CM-CJ*CJ)	BAB 0680
	SR4=SQRT(CMP*CMP-CJP*CJP)	BAB 0690
	SUM=(CMP*SR2-CM*SR3-CMP*SR4-CJ*CJ*ALOG((CMP+SR2)/(CM+SR3)))	BAB 0700
	IF(M.NE.(J+1)) GO TO 130	BAB 0710
	FS(J,M)=(SUM+CJP*CJP*ALOG((CMP+SR4)/CM))/(DA*(CMP-CM))	BAB 0720
	GO TO 150	BAB 0730
130	SR5=SQRT(CM*CM-CJP*CJP)	BAB 0740
	FS(J,M)=(SUM+CM*SR5+CJP*CJP*ALOG((CMP+SR4)/(CM+SR5)))/DA*(	BAB 0750
	CM-CM)	BAB 0760
150	CONTINUE	BAB 0770
160	CONTINUE	BAB 0780
200	CONTINUE	BAB 0790
C	COMPUTE TRANSFORMATION MATRIX AS(I,K,J,M)	BAB 0800
	DO 400 J=1,10	BAB 0810
	DO 390 M=J,10	BAB 0820
	DO 380 I=1,NA	BAB 0830
	DO 370 K=1,NA	BAB 0840
	L=K+((I-1)*NA-((I-1)*I))/2	BAB 0850
	N=M+(J-1)*10-((J-1)*J)/2	BAB 0860
	AS(L,N)=GS(I,K)*FS(J,M)/6.2832	BAB 0870
370	CONTINUE	BAB 0880
380	CONTINUE	BAB 0890
390	CONTINUE	BAB 0900
400	CONTINUE	BAB 0910
C	COMPUTE VOLUME DISTRIBUTION OF CRACKS NPR(I,J)	BAB 0920
C	READ AND WRITE DATA FOR EACH ZONE	BAB 0930
	DO 1000 NZ=1,NZONES	BAB 0940
	PRINT 1611	BAB 0950
	IF(NPHOTOS.LE.7) 651,652	BAB 0960
651	READ (5,1802) A1,A2, (AREA(I),I=1,NPHOTOS)	BAB 0970
	WRITE(6,1802) A1,A2, (AREA(I),I=1,NPHOTOS)	BAB 0980
	GO TO 653	BAB 0990
652	READ (5,1802) A1,A2, (AREA(K),K=1,7)	BAB 1000
	WRITE(6,1802) A1,A2, (AREA(K),K=1,7)	BAB 1010
	READ (5,1803) (AREA(K),K=8,NPHOTOS)	BAB 1020
	WRITE(6,1803) (AREA(K),K=8,NPHOTOS)	BAB 1030
653	PRINT 1804, (M,M=1,10)	BAB 1040
	DO 660 K=1,NPHOTOS	BAB 1050
	READ (4) A1,A2, ((NAC(I,J,I,K),I=1,NA),J=1,10)	BAB 1060
	PRINT 1805, A1,A2, (J, (NAC(I,J,I,K), I=1,NA),J=1,10)	BAB 1070
C	NORMALIZE ALL NACI TO NACN FOR AREA, AVERAGE OVER PHOTOS	BAB 1080
	DO 660 I=1,NA	BAB 1090
	DO 660 J=1,10	BAB 1100
	NACN(J,I,K)=NAC(I,J,I,K)/AREA(K)	BAB 1110
660	CONTINUE	BAB 1120
	DO 710 I=1,NA	BAB 1130
	DO 710 J=1,10	BAB 1140
	SUMNACN=0.	BAB 1150
	DO 705 K=1,NPHOTOS	BAB 1160
	SUMNACN=SUMNACN+NACN(J,I,K)	BAB 1170
705	CONTINUE	BAB 1180
	NAC(I,J)=SUMNACN/NPHOTOS	BAB 1190
710	CONTINUE	BAB 1200
	DO 730 I=1,NA	BAB 1210
	DO 730 J=1,10	BAB 1220
	AVG(I,J)=FA*NAC(I,J)	BAB 1230
	IF (I .GT. 1) AVG(I,J)=AVG(I,J)+FB*NAC(I-1,J)	BAB 1240
	IF (I .LT. NA) AVG(I,J)=AVG(I,J)+FB*NAC(I+1,J)	BAB 1250
	IF (J .GT. 1) AVG(I,J)=AVG(I,J)+FB*NAC(I,J-1)	BAB 1260
	IF (J .LT. 10) AVG(I,J)=AVG(I,J)+FB*NAC(I,J+1)	BAB 1270
730	CONTINUE	BAB 1280
	DO 750 I=1,NA	BAB 1290
	DO 750 J=1,10	BAB 1300
	NAC(I,J)=FA*AVG(I,J)	BAB 1310
	IF (I .GT. 1) NAC(I,J)=NAC(I,J)+FB*AVG(I-1,J)	BAB 1320
	IF (I .LT. NA) NAC(I,J)=NAC(I,J)+FB*AVG(I+1,J)	BAB 1330
	IF (J .GT. 1) NAC(I,J)=NAC(I,J)+FB*AVG(I,J-1)	BAB 1340
	IF (J .LT. 10) NAC(I,J)=NAC(I,J)+FB*AVG(I,J+1)	BAB 1350

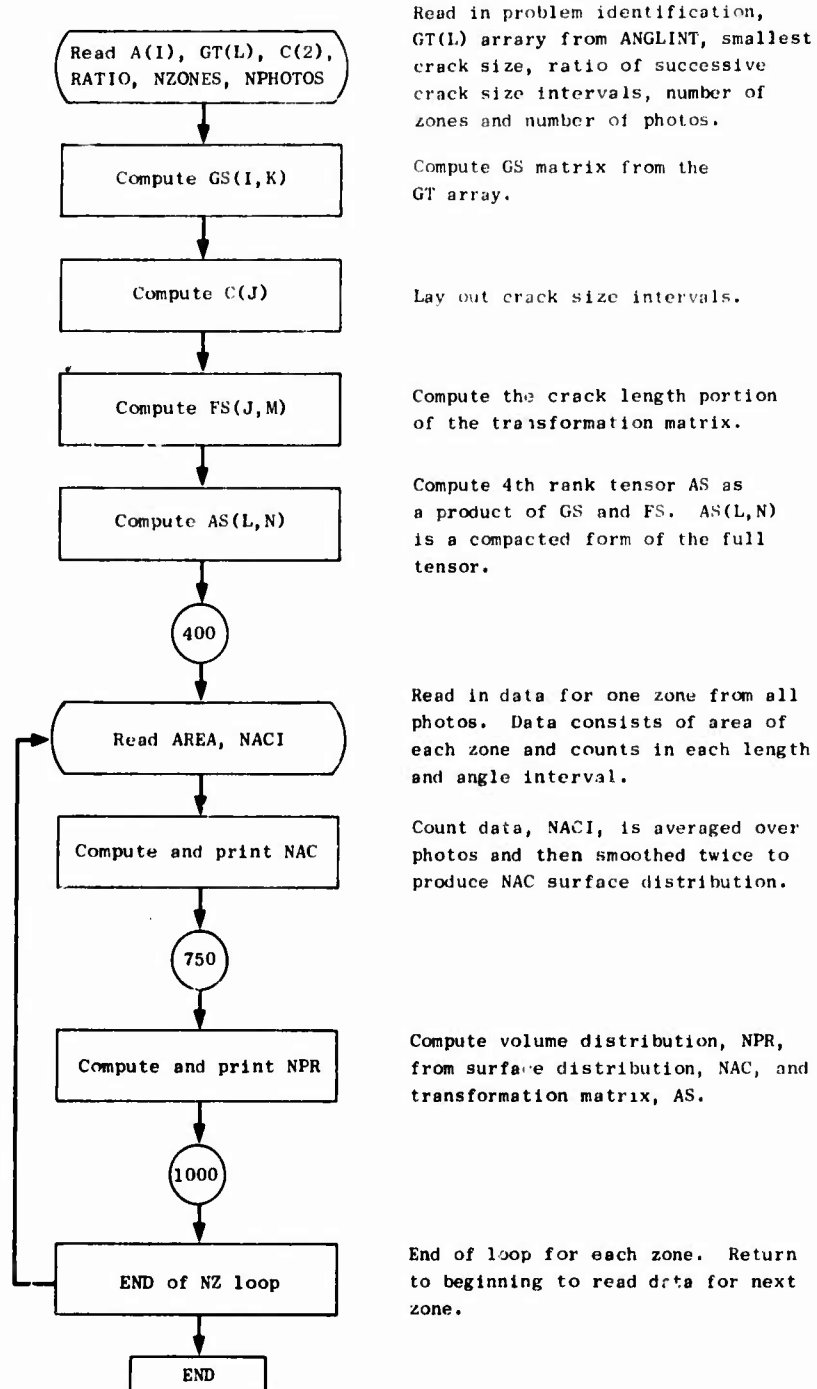
LISTING OF PROGRAM BABS2 (Continued)

750	CONTINUE	BAB 1360
	WRITE (6,1705)	BAB 1370
	WRITE (6,1703) ((NAC(I,J), I=1,NA),J=1,10)	BAB 1380
	DO 500 II=1,NA	BAB 1390
	I=NA+1-II	BAB 1400
	DO 490 JJ=1,10	BAB 1410
	J=11-JJ	BAB 1420
	SUM=0.	BAB 1430
	IF (I .EQ. NA) GO TO 430	BAB 1440
	KK=I+1	BAB 1450
	N=J+(J-1)*10-((J-1)*J)/2	BAB 1460
	DO 425 K=KK,NA	BAB 1470
	L=K+(I-1)*NA-((I-1)*I)/2	BAB 1480
425	SUM=SUM+AS(L,N)*NPR(K,J)	BAB 1490
430	IF (J .EQ. 10) GO TO 460	BAB 1500
	MM=J+1	BAB 1510
	DO 450 M=MM,10	BAB 1520
	N=M+(J-1)*10-((J-1)*J)/2	BAB 1530
	DO 450 K=I,NA	BAB 1540
	L=K+(I-1)*NA-((I-1)*I)/2	BAB 1550
450	SUM=AS(L,N)*NPR(K,M)+SUM	BAB 1560
460	L=I+(I-1)*NA-((I-1)*I)/2	BAB 1570
	N=J+(J-1)*10-((J-1)*J)/2	BAB 1580
	NPR(I,J)=(NAC(I,J)-SUM)/AS(L,N)	BAB 1590
490	CONTINUE	BAB 1600
500	CONTINUE	BAB 1610
	WRITE (6,1705)	BAB 1620
	WRITE (6,1608) ((NPR(I,J), I=1,NA),J=1,10)	BAB 1630
	DO 800 J=1,10	BAB 1640
	DO 800 I=2,NA	BAB 1650
800	NPR(I,J)=NPR(I,J)+NPR(I,J)	BAB 1660
	WRITE (6,1612) (NPR(I,J),J=1,10)	BAB 1670
1000	CONTINUE	BAB 1680
	GO TO 100	BAB 1690
1600	FORMAT(8E10.3)	BAB 1700
1601	FORMAT(2(A10,E10.3),2(A10,I10))	BAB 1710
1602	FORMAT(/* GT(L) = *,10E10.3)	BAB 1720
1604	FORMAT(9A10)	BAB 1730
1606	FORMAT(10X,10E10.3)	BAB 1740
1608	FORMAT(2X,*NPR(ANG,LEN)=*,10E12.3)	BAB 1750
1609	FORMAT(* C=*,11E11.3/)	BAB 1760
1611	FORMAT(1H1,//)	BAB 1770
1612	FORMAT(///2X,*NPR(LEN)=*,4X,10E12.3/)	BAB 1780
1703	FORMAT(2X,*NAC(ANG,LEN)=*,10E12.3)	BAB 1790
1704	FORMAT(20X,*FA =*, E12.3, 10X, *FB =*, E12.3//)	BAB 1800
1705	FORMAT(///)	BAB 1810
1802	FORMAT (2A5,7F10.4)	BAB 1820
1803	FORMAT (8F10.4)	BAB 1830
1804	FORMAT(//26X,*I=*,2X,10I10/)	BAB 1840
1805	FORMAT(2X,2A10,5X,*J=*,15,10I10/9(27X,*J=*,15,10I10/))	BAB 1850
	END	BAB 1860

LISTING OF PROGRAM BABS2 (Concluded)

BABS 2

This program transforms surface crack counts to volume distributions of cracks, grouped according to length and orientation.



FLOW CHART FOR PROGRAM BABS2 (Complete)

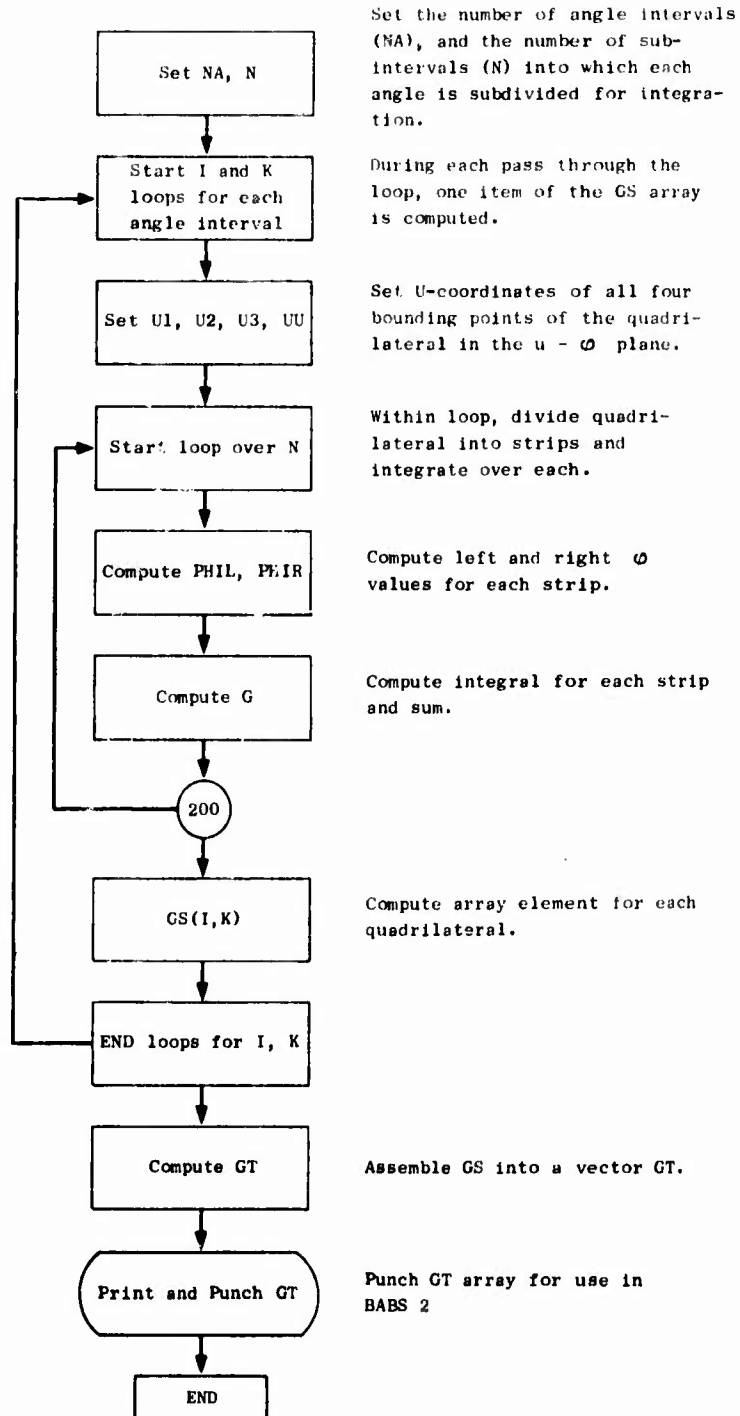


	PROGRAM ANGLINT(OUTPUT,PUNCH)	ANG 010
	DIMENSION GS(20,20),A(50),GT(210)	ANG 020
C	PROGRAM COMPUTES THE ANGLE FUNCTION GS(I,K) FOR USE IN BABS 2.	ANG 030
C	(CHECK DIMENSIONS OF GT(NA*(NA+1)/2) AND GS(NA,NA) WITH NA.)	ANG 040
	NA=20	ANG 050
	NF=NA*(NA+1)/2	ANG 060
	PRINT 1300	ANG 070
	DA=3.1416/(2*NA)	ANG 080
	N=50	ANG 090
	DO 1000 I=1,NA	ANG 100
	DO 900 K=1,NA	ANG 110
	ALPHA= DA*(I-1)	ANG 120
	TANA=TAN(ALPHA)	ANG 130
	PHI=DA*(K-1)	ANG 140
	TANP=TAN(PHI)	ANG 150
	UU=3.1416/2.	ANG 160
	UL=0.	ANG 170
	IF (I.NE.1.AND.I.NE.NA) UL=ASIN(TANA/TAN(DA*K))	ANG 180
	IF(K.NE.1) UU=ASIN(TAN(DA*I)/TANP)	ANG 190
	G=0.	ANG 200
	DU=(UU-UL)/(2.*N)	ANG 210
	U1=UU	ANG 220
	IF(K.NE.1) U1=ASIN(TANA/TANP)	ANG 230
	U3=UU	ANG 240
	IF(K.NE.1)U3=ASIN(TAN(DA*I)/TAN(DA*K))	ANG 250
	DO 200 J=1,N	ANG 260
	U=UL+(2*J-1.)*DU	ANG 270
	SINU=SIN(U)	ANG 280
	PHIL=PHI	ANG 290
	IF (U .LT. U1) PHIL=ATAN(TANA/SINU)	ANG 300
	PHIR=DA*K	ANG 310
	IF (U .GT. U3) PHIR=ATAN(TAN(DA*I)/SINU)	ANG 320
200	G=G+(ASIN(SINU*SIN(PHIR))-ASIN(SINU*SIN(PHIL)))/SINU	ANG 330
	GS(I,K)=(UU-UL)*G/N	ANG 340
900	CONTINUE	ANG 350
1000	CONTINUE	ANG 360
	L=0	ANG 370
	DO 1150 I=1,NA	ANG 380
	DO 1150 K=1,NA	ANG 390
	L=L+1	ANG 400
1150	GT(L)=GS(I,K)	ANG 410
	PRINT 1310,(GT(L),L=1,NF)	ANG 420
	PUNCH 1310,(GT(L),L=1,NF)	ANG 430
1300	FORMAT (1H1,* PROGRAM ANGLINT *)	ANG 440
1310	FORMAT (8F10.8)	ANG 450
	END	ANG 460

LISTING OF PROGRAM ANGLINT (Complete)

ANGLINT

Program evaluates double integrals to provide GS array,  
a factor in the AS transformation matrix of BABS 2.



FLOW CHART OF PROGRAM ANGLINT (Complete)

PROGRAM ANGLINT

.24623314	.12057959	.05820052	.03547799	.02250678	.01397291	.00806329	.00401032
.00144948	.00020515	.12258476	.08233709	.04142169	.02502317	.01517297	.00863217
.00425531	.00152963	.00021592	.09641648	.06605313	.03195899	.01814651	.00997320
.00481393	.00170885	.00023970	.08438808	.05628409	.02498744	.01269586	.00587723
.00203735	.00028266	.07823458	.04885218	.01880188	.00794690	.00263444	.00035820
.07523224	.04161387	.01269081	.00380851	.00049805	.07373263	.03282724	.00665216
.00079279	.07146699	.02132680	.00160207	.06330977	.00779506	.03410603	

PRINTOUT FROM ANGLINT FOR NA = 10



NAC(ANG,LEN)=	4.310E-01	0.	0.	4.336E-01	8.671E-01	8.960E+00	9.394E+00	8.671E-01	0.	4.336E-01
NAC(ANG,LEN)=	8.045E+00	8.620E-01	1.298E+00	8.527E+00	9.394E+00	4.846E+01	5.569E+01	9.394E+00	1.301E+00	8.093E+00
NAC(ANG,LEN)=	3.927E+01	9.341E+00	1.657E+01	4.036E+01	9.394E+00	1.792E+01	4.846E+01	9.394E+00	8.527E+00	3.907E+01
NAC(ANG,LEN)=	1.657E+01	9.774E+00	4.013E+01	1.614E+01	2.165E+00	9.394E+00	9.394E+00	8.671E-01	8.671E-01	8.093E+00
NAC(ANG,LEN)=	3.950E+01	8.955E+00	8.479E+00	1.729E+00	8.093E+00	3.950E+01	8.527E+00	4.336E-01	0.	4.336E-01
NAC(ANG,LEN)=	8.093E+00	8.671E-01	4.310E-01	0.	8.671E-01	8.093E+00	8.671E-01	0.	0.	0.
NAC(ANG,LEN)=	4.336E-01	0.	0.	0.	0.	4.336E-01	0.	0.	0.	0.
NAC(ANG,LEN)=	0.	0.	0.	0.	0.	0.	0.	0.	0.	0.
NAC(ANG,LEN)=	0.	0.	0.	0.	0.	0.	0.	0.	0.	0.
NAC(ANG,LEN)=	0.	0.	0.	0.	0.	0.	0.	0.	0.	0.
NPR(ANG,LEN)=	-2.519E+02	2.381E+03	2.349E+03	6.463E+03	1.372E+04	-2.679E+04	-5.520E+04	-2.033E+04	8.941E+02	-6.187E+01
NPR(ANG,LEN)=	-1.049E+04	-6.116E+03	3.142E+03	-8.011E+04	-8.563E+04	1.090E+05	1.690E+05	3.156E+04	-2.679E+03	-9.797E+04
NPR(ANG,LEN)=	2.300E+04	2.282E+04	-6.797E+04	7.077E+04	8.864E+03	-7.638E+04	1.285E+05	2.412E+04	2.804E+02	2.422E+05
NPR(ANG,LEN)=	-1.112E+03	-2.922E+04	4.010E+04	2.798E+04	1.087E+04	-2.802E+04	1.005E+04	1.299E+03	-2.330E+03	3.654E+04
NPR(ANG,LEN)=	1.275E+04	1.122E+03	6.063E+03	6.236E+02	-2.045E+04	4.546E+04	1.188E+04	6.963E+02	-1.744E+02	1.417E+03
NPR(ANG,LEN)=	2.283E+03	3.126E+02	-5.915E+01	3.625E+02	-4.249E+03	7.867E+03	9.447E+02	0.	0.	0.
NPR(ANG,LEN)=	1.019E+02	1.964E+00	-2.158E+01	4.078E+01	-2.116E+02	3.388E+02	0.	0.	0.	0.
NPR(ANG,LEN)=	0.	0.	0.	0.	0.	0.	0.	0.	0.	0.
NPR(ANG,LEN)=	0.	0.	0.	0.	0.	0.	0.	0.	0.	0.
NPR(ANG,LEN)=	0.	0.	0.	0.	0.	0.	0.	0.	0.	0.
NPR(LEN)=	-7.682E+04	6.969E+04	4.263E+05	6.615E+04	5.939E+04	7.462E+03	2.503E+02	0.	0.	0.

SAMPLE OUTPUT FROM BABS2, NORMALIZED SURFACE COUNT DATA AND VOLUME DISTRIBUTION

NOMENCLATURE FOR APPENDIX X

BABS 2 and ANGLINT INPUT and COMMON TERMS

A(I)	Label in ANGLINT referring to region of integration. A(I) appears in output as A, B, C, or D corresponding to junctions 101, 102, 103 and 104 in the flow diagram for ANGLINT.
ALPHA	angle $\alpha$ in Appendix IX
AREA (I)	input-area of I'th zone on a photo, $\text{cm}^2$
AS(I,K,J,M)	transformation matrix from surface count to volume count
C(I)	crack size $c_i$
FS(J,M)	part of AS(I,K,J,M) referring to size distribution
GS(I,K)	part of AS(I,K,J,M) referring to angle distribution
GT(L)	re-listing of GS(I,K), $L=(I-1)(K_{\text{max}}-1/2)+K$
N	number of intervals used to evaluate (G(I,K) in ANGLINT
NA	number of angle intervals between 0 and $\pi/2$
NAC(I,J)	surface crack distribution function, number/ $\text{cm}^2$
NPHOTOS	number of photos for a given zone
NPR(I,J)	volume crack distribution function, number/ $\text{cm}^3$
NZONES	number of zones for a given specimen
PHI	angle $\phi$ in Appendix IX
PHIL	lower limit of integration over $\phi$ in ANGLINT
PHIR	upper limit of integration over $\phi$ in ANGLINT

U             $u = \sin^{-1} (\tan \alpha / \tan \phi)$ , variable in ANGLINT

U1           an intermediate integration limit for U in ANGLINT

U3           an intermediate integration limit for U in ANGLINT

UL           lower limit of integration over U in ANGLINT

UU           upper limit of integration over U in ANGLINT

## REFERENCES

1. Barbee, T.; Seaman, L.; and Curran, D.; Dynamic Fracture Criteria of Homogeneous Materials, Volume One: Theory and Flyer Plate Experiments, Ductile and Brittle Materials. Volume Two: (U) Calculations of Ductile Fracture in Copper Radiated in MIDI MIST (Secret), F29601-70-C-0070, Semiannual Summary Report, Air Force Special Weapons Center, Kirtland AFB, New Mexico, December 21, 1970.
2. Berg, C. A.; "The Motion of Cracks in Plane Viscous Deformation," Proceeds Fourth U.S. National Congress of Applied Mechanics 2, 885 1962.
3. McClintok, F. A.; Kaplan, S. M.; Berg, C. A.; "Ductile Fracture by Hole Growth in Shear Bands," Int. J. Fracture Mech., 2, 614 (1966).
4. McClintok, F. A.; "A Criterion for Ductile Fracture by the Growth of Holes," J. Appl. Mech., 35, 363 (1968).
5. MacKenzie, J. K.; "The Elastic Constants of a Solid Containing Spherical Holes," Proc. Phys. Soc. B, 63, 2 (1950).
6. Buch, A.; Goldschmidt, S.; "Influence of Porosity on Elastic Moduli of Sintered Materials," Mater. Sci. Eng. 5, 111 (1969).
7. Tuler, F. R.; Butcher, B. M.; "A Criteria for the Time Dependence of Dynamic Fracture," Int. J. Frac. Mech., 4, 431 (1968).
8. Herrmann, W.; Equation of State of Crushable Distended Materials, SC-RR-66-2678, Sandia Corporation, Albuquerque, New Mexico; March 1968; Herrmann, W.; On the Elastic Compression of Crushable Distended Materials, SC-DR-68-321, Sandia Laboratory, Albuquerque, New Mexico, June 1968.
9. Seaman, L.; Linde, R. K.; Distended Material Model Development, Vol. I, Experiments and Theory for the Model, Technical Report No. AFWL-TR-68-143, Air Force Weapons Laboratory, Kirtland AFB, New Mexico, May 1969.
10. Butcher, B. M.; Spallation of 6061-T6 Aluminum: Behavior of Dense Media Under High Dynamic Pressure, Gordon and Breach, New York, 1968, p. 245.



11. Kaufman, J. G.; Schilling, P. E.; and Nelson, F. G.; "Fracture Toughness of Aluminum Alloys," Metals Eng. Quart., 39, 40 (1969).
12. Barbee, T.; Seaman, L.; Crewdson, R. C.; Dynamic Fracture Criteria of Homogeneous Materials, Technical Report No. AFWL-TR-70-99, Air Force Weapons Laboratory, Kirtland AFB, New Mexico, November 1970.
13. Walsh, J. M.; Rice, M. H.; McQueen, R. G.; Yarger, F. L.; "Shock-Wave Compression of Twenty-Seven Metals. Equations of State of Metals," Phys. Rev., 108 196 (1957).
14. Barker, L. M.; Hollenbach, R. E.; "Shock-Wave Studies of PMMA, Fused Silica, and Sapphire," J. Appl. Phys., 41 4208 (1970).
15. Johnston, W. G.; Gilman, J. J.; "Dislocation Velocity, Dislocation Densities, and Plastic Flow in Lithium Fluoride Crystals," J. Appl. Phys. 30, 129 (1959).
16. Granato, A; Lücke, K.; "Theory of Mechanical Damping Due to Dislocations," J. Appl. Phys., 27, 583 (1956).
17. Ferguson, W. G.; Kumar, A.; Dorn, J. E.; "Dislocation Damping in Aluminum at High Strain Rates," J. Appl. Phys., 38, 1863 (1967).
18. Kumar, A.; Hauser, F. E.; Dorn, J. E.; "Viscous Drag on Dislocations in Aluminum at High Strain Rates," Acta Met., 16, 1189 (1968).
19. Bland, D. R.; "On Shock Structure in a Solid," Journal of the Institute of Mathematics and Its Applications, 1, 56 (1965).
20. Kelly, J. M.; Gillis, P. M.; "Shock Thickness in Viscoplastic Solids," J. Appl. Mech., 37, 163 (1970).
21. Barker, L. M.; "Fine Structure of Compressive and Release Wave Shapes in Aluminum Measured by the Velocity Interferometer Technique," Behavior of Dense Media Under High Dynamic Pressure, Gordon and Breach, New York, 1968, p. 483.
22. Rice, M. H.; "Capacitor Technique for Measuring the Velocity of a Plane Conducting Surface," Rev. Sci. Instr. 32, 449 (1961).
23. Kumar, A.; Kumble, R. G.; "Viscous Drag on Dislocations at High Strain Rates in Copper," J. Appl. Phys., 40, 3475 (1969).

24. Greenman, W. F.; Vreeland, T.; Wood, D. S.; "Dislocation Mobility in Copper," J. Appl. Phys., 38, 3595 (1967).
25. Jassby, K. M.; Vreeland, T.; "An Experimental Study of the Mobility of Edge Dislocations in Pure Copper Single Crystals," Phil. Mag., 21, 1117 (1970).
26. Edington, J. W.; "The Influence of Strain Rate on the Mechanical Properties and Dislocation Substructure in Deformed Copper Single Crystals," Phil. Mag., 19, 1189 (1969).
27. Gorman, J. S.; Wood, D. S.; Vreeland, T.; "Mobility of Dislocations in Aluminum," J. Appl. Phys. 40, 833 (1969).
28. Sylwestrowicz, W. D.; "Mechanism of Ultrasonic Loss in Silicon and Aluminum," J. Appl. Phys., 37, 535 (1966).
29. Grace, F. I.; "Shock-Wave Strengthening of Copper and Nickel," J. Appl. Phys., 40, 264<sup>c</sup> (1969).
30. Kaechele, L. E.; Tetelman, A. S.; "A Statistical Investigation of Microcrack Formation," Acta. Met., 17, 463 (1969).
31. Griffith, A. A.; "The Phenomena of Rupture and Flow in Solids," Phil. Trans. A, 221, 163 (1921).
32. Irwin, G. R.; "Fracture," Handbuch der Physik VI, ed. S. Flügge, Springer Verlag, Berlin-Göttingen-Heidelberg, 1958, p. 551.
33. Mott, N. F.; "Fracture of Metals: Theoretical Considerations," Engineering 165, 16 (1948); and "Fracture in Metals," J. Iron Steel Inst. (London), 183, 233 1956.
34. Sneddon, I. N.; Lowengrub, M; Crack Problems in the Classical Theory of Elasticity, John Wiley and Sons, Inc., New York, 1969.
35. Dulaney, E. N.; Brace, W. F.; "Velocity Behavior of a Growing Crack," J. Appl. Phys., 31, 2233 (1960).
36. Neuber, H.; "Ein neuer Ansatz zur Lösung räumlicher Probleme der Elastizitätstheorie," Z. Ang. Math. Mech. 14, 203 (1934).
37. Barenblatt, G. I.; "The Mathematical Theory of Equilibrium Cracks in Brittle Fracture," Advances in Applied Mechanics, ed., H. L. Dryden, T. Von Karman and G. Kuerti, Vol. 7, Academic Press, New York, London, 1962, p. 55.

38. Charest, J.; Measurement of Spall Thresholds and Stress Wave Characteristics in 1.76 gm/cm<sup>3</sup> Graphite, EG&G Report, Air Force Weapons Laboratory, Kirtland AFB, New Mexico, September 1971.
39. Ubbelohde, A. R.; Lewis, F. A.; Graphite and Its Crystal Compounds, Oxford, at the Clarendon Press, London, 1960.
40. Stroh, A. N.; "Brittle Fracture and Yielding," Phil. Mag., 46 968 1955.
41. Hahn, G. T.; Averbach, B. C.; Owen, W. S.; Cohen, M.; Fracture, ed., B. C. Averbach, D. K. Felbeck, G. T. Hahn, and D. A. Thomas, John Wiley and Sons, Inc., New York, 1959, p. 91.
42. Zhurkov, S. N.; Int. J. Frac. Mech., 1, 311 (1965).
43. Poritsky, H; "The Collapse or Growth of a Spherical Bubble or Cavity in a Viscous Fluid," Proceedings of the First U.S. National Congress of Applied Mechanics, ASME, New York, 1952, p. 813.
44. Bornhorst, W. J.; Hatsopoulos, G. N.; "Bubble-Growth Calculations without Neglect of Interface Discontinuities," J. Appl. Mech., 34, 847 (1967).
45. Hashin, Z.; "The Elastic Moduli of Heterogeneous Materials," J. Appl. Mech., 29 143 (1962).
46. Hill, R.; The Mathematical Theory of Plasticity, Clarendon Press, Oxford, 1959.
47. Love, A.E.H.; "A Treatise on the Mathematical Theory of Elasticity," Dover Publications, Inc., New York, 1944.
48. Wilkins, M. L.; "Calculation of Elastic-Plastic Flow," Methods in Computational Physics, ed. B. Alder, Academic Press, New York, 1964, p. 211.
49. Wilkins, M. L.; "The Calculation of the Dynamic Resistance of a Material," presented at the IUTAM Symposium on High Dynamic Pressure, Paris, 1968.
50. Timoshenko, S.; Goodier, J. N.; Theory of Elasticity, McGraw-Hill Book Company, Inc., New York, 1951.

51. Rouse, H., ed., Advanced Mechanics of Fluids, John Wiley and Sons, Inc., New York, 1959.
52. Prager, W.; Introduction to Mechanics of Continua, Ginn and Company, New York, 1961.
53. Richtmyer, R. D.; Morton, K. W.; Difference Methods for Initial-Value Problems, second edition, Interscience Publishers, New York, 1967.
54. Herrmann, W.; Holzhauser, P.; Thompson, R. J.; WONDY, A Computer Program for Calculating Problems of Motion in One Dimension, SC-RR-66-001, Sandia Corporation, Albuquerque, New Mexico, February 1967.
55. Seaman, L.; SRI PUFF 3 Computer Code for Stress Wave Propagation, Technical Report No. AFWL-TR-70-51, Air Force Weapons Laboratory, Kirtland AFB, New Mexico, September 1970.
56. Scheil, E.; "Die Berechnung der Anzahl und Grossenverteilung kugelformiger Kristalle in undurchsichtigen Körpern mit Hilfe durch einen ebenen Schnitt erhaltenen Schnittkreise," Z. Anorg. Allgem. Chem., 201 259 (1931).
57. Scheil, E.; "Statistische Gefügeuntersuchungen I," Z. Metallk., 27, 199 (1935).
58. Saltykov, S. A.; Stereometric Metallography, Second Edition, Metallurgizdat, Moscow, 1958, p. 446.
59. Butcher, B. M.; Barker, L. M.; Munson, D. E.; Lundergan, C. D.; "Influence of Stress History on Time-Dependent Spall in Metals," American Institute for Aeronautics and Astronautics Journal, 2, 977 (June 1964).

UNCLASSIFIED

Security Classification

## DOCUMENT CONTROL DATA - R &amp; D

(Security classification of title, body of abstract and indexing annotation must be entered when the overall report is classified)

1. ORIGINATING ACTIVITY (Corporate author) Stanford Research Institute 333 Ravenswood Avenue Menlo Park, California 94025		2a. REPORT SECURITY CLASSIFICATION Unclassified	
		2b. GROUP	
3. REPORT TITLE  DYNAMIC FRACTURE CRITERIA OF HOMOGENEOUS MATERIALS			
4. DESCRIPTIVE NOTES (Type of report and inclusive dates) June 1970 through October 1971			
5. AUTHOR(S) (First name, middle initial, last name)  L. Seaman, T. W. Barbee, Jr., D. R. Curran			
6. REPORT DATE February 1972		7a. TOTAL NO. OF PAGES 390	7b. NO. OF REFS 59
8a. CONTRACT OR GRANT NO. F29601-70-C-0070		9a. ORIGINATOR'S REPORT NUMBER(S)  AFWL-TR-71-156	
b. PROJECT NO. 5710		9b. OTHER REPORT NO(S) (Any other numbers that may be assigned this report)	
c. Task AA114		Contractor's Rept No. SRI Project PYU 8678	
d.			
10. DISTRIBUTION STATEMENT Distribution limited to US Government agencies only because of test and evaluation (February 1972). Other requests for this document must be referred to AFWL (SRR), Kirtland AFB, NM 87117			
11. SUPPLEMENTARY NOTES		12. SPONSORING MILITARY ACTIVITY  AFWL (SRR) Kirtland AFB, NM 87117	
13. ABSTRACT (Distribution Limitation Statement B) A successful computational and experimental procedure has been developed for predicting shock-induced damage in brittle and ductile materials. This procedure results in the determination of two material functions namely, the nucleation rate and the growth rate for microscopic voids, which eventually coalesce for form fracture. These nucleation and growth rate material functions are dependent on stress, temperature, and time. During this project we have measured the stress and time dependence of these functions at room temperature for 1145 Al, OFHC copper, and Armco iron. Additional but less complete data have been obtained for 2024-T81 Al, high purity Al, high purity iron, and Los Alamos Scientific Laboratory (LASL) graphite. The dependence of the growth rate functions on other material properties has been found in some detail for ductile aluminum and copper and for brittle Armco iron. A comparable understanding of the measured nucleation rate functions has not yet been attained. In addition to the progress listed above, the following new contributions have been made during the course of the project: (1) Development of a computer code, BABS 2, which converts observed crack surface distributions to crack volume distributions, and which shows promise of wide application, (2) Development of computer subroutines DFRAC and BFRAC which, together with SRI PUFF, allow the computation of stress waves in materials that undergo ductile fracture by void growth or brittle fracture by crack growth, (3) Development of the computer code VOID, which computes void growth and collapse in two space dimensions. Modifications of the code are already in use at Stanford Research Institute in applications ranging from cavitation in liquid			

(See next page)

DD FORM 1473  
1 NOV 65

UNCLASSIFIED

Security Classification

14 KEY WORDS	LINK A		LINK B		LINK C	
	ROLE	WT	ROLE	WT	ROLE	WT
Dynamic fracture Prediction of fracture Ductile materials Brittle materials						
ABSTRACT (cont'd)  propellants to prediction of impact damage in human heads. This finite element code includes a new method for computing momentum transfer and utilizes a multidimensional stress relaxation model, (4) Development of an experimental technique, using a tapered projectile head, for obtaining incipient damage data from a single impact experiment, and (5) Development of constitutive relations for damaged material.						